# Evaluating different remote sensing techniques for detection of Saharan dust and characterisation of dust sources

Abushufa, Tarek

*Awarding institution:*
King's College London

**Title:** Evaluating different remote sensing techniques for detection of Saharan dust and characterisation of dust sources

**Author:** Tarek Abushufa

# Evaluating different remote sensing techniques for detection of Saharan dust and characterisation of dust sources

**BY TAREK ABUSHUFA**

**UNDER SUPERVISION OF**
**DR. NICK DRAKE**

**PhD Thesis**

**KING'S COLLEGE LONDON, UNIVERSITY OF LONDON**
**SCHOOL OF SOCIAL SCIENCES AND PUBLIC POLICY**
**PHYSICAL GEOGRAPHY**

**SEPTEMBER 2011**

## Abstract

Mineral dust aerosols play an important role in climate and the Earth's energy budget. However, the nature and complexity of dust sources is poorly understood. Traditional techniques used for mapping the Sahara dust sources like the analysis of surface dust observations, back trajectory analysis of isobar data, and mineral tracers all tell a different story regarding the location of dust sources, they only agree that the Bodélé Depression and western Hoggar Mountains are important sources. Remote sensing techniques have more recently been used to identify Saharan dust sources and the different methods provide more agreement about more Saharan dust sources and also identify the Bodélé Depression and the western Hoggar Mountains as important source of dust.

While there are several remote sensing techniques that can be used to identify desert dust sources yet no comprehensive comparison has yet been done to evaluate their utility. This thesis has evaluated the utility of nine different methods that can be employed to detect dust using MODIS have been investigated by comparing them to sun-photometer aerosol optical thickness (AOT) measurements at a wavelength of 1020µm from Banizoumbou (Niger). The five established techniques that were evaluated, these were: Ackerman (1989), Miller (2003), Handley (2004), Hansell et al., (2007) and the Deep Blue NASA aerosol product Hsu et al., (2003). Many of these methods employ brightness temperature differences (BTD). To determine the effectiveness of this approach all possible MODIS BTD's were computed and evaluated, these were: BTD (12 µm-11 µm), BTD (3.7 µm-12 µm), BTD (8.6 µm-11 µm), and BTD (8.6 µm-12 µm).

To evaluate the accuracy of these dust indices the correlation between the sun-photometer AOT and the result of each MODIS dust index were determined. The results show that the Deep Blue Algorithm gives the highest correlation ($R^2$= 0.91), however the deep blue product has a 10km spatial resolution and thus is not good at locating dust sources, the ultimate aim of this project, furthermore the cloud mask applied to the product routinely masks out most of the dust. The other methods all have a spatial resolution of 1km and thus are more appropriate for this purpose.

Of these methods the Ackerman (1989) shows a high $R^2$ value ($R^2$= 0.71) as do many other methods.

The effect of different surface materials on dust detection was evaluate by studying five different backgrounds in order to see how the dust can be distinguished from these backgrounds using the M test. Over Limestone background, Miller (2003) has got the highest M value followed by Deep Blue and Ackerman (1989), excluding Deep Blue due to the poor cloud mask and visually difficult to trace the dust to their sources, Ackerman (1989) comes second and has an M value close to Miller (2003). However, Ackerman (1989) shows the best result visually. Based on the five tested backgrounds result using different techniques (visually, M test, and statistically) Deep Blue, Miller, and Ackerman present reasonable results.

Based on these results Ackerman (1989) was selected to detect the dust sources over Cyrenaica (Libya) with using MODIS and SEVIRI data. SEVIRI images are also used to study the meteorology of the dust storms in order to provide more information on the wind direction, cause, and lifetime of dust storm. The highest percentage of the dust storms generated from Cyrenaica are caused by Anticyclone 70%. The majority last for six hours, starting at 8:00 am and ending at 14:00 pm. MODIS is used to detect the location of the dust sources and Landsat and Google Earth images are used to identify the geomorphology of the dust sources. Total of 53 dust sources are detected during 2008, 45% from alluvial fans, 15% from lake, 13% from alluvial plains, 6% from agriculture, 6% from river, 2% from multiple landforms in a single MODIS pixel and thus their nature could not be determined, while 13% were diffuse and no source could be detected. Alluvial fans were the most active sources and almost half of these dust sources are located at one large fan located south east of Benghazi.

# ACKNOWLEDGEMENT

This thesis is dedicated to my parents, my wife, and my Kids.

I would like to express my since appreciation to Robyn Inglis (University of Cambridge) as she has kindly provided her results of the grain size analyses. My thanks also to the various individuals and organisations who contributed to the fulfilment of this research and help to make this work interesting and worthwhile.

I am deeply grateful to Dr. Nick Drake, my supervisor for his patience, guidance, encouragement, and support in completing the study. His numerous valuable contributions have been most helpful throughout my entire postgraduate study.

Appreciation is also extended to Professor Amin Missallati for his enthusiastic encouragement throughout my work at BRSC under his supervision.

Finally, the most loving appreciation is due to my wife for her help, patience, and understanding during the last four years.

**Contents**

**List of Figures.**

**List of Tables**

**List of Abbreviations**

| | |
|---|---|
| AERONET | AErosol RObotic NETwork |
| AI | Aerosol Index |
| AIRS | Advanced Infrared Radiation Sounder |
| AIRS | Atmospheric Infrared Sounder |
| AOT | Aerosol Optical Thickness |
| ASTER | Advanced Spaceborne Thermal Emission and Reflection Radiometer |
| AVHRR | Advanced Very High Resolution Radiometer |
| AVIRIS | Airborne Visible and Infrared Imaging Spectrometer |
| BTD | Brightness Temperature Difference |
| CCN | Cloud Condensation Nuclei |
| CSM | Cerebro Spinal Meningitis |
| DAI | Deep Blue Aerosol Index |
| DEM | Digital Elevation Model |
| DSA | Dust Sources Activations |
| DSAF | Dust Source Activation Frequency |
| DSD | Dust Storms Day |
| ED | Emissivity Difference |
| EOMET | Electro Optical and Meteorological |
| ERTS | Earth Resources Technology Satellite |
| ETM | Enhanced Thematic Mapper |
| EUMETSAT | European Organisation for the Exploitation of Meteorological Satellites |
| FOV | Field Of View |
| GCM | Global Climate Model |
| GOES | Geostationary Operational Environmental Satellites |
| GOME | Global Ozone Monitoring Experiment |
| HIRS | High Resolution Infra Red Radiation Sounder |
| HRV | High Resolution Visible |
| IDDI | Infra-Red Different Dust Index |
| IPCC | Intergovernmental Panel of Climate Change |
| IR | Infra Red |
| JHU | Johns Hopkins University |

| | |
|---|---|
| JPL | Jet Propulsion Laboratory |
| LAADS | Level 1 and Atmosphere Archive and Distribution System |
| LEB | Lake Eyre Basin |
| LIDAR | Light Detection and Ranging |
| LLJ | Low Level Jet |
| MISR | Multiangle Imaging Spectro Radiometer |
| MODIS | Moderate Resolution Imaging Spectrometer |
| MSG | Meteosat Second Generation |
| MSS | Multi Spectral Scanner |
| NASA | National Aeronautics and Space Administration |
| NAPAP | National Acid Precipitation Assessment program |
| NDDI | Normalized Difference Dust Index |
| NDSI | Normalized Difference Snow Index |
| NDVI | Normalized Difference Vegetation Index |
| NOAA | National Oceanic and Atmospheric Administration |
| OMI | Ozone Monitoring Instruments |
| RF | Radiative Function |
| RGB | Red Green Blue |
| RMS | Root Mean Square |
| SAL | Saharan Air Layer |
| SEVIRI | Spinning Enhanced Visible an InfraRed Imager |
| SMS | Synchronous Meteorological Satellite |
| SRTM | Shuttle Radar Topography Mission |
| SYNOP | Surface Synoptic Observations |
| TAR | Third Assessment Report |
| TDI | Thermal-infrared Dust Index |
| TM | Thematic Mapper |
| TOMS | Total Ozone Mapping Spectrometer |
| USGS | United State Geological Survey |
| UV | Ultra Violet |
| VISSR | Visible and Infrared Spin Scan Radiometer |
| WMO | World Meteorological Organization |

## 1.1Introduction

Dust is one of main aerosol types in the atmosphere and plays an important role in modulating climate via a number of complex processes (Liu et al., 2008). Bagnold (1941) defined dust as particles having diameters less than 80 µm. The Sahara Desert is the largest desert in the world, covering about 8,600,000 km² and it has recently been shown that it is the dominant source of dust in the world (Prospero et al., 2002). However, the exact nature of the sources of dust is as yet unclear (Goudie and Middleton, 2001).

Each year large somewhere between 400-700 million tons of dust are transported out of the Sahara desert and blown in to the Atlantic Ocean, and some also reaches parts of South America, in particular the Amazon (Swap et al., 1992; Washington et al., 2006). Dust has a major influence on climatology, geomorphology and human geography. It is thought to have a significant impact on climate change (Vermote et al., 2001). There have been a several studies that have focused on the geomorphologic transport mechanisms, origin and environmental impact of dust storms (Washington et al., 2006; Goudie and Middleton, 2001). However the global impact of windblown desert dust is poorly understood and thus is a major concern in the study of the Earths system.

There are a number of important questions that should be considered in order to improve our understanding of dust storms; where the dust is coming from, how often the dust is blown in the air, what is the frequency of the dust storms, what is the concentration of the dust in the air and where the dust is going to deposit (Goudie and Middleton, 2001).

Monitoring and tracing dust using meteorological stations was used before satellite technology. However, the former method was limited due to the temporal and spatial limitations of the stations (Goudie and Middleton, 2001). The high spatial, temporal and spectral resolution of remote sensing data, provides a better chance to monitor and track dust storms, and opens the door for researchers to gain a wider view of aerosol characteristics. Most of the previous work used to detect dust storms using remote sensing has focused on the differentiation between the ground surface, dust and other aerosols, to find a means of quantifying the total amount of dust transport and identify the dust sources. Several techniques have been used for dust storms detection, using different types of sensors. However, no quantitative comparison has been made between them.

## 1.2 Dust and its Effects

In the following section the different environmental effects of dust are explained (rainfall and clouds effects, radiative effects, fertilization, and health effects), as is the dust cycle (production, transport, and deposition of dust).

### 1.2.1 Rainfall and Clouds Effects

Dust particles from dust storms can act as ice and cloud condensation nuclei (CCN) which are essential for the formation of rain (Goudie and Middleton, 2001). An abundance of dust particulates will cause an increase in the number of droplets and an overall decrease in drop size (Tegen 2003; Wurzler et al., 2000). Numerous aerosols will generally lower the precipitation potential, because the high concentrations of mineral aerosols lead to the formation of many small CCN, but few large CCN that can form rain sized droplets. Thus dust emission may not be a consequence of low rainfall, but instead its cause. The efficiency with which dust particles form CCN depends on their ability to absorb humidity from the air (Wurzler et al., 2000).

Thus CCN play an important factor for modifying the cloud characteristics by modifying microphysical and radiative properties (Sassen et al., 2003). Toon (2003) explains how the dust affects clouds: ‘Dust may affect clouds in two ways. All water droplets start off by forming on pre-existing particles. As the number of particles increases, for instance due to a dust storm, the number of cloud droplets may increase. If there are more cloud droplets, the droplets will be smaller because the mass of condensing water is usually fixed by air motions and ambient humidity. Smaller cloud droplets make for a greater surface area and hence brighter clouds. A less well-studied phenomenon is that smaller droplets are also much less likely to collide with each other and create precipitation. By acting as nuclei for triggering ice formation, dust particles can also affect clouds by causing the water droplets to freeze at higher temperatures than expected. Dust may thus be triggering precipitation in low-altitude clouds that otherwise would be too warm to have produced rain, or be triggering rain at lower levels in convective clouds that otherwise would not have produced rain until reaching much higher altitudes where it is colder. Dust may therefore inhibit precipitation by making more and smaller droplets, or enhance it by adding ice particles to warm clouds'. Thus it appears that dust does not always reduce rainfall, whether it does or not depends on the type of cloud and its temperature (Toon, 2003).

### 1.2.2 Radiative Effects

Dust can impact the climate through light absorption and scattering (Wurzler et al., 2000). It can affect short-wave radiation emitted from the sun by reflecting and scattering it back to space, thereby reducing the energy from the sun's rays that reach the Earth, and cooling the atmosphere. In other hand it may warm the atmosphere through absorbing solar and long wave radiation emitted from the land surface. This depends on the particle size and the chemical composition of the dust (King et al., 1999).

Sokolik et al., (1996) used a simple model (Equation 1.1) to assess the direct radiative forcing of airborne dust.

$$\Delta F = K_{atm} K_{opt} \tau \qquad (1.1)$$

$\tau$= global mean dust optical depth

$K_{atm} = (S_o/4)\, T^2\, (1\text{-}N) = 85.5\ Wm^{-2}$

$K_{opt} = \omega\, (1\text{-}g/2)\, (1\text{-}a)^2 - 4a\, (1\text{-}\omega)$

$S_o$ solar constant = 1.370 $Wm^{-2}$

T atmospheric transmission = 0.79

N cloud fraction = 0.6

$\omega$ aerosol single scattering albedo (Ratio)

g asymmetry parameter

a= globally averaged surface albedo

The coefficient $K_{atm}$ depends on water vapour and cloud conditions, while the coefficient $K_{opt}$ provides the aerosol characterization and can be estimated from available dust optical models. These models gives a short-wave radiative forcing, of 0.24 to 0.55 $Wm^{-2}$ over ocean and -0.08 to 0.35 $Wm^{-2}$ over land, resulting in a net global radiative forcing of -0.46 $Wm^{-2}$.

Schwartz et al., (1995) also illustrate the sensitivity of the shortwave radiative forcing by dust to the composition and microphysical properties of clouds estimating an annual average reduction value of about -1$Wm^{-2}$.

Dust can change cloud properties by increasing the reflectance of clouds by enhancing the concentration of aerosol particles, moreover it can increase cloud lifetime which plays an important factor in cooling (Koren et al., 2003; Schwartz et al., 1995; King et al., 1999).

Thus airborne mineral dust plays an important global role due to its radiative-forcing effect on the climate system (Haywood et al., 2001; Washington et al., 2003). Satheesh et al., (2005) presents a simplified block diagram that shows the radiative effects of sea salt aerosols, oceanic sulphate aerosols, and soil dust aerosols (Figure 1.1). Dust production in the first stage depends on surface wind speed, which will affect the dust production rate, if the dust is transported for a long distance, it will cross the Ocean causing a reduction in surface solar flux over the Ocean. Dust deposition can lead to emission of dimethyl sulphide from the oceanic phytoplankton due to iron fertilisation leading to natural production of sulphate aerosols over the ocean, that are also good condensation nuclei for formation of clouds.

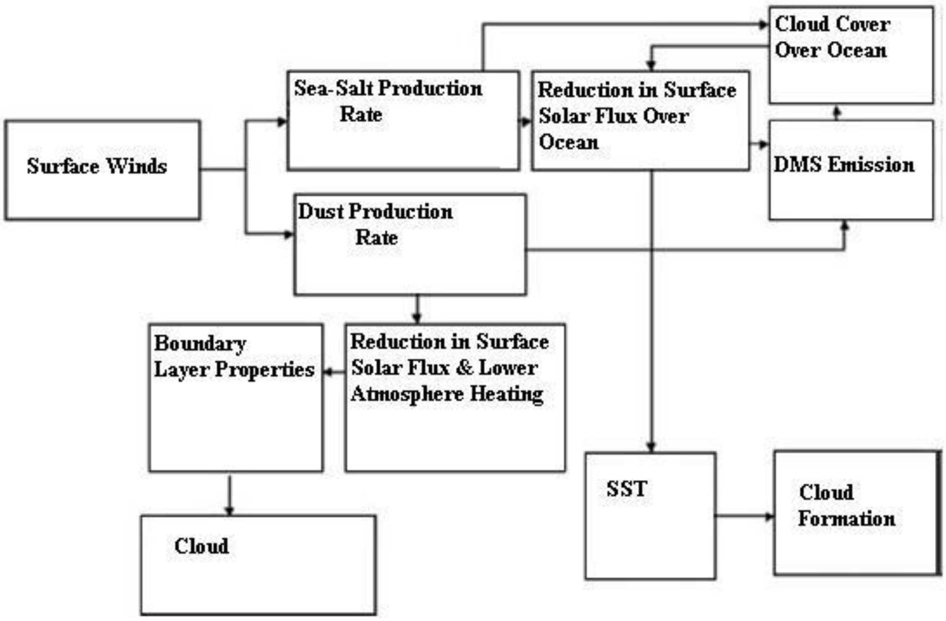


Figure 1.1 Block diagram showing the climate impact of aerosols. (Source: Satheesh et al., 2005)

The level of scientific understanding of the climate radiative forcing of atmospheric aerosols (Figure 1.2) is illustrated by the Intergovernmental Panel on Climate Change (IPCC, 2007). It is concluded that the radiative function RF of mineral dust lies between 0.4 to -0.6 $Wm^{-2}$, with the large uncertainty due to difficulties in determining the anthropogenic contribution to the dust loading and the uncertainty in the optical properties of dust. Tegen et al., (1995) estimated the anthropogenic contribution to mineral dust to be 30 to 50 % of the total dust in the atmosphere, however in contrast Yoshioka et al., (2005) used TOMS AI and suggested cultivation source in the Sahel region contribute 0 to 15% to the total dust emissions in North Africa.

It is clear that our understanding regarding the radiative forcing of mineral dust and aerosols in general are still very low. Moreover the high uncertainty is keeping the door open for the researchers to investigate more about these aerosols effects.

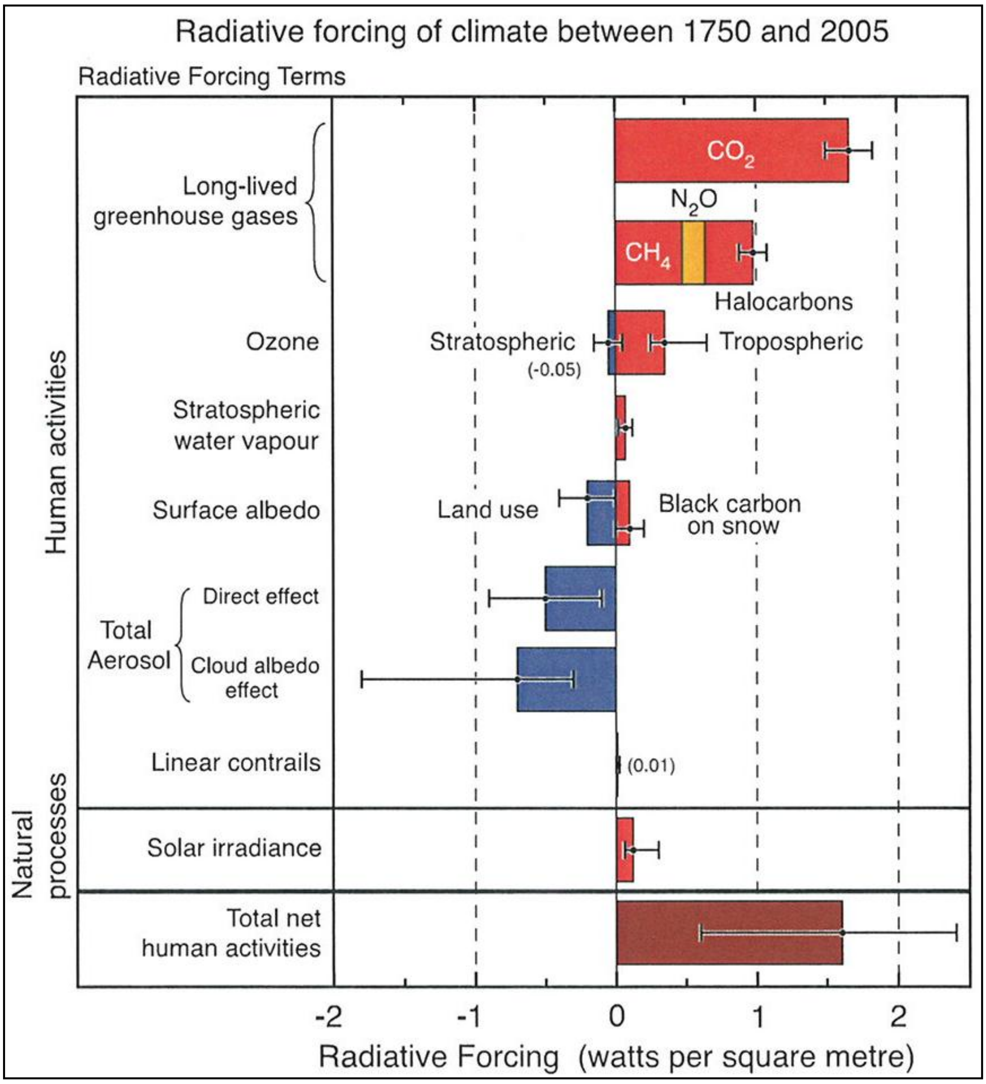


Figure 1.2 Level of scientific understanding regarding the radiative forcing of mineral dust and aerosols. The error bars shows that the highest uncertainty of understanding are from the mineral dust and aerosol. (Source: IPCC 2007)

## 1.2.3 Fertilization Effects

Dust blowing from Sahara has been identified as a significant source of primary nutrients (iron, calcium, etc.) to the oceans and it has been estimated that approximately 50% of the phosphorus transported to the oceans through the atmosphere comes from North African deserts (Savoie and Prospero, 1982). Iron is an important nutrient for all organisms. Dust from Sahara is the dominant source of iron to the ocean, (when dust transport from the land to the oceans actually) and it increases ocean productivity (Falkowski et al., 1998). Prospero et al., (2002) described the relationship between iron and nitrogen fixation stimulation in ocean waters and their link with cyanobacteria. Input of iron, nitrates and ammonia in dust reduces nutrient stress on phytoplankton communities increasing productivity (Gruber and Sartmiento 1997). The Amazon rain forest in South America also derives essential nutrients, mainly phosphate, from Saharan dust (Swap et al., 1992). Kaufman et al., (2005) found 50Tg from a total of 240Tg of dust transported annually across the Atlantic Ocean fertilizes the Amazon Basin. Thus one of the benefits of this dust transport is increased rainforest productivity through the phosphate that Saharan dust contains (Swap et al., 1992). Swap et al., (1996) describe the influence of micronutrients deposited within aeolian dust on the carbon and nitrogen cycles. Deposition in rainforests delivers minerals that act as limiting nutrients for organisms, thereby increasing carbon uptake (Swap et al., 1996).

### 1.2.4 Health Effects

#### 1.2.4.1 Direct Effects of Dust on Human Health

Dust in high concentrations has been linked to problems of public health (Goudie and Middleton 2001; Prospero 1991). Fine aerosols are inhaled leading to deposition in the lung, particulates smaller than 25 μm have been linked with cardiopulmonary mortality, lung cancer, impaired lung functioning, chronic bronchitis symptoms, and liver silicosis (Simpson et al., 2003). Saharan dust events have been shown to be a major source for these particulates both in-situ and in Southern Europe. Wiggs et al., (2003) investigated the health implications of dust produced by the receding Aral Sea. High dust concentrations were blamed for childhood pneumonia, interstitial lung diseases, oesophageal cancer and anaemia. In addition government statistics showed that 50% of childhood diseases were linked to respiratory diseases. Their work indicated an inverse relationship between the amount of dust deposition and indices of human respiratory health.

#### 1.2.4.2 Dust Transport of Disease

Saharan dust is often linked with the cerebrospinal meningitis (CSM) although no direct association has yet been established between the Saharan dust particles and the disease. However, the disease control unit of the ministry of health in Ghana has recorded many cases of CSM during dust storm periods compared with the rest of the year. It is known, that the disease is caused by a bacteria that is deposited in the respiratory tract, possibly through respiration of dust particles (Afeti et al., 2000).

It has been demonstrated that Saharan dust can carry microorganisms. Griffin et al., (2003) have tested twenty six air samples over Virgin Islands and seventeen air samples from aboard ship were collected during Saharan dust storms events and non-dust storms events and screened them for the presence of bacteria and fungi. In non-dust storms events they found the presence of bacteria and fungi was 0.5% and 0.7% respectively from a total of 3652 litres of air. However, during Saharan dust storms events 7.2% and 3.2% respectively was found from a total of 2369 litres of air.
Viable microorganisms, macro- and micro nutrients, trace metals, and an array of organic contaminants carried in the dust air masses and deposited in the oceans and on land may play important roles in the complex changes occurring on coral reefs worldwide (Garrison et al., 2003). For example Shinn et al., (2000) show that much of the coral reef decline in the Caribbean is a result of pathogens transported in dust from North Africa.

## 1.3 Chemistry of Dust

Because the chemistry of the dust involved in dust storms is important in understanding their effects on different fields such as; possible effects on soils, precipitation chemistry, ocean biogeochemistry, and weathering phenomena.

Table 1.1 presents the major element concentrations of Saharan dust and the world mean for each mineral as sampled from the Harmattan source areasconsistent with world samples, Saharan dust is dominated by $SiO_2$ and $Al_2O_2$, the large amount of $SiO_2$ indicates the importance of quartz in the aeolian dust. Saharan dust also has appreciable amounts of $Al_2O_3$ and $Fe_2O_3$, however it is less rich of MgO and CaO.

Table 1.1 The element analysis of deposited dust at Harmattan, compared to the world mean (Source: Goudie and Middleton 2001)

| Mineral | Sahara (Harmattan) | World Mean |
|---|---|---|
| $SiO_2$ | 60.95% | 59.9% |
| $AL_2O_3$ | 11.02% | 14.13% |
| $Fe_2O_3$ | 4.50% | 6.85% |
| MgO | 0.76% | 2.60% |
| CaO | 2.31% | 3.94% |
| $K_2O$ | 2.81% | 2.35% |

## 1.4 Production of Dust

The Saharan desert is recognized for the most production of dust in the world, as shown in (Figure 1.3). The exact nature of the sources of this dust is as yet unclear. Goudie and Middleton (2001) review the recent work on the dust sources, acknowledge that the Sahara is the largest source of dust in the world and conclude that our knowledge about the precise location of Saharan dust sources still remains poor. Moreover, there is no link between the sources and the seasonal Sahara dust transport pathways.

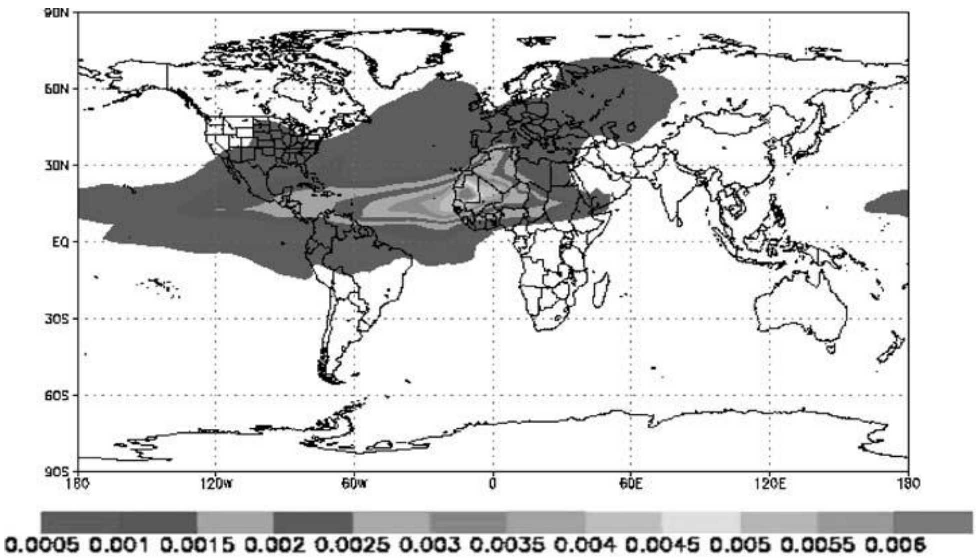


Figure 1.3 Model simulation of distribution of mean column dust mass (kgm−2) for Sahara dust storms in July, 2000. (Source: Prospero et al., 2002)

Prospero et al., (2002) used the Total Ozone Mapping Spectrometer (TOMS) to map the world major dust source regions, they found the most dust sources are clearly in the "dust belt" located in the northern Hemisphere which is recognized as the dominant source of dust and the Sahara is the most active dust source in the "dust belt". However, our understanding regarding the climatic and geomorphologic nature of the dust sources still remains low. For example Goudie and Middleton (2001) suggest dust sources peak in the rainfall range of 100mm to 200mm mean annual rainfall. However, the Sahara's two major sources (the Bodélé Depression and an area covering eastern Mauritania, West Mali, and southern Algeria) are located in areas that receive very low rainfall, and thus do not match the view of Goudie and Middleton (2001). Prospero et al., (2002) conclude that most of the world dust sources are located in topographic lows. A few of these topographic depressions have since been looked at in detail. One that has recently been studied in the Bodélé Depression. Warren et al., (2007) show that the diatomite sediments left behind by the desiccation of a giant lake know as Lake Mega Chad is the source of the dust. They suggest two factors controlling dust production; (1) the uplift of dust depends on the low level jet (LLJ); (2) the breakdown of the diatomite by the impact of saltating sand grains. Warren et al., (2007) found that the Bodélé Depression as a dry lake emits the largest quantity of dust compared to the other dry lakes, because the wind is stronger than the other part of the Sahara and the diatomite in the Bodélé Depression has low density compared to the quartz, thus being easily broken down into dust sized particles.

Though these studies identify the general nature of one or two sources, the poor spatial detail of TOMS means that for many sources we do not know exactly what landform the dust is derived from. Thus the nature of these sources often remains an enigma and the reason for the large amount of dust coming from the Sahara remains unexplained.

### 1.4.1 Factors Controlling Dust Production

Dust production depends on several factors: uplift, wind speed, and the supply of wind erodible material (Prospero et al., 2002). Dust production arises from saltation sandblasting, when winds above a threshold velocity transport sand grains horizontally, producing smaller particles by impact other controls are on rainfall, surface roughness, topography, friction, clay, water, and vegetation cover (Prospero et al., 2002). These controls are discussed in turn below.

Figure 1.4 displays the process of dust entrainment. This occurs when winds pick up particles, the size of sand or dust and moves them. The faster the wind the heavier the particle can be carried. The heavy grains which are >500 µm will creep on the surface, while the particle that have the size from 70 to 500 µm will saltate on the surface generating new particles, by abrasion, while the particles of the size 20 to 70 µm will experience short term of suspension, and the particle of size <20 µm will stay in the air for long term suspension in the atmosphere. The sandblasting process (Figure 1.4) happens when the fine particles are impacted by saltating particles and ejected into the air.

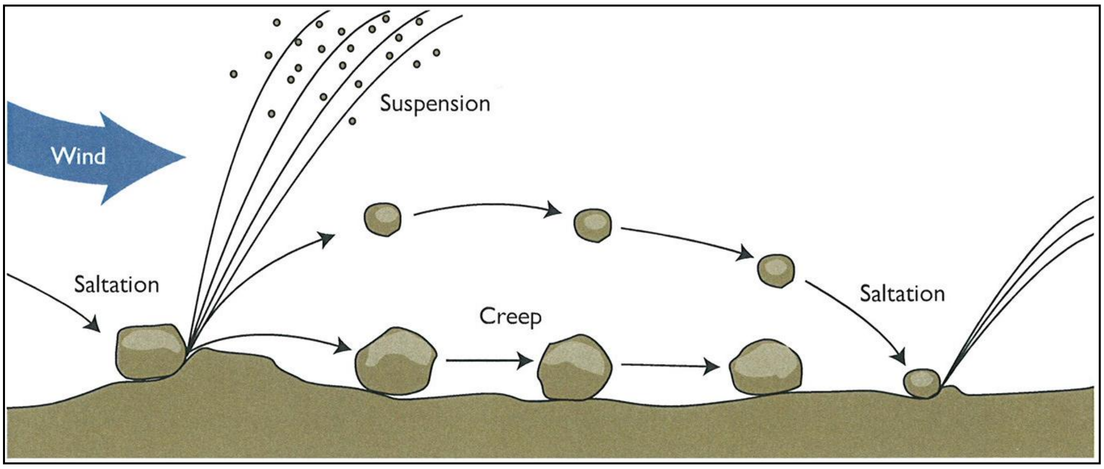


Figure 1.4 Process of dust transport. (Source: McCauley, et al., 2005)

The drag velocity $u_*$ (ms$^{-1}$) is the energy needed to uplift the particle from the surface (Equation 1.2), is provided by high wind near the surface.

$$u_* = \sqrt{\tau_0 / \rho_a} \qquad (1.2)$$

$\tau_0$ is the drag force per unit area (cm¯¹/sec¯²)

$\rho_a$ is the density of the air (g cm¯³)

The energy available for dislodging, entraining and transporting particles comes from the wind. Velocities near the bed provide high shear forces. Shear is best expressed in terms of the shear velocity. Both $u_*$ and $\tau_0$ increase as the wind velocity (u) increases. At some critical point grains on the bed start to move (Pye, 1987).

This point is referred to by Bagnold (1941) as the 'fluid threshold' and can be expressed by:

$$u_{*t} = A\sqrt{\frac{\rho_p - \rho_a gD}{\rho_a}} \tag{1.3}$$

In neutral, stably stratified atmosphere, with high Reynolds number, velocity usually increases logarithmically with height above the surface and can be expressed by.

$$u_z / u_* = 1/K \ln z / z_0 \tag{1.4}$$

$u_{*t}$ is the wind velocity at height z

$z_0$ is the height at which the velocity is zero

K is von Karman's constant usually =0.4

If the surface is rough, $u_*$ is higher for the same ambient wind speed than over smooth surface.

There are two forces that control the loose particles on the surface: the horizontal drag force and vertical lift force, these forces are proportional to $\rho_a d^2 u_*$ where, ( $\rho_a$ ) is the density of the air, (d) is the particle diameter, and ( $u_*$ ) is the drag velocity. However, the particle is under the force of gravity $g(\rho_p - \rho_a)d^3$ where ($\rho_p$) is the particle density, and (g) is the gravitational force. Lift may raise grains slightly more effectively on a rough surface than on smooth surface and on grains already in motion than on static grains. Moreover lift is important to the initial start of the particle ejection. There are two types of drag: surface drag which is the skin friction between the particle and the air, and form drag. Form drag is the difference between windward pressure and pressure on the lee sides of the grain. The size and shape of the body play important factor in the form drag. Due to the high friction between the air and the top part of the grain rolling and sliding may be encouraged (Pye, 1987).

### 1.4.2 The Effects of Surface Characteristics

There are several characteristics of the surface that can affect dust entrainment. One of these is turbulence, the main effect of turbulence is to vary lift and drag forces on the surface. Rasmussen et al., (1985) found that $u_*$ can vary by 10% if the turbulence is exceeded by 240 seconds. Nickling (1978) found a good correlation between the rate of dust transport and the levels of turbulence.

Surface roughness plays a big role in wind erosion and has significant influence on the particle entrainment close to the surface, when the surface roughness increases, ( $z_0$ ) will increase the threshold speed of the particle movement will increase and the sand emission from the surface will decrease. Thus the roughness height ( $z_0$ ) is a critical factor in sand transportation. Greeley et al., (1990) has shown that the ( $z_0$ ) depends on the height, size, shape and roughness elements. However, each of these factors has a relative role which is difficult to discover. In the case of vegetation Gillette et al., (1980) present a list of ( $z_0$ ) values to cover most desert surfaces. In most near-uniformly vegetated surfaces, there are three characteristics of vegetation that have influence on the value of ( $z_0$ ): height of plants, density of planet cover, and plant litter. Gillette et al., (1988) notes that vegetative residue has significant effects to the movement of dust based on the amounts of the residue.

Moisture has a significant effect on the wind by increasing the threshold of movement, were the threshold of movement is defined as "the size limit of particles that can be carried by a wind of a given velocity" (Cooke et al., 1993). Azizov et al., (1979) estimate that 4% of water in the soil limits of the wind erosion whereas Goldsmith et al., (1988) notes that there is no particle movement if soil moisture is as low as 1.8% by weight, even in high wind conditions. Hotta et al., (1984) found problems in comparing the moisture concentrations, because of differences in the content of organic matter such as algae and bacteria that also have a valuable effect on entrainment. Moreover they stated that during windy conditions the evaporation increases, and the threshold on a wet surface may rapidly become similar to the threshold on a dry surface.

Grain size has a big influence to the transport of dust. The distance which the grain can be travel from the source to the destination based on the size of the particle, in general particle that have a size less than 70 µm can travel in the air, while grains more than 70 µm will creep on the surface. Udden (1898) found that most of the samples he collected under different conditions of deposition were in the size range from 62.5 µm to 15.6 µm. Dust from 62 µm to 31 µm might travel 320 km from its source, dust from 31 µm to 16 µm might travel 1600 km from its source were dust have size less than 16 µm might stay in suspension for long time and travel further around the globe (Udden, 1898). Prospero et al., (1970) found that dust larger than 20 µm travelled more than 4000 km from its Saharan source. Middleton et al., (2001) show that Saharan dust with a particle size > 62.5 µm can travel more than 3000 km.

### 1.4.3 Management of Soil Erosion

Soil erosion can be managed by controlling those factors outlined above that reduce erosion. Soil management is particularly issue in the Sahel as it is thought by some to produce a significant amount of North African dust. Management to control wind erosion are critical and should be considered on clay and silty soils that are potential dust sources. There are several ways can be used in order to manage soil erosion from the dust storms which will lead to soil erosion such as; crop and residue cover, crop rotation, tillage practices, and contour and strip cropping. Several consortia have been established through the Soil, Water, and Nutrient Management (SWNM) of the Consultative Group on International Agriculture Research (CGIAR) to encourage implementation of erosion control measures. These consortia use an integrated, interdisciplinary, and community based approach that involves the land users. It focuses on the impact of the soil erosion, emphasizes community involvement, and provides scientific data for a rational erosion control decision making.

## 1.5 Transport and Deposition of Dust

Dust transported in the atmosphere is usually less than 100 μm but the actual size depends on the physical characteristics of the airflow. Deposited samples give information on particle size and mineral content of dust. Samples that contain substantive clay particles (< 2 μm) have been reported, moreover grains in excess of 150 μm have been reported as well, and though fallout is dominated by fine grains, particles greater than 20 μm have been known to be transported more than 4000 km (Goudie and Middleton 2001). The relative importance of each transport mode depends on the particle size characteristics, the structure of the deflated material and the nature of turbulent diffusion in the area concerned (Anderson and Hallet, 1986). Dust removal from the atmosphere occurs by rain washout otherwise known as "wet deposition" and by gravitational settling "dry deposition" (Tegen and Fung 1994).

Pye (1987) has listed three mechanisms for dry deposition of dust:

1- A reduction in wind velocity.

2- If the dust particles interact with a rough surface or moisture.

3- If the particles become charged.

Dust returns to the ground in a very short time if the settling velocity of dust exceeds the vertical velocity of wind, or stays in suspension if the vertical velocity of wind exceeds the settling velocity of dust, were the settling velocity of dust depends on its mass and shape (Pye, 1987). The settling velocity can be calculated using Stoke's Law as a function of square of the grain diameter (Equation 1.5) (Pye, 1987).

$$U_f = KD^2 \tag{1.5}$$

$U_f$ is the settling velocity (cms$^{-1}$)

$D$ is the grain diameter (9cm)

$K = \rho_p g / 18\,\mu$

$\rho_p$ is the particle density of the grains (2.65 g cm$^{-3}$ for quartz)

$g$ is the acceleration due to gravity (cm s$^{-2}$ )

μ is the dynamic viscosity of the air (N.s/m$^2$) x 10$^{-5}$

Using the ratio $U_f / u_*$ dust must have a ratio of upward to downward movements >1 to remain in the atmosphere for a considerable time (Pye, 1987). Patterson and Gillette, (1977a) showed that, if the ratio of upward to downward movements =0.5 for grains have a settling velocity0.4 $u_*$ it is mean dust will return back to the surface very quick because of the force required to hold the dust in air is not enough and cannot resist the settling velocity. The smaller particles can remain in the atmosphere for weeks, most of the dust transportation occurs at altitudes of several kilometers.

Wet deposition may occur in two ways, the first occurs within a cloud when the dust particles merge with the water droplets and fall to earth in rain, the second occurs below a cloud when raindrops scavenge dust during their fall to Earth. The amount of the wet deposition is based on the season, location, and amount of rainfall (Goudie and Middleton 2006).

## 1.6 Modeling Dust

Modeling dust depends upon the capability to simulate the physical processes of the emission, transport, and deposition of the dust cycle. Several models have been developed to help understand the mechanism of the dust entrainment. Gillette and Passi (1988) developed the first model to estimate the dust emissions caused by wind erosion for the United States for the National Acid Precipitation Assessment program (NAPAP), using the dust emission function (Equation 1.6). The model is a result of combining the expected dust production caused by wind erosion with the land surface properties. Several effects were considered in this model including the effects of vegetative residue, live standing plants, roughness of the soil, soil texture, and atmospheric precipitation. The model is based on a dust emission function:

$$E = C\sum_{i=1}^{N} R_i g(L_i) A_i \Delta T \int_{U_{ri}}^{\infty} G(U)\, p_i(U)\, dU \qquad (1.6)$$

E is the mass of dust emitted in the time period ΔT

C Constant

$R_i$ Effect of soil roughness

$g(L_i)$ Effect of field length, $L_i$

$A_i$ Area of the land being considered

G(U) Vertical mass flux of dust as a function of the wind speed

$P_i(U)$ Probability density function of the wind speed

dU Change of wind speed

Alfaro et al., (2004) has also modeled the process of mineral dust emission by wind erosion in arid and semi-arid areas, by combining saltation and sandblasting models. The saltation model which was developed by Marticorena and Bergametti (1995) mainly depends on the dry size distribution of the wind-erodible fraction of the soil surface to find $p(D)$ of each class of soil. The threshold of motion ( $u_{*t}$ ) for each soil class were computed to assess the magnitude of saltation $f_h(D)$ .

The total saltation flux $F_h$ can be calculated by summing the magnitude of saltation weighted by wind-erodible fraction as is shown in (Equation 1.7).

$$F_h = \sum p(D) f_h(D) \tag{1.7}$$

P(D) Soil aggregate size class

$f_h$ (D) Magnitude of saltation

Soil aggregate size class

Alfaro et al., (1997) develop a model using the wind tunnel to provide the mass size distribution of dust raised from the ground by the sandblasting process. Alfaro et al., (1998) developed the sandblasting model using the wind tunnel simulations of wind erosion, using different natural soils from dust source areas. To a first approximation, the size characteristics of these populations seem to be independent of the soil texture and mineral composition. Moreover, the experiments showed that the largest particles could be released even at slow wind speeds, but that it took increasingly larger energies to produce the second finest and finest types of particles. In other words, the finer the particles, the higher their binding energy within the soil aggregates. The experiments show that most of sand grains during the saltation process do not rebound and remain on the clay surface. By comparing the value of kinetic energy ($e_c$) to $d_{fine}$ (The energy of cohesion for the fine particle) and $d_{ag}$ (The energy of cohesion for the aggregate particle), three cases can be distinguished:

In the first case, $e_c < e_{ag} < e_{fine}$ the kinetic energy of the saltating grains is too low to remove particles from the surface

In the second case, $e_{ag} < e_c < e_{fine}$ aggregates only can be removed from the ground.

In the third case, $e_c > e_{fine}$ aggregates can be removed from the ground and part of the fine particles can be sandblasted.

This experiments show that the proportion $p_{fine}$ of fine to aggregates increases with increasing values of $u_*$. the following expressions that are linked with the previous cases were adopted.

1- If $e_c > e_{fine} > e_{ag}$ then and $p_{ag} = 1 - p_{fine}$ (1.8)

2- If $e_{fine} > e_c > e_{ag}$ then $p_{fine} = 0$ and $p_{ag} = 1$ (1.9)

3- If $e_{fine} > e_{ag} > e_c$ then $p_{fine} = p_{ag} = 0$ (1.10)

For a given value of $u_*$, by combining the lognormal distribution in equations 1.8, 1.9, and 1.10, it is possible to compute the mass size distribution of the aerosol. The $\sigma_{fine}, e_{fine}$, and $e_{ag}$ can be calculated by using an iterative procedure of data inversion to provide a mass size distribution close to the experimental mass size distribution. Alfaro et al., (1997) conclude that the sandblasting model shows good correlation between the measured and the experimental mass size distribution. Moreover, they found the size distribution of the dust produced by sandblasting in arid areas has the diameter range of 1-10 µm.

When this model is scaled up and applied over large areas a map of the amount of fine particles and sand is needed. Yet our poor understanding of the nature of such source areas and their exact location currently precludes the development of such maps. Ginoux et al., (2001) used 1° x 1° topographic elevation map as a preferential source map for his global dust model. He indicates that the dried lake beds provide the optimum condition for the preferential source map. Such deposits are found in depressions, thus depressions in the Digital Elevation Model (DEM) were identified and scaled to simulate areas that contain dry lakes. Tegen et al., (2002) also used a topographic map to compute dust emissions at global scale, by specifying the extent of the depressions. However due to lack information about soil properties in the preferential source map, large uncertainties in the result extracted from these models can be expected. In particular the Bodélé Depression does not have enough information to feed in the model due to the difficult access to the site Tegen et al., (2002).

## 1.7 Daily and Seasonal Timing of Dust Storms

There are several factors that can affect the seasonality of dust storms, such as: rainfall, snow cover, the desiccation of closed lake basins, wind conditions, convectional activity, and agronomic practices (Goudie and Middleton 2006). Dust storms are usually activated at certain parts of the day. Wang et al., (2005a) identified that most of dust storms in China are active in the afternoon and few by night, a similar period of time is found in the Gobi desert (Middleton 1991). Middleton (1986a) established that most of the dust activity in the Middle East region is during the day time, for example in Kuwait 50% of dust storms was detected between 12:00 and 17:00 hours (Safar 1985). Orgill and Sehmel (1976) established that in the United States America most of the dust activity happens during the afternoon, Godon and Todhunter (1998) confirmed that 70% of dust activity in North Dakota occurs between 12:00 and 18:00 hours. In the Sahara desert the dust maximum occurs between the morning and mid-afternoon (N'T Chayi et al., 1997).

Table 1.2 summarized the seasonality of each major region in Africa. The most active season of the dust storms in the Sahara is during summer, were at the Sahel region dust active during winter and that is depends on the seasonal wind cycle crossing each region.

Table 1.2 Seasons or months of maximum dust storm activity (Goudie and Middleton 2006)

| Location | Season (months) |
|---|---|
| Bodélé | Early summer (April-June) |
| Egypt | Winter/Spring (December-May) |
| Etosha (Namibia) | Autumn (August-November) |
| Eritrea | Summer (June-August) |
| Northern Sahara | Summer (April-August) |
| Sahel | Winter (November-March) |
| Tokar delta (Sudan) | Summer (June-July) |

Goudie and Middleton (2006) presented data in (Table 1.3) showing the percentage number of days with blowing dust/sand per month throughout the year in the Sahara using the meteorological data. The two months showing the highest percentage of dust transportation per day were highlighted in yellow. In the southern of Sahara such as Abidjan and Dakar, the highest percentage is recorded between December and March and this matches the time of the Harmattan wind. In the Northern and central of Sahara the highest percentage is between March and August.

Table 1.3 Seasonality of blowing sand/dust in North Africa in percentage number of day form

| Location | Jan. | Feb. | Mar. | Apr. | May | June | July | Aug. | Sep. | Oct. | Nov. | Dec. |
|---|---|---|---|---|---|---|---|---|---|---|---|---|
| Abidjan | 45.5 | 9.1 | 9.1 | - | - | - | 9.1 | - | - | - | - | 27.3 |
| Karia | 15.9 | 12.6 | 12.6 | 7.3 | 2.0 | 2.0 | 1.3 | 3.3 | 3.3 | 9.9 | 15.2 | 14.6 |
| Maiduguri | 16.1 | 13.3 | 15.0 | 11.1 | 3.9 | 1.1 | 1.1 | 0.6 | 1.1 | 7.2 | 13.9 | 15.6 |
| Sokota | 13.2 | 12.0 | 15.0 | 11.4 | 6.0 | 2.4 | 1.8 | 1.2 | 1.8 | 7.8 | 14.4 | 13.2 |
| Niamey | 13.7 | 11.8 | 14.3 | 11.8 | 7.5 | 4.3 | 1.9 | 1.2 | 2.5 | 8.1 | 10.6 | 12.4 |
| Zinder | 11.8 | 10.8 | 11.8 | 10.3 | 8.7 | 7.2 | 3.1 | 1.0 | 4.1 | 9.7 | 10.8 | 10.8 |
| Mopti | 13.6 | 12.8 | 14.4 | 12.0 | 8.0 | 8.0 | 4.0 | 0.8 | 2.4 | 6.4 | 6.4 | 11.2 |
| Dakar | 15.7 | 13.0 | 14.8 | 13.0 | 9.3 | 3.7 | 1.6 | 0.9 | 2.8 | 6.5 | 7.4 | 11.1 |
| Timbuktu | 9.0 | 7.8 | 10.1 | 10.1 | 9.6 | 11.7 | 9.6 | 6.4 | 6.4 | 6.4 | 4.8 | 7.8 |
| Agadez | 8.1 | 7.7 | 9.9 | 9.0 | 10.8 | 10.8 | 10.7 | 6.3 | 5.9 | 6.8 | 7.2 | 7.2 |
| Nouakchott | 9.2 | 8.4 | 9.9 | 9.9 | 10.6 | 9.5 | 7.7 | 6.2 | 7.0 | 7.3 | 6.6 | 7.7 |
| Bilma | 8.3 | 8.3 | 10.6 | 9.3 | 9.3 | 9.3 | 10.2 | 8.8 | 6.9 | 6.0 | 6.0 | 6.9 |
| Atar | 8.1 | 6.7 | 9.1 | 7.7 | 7.7 | 9.6 | 12.4 | 12.0 | 9.6 | 5.7 | 5.3 | 6.2 |
| Touadhibou | 7.7 | 7.3 | 9.8 | 9.8 | 10.6 | 10.6 | 10.2 | 8.9 | 8.1 | 6.1 | 5.3 | 5.7 |
| Ad Dakhla | 8.4 | 6.7 | 7.6 | 4.2 | 6.7 | 8.4 | 13.4 | 14.3 | 8.4 | 6.7 | 6.7 | 8.4 |
| Sousse | 9.7 | 7.5 | 6.0 | 9.0 | 9.0 | 9.7 | 17.2 | 12.7 | 6.7 | 3.7 | 7.5 | 1.5 |

## 1.8 Concentration of Dust in the Air

Numerous observations have now been made on the dust concentration of air to help indicate areas were dust is concentrated. Duce (1995) used high volume filtration systems to measure dust concentration, they found dust concentrations are in the range between $10^2$μg m-$^3$ and $10^5$μg m-$^3$ in the Tar desert of North West India and the Great Plains of United States. Offer and Azmon (1994) recorded dust concentrations range between 1578μg m-$^3$ and 4204μg m-$^3$ during dust storms. Leple and Brine (1976) stated that during some dust storms concentrations generated from West Africa can reach 13421μg m-$^3$. This has been confirmed by Gillies et al.,

(1996) who found high dust concentrations in West Africa during some dust storms and recorded levels as high as 13735µg $m^{-3}$.

Figure 1.5 illustrate the relation between the mass concentration of dust in the air and the visibility of the dust, when the mass concentration of dust is over 300µg $m^{-3}$ the visibility will reduced to less than 2 km, where if the mass concentration of dust is less than 100µg $m^{-3}$ the visibility will be good. This forms the bases for measuring the amount of dust in the atmosphere, as discussed in the following section.

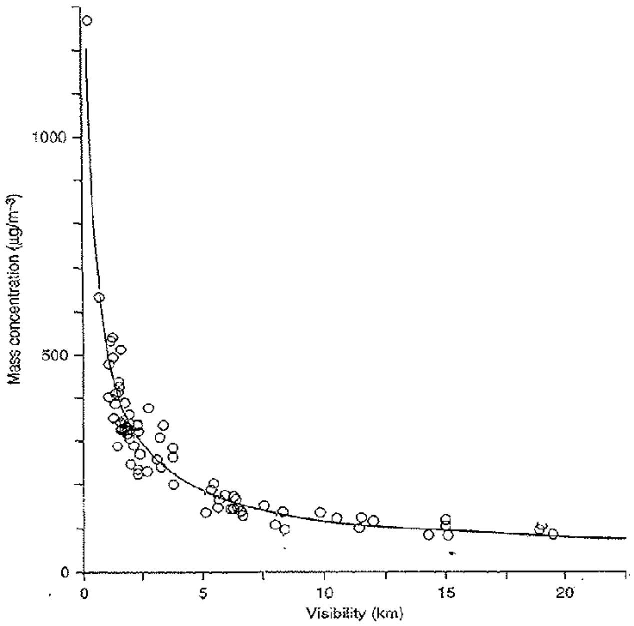


Figure 1.5 Graph of total mass concentration versus visibility of the dust with the corresponding regression curve. (Source: Goudie and Middleton 2006)

## 1.9 Measuring Dust Using Ground Based Techniques

Dust activity can be monitored using ground-based instruments such as sun-photometer and human observations. There are numerous means to determine the sources of dust such as the analysis of mass size distributions, mineralogy, isotopic ratios, fossil content, plant waxes and pollen, electron spin resonance, and three dimensional back trajectory analyses (Goudie and Middleton 2006). Table 1.4 listed some methods used to detect dust sources using ground –based instruments.

Table 1.4 Methods used for dust monitoring and identification of source areas (Source: Goudie and Middleton 2006)

| **Dust characteristic** | **Selected references** |
|---|---|
| Mass size dust | Prospero et al., (1970) |
| Mineralogy and elemental composition | Paquet et al., (1984) |
| Stable isotopes | Aleon et al., (2002), Wang et al., (2005b) |
| Lead isotopes | Turkian and Cochran (1981) |
| Radon-222 | Prospero and Carlson (1972) |
| Magnetic mineral assemblages | Oldfield et al., (1985) |
| Aluminium concentration | Duce et al., (1980) |
| Aerosol-crust enrichment | Rahn et al., (1981) |
| Rare earth element (REE) signature | Gaiero et al., (2004) |
| Single scattering albedo (SSA) signature | Collaud Coen et al., (2004) |
| Scanning electron microscopy of individual grain features | Prodi and Fea (1979) |
| Continentally derived liqids | Gagosian et al., (1981) |
| Pollen, plant waxes | Franzen et al., (1994), Dahl et al., (2005) |
| Enzyme activities | Acosta-Martiez and Zobeck (2004) |
| Trace elements | McGowan et al., (2005), Marx et al., (2005a,b) |
| Foraminifera | Ehrenberg (1849) |
| Electron spin resonace | Toyoda and Naruse (2002) |

The traditional method involves looking from the window and seeing if the visibility has changed compared to the normal visibility in clear sky conditions. Dust causes a reduction in visibility (Figure 1.5) and this confirms the presence of dust. Estimating how far it is possible to see indicates the amount of dust. This is a qualitative method but it has been widely used and this sort of data is widely available. However, using ground station methods provides good temporal information but the spatial distribution of the stations is limited. Middleton and Goudie (2001) reviewed the methods used in the past to identify the source areas of dust storms using; analysis of surface dust observations at meteorological stations, back trajectory analysis of isobar data, and mineral tracers. The classic study of dust detection employs the analysis of observational data recorded at meteorological stations using set of standardized codes to study and map the dust in the atmosphere. This method suffers from the lack of stations in the Sahara. Moreover, at the few stations that exist, the data is poorly archived and recorded only one or two times a day. Notwithstanding thus in the past 25 years, a number of studies have intensively used the coded weather observation data for dust storms detections. For example O'Loingsigh et al., (2010) used data from weather stations to compare and investigate how different methods of recording and archiving Surface Synoptic Observations (SYNOP) codes (Table 1.5) defined by the World Meteorological Organization (WMO) relating to wind erosion and dust transport. By examining 8 years of wind erosion data in the Lake Eyre Basin of central Australia from 2000 to 2008 it was shown that such data can be inaccurately recorded. They conclude that the dust days per year in the Lake Eyre were under-estimated by 7%.

Table 1.5 Dust related codes as part of the 100 SYNOP internationally recognised (WMO) weather codes (Source: O'Loingsigh et al., (2010)

| SYNOP code | Weather description |
|---|---|
| 06 | Dust Haze |
| 07 | Raised dust or sand |
| 08 | Well-developed dust whirls |
| 09 | Distant or past dust storm |
| 30 | Decreased slight or moderate sand or dust storm with visibility <1000m but >200m |
| 31 | Stable slight or moderate sand or dust storm with visibility <1000m but >200m |
| 32 | Begun or increasing slight or moderate sand or dust storms with visibility <1000m but >200m |
| 33 | Decreased severe dust storm with visibility <200m |
| 34 | Stable severe dust storm with visibility <200m |
| 35 | Begun or increasing severe dust storms with visibility <1000m but >200m |
| 98 | Thunderstorm with dust or sand storm |

The back trajectory analysis of isobar data can be applied to major dust transport events over long dust transport distances such as dust transported from the Sahara to the Europe and Caribbean basin (Middleton and Goudie 2001).

Mineral tracers can also be used to determine dust sources (Middleton and Goudie 2001). The method is based on our knowledge of the mineralogy of surface deposits in source areas. However, there are large regions of the Sahara where we do not have information about the mineralogy of the area where the dust is expected to come from. Thus the method is not commonly used.

Ground-based sun-photometric measurements are the most effective way to determine dust quantitatively (Holben et al., 1998). To operate Ground-based sun-photometric station, considerable manpower is needed. Because the change of the output voltage caused by aerosols are very small most of the time, so careful calibration must be under taken. Moreover, it does not provide global coverage and most of the ground stations have limited archives due to the limited operational time. The AErosol RObotic NETwork (AERONET) is used in this study to evaluate the different remote sensing techniques for measuring dust.

The AERONET program is a ground-based remote sensing aerosol networks established by National Aeronautics and Space Administration (NASA). AERONET provides a long-term, continuous and readily accessible public domain database of Aerosol Optical Thickness (AOT), microphysical and radiative properties for aerosol research and characterization and validation of satellite retrievals (Source: http://aeronet.gsfc.nasa.gov/). AERONET data has not been used to look at Saharan dust sources because of several limitations: (1) the stations around Sahara are located far from the main dust sources due to difficulty of access to the sources, (2) only few stations from the 29 North African stations have full archives of data, (3) some of these stations do not operate any more.

Figure 1.6 Sun-Photometer Ground station, one of the 29 ground stations distributed over Sahara to measure the (AOT) of the atmospheric aerosol. (Source: http://aeronet.gsfc.nasa.gov/)

AERONET provides observations of AOT measured by using Sun-Photometer ground stations as shown in (Figure 1.6). The sensors are placed on the moving platform of the automatic solar tracking unit and pointed towards to the Sun from 7am-7pm.

AOT is expression for the aerosol concentration transmitted through the atmosphere, by measuring the AOT we actually measure how much sunlight passes through the atmosphere to reach the Earth’s surface. This includes the scattering of light by molecules in the atmosphere, which occurs even when no aerosol are present. The Sun-photometer is an instrument that used to measure the AOT by measures direct light from the sun at a particular wavelength. The Sun-photometer measures the AOT in units of voltage and by using the globe data server, the voltage can be converted to aerosol.

The voltage measured by a sun-photometer is proportional to the spectral irradiance: ( $I_1$ ) the intensity of sunlight of a particular wavelength. The sensors provide information to calculate the columnar AOT by measuring the diffuse and the direct components of the solar radiation based on the Beer Lambert Law (Equation 1.11).

$$I_1 = I_o e^{-(am)} \tag{1.11}$$

Where ( $I_0$ ) the intensity of sunlight just above Earth's atmosphere by sun-photometer measurements estimated by the sun photometer using the Langley extrapolation. AOT can be estimates by

$$AOT = a = -\mathrm{Log}_{10}(I_1 / I_0) \tag{1.12}$$

$$a = a_a + a_R(p / p_0) \tag{1.13}$$

$a$ The total atmospheric optical thickness
$a_a$ The aerosol scatter
$a_R$ The Rayleigh scattering

The Rayleigh scattering is proportional to the ratio of atmospheric pressure $p / p_o$ at the observer's location.

AOT data are computed for three data quality levels: Level 1.0 (unscreened), Level 1.5 (cloud-screened), and Level 2.0 (cloud-screened and quality-assured). In this study Level 2.0 has been used to insure that AOT has got the highest level of data quality.

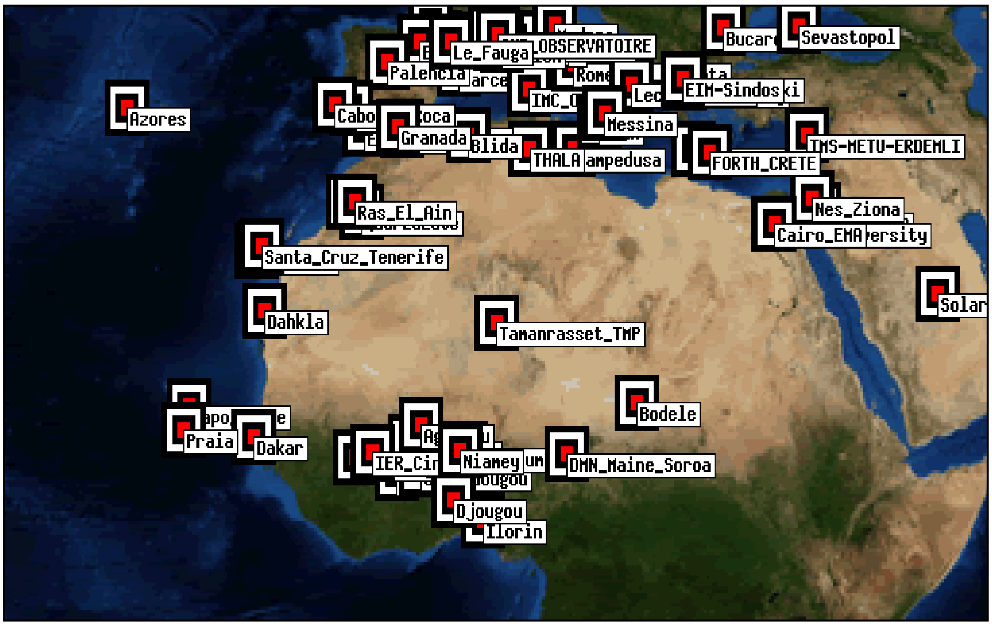


Figure 1.7 Distribution of 29 AERONET station over Sahara. (Source: http://aeronet.gsfc.nasa.gov)

There are around 29 AERONET stations distributed over the Sahara as shown in (Figure 1.7), some of these stations have limited temporal coverage and could not help this study. Most of the stations are distributed in the western and northern regions of the Sahara. The Tamanrasset AERONET station is in the optimum location, because it’s in the centre of the Sahara. However, it was not possible to use it, due to limited archiving of data during dust storms. The Banizoumbou AERONET station (Figure 1.8) as selected for this study because it has full coverage during the years 2006 and 2007, and also has a good location compared with the other stations which are very close to the coast or have a lot of cloud cover. In this study the AERONET sun-photometer data from the Banizoumbou station were used to evaluate the different remote sensing techniques used for measuring dust.

Figure 1.8 Sun-Photometer Ground station at Banizoumbou to measure the (AOT) of the atmospheric aerosol. (Source: http://aeronet.gsfc.nasa.gov/)

## 1.10 Global Dust Sources Derived Using Ground Based Measurement

The major sources of mineral dust are found in the desert regions of the northern hemisphere stretched from West Africa to Central Asia, while some sources are found in the other desert areas of the world (Figure 1.9). Based on TOMS AI, the major sources of dust are: (1) from sub-tropical desert regions which occur in a broad belt from West Africa to Central Asia; and (2) semi-arid and sub-humid regions. Saharan Desert is the largest desert in the world, covering about 8,600,000 km². Moreover, Saharan Desert is recognized as the most important source of dust in the world (Washington et al., 2006).

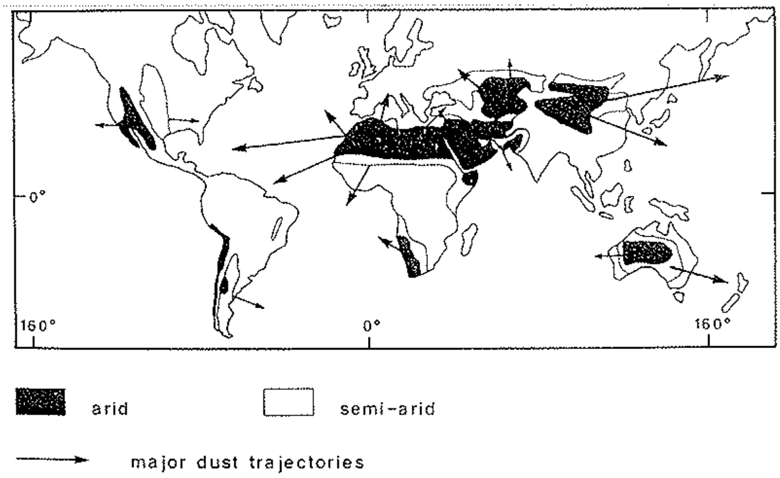


Figure 1.9 Distribution of areas with high dust storm activity and major dust trajectories (Modified after Coude`-Gaussen 1984). (Source: Pye 1987)

### 1.10.1 Saharan Dust Sources Derived from Ground based Techniques

Since the mid of the twentieth century studies have focused on the dust sources of the Sahara. Before the advantages of the remote sensing techniques, a number of different methods were used to map dust sources; analysis of surface dust observations at meteorological stations, back trajectory analysis of isobar data, and mineral tracers. At the beginning of the mid of the twentieth century, Dubief (1953) used the back trajectory method to map the dust sources in the Sahara (Figure 1.10).

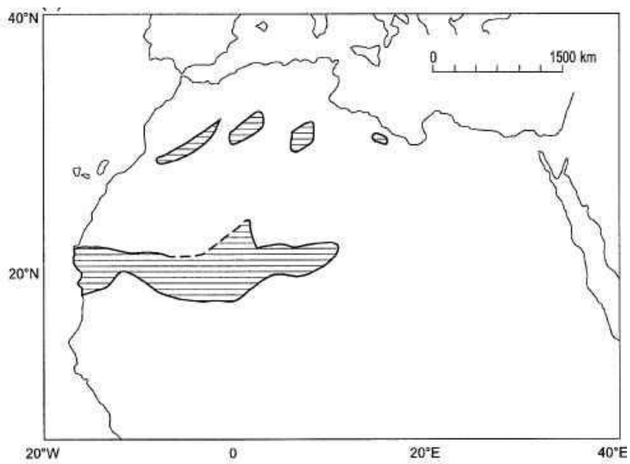


Figure 1.10 Saharan dust sources mapped using back trajectory method, Modified after Dubief 1953. (Source: Middleton and Goudie 2001)

The largest identified source area stretched from the middle of the western of Africa to the Centre Sahara and three smaller areas were located in southern of Tunisia, the Centre of Algeria, and southern of Morocco. This attempt delimited the western part of the Sahara but nothing detected in the eastern part of the Sahara as seen in the (Figure 1.10).

Kalu (1979) used a synoptic model produced by Kalu (1975) and visibility analysis for aerosol particles to map the Saharan dust sources, he found Bilma and Faya southern of Tibesti Mountain and Tamanrasset southern west of Ahaggar Mountain are the two main dust sources area in the Sahara (Figure 1.11). These sources are commonly reported by most of the authors talking about the Saharan dust sources as the most important dust sources in the world. However, these sources did not map clearly by the previous attempts presented by Dubief (1953) (Figure 1.10).

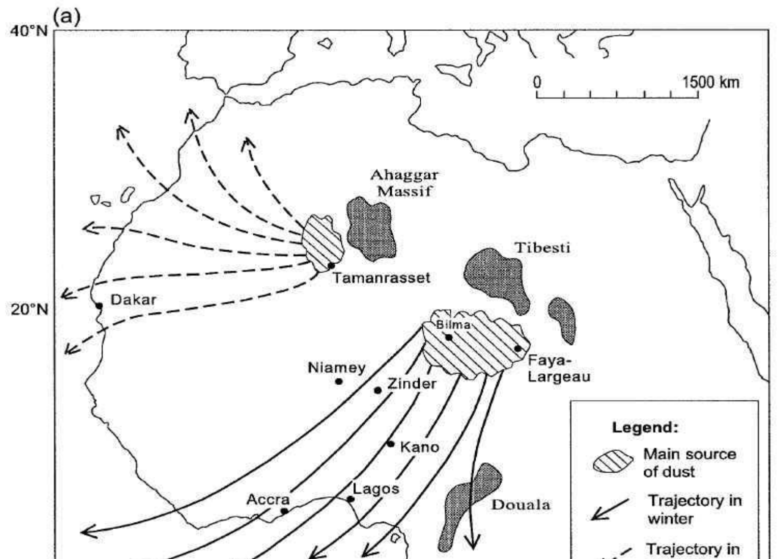


Figure 1.11 Saharan dust sources and trajectory mapped using back trajectory method, Modified after Kalu 1979. (Source: Middleton and Goudie 2001)

D`Almedia (1986) distributed 11 Sun-Photometer stations in the Sahara for duration of two years in order to map the Saharan dust sources. Four main dust sources were identified (Figure 1.12): The first dust source extended from the Spanish Sahara to North Mauritania. The second dust source area surrounded by Hoggar, Adrar, and

Air mountains. The third dust source is located north of Bilma (Niger) west of Tibesti Mountain (Chad). The fourth dust source is situated north of Sudan. D`Almedia concludes that: (1) the dust storms in the Sahel region and the Gulf of Guinea are mainly generated from all four dust sources and they frequently happen in wintertime, (2) the third dust source responsible for the dust transported southward, (3) the first dust source has the highest dust production, (4) the second dust source is the main source for dust transported during summer towards Europe, (5) the contribution of the fourth dust source is relatively small, (6) the dust production in the summer season is usually entrained by the monsoon air mass, (7) the results shows dust transport takes place throughout the year but is particularly strong from March to June.

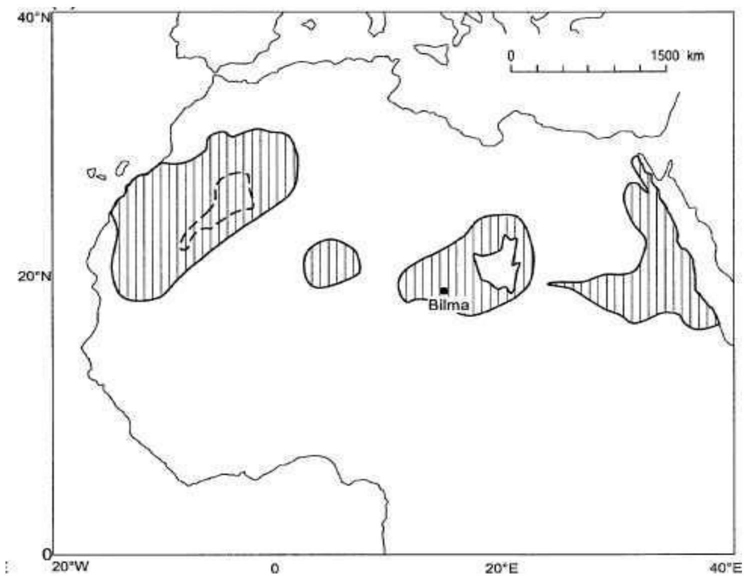


Figure 1.12 Saharan dust sources mapped using back trajectory method, Modified after D`Almeida 1986. (Source: Middleton and Goudie (2001)

Middleton (1986) produced a map that shows the Saharan dust sources, trajectories, and the seasons of the trajectory by using the meteorological stations (Figure 1.13). The mapped sources of this image are more numerous than the previous attempts and delimit most of the sources which are identified by the previous attempts. The Bodélé Depression and areas covering southern of Mauritania, western of Mali, and southern of Algeria are again mapped. A large swathe of area covering the most part of Libya and the Horn of Africa are mapped in this map where it has not been mapped by the previous attempts.

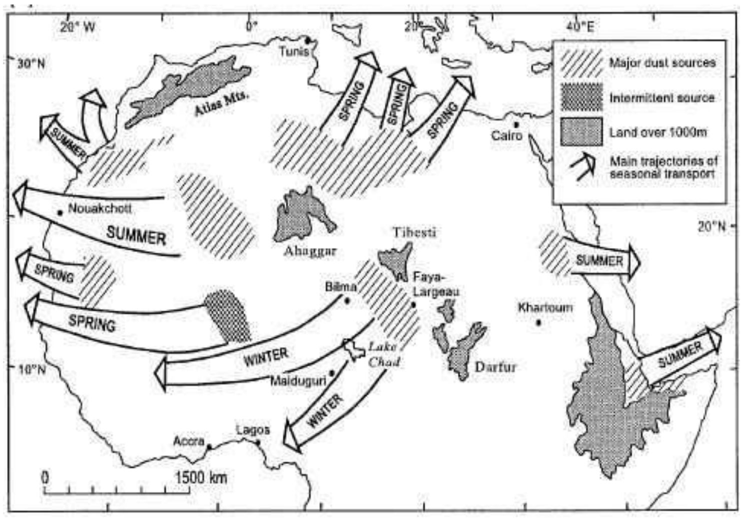


Figure 1.13 Saharan dust sources mapped using back trajectory method, Modified after Middleton 1986. (Source: Middleton and Goudie 2001)

These results are different from the next attempts to delimit the Saharan dust sources area. The dust source area in the mid of the north of Libya has not been mapped by the other mentioned attempts used the back trajectory method, however it has been mapped in the map produced by using the remote sensing technique by Brooks and legrand (2000).

## 1.10.2 Comparison Between Methods

The previous attempts to delimit the Saharan dust sources by (1) Dubief (1953), (2) Kalu (1979), (3) D`Almeida (1986), and (4) Middleton (1986) have been merged into one map as shown in (Figure 1.14). It is clear that most maps outline different source areas from each other, though sources overlap in the Bodélé Depression in Chad and the western flank of the Hoggar Mountains. Thus perhaps this is where the main dust sources are located. However, these maps need to be treated with caution as all are mapped using techniques that do not directly identify sources.

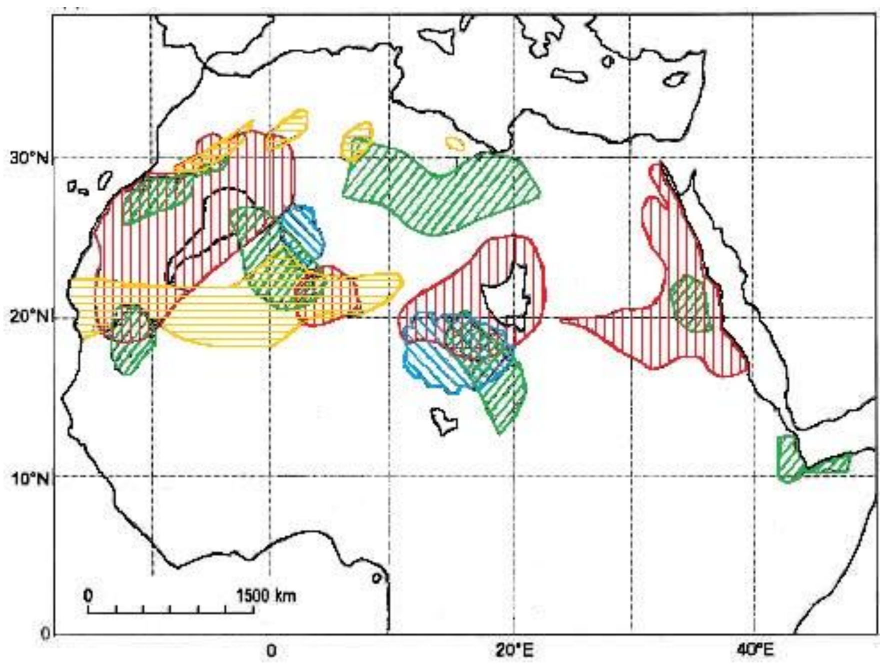


Map Key:

Dubief (1953) Kalu (1979) D`Almeida (1986) Middleton (1986)

Figure 1.14 Composite of Saharan dust sources maps produced by (1) Dubief (1953), (2) Kalu (1979), (3) D`Almeida (1986), and (4) Middleton (1986). (Source: after Middleton and Goudie 2001)

## 1.11 Trajectories of Saharan Dust Transport Using Ground Based Methods

Research has shown that there are four main transport paths which the Saharan dust is generally transported from as outlined below.

### 1.11.1 Westward over the North Atlantic Ocean

Several authors have recorded the transport and the deposition of Saharan dust crossing the Atlantic Ocean. The North Atlantic Ocean trajectory is one of the three main dust transport path in the Sahara and it has the highest amount of record dust transport from Sahara, around 40% of the total (Schütz et al., 1981). Darwin (1893) was the first to report that dust from Sahara transported westward to the North Atlantic Ocean causing hazy atmosphere over the Cape Verde Islands and stated “I have found no less than fifteen different accounts of dust having fallen on vessels when far out in the Atlantic. From the direction of the wind whenever it has fallen, and from its having always fallen during those months when the harmattan is known to raise clouds of dust high in to the atmosphere, we may feel sure that it comes from Africa”. Most of the dust plumes over the North Atlantic Ocean are usually linked with easterly waves that come from the African coast.

Kalu (1979) defined and described the African dust plume characteristics and propagation, he found that most of dust cross the Atlantic comes from Tamanrasset in the winter season and from Bilma and Faya in the summer season (Figure 1.11).

### 1.11.2 Northward Across the Mediterranean to Southern Europe

Saharan dust is often deposited over Southern Europe. Fiol et al., (2005) documented 253 Saharan dust storms in Mallorca between year 1982 and 2003. In Italy Pisano et al., (2005) used Lidar observations to record the aerosol loading at Napoli and suggest that 15% of aerosol load is influenced by Saharan dust. Papayannis et al., (2005) reported a Europe wide study for three years between 2000 and 2003 using the co-ordinated aerosol lidar network based on 21 stations. The network observed 90 significant events of tropospheric dust layers in Europe. D`Almedia (1986 stated that a major source area of dust in Sahara transport to Western Europe is from Algeria between Hoggar and Adrar. Western Sahara-Southern Morocco area is also recognised as a major source of dust towards Southern Europe by D`Almedia (1986. Avila et al., (1997) used back-trajectory analysis for dust deposited over North-eastern Spain and traced deposition events back to three main areas: Western Sahara, the Moroccan Atlas, and central Algeria. Bergametti et al., (1989) found after one year monitoring on Corsica that 20 dust events been originated from three dust sources areas: eastern Algeria/Tunisia/western Libya, Morocco/western Algeria and ‘south of 30º N’. Middleton (1986) shows on a map the trajectory of the Saharan dust Figure 1.15. The northward trajectory across the Mediterranean to southern Europe comes from the north of Sahara sources during the spring season.

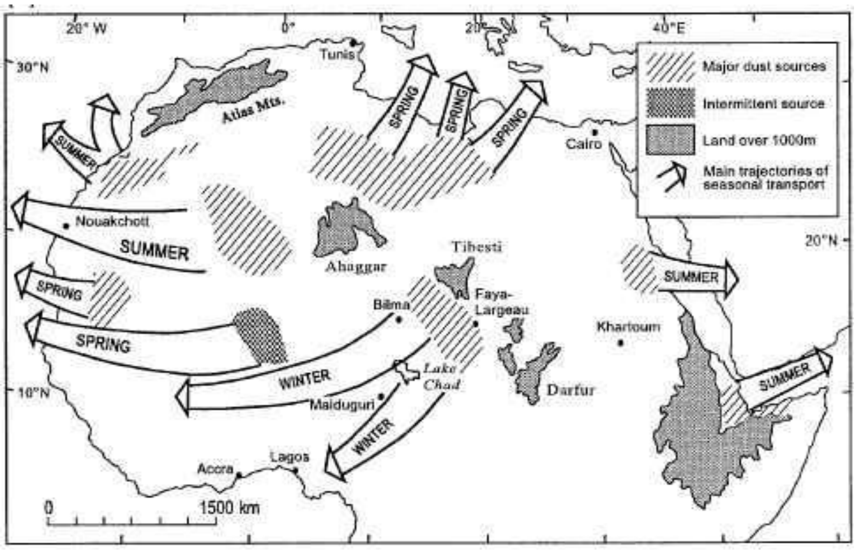


Figure 1.15 Saharan dust sources mapped by Middleton (1986). (Source: Middleton and Goudie 2001)

## 1.11.3 Eastward Across the Eastern Mediterranean to the Middle East

Dust transport from North Africa towards eastern Mediterranean usually happens during the spring and is often associated with the low-pressure systems (Kubilay et al., 2003). Ganor et al., (1991) recorded 23 heavy dust events falls over the Middle East during a 20 year period that came from North Africa. Alpert and Ganor (1993) suggest that dust transport from North Africa to the eastern Mediterranean is usually associated with a cold front with a significant downward-flowing jet steam and is followed by rain. Israelevich et al., (2003) documented that dust reached Israel comes from Chad, Egypt, and Libya in different seasons.

## 1.11.4 Soil Erosion in the Sahel

One issue that the above mentioned studies on dust sources do not pick up is the role of the Sahel in North African dust production. The scientific data on soil erosion in the Sahel, good as they are in global context, are insufficient to judge the severity of the problem. Indeed Mazzucato and Niemeijer (2000, 2001) are sceptical about the evidence for severe soil degradation and erosion in the Sahel. Chappel et al., (1998) directly address this issue. The find that soil is being eroded from Fandou Be´ri, in south western Niger, at rates of approximately 48 t $ha^{-1}$ $yr^{-1}$, as measured by the $^{137}Cs$

method to make net time integrated (30 years) measurements of soil flux. The $^{137}Cs$ method is an artificial isotope that is produced in nuclear reactions (Chappel et al., 1998). Large quantities were spread to the atmosphere by bomb testing in the early 1960s and mixed within each hemisphere and deposited on soil surfaces by rainfall. The present $^{137}Cs$ content in a soil profile gives a measure of soil loss over a 30- to 40-year period (Warren et al., 2003). Their result shows that average annual net soil flux over the last 30 years (48 t $ha^{-1}$ $yr^{-1}$, as) was four times larger than the last estimate for the same area by (Lal, 1993). They conclude that cultivated agriculture area is largely eroded.

Further research is needed in other parts of the Sahel to address erosion rates. Warren et al., (2003) have listed four ways to evaluate the role of erosion in Sahelian agriculture at the village scale.

- First is to analyse erosion rates themselves and their effects on yield, using a wide range of measurement and modeling techniques (such as the EPIC model).
- Second, resource economics, as deployed by de Graaf (1996) and Kunze (2000), assesses the monetary value of erosion to a household or individual, and/or the ‘‘willingness-to-pay’’ for soil conservation.
- Third, is the finer-grained, multi-disciplinary analysis of household behavior in relation to erosion, combining surveys with scientific measurements.
- Fourth approach is the ethnographic analysis of farmers’ own views, assessing their technical and practical knowledge of erosion through local taxonomies and value systems.

These methods need to be implemented in the Sahel to determine the severity of the soil erosion problem.

## 1.12 Conclusion

This chapter has reviewed the Saharan dust effects, the dust cycle, models used to simulate the dust cycle, the sources of Saharan dust, the rates of Saharan dust deposition, and the transport paths of material away from the Sahara.

Dust has different effects in different fields. Study of the dust cycle shows that dust had both positive and negative effect. The main advantage of dust is fertilization of the ocean and the Amazon rain forest in South America. Saharan dust is the dominant source of the iron to the Ocean (Savoie and Prospero, 1982) and it is estimated that 50% of the phosphours deposited in the Ocean comes from Sahara. On the other hand dust has disadvantages; it has detrimental effects on the human health and can transport disease over long distances.

Based on the information from the (IPCC, 2007) (Figure 1.3) there is still high uncertainty about the radiative forcing of mineral dust due to the uncertainty in estimating dusts radiative properties.

The Sahara desert is recognized as producing the most dust in the world. Studying the Saharan dust cycle provides information about the quantity of dust emission, the type of dust, the nature of the sources, and the activity of each source. However, it is clear that there are many gaps in our understanding of the Saharan dust cycle due to our limited knowledge regarding the precise dust source locations and the landforms at these sources. There is also much speculation about the transport mechanisms linked to the distribution of the atmospheric dust (e.g. Washington et al., 2003).

Hermann et al., (1999) reviewed previous study of Saharan dust sources and remarked “Astonishingly, the results with regard to source areas are totally different. No overlapping can be detected which could serve as a confirmation of results”. The review presented in this chapter provides a slightly different interpretation. Though all of the work done in the past using the traditional techniques to determine the dust sources like; analysis of surface dust observations, back trajectory analysis of isobar data, and mineral tracers tell a different story regarding the dust sources, the main sources area of dust such as Bodélé Depression is agreed upon between most of these techniques.

There is more agreement on where this Saharan dust goes. Based on Middleton (1986) results for tracking the trajectories of the Saharan dust transport, four main transport paths have been recorded, westward crossing the north Atlantic Ocean, northward crossing the Mediterranean Sea, eastward crossing the Middle East, and southward crossing the southern of Sahara. Moreover, each trajectory has different transport seasons. However, the links between dust sources areas of Sahara and seasonal dust pathways are not well known (Goudie and Middleton 2001).

Next section will review the different techniques used to measure the dust using remote sensing and investigate how they can be used to monitor and identify the dust sources.

# 2. Remote Sensing of Dust

## 2.1 Radiative Transfer Process in Remote Sensing of Dust

The scattering process descried in section 1.2.2 can be used to understand how remote sensing is employed in dust detection. Atmospheric aerosol particles affect the Earth's radiative balance both directly by scattering and absorbing solar radiation and indirectly by modifying the optical properties and lifetime of clouds (King et al., 1999). Both long and short wavelengths can be used for detecting dust. Legrand et al., (2001) shows the radiative forcing of dust through mechanisms explaining the depression of thermal infrared radiance outgoing to space during daytime in the presence of the dust over land. Temperature depression at the surface is due to a decrease of downward SW flux prevailing over the increased downward LW flux. The temperature depression is, however, damped by the presence of vegetation and soil moisture (Figure 2.1). The dust layer absorbs more IR radiance than it emits, because it is colder the ground surface.

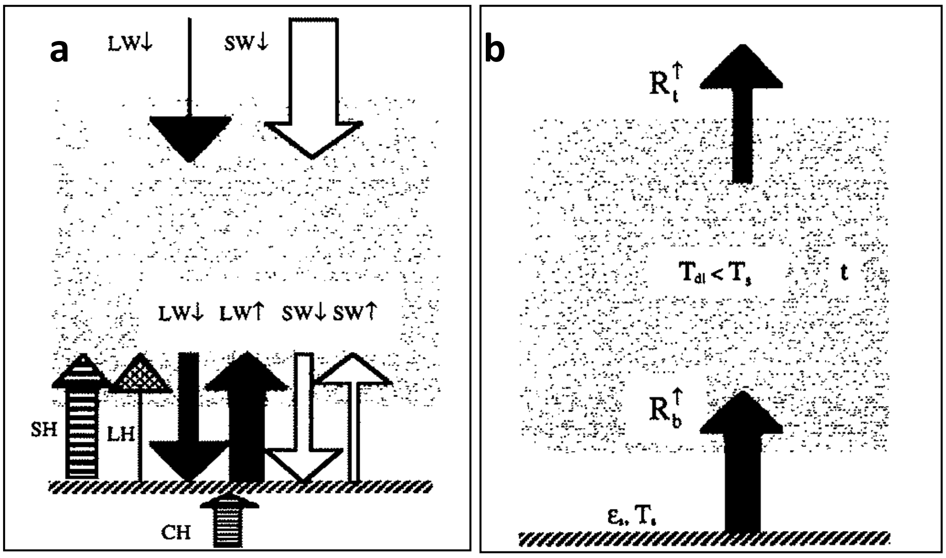


Figure 2.1 Mechanisms explaining the depression of thermal infrared radiance outgoing to space during daytime in the presence of the dust layer. CH conduction heat, SH sensible heat, LH laten heat, SW shortwave, LW longwave, $T_s$ temperature of the surface, $T_{dt}$ mean temperature, R radiance depresion . (Source Legrand et al., 2001)

Using a single IR channel is possible to monitor dust but it is difficult to distinguish between dust and other type of aerosol (Ackerman 1997). Brightness Temperature Difference (BTD) split windows can be used to detect dust based on the difference in scattering between different wavelengths. In general scatting of radiation by dust increases with wavelength. Because of this Ackerman (1989) used BTD (3.7 µm-11 µm) to track dust sources, he found large differences in scattered energy exist between wavelengths of 3.7 µm and 11 µm. This is because the imaginary part of the index of refraction at 11 µm is approximately an order of magnitude greater than at 3.7 µm. Thus, in the presence of dust, a large difference may exist in the equivalent black-body temperatures at 3.7 µm and 11 µm. Quartz displays a strong spectral dependence in the imaginary index of refraction, suggesting that BTD techniques may be successful in detecting dust (Hu et al., 2008). There are though several other factors that can control the readiative transfer of the dust such as the chemistry of dust, particle size, shape of particle, and concentration of dust (Wald et al., 1998).

## 2.2 Measuring Dust Aerosols Using Remote Sensing Techniques

Remote sensing of dust using earth observation satellite goes, as far back as the 1970's. Remote sensing techniques have the advantage over the ground station measurements by monitoring dust globally. Moreover, using remote sensing data allow the monitoring of individual dust storms and can give information to identify the source, movement and optical thickness of the aerosols. Two main types of remote sensing platforms have proved to be useful: geostationary meteorological satellites and polar orbiting satellites. Different sensors have been used for identifying, tracking and analysing different scale dust storms. This can be achieved every sixteen days Landsat Thematic Mapper (TM), daily Moderate Resolution Imaging Spectrometer (MODIS), or several times a day Spinning Enhanced Visible an InfraRed Imager (SEVIRI).

The measured signals from the remote sensing sensors are a combination between the earth surfaces contribution and atmospheric influence. To identify the dust signal detected by the satellite sensors, several techniques have been used to study the radiative effect of atmospheric aerosols.

Table 2.1 Example of the use of remote sensing in the study of dust storms and dust aerosols (Source: Goudie and Middleton 2001).

| Sensors | Reference |
|---|---|
| MODIS (Terra/Aqua) | Koren and Kaufman (2004), Kaufman et al., (2005). |
| TOMS/OMI | Alpert et al., (2000), Alpert and Ganor (2001), Chiapello and Moulin (2002), Colarco, et al., (2002), Ginoux and Torres (2003), Barkan et al., (2004), Mahowald and Dufresne (2004). |
| Meteosat/ SEVIRI | Legrand et al., (1994), Brooks (1999), Karyampudi et al., (1999), Brooks and Legrand (2000), Chiapello and Moulin (2002), Schepanski et al., (2007), De Paepe et al., (2009) |
| AVHRR | Husar et al., (1997), Cakmur et al., (2001) |
| LIDAR | Karyampudi et al., (1999), Chazette et al., (2001), Gobbi et al., (2002). |
| MISR | Zhang and Christopher (2003), Christopher et al., (2004). |
| GOME | Guzzi et al., (2001), De Graaf et al., (2005) |
| AIRS | Pierangelo et al., (2004) |
| VISSR | Lino et al., (2004) |

Remote sensing of aerosols from satellites is the only way to achieve global information on aerosol spatial and temporal distribution. Numerous satellite sensors have been used to do this (Table 2.1). The key sensors are outlined below. However, detecting dust over dark land surfaces such as vegetated areas or over ocean it is more effective than over desert surfaces because reflection of sunlight over bright surfaces can interfere with the backscattered radiation by the aerosol layer (Kaufman et al., 1997).

## 2.3 UV Sensors

### 2.3.1 TOMS

The Total Ozone Mapping Spectrometers (TOMS) placed in a sun-synchronous orbit, and has been working since 1978 on different platforms; Nimbus 7 (1978), Meteor 3 (1991), Earth Probe (1996), and Ozone Monitoring Instrument OMI (2004). TOMS was designed to produce accurate global estimates of total column ozone, $SO_2$ (gas) and $H_2SO_4$ (sulphate) aerosols in the stratosphere, and UV absorbing aerosols such as dust. These data make it possible to monitor the dust storms using the TOMS Aerosol Index (AI), though the spatial resolution of the sensors is low with Nimbus 7 TOMS being 50 km and gradually improving with Earth-Probe Toms being 39 km and OMI being 13x14 km Table 2.2 (Prospero et al., 2002).

Table 2.2 Different TOMS sensors and their characteristic (Source: This thesis)

| **Sensor** | **Life Time** | **Resolution** | **Wavelengths** |
|---|---|---|---|
| Nimbus 7 (1978) | October 1978 to May 1993 | 50 km × 50 km | UV 312.5, 317.5, 331.3, 339.9, 360.0 and 380.0 |
| Meteor-3/TOMS | August 1991 to December 1994 | 50 km × 50 km | As above |
| Earth-Probe TOMS | July 1996 | 39 km × 39 km | As above |
| OMI | July 2004 | 13 km × 24 km | Visible 350 - 500 nm<br>UV-1 270 - 314 nm<br>UV-2 306 - 380 nm |

## 2.3.2 Techniques to Detect Dust Storms Using Ultra Violet (UV)

TOMS data have been widely used to study dust. Prospero et al., (2002) used the TOMS Aerosol Index (AI) (Equation 2.1), based on the UV radiance coupled with an atmospheric model. Whereby,

$$AI = -100 \log_{10}[I_{meas} - I_{calc}] \quad (2.1)$$

$$I_{meas} = (I_{340}/I_{380}) \text{ measured backscatter at a given wavelength} \quad (2.2)$$

$$I_{calc} = (I_{340}/I_{380}) \text{ model calculated radiance at a given wavelength} \quad (2.3)$$

The subscript $I_{meas}$ indicates the backscattered radiance at a fixed wavelength measured by TOMS and the subscript $I_{calc}$ indicates the radiance calculated with a radiative transfer model describing a pure Rayleigh atmosphere. In the presence of absorbing aerosols the AI provides positive values, if there are no such aerosols, the AI has negative vales (Prospero et al., 2002).

TOMS has provided useful information on aerosol distribution in the atmosphere. The advantage of UV bands over the visible bands that the UV bands does not have the limitation of the visible wavelength because the UV surface reflectivity is low and similar over both land and water. However, detecting aerosols less than 1 km from the surface can be difficult by using UV bands because TOMS AI is sensitive to the height of the dust layer preferentially measures high dust and measurements of AI under 1 km are underestimated (Kubilay et al., 2005). Chiapello et al., (1999) notes a good correlation between ground based studies in the tropical Atlantic and TOMS data.

Prospero et al., (2002) and Washington et al., (2003) have mapped the global aerosol budget using TOMS for almost 15 years providing a long term database for study. Figure 2.2 shows the most active areas of dust emission and transport in the world determined from TOMS. They are contained in a dust belt stretching from the eastern subtropical Atlantic, through the Sahara to South-west Asia.

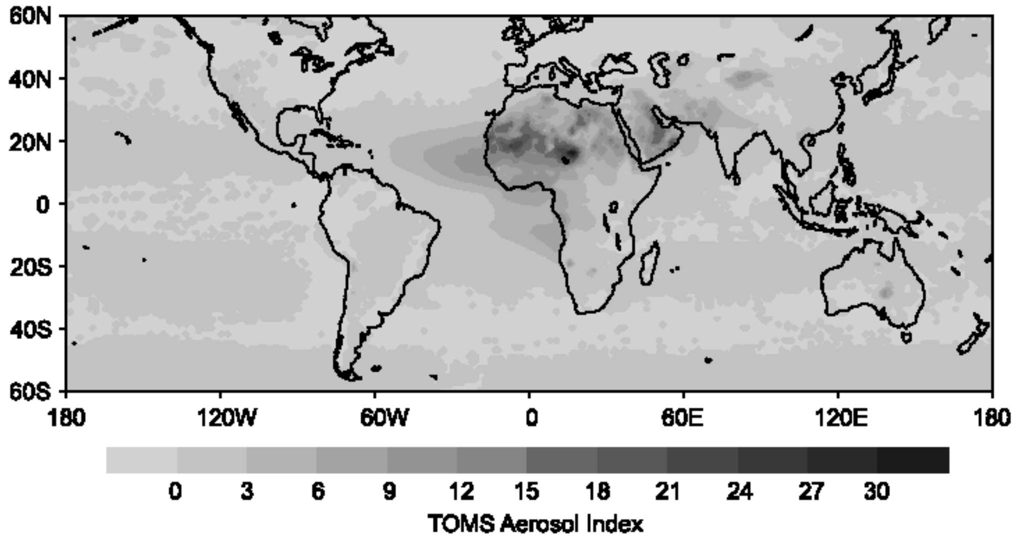


Figure 2.2 Global distribution of mean AI values, derived from TOMS. (Source: Washington et al., 2003)

Table 2.3 is a summary of the major dust source regions in the Sahara. Three of the world's most important dust sources are in the Sahara; the Bodélé Depression, West Sahara in Mali and Mauritania and Eastern Sahara in Libya representing the most important sources in the world (Goudie et al., 2003).

Table 2.3 Maximum mean Aerosol Index (AI) values for major global dust sources determined from TOMS (Source: Goudie and Middleton (2001).

| Location | Mean (AI) values |
|---|---|
| Bodélé Depression of Central Sahara | >30 |
| West Sahara in Mali and Mauritania | >24 |
| Eastern Sahara Libya | >15 |

TOMS has shown that there are two seasonal dust storm trajectories that originate from Sahara. Summer dust storms, where large amount of dust cross the Mediterranean to the southern cost of Europe and Middle East (Moulin et al., 1998). They also cross the Atlantic Ocean reaching the south-eastern cost of United States (Prospero 1999). The second seasonal dust storms happen in winter where large amounts of dust are transported to South America (Prospero et al., 1981). The UV technique is found to be sensitive to aerosol altitude being able to detect high altitude dust better than that in the lower atmosphere (Torres et al., 1998). It is quite difficult to detect dust under 1.5 km height using Ozone Monitoring Instruments (OMI) (Herman et al., 1997), because the detection of dust using UV bands depends on the vertical distribution of dust and is more sensitive to dust that is higher in the atmosphere.

TOMS also indicates that there are many smaller dust sources contained within the Sahara usually linked with topographic lows, high mountains or sand seas; as these provide suitable weathering agents and trigger mechanisms (Prospero et al., 2002 Table 2.3). However, determining precise sources and transport mechanisms of dust still remains a gap because tracing small dust sources require high spatial and temporal resolution.

Middleton and Goudie (2001) also used TOMS to map the Saharan dust sources based on the TOMS AI (Figure 2.3). Based on TOMS AI values, there are three major dust sources area in Sahara: the Bodélé depression, area covers western Mali and southern Algeria and eastern Sahara Libya. These results are very similar to those outlined by Prospero et al., (2002).

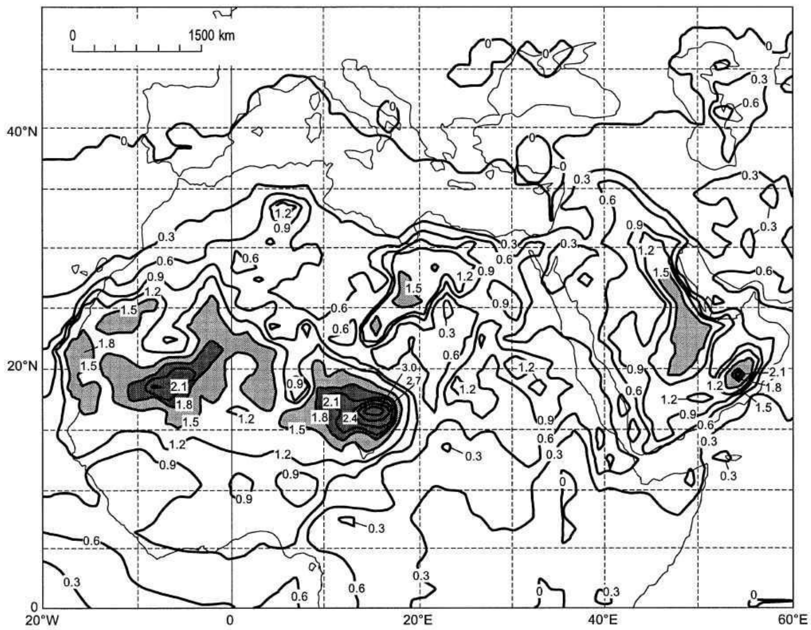


Figure 2.3 Annual mean AI values from TOMS data from (1980-1993, 1997-2000). (Source: Middleton and Goudie 2001)

## 2.4 Visible and Infrared Sensors for Detecting Dust Sources.

The most commonly used visible and infrared sensors for monitoring dust are briefly outlined below.

### 2.4.1 Moderate Resolution Imaging Spectrometer (MODIS)

The MODIS is flown on NASA's EOS Terra (a.m. equatorial crossing time) and Aqua (p.m. equatorial crossing time) satellites. MODIS provide long-term observations to derive an enhanced knowledge of global dynamics and processes occurring on the surface of the earth and in the atmosphere (King et al., 2003; NASA MODIS 2006). It yields simultaneous observations of high-atmospheric (cloud cover and associated properties), oceanic (sea-surface temperature and chlorophyll), and land-surface (land-cover changes, land-surface temperature, and vegetation properties) features (Source: http://modis.gsfc.nasa.gov).

MODIS is in a 750 km Sun-synchronous orbit. It has a field of view of ±55° off-nadir, with swath width of 2,330 km. The MODIS sensor views the entire surface of the Earth every day and night. Using Terra data in the morning and Aqua data in the afternoon, the temporal resolution can be up to four times a day. MODIS obtains high radiometric resolution images (12-bit) of daylight-reflected solar radiation and day/night thermal emission over the world. MODIS collects data in 36 spectral bands: 20 bands from 0.4 to 3 µm and 16 bands from 3 to 15 µm. MODIS has variable spatial resolution, 250×250 m (bands 1 and 2), 500×500 m (bands 3 to 7), and 1×1 km (bands 8 to 36). Table 2.4 show the 36 bands and their utility MODIS data are processed to create several global datasets, such as cloud fraction, cloud optical thickness, and aerosol optical thickness (Source: http://modis.gsfc.nasa.gov).

Table 2.4 MODIS bands and their principal areas of application
(Source: http://modis.gsfc.nasa.gov/about/specifications.php).

| Primary Use | Band | Bandwidth (nm) | Wavelength | Pixel Size(m) |
|---|---|---|---|---|
| Land/Cloud/Aerosols | 1 | 620 - 670 | 645 | 250 |
| Boundaries | 2 | 841 - 876 | 856 | 250 |
| Land/Cloud/Aerosols | 3 | 459 - 479 | 465 | 500 |
| Properties | 4 | 545 - 565 | 553 | 500 |
| | 5 | 1230 - 1250 | 1241 | 500 |
| | 6 | 1628 - 1652 | 1629 | 500 |
| | 7 | 2105 - 2155 | 2114 | 500 |
| Ocean Colour/ | 8 | 405 - 420 | 411 | 1000 |
| Phytoplankton/ | 9 | 438 - 448 | 442 | 1000 |
| Biogeochemistry | 10 | 483 - 493 | 486 | 1000 |
| | 11 | 526 - 536 | 529 | 1000 |
| | 12 | 546 - 556 | 546 | 1000 |
| | 13 | 662 - 672 | 665 | 1000 |
| | 14 | 673 - 683 | 676 | 1000 |
| | 15 | 743 - 753 | 746 | 1000 |
| | 16 | 862 - 877 | 866 | 1000 |
| Atmospheric | 17 | 890 - 920 | 904 | 1000 |
| Water Vapour | 18 | 931 - 941 | 935 | 1000 |
| | 19 | 915 - 965 | 935 | 1000 |

| | | | | |
|---|---|---|---|---|
| Surface/Cloud | 20 | 3,660 – 3,840 | 3,785 | 1000 |
| Temperature | 21 | 3,930 – 3,989 | 3,960 | 1000 |
| | 22* | 3,930 – 3,989 | 3,960 | 1000 |
| | 23 | 4,020 – 4,080 | 4,056 | 1000 |
| Atmospheric | 24 | 4,433 – 4,498 | 4,472 | 1000 |
| Temperature | 25 | 4,482 – 4,549 | 4,545 | 1000 |
| Cirrus Clouds | 26 | 1,360 – 1,390 | 1,383 | 1000 |
| Water Vapour | 27 | 6,535 – 6,895 | 6,752 | 1000 |
| | 28 | 7,175 – 7,475 | 7,334 | 1000 |
| Cloud Properties | 29 | 8,400 – 8,700 | 8,518 | 1000 |
| Ozone | 30 | 9,580 – 9,880 | 9,737 | 1000 |
| Surface/Cloud | 31 | 10,780 – 11,280 | 11,017 | 1000 |
| Temperature | 32 | 11,770 – 12,270 | 12,032 | 1000 |
| Cloud Top | 33 | 13,185 – 13,485 | 13,359 | 1000 |
| Altitude | 34 | 13,485 – 13,785 | 13,675 | 1000 |
| | 35 | 13,785 – 14,085 | 13,907 | 1000 |
| | 36 | 14,085 – 14,385 | 14,192 | 1000 |

### 2.4.2 SEVIRI

The SEVIRI is on board the Meteosat-8/MSG-1 satellite and Meteosat-9/MSG-2 satellite. SEVIRI is in a 35,800 km altitude geostationary orbit. The sensor covers area Longitude 60ºW to 60ºE and Latitude 60ºS to 60ºN. It can obtain full coverage after 1250 scan line steps. The satellite spin of 100 rpm allows completing a full image in about 12.5 minutes, leading to overall repeat cycle of maximum 15 minutes. SEVIRI has 12 bands as described in (Table 2.5). It has two different resolutions 1 km for the high-resolution visible channel and 3 km for the other visible bands and the infra-red (Schepanski et al., (2007).

Table 2.5 SEVIRI bands and their spectral range and resolution
Source (http://www.sat.dundee.ac.uk/seviri.html)

| Channel | Bands | Spectral Band µm | Resolution |
|---|---|---|---|
| HRV | Visible | 0.6 - 0.9 | 1 km |
| VIS 0.6 | | 0.56 - 0.71 | 3 km |
| VIS 0.8 | | 0.74 - 0.88 | 3 km |
| IR 1.6 | near Infra-red | 1.50 - 1.78 | 3 km |
| IR 3.9 | Thermal Infra-red | 3.48 - 4.36 | 3 km |
| IR 8.7 | | 8.30 - 9.10 | 3 km |
| IR 10.8 | | 9.80 - 11.80 | 3 km |
| IR 12.0 | | 11.00 - 13.00 | 3 km |
| IR 6.2 | | 5.35 - 7.15 | 3 km |
| IR 7.3 | | 6.85 - 7.85 | 3 km |
| IR 9.7 | | 9.38 - 9.94 | 3 km |
| IR 13.4 | Far Infra-red | 12.40 - 14.40 | 3 km |

### 2.4.3 Dust Storms Detection Using MODIS, SEVIRI, and Similar Sensors

Several techniques have been used to detect dust storms using different visible and infrared, some of these techniques have used the visible bands, some thermal bands and some of them have combined between different bands. These different methods are outlined below.

#### 2.4.3.1 Techniques to Detect Dust Storms Using Visible and IR Bands (0.4 - 13 µm)

Several authors have investigated the use of visible channels to detect aerosols. In one of the first studies Griggs (1975) utilized the multispectral scanner Multi Spectral Scanner (MSS) radiance data from the ERTS-1 satellite to investigate the radiance measured by the MSS visible channels (0.55, 0.65 and 0.75 µm) and ground-based observations of aerosol optical thickness and found a linear relationship between the MSS data and the aerosol optical thickness over water. Griggs (1978) further investigated this technique over the oceans using National

Oceanic and Atmospheric Administration (NOAA 5) Advanced Very High Resolution Radiometer (AVHRR) and Geostationary Operational Environmental Satellites (GOES) during the Electro Optical and Meteorological (EOMET) cruise in 1977 over the Atlantic Ocean and the Mediterranean Sea and found a linear relationship between the upwelling radiance and the aerosol optical thickness for both satellites. However the relationships for each satellite did not match each other because of the different radiometric calibrations of each sensor.

Carlson (1978) demonstrated the use of satellite measurements to map dust outbreaks using the AVHRR imagery derived from the NOAA3 satellite. The imagery were calibrated to radiances using the sensor conversion formula and radiative transfer calculations were made using a Monte Carlo model described by (Wendling, 1977) to convert radiance to optical depth with the phase function computed using Mie scattering theory. As a result isopleth contours of aerosol optical depth at visible wavelength for Saharan dust were plotted. However, measurement over land is difficult due to the high reflectivity of the bright underlying desert surface.

Norton et al., (1980) designed a model to measure the radiance in the visible spectrum of the Synchronous Meteorological Satellite (SMS) by computing the single scattering properties of air and dust layers and the phase functions from a Mie scattering model to give the intensity and polarization for scattering by homogeneous isotropic spheres for an incident plane wave in an arbitrary state of polarization (Liou et al., 1971). It was found that it was possible to monitor dust outbreaks and estimate the optical thickness of Saharan dust. The GATE dust turbidity measurements technique was used to validate the method. However the GATE measurement was limited because there were few stations and they were distributed mostly in the eastern Atlantic. Moreover these data are available in the summer of 1974 only (Norton et al., 1980).

The MODIS aerosol product monitors (AOT) over the oceans and part of the land. Daily data are produced at spatial resolution of 10 km by 10 km at nadir. The MODIS aerosol product is comprised of two different algorithms, one designed for retrieval aerosol over land (Kaufman et al., 1997), and the other over the ocean (Tanre et al., 1997).

Kaufman et al., (1997) established correlation between the surface reflection at 0.49 µm, 0.66 µm and 2.1 µm wavelength using atmospherically corrected Landsat TM and AVIRIS aircraft images to detect aerosol over dark surfaces. This works because the 2.1 µm channel is not affected by aerosols except dust, moreover it can be used to identify dark pixels, and estimate the reflectance of the dark pixel in the visible bands, the reflectance ratio of 0.47 and 0.66 µm is used to separate dust from smoke or sulphates. This method has become the MODIS (MYD) aerosol product, it works well over vegetated surfaces but does not provide any information about aerosols over bright bare ground.

Kaufman et al., (2000) used the reflected solar bands 0.47, 0.64 and 2.1µm from Landsat 5 TM to detect dust over deserts by extending the work done by (Kaufman et al., 1997) to detect aerosols over vegetation. As with the Kaufman et al., (1997) method the 2.1µm band is used to determine surface properties. In this case the ratio of the reflectance of 0.47µm and the 2.1µm and 0.64µm and the 2.1µm are used to detect aerosols. The technique is very sensitive to the dust absorption and works better over bright surfaces bur there are still problems over bright areas and like many of these visible and near-infrared methods it works well over water but not so well over land, where dust effects on the surface are small.

Chu et al., (2002) has validated the use of MODIS aerosol L2 V5 product over vegetated areas by using AERONET, and found that it can be used in many applications with possible errors for clouds and water contamination, the MODIS aerosol retrievals are found to be within ±0.05, the RMS error are ≤0.1 in the continental regions inland and ±0.3 in the coastal regions  However, the product does not work over the Sahara because of errors in aerosol retrieval over the bright surfaces and it has got other limitations, such as for sub-pixel cloud, moreover the ground pixel resolution of the MODIS product is 10 km, thus limiting its application for dust source detection.

Hsu et al., (2003) designed a satellite aerosol algorithm called "Deep Blue" using visible bands from MODIS to study and describe the properties of aerosols over dust source regions such as arid and semiarid surfaces. Deep Blue has now become a

MODIS aerosol product. Figure 2.4 shows the fundamentals of the Deep Blue algorithm.

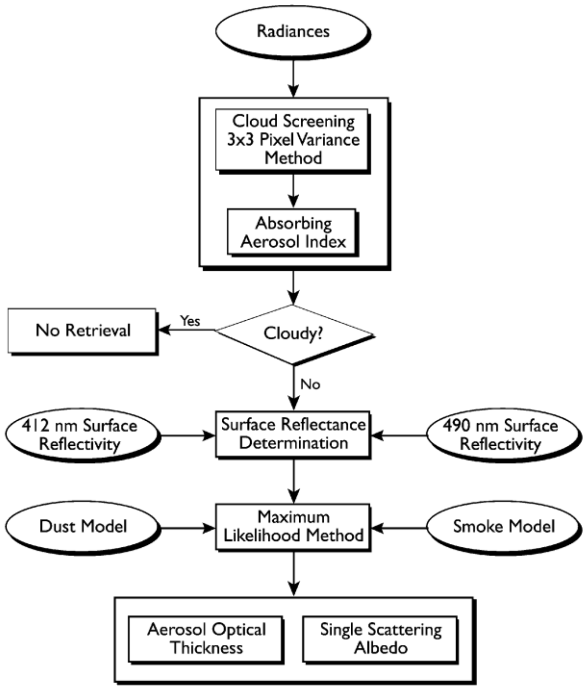


Figure 2.4 Flow chart of the Deep Blue algorithm. (Source Hsu et al., 2003)

The first step is to screen out the cloudy images using two procedures; firstly by applying a spatial variance method to the radiance at 0.41 µm over a 3 pixel × 3 pixels window detect cloud and distinguish between the thick dust and the cloud.

Secondly the absorbing Deep Blue aerosol index (DAI) is calculated.

$$DAI= -100[\ \log_{10}(I_{0.41\ \mu m}/I_{0.49\ \mu m})_{meas} - \log_{10}(I_{0.41\ \mu m}/I_{0.49\ \mu m})_{calc}] \quad (2.4)$$

$I_{meas}$ = measured reflectance at a given wavelength

$I_{calc}$ = model calculated reflectance at a given wavelength from the lookup tables.

$I_{calc}$ is calculated with a radiative transfer model describing a pure Rayleigh atmosphere, and $I_{meas}$ is calculated using the radiance at the given wavelength.

To implement DAI the model generates lookup tables of estimated $I_{calc}$ radiances at 0.41 µm and 0.49 µm, for each pixel by considering the solar zenith, satellite zenith, relative azimuth angles, surface reflectance, single scattering albedo. $I_{calc}$ is estimated using a polarized radiative transfer model (Equation 2.5) designed by Dave (1972) to calculate the reflected intensity where:

$$R(\mu,\mu_0,\phi)=\frac{\pi I(\mu,\mu_0,\phi)}{\mu_0 F_0} \tag{2.5}$$

R is the normalized radiance

$F_0$ is the extraterrestrial solar flux

I is the radiance at the top of the atmosphere

μ is the cosine of the view zenith angle

$\mu_0$ is the cosine of the solar zenith angle

$\phi$ is the relative azimuth angle between scattered radiation and incident solar direction

The assumption made in this algorithm is that the underlying surface is Lambertian and homogeneous. The model computes I as a function of surface reflectance whereby:

$$R(\mu,\mu_0,\phi)=R_0(\mu,\mu_0,\phi)+\frac{TA_s}{1-sA_s} \tag{2.6}$$

$R_0$ is the path radiance

T is the transmission function

$A_S$ is the Lambertian reflectance

S is the spherical reflectance of the atmosphere

The next step is determining the surface reflectance ratio for the given pixel at 0.41 µm and 0.49 µm. The estimated reflectance is then compared to measured reflectance using (Equation 2.6).

The final step use a maximum likelihood method to compute a mixing ratio between dust and smoke using models, this operation iterates until the result make the best match with the calculated spectral reflectance.

Hsu et al., (2003) used five AERONET sites to validate and to compare between the AOT from Deep Blue and the AOT from the AERONET. The comparisons show that the aerosol optical thickness derived from the Deep Blue algorithm are within 20% to 30% of the AOT derived from different sun-photometer stations from the AERONET.

### 2.4.3.2 Techniques to Detect Dust Storms Using Thermal Infrared Bands (7 – 14 μm)

The thermal infrared has the ability to separate the dust signal from other similar components because dust reduces the temperature and increases the scattering of radiation as the wavelength increases, and can be used for aerosol detection, using satellites to monitor the dust storms. Some thermal infrared wavelengths have advantage over visible wavelengths for detecting dust storms by providing data during day and night, and the capability to detect dust over bright surfaces (Ackerman 1997). Several authors have used channels in the thermal spectrum to investigate the detection of dust storms over land.

#### 2.4.3.2.1 Regression Analysis of Brightness Temperature and AOT

Hao and Qu (2007) utilized the brightness temperature of four MODIS channels 3.7, 9.7, 11.0 and 12.0 μm over northern Atlantic Ocean during the period from year 2004 to 2006 to investigate the Saharan dust storm detection, through statistical analysis to develop a new Thermal-infrared Dust Index (TDI),

$$TDI = C0 + C1 * BT_{3.7\ \mu m} + C2 * BT_{9.7\ \mu m} + C3 * BT_{11\ \mu m} + C4 * BT_{12\ \mu m} \qquad (2.7)$$

The coefficients C0 to C4 can be determined through regression analysis between the BT and the AOT. This new index shows a good match with MODIS AOT at 0.5μm, and can detect dust at night time because it uses thermal bands only.

### 2.4.3.2.2 BTD Methods for Detecting Dust

Differences between bands of different wavelength are commonly used to separate an atmosphere with clear sky conditions from an atmosphere contaminated by aerosols. To achieve these brightness temperature differences are usually used. BTD is the difference between two separate brightness temperature observations. It can refer to the difference between observations at the same wavelength at different times (e.g. Kluser and Schepanski, 2009) or (as used here) between two different wavelengths (e.g. Ackerman 1989, Miller 2003, Handly 2004, and Hansell et. al. 2007).

The BTD method is also called the IR split windows technique. Because dust causes a BT difference between two wavelengths, it can allow its identification. Studies show that differences between two infrared spectral bands are very useful for detecting dust and clouds because the aerosols have a high reflectance when compared the background in the wavelengths range from 8µm to 12 µm while within this range the atmosphere is fairly transparent. Furthermore, the atmospheric aerosol and gas, absorption is weak and aerosol scattering is strong at this spectral region. Moreover at the spectral regions 3µm to 12 µm as wavelength increase the scattering by aerosol increase thus BTD can detect dust by differencing shorter and longer wavelengths (Ackerman 1997).

There is another atmospheric between 3 µm and 5 µm, however, here the brightness temperature is complicated by overlap with reflected solar radiation. Thus it is generally thought that the best atmospheric window to use is lies between about 8 µm and 14 µm. Notwithstanding this, many minerals can be diagnosed spectrally in the range of 3µm - 14 µm including the silicates which is the dominant component of continental surface rocks (Pieters and Englert 1993). Thus the BTD of the background may well be quite variable. This problem has not been considered in the literature but is evaluated in this thesis. Figure 2.5 shows the transmission for six different minerals, each mineral deviates from the thermal emittance curve of a perfect blackbody in a different way due to the difference in the structure of the silicates. Three thermal bands from MODIS data are plotted in the graph to show the effect of these mineralogical backgrounds in each band. For example the background effect in the quartz is large between BTD (11 µm-12 µm) and less between BTD (8.6

μm-11 μm). Thus, using split window between BTD (8.6 μm-11 μm) will have minimum background effect over a quartz background. The details of the background effects emissivity will be evaluated in (Chapter 4).

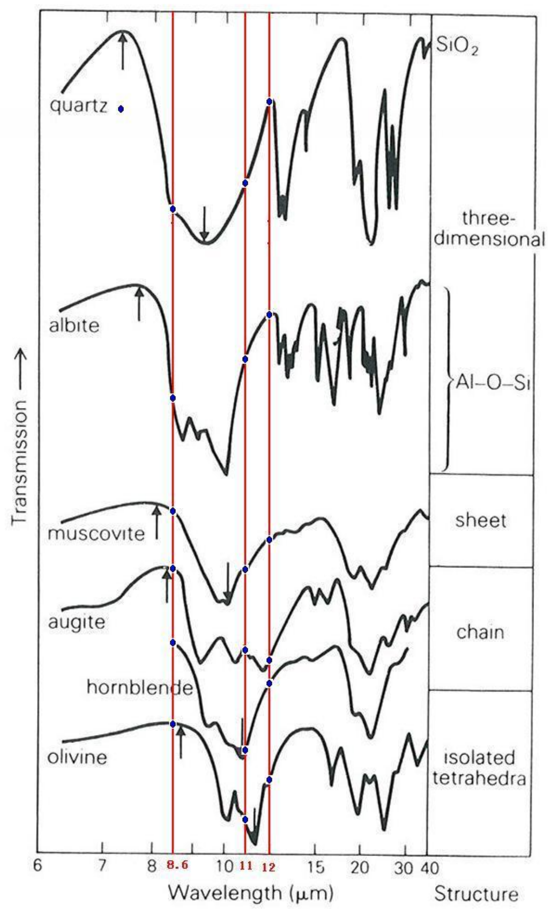


Figure 2.5 Thermal infrared transmission spectra of Silicate minerals. (Source: Drury 1990)

There are several infrared different split windows suggested by the literature to monitor dust, these are outlined below:

### 2.4.3.2.3 BTD (11 μm-12 μm) Split Window

The BTD (11μm - 12μm) split window has been suggested to discriminate between dust and clouds. Dust decreases the BTD (11 μm-12 μm) (Ackerman 1997; Wald et al., 1998). Ice and water preferentially absorb long wavelengths, silicates absorb shorter wavelengths therefore particles of dust should give a negative brightness temperature (Prata 1989). The amount of negative sign of the BTD (11 μm-12 μm) depends on the optical thickness of the dust layer. Moreover the method can discriminate dust from clouds as clouds have a high and usually positive BTD (Ackerman 1997, Hao and Qu 2007).

Bullard et al., (2008) used MODIS BTD 11 µm and 12 µm data from 2003 to 2006 to determine the dust emissions in the Lake Eyre Basin (LEB). Focusing on high intensity dust storms. Dust Storms Day (DSD) were selected when the meteorological stations in the LEB recorded a dust visibility less than >1 km. Each DSD was studied using MODIS Terra and Aqua, and meteorological data was employed to identify the direction of the dust transport. The results were combined with higher resolution Landsat TM data in order to interpret the dust sources and showed 529 dust plumes recorded during that period that were classified as following: 37% of dust plumes originated from Aeolian deposits, 30% from alluvial deposits and floodplains, and 29% from ephemeral lakes. They conclude that 4% of dust plumes recorded at this study originated from Lake Eyre itself. However, previous studies using TOMS suggest the Lake Eyre is the main source of dust emission in Australia.

Zhang et al., (2008) used MODIS data during 2000-2006 to monitor dust storms events in China and Mongolia. A combination of MODIS colour composites, BTD (11 µm - 12 µm), and the NOAA Hybrid Single-Particle Lagrangian Integrated Trajectory model used to track the dust sources. MODIS colour composites are employed to differentiate dust from land and clouds. BTD 11 µm and 12 µm used to show the location of the dust outbreak, its transport, and deposition. They recognized 55 dust plumes, and five distinguishable sources of long distance transported dust were identified and classified from them: (1) 42% from sandy lands and stony deserts in northern China and Mongolia, (2) 20% from Gobi Desert in Mongolia and western part of Mongolia, (3) 10% originates from Gobi Desert in southern Mongolia and the adjacent desert in Inner Mongolia, (4) 18% from sandy lands and deserts along the middle reaches of the Yellow River, (5) 10%originates from the Taklimakan Desert. Thus the sandy lands and stony deserts in northern China and Mongolia were found to be the most active source. These results do not agree with the previous information on dust sources in China. Unfortunately, the study does not tell us the geomorphic nature of the sources using higher resolution data and thus it is not clear exactly what landforms the dust is coming from and the results cannot be compared to those of Bullard et al., (2008).

### 2.4.3.2.4 BTD (3.7 µm-11 µm) Split Window

Ackerman (1989) has investigated the BTD (3.7µm - 11µm) to track dust outbreaks. This technique works best during the day because the spectral radiances are largest during the day, however the technique is still applicable at night but with less sensitivity. Ackerman, (1989) has also indicated that the 'atmospheric temperature moisture profiles, the microphysical properties of the dust, the vertical distribution of the dust, solar zenith angel, satellite viewing angel, and the surface radiative properties' can affect the satellite measured radiance at 3.7 and 11 µm, and conclude from the comparison between the satellite observation of radiative temperature difference between 3.7 and 11 µm and the surface estimates that this BTD is a useful tools to monitor the dust outbreaks and the dust layer optical thickness.

### 2.4.3.2.5 BTD (8.6 µm-11 µm) Split Window

The BTD (8.6µm -11µm) split window has also been suggested by (Ackerman, 1997) to give a negative sign for the dust. Furthermore, large positive brightness temperature BTD (8.6µm -11µm) split window indicate the presence of cirrus clouds (Hansell et. al., 2007). Indeed, most of the different types of clouds have positive values in this BTD (8.6µm -11µm) split window.

### 2.4.3.2.6 BTD (3.7 µm-12 µm) and BTD (8.6 µm-12 µm) Split Windows

The BTD (3.7-12 µm) split window and BTD (8.6-12 µm) split window have not been tested before. Thus their utility is evaluated in this study.

Table 2.6 shows the five different split windows and their wavelengths which have used for this study to identify dust.

Table 2.6 Summary of thermal split windows used in this study

| Split Window | Reference |
|---|---|
| (BT11 µm-12 µm) | Miller (2003) / Handley (2004) / Hansell et al., (2007) |
| (BT3.7 µm-11 µm) | Ackerman (1989) / Handley (2004) |
| (BT8.6 µm-11 µm) | Hansell et al., (2007) |
| (BT3.7 µm-12 µm) | New |
| (BT8.6 µm-12 µm) | New |

## 2.4.3.2.7 Combined Split Windows

In 1997 Ackerman utilized the brightness temperature of the infrared wavelengths at 8.5, 11 and 12 µm derived from AVHRR and HIRS/2 to detect volcanic and soil derived aerosol over oceans by using the BTD (11 µm-12 µm) and BTD (8 µm-11 µm). Moreover the detected aerosols were investigated with theoretical simulation. Ackerman (1997) concluded that the above mentioned wavelengths are useful for detecting aerosols over water but notover land due to variation of the surface emissivity. Further research has shown that BTD values from 8.5, 11, and 12 µm are sensitive to temperature difference that exist between the ground surface and cooler mineral aerosol while at the same time are largely unaffected by absorption from other atmospheric gases (Darmenov and Sokolik 2005).

## 2.4.3.2.8 Infrared Difference Dust Index (IDDI)

Legrande et al., (2001) described the use of the Infra-Red Different Dust Index (IDDI) using the Meteosat 10.5-12.5 µm channel. The method utilises the fact that the flux of heat from the surface upwards into atmosphere is reduced by dust. Furthermore, the dust intercepts incoming signal to the ground causing a reduction of outward long wave signal. The net result of this is a cooling in comparison to the surface in daytime. This technique was used to produce a 1°x1° gridded dataset giving indirect measurement of aerosols over Africa based on 18 years of Meteosat-IR data for the period 1983-2000. The IDDI has been validated using statistical comparison of IDDI data with visibility measured at synoptic stations. The results show that IDDI works well over the arid regions of northern Africa. Moreover, IDDI was validated successfully with the optical depth derived from Meteosat-VIS imagery. This study showed that IDDI has limitations such as: (1) the effect of water vapour on the measured dust can be varying between regions, and (2) processing of can cause a spatial shift due to averaging and statistical computations for large number of images.

Brooks and Legrand (2000) used IDDI to identify the major African dust sources by mapping the distribution of the atmospheric dust over Africa (Figure 2.6). The IDDI dataset showed that most of the dust transported from Sahara comes from the Sahel-Sahara Zone, the Bodélé Depression and a large area covering Mauritania, north-western Mali, and southern Algeria. Other areas are detected with a lower dust concentration but were also are recognised as important dust source areas such as: the Horn of Africa, southern Egypt and northern Sudan. Moreover, there are some small sources in Libya and Egypt.

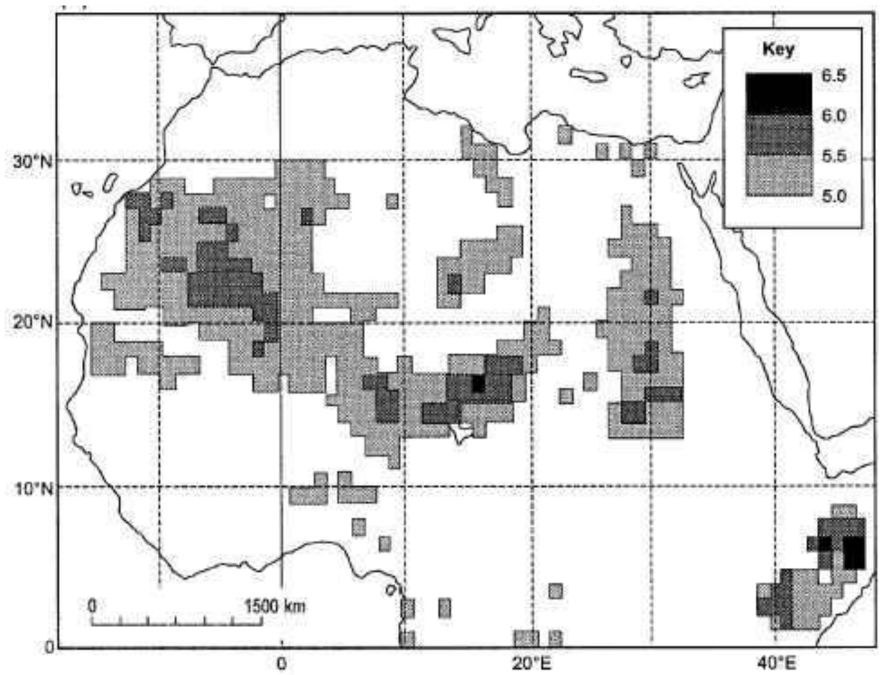


Figure 2.6 Saharan dust sources mapped using annual average dust production over Africa as indicated by time-averaged IDDI values for 1984-1993. High IDDI values indicate large atmospheric dust loading (Modified after Brooks and legrand (2000). (Source: Middleton and Goudie 2001)

## 2.4.3.2.9 BTD Colour Composite

Eumetsat (http://www.eumetsat.int) designed a colour composite to allow SEVIRI to monitor the evolution of dust storms during both day and night over deserts using thermal bands at 12.0 μm, 10.8 μm, and 8.7 μm. The Red-Green-Blue (RGB) combination is based on the difference in the emissivity of dust, cloud and the background as well as the temperature difference between the hot desert surface and the cooler dust. The method uses the following RGB colour composed combination

R= BTD 12.0μm - 10.8μm (2.8)

G= BTD 10.8μm - 8.7μm

B= The 10.8μm channel.

Dust appears pink or magenta in this RGB combination as shown in (Figure 2.7). The dust is clearly distinguished from the cloud and the background. Dry land looks pale blue (day time) to pale green (nigh time). Thick clouds have red-brown tones and thin clouds appear dark. Though the method appears to work well, no quantitative accuracy assessment was carried out.

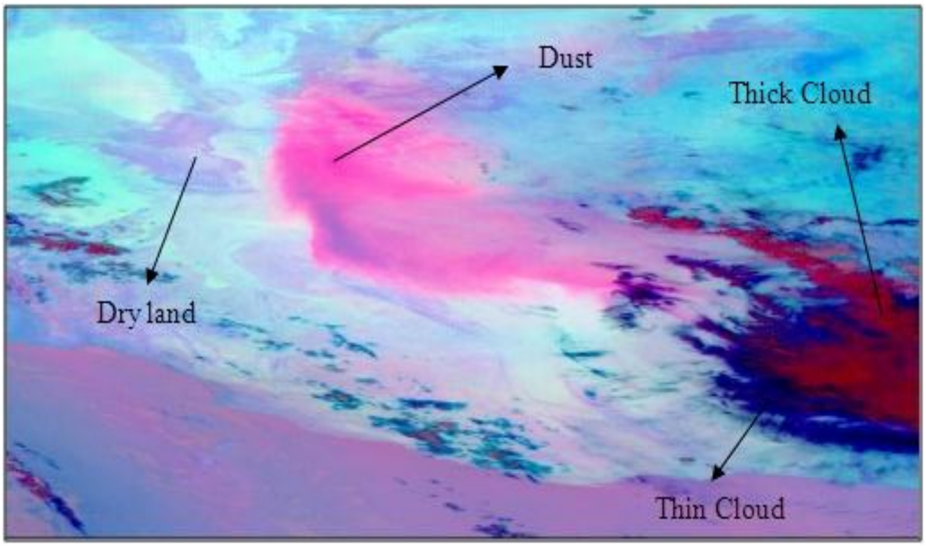


Figure 2.7 Display the dust RGB result for SEVIRI data. Dust displayed in pink Colour and cloud displayed in red colour.

Using the SEVIRI colour composite and BTD methods Schepanski et al., (2007) compiled a new Dust Source Activation Frequency (DSAF) map on a monthly 1º*1º basis for the March 2006 to February 2007 showing dust outbreak areas for the Sahara and Sahel region. Schepanski et al., (2007) performed correlation between BTD (12.0μm - 10.8μm) and AOT from the AERONET stations at Banizoumbou (R=0.73), at Cinzana (R=0.63), and at Dakar (R=0.55) suggesting that the BTD for detecting dust that the colour composite is based on are suitable for detecting the presence of dust. They conclude that the methods generally worked well and the high temporal resolution of MSG improved the detection of atmospheric dust close to its sources. However, there are some limitations such as the difficulty in detecting dust under the cloud, as well as there being doubts about the exact location of dust sources derived from MSG because SEVIRI has a low spatial resolution when compared to MODIS 3 km/1 km.

Schepanski et al., (2009) used these data to calculate the SEVIRI Dust Sources Activations (DSA) per day over Sahara (Figure 2.8). The results show that the Bodélé depression has the highest DSAF. The area covering western Mali and southern Algeria also has a high DSAF. The northern south part of Libya (Benghazi) and eastern Sudan also have got a high DSAF. It is concluded that in general depressions and mountain foothills have a high DSAF.

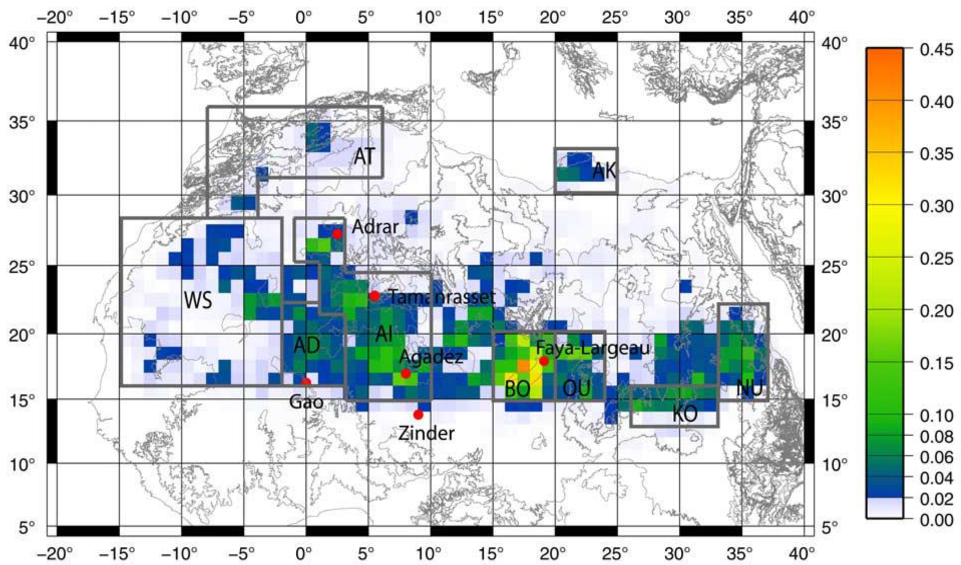


Figure 2.8 Fraction of dust source activation (DSAF) per day during March 2006 to February 2008 derived from MSG IR dust index. (Source: Schepanski et al., 2009)

### 2.4.3.3 Techniques to Detect Dust Storms Using Combined Bands Visible and BTD

A few studies have sought to combine visible and thermal bands into a single index for dust detection. Miller (2003) developed a technique for detecting daytime airborne dust over both water and land. The technique uses MODIS reflectance channels at wavelengths 0.64 µm, 0.46 µm, 0.55 µm, and 1.38 µm and combines it with the brightness temperature difference between 12 µm and 11 µm. The premise of Miller (2003) is that over land elevated dust generates low temperature compared to the surrounding land surface and thus dust and cloud can be differentiated on their radiometric temperature. Furthermore airborne dust produces a positive BTD (12 µm - 11µm) because at 12 µm dust has higher BT than at 11µm and by increasing the dust optical thickness initially will increase the BTD (12 µm – 11 µm). The BTD (12 µm – 11 µm) is opposite in sign for cirrus clouds because negative BTD (12µm – 11 µm) means the presence of water vapour, thus by increasing the amount of the water vapour the BTD (12 µm – 11 µm) becomes more negative. The dust index is calculated using the following method.

$$\text{Dust Index} = L1 + L3 - L4 + (1.0 - L2) \qquad (2.9)$$

where $L1 = BTD\ (_{12\ \mu m - 11\ \mu m})$

ρ radiance

$L2 = BT_{11\ \mu m}$

$L3 = [\,2\rho_{\mathbf{0.64}\ \mu m} - \rho_{\mathbf{0.46}\ \mu m} - \rho_{\mathbf{0.55}\ \mu m}\,] - BT_{11\ \mu m}$

$L4 = \rho_{1.38\ \mu m} > 0.05 = 0$, else = 1

Term L1 uses the principles that the elevated dust produces a depressed brightness temperature against the surface temperature of the land background as outlined above.

Term L2 is used to take into account the fact that the cool dust or cloud may be confused with cold surface.

Term L3 is used to look for the spectral contrasts between the dust and other elements of the image in visible wavelengths, and these contrasts are used to enhance the image for dust.

Term L4 is used to account the cloud from their spectral properties using 1.38 µm.

This technique cannot be used at night, and cannot detect dust which is covered by clouds; it may also give a false indication of dust during cool periods. Moreover, not all dust produces large positive split window, it is vary from background to other.

Handley (2004) combined two split windows, the first split window BTD (3.7 µm-11 µm) to give a big contrast between the dust and background, the second split window BTD (12 µm-11 µm) giving dust a positive value and background a negative one. By multiplying the two windows together re-enforces the large difference between the dust and background and multiplying the product with reflectance at 0.4 µm gives a high index for dust and low values for cloud.

$$\text{Dust Index} = \rho\,(_{0.4\ \mu m}) * BTD\,(_{3.7\ \mu m-11\ \mu m}) * BTD\,(_{12\ \mu m-11\ \mu m}) \tag{2.10}$$

Roskovensky et al., (2005) devised a similar technique to detect and separate airborne dust from clouds using differences in the reflective and emissive wavelength by combining the 0.54 µm/0.86 µm reflectance ratio (rr) with the brightness temperature differences BTD (11 µm-12 µm).

$$D = \exp\{[(rr)*a + (BTD\,(_{11\ \mu m-12\ \mu m})) - b]\} \tag{2.11}$$

Where a= scaling factor and b= a thermal offset.

They show the underlying mechanics using the radiative transfer simulation to test the ability for separating dust from cirrus cloud. They found that the D-parameter algorithm is strong enough to separate dust from cirrus cloud. The limitation of the method, and that of Handly (2004) can be used only during day time because it requires reflectance data.

Hansell et al., (2007) developed the method by combining the three independent approaches to detect dust and discriminate it from cirrus cloud. The first approach used the different properties of the reflective and emissive bands by combining the

0.54 µm/0.86 µm reflectance ratio (rr) with the brightness temperature differences BTD (11 µm-12 µm) (Roskovensky et al., 2005).

$$D= \exp \{[(rr)*a+ (BTD_{(11\,\mu m-12\,\mu m)})-b]\} \tag{2.12}$$

For night time imagery a new D*-parameter technique (Equation 2.13) was developed by Hansell et al., (2007) that depends only on the brightness temperature difference of infrared channels.

$$D^*=\exp \{[BTD_{(11\,\mu m-12\,\mu m)}-C]/[BTD_{(8\,\mu m-11\,\mu m)}-E]\} \tag{2.13}$$

C= thermal offset for BTD $_{(11\,\mu m-12\,\mu m)}$

E= thermal offset for BTD $_{(8\,\mu m-11\,\mu m)}$

A second approach developed by Hansell et al., (2007) uses the slope of the best-fit straight line of BTD $_{(8\,\mu m-11\,\mu m)}$ vs. BTD $_{(11\,\mu m-12\,\mu m)}$ to separate dust from cloud. If the slope is negative then the pixel is flagged as dust, if it is the opposite sign to dust the pixel is flagged as cloud. A third approach uses the BTD $_{(3.7\,\mu m-11\,\mu m)}$ vs. $BT_{11\,\mu m}$ to differentiate between clear-sky, dust and cirrus clouds. By combining the three approaches they can be used to detect dust and separate dust from cirrus during day and night-time.

Qu et al., (2006) has utilized the MODIS solar reflected bands to monitor dust storms using a normalized difference dust index (NDDI).

$$NDDI= (\rho 2.13\mu m - \rho 0.47\mu m) / (\rho 2.13\mu m + \rho 0.47\mu m) \tag{2.14}$$

After analyzing several cases of dust storms over the Gobi region the authors suggest that the NDDI can distinguish dust storms from the ground features. However, it could not separate dust storms from sand and dust on the ground. Thus, the brightness temperature of MODIS 11 µm band has been used to separate the sand and dust storms from the ground sand and dust. Therefore this technique could distinguish between dust, background and clouds. The utility of the NDDI index over African regions has been tested by Wu et al., (2006) using the atmospheric infrared sounder (AIRS) to evaluate the effect of the Saharan Air Layer (SAL) on the Hurricane Isabel (2003), and the method was found to work reasonably well.

EUMETSAT (2001) developed algorithms to detect dust at day time from SEVIRI. The method is based on series of tests involving defined and contextual thresholds in the visual (0.6 μm) and thermal channels (3.9, 8.7, 10.8 and 12 μm) as described in (Equation 2.16). Over land at daytime, a pixel is classified as contaminated by dust if:

$\rho$ (0.6μm) threshold – 15% < $\rho$ (0.6μm) < $\rho$ (0.6μm) threshold +30% (2.15)

0°C < T (10.8μm) < 37°C

BTD (3.9μm - 10.8μm) > threshold

BTD (10.8μm - 12.0μm) > threshold

BTD (8.7μm - 10.8μm) > threshold

SD(10.8μm) < 0.4°C and SD(0.6μm) <0.6%

SD = Standard Deviation This algorithm is not applicable at night-time due to the reflectance bands and even a visual identification of dust is difficult.

None of these combined methods has as yet been used to look at dust sources but they may have potential in this regard. Thus many of them will be investigated in this thesis.

## 2.5 Comparison of Methods of Dust Sources Detection and Monitoring

Baddock et al., (2009) used MODIS data to do a qualitative comparison between commonly used methods: (1) MODIS colour composite (2) BTD (3) Ackerman (1997) (4) Miller (2003) and (5) Roskovensky et al., (2005). Four dust storm events from the Lake Eyre Basin Australia were used to evaluate between these techniques. They found that BTD methods are the most consistently reliable techniques for detecting dust sources in the Lake Eyre Basin where there are multiple dust sources and these sources that have different chemistry. It was found that the BTD are not affected significantly by the differentiation in dust mineralogy. They conclude that: (1) all of the techniques detect dust successfully when compared to MODIS colour composites; (2) the most effective technique for source determination varied from event to event and depended on several factors such as dust mineralogy and surface reflectance.

### 2.5.1 Comparison of Methods for Remote Sensing of Saharan Dust Sources

Schepanski et al., (2007) compared the Sahara dust source map derived from SEVIRI with OMI AI during July 2006 and found a large difference between the SEVIRI and OMI AI that was attributed to downwind transport of the dust storm in the OMI AI retrieval (Figure 2.9). They added ‘The regional shift between the patterns in the two data sets can be explained by the lower sampling rate of AI. OMI has its sun-synchronous overpass over the equator at 13:45 local time, but most dust sources are activated during mornings or during the afternoons and evenings. Thus, at the OMI overpass time, the airborne dust has already been mixed into the atmosphere and transported by local and regional wind systems, thus probably causing a bias in the OMI retrieved source locations. Furthermore, dust detection by OMI below 1.5 km height is difficult (Herman et al., 1997), so that mineral dust in proximity to its source may not be detected’.

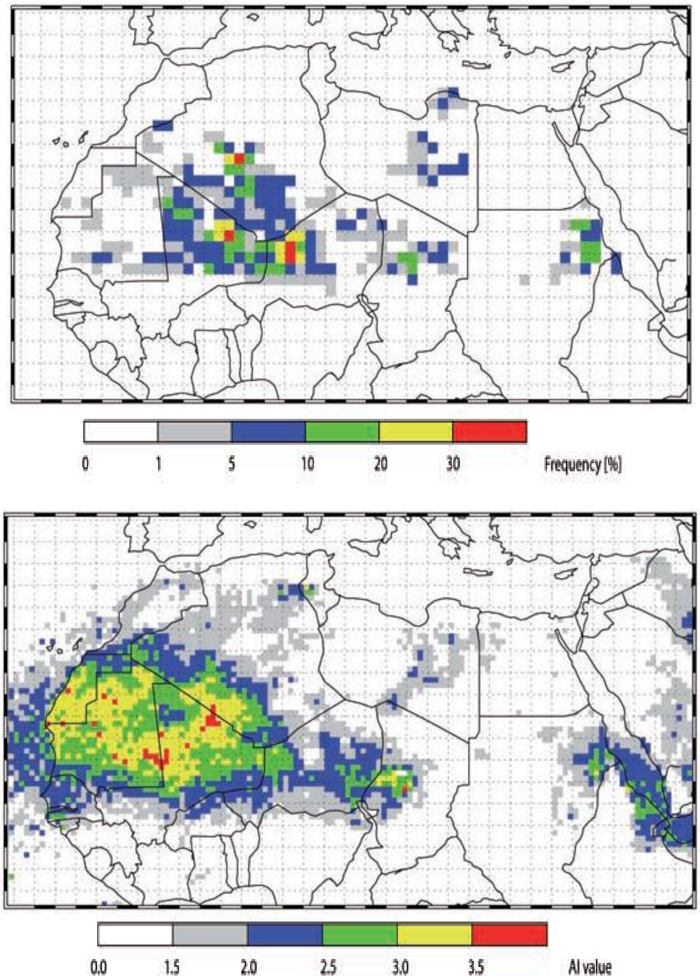


Figure 2.9 Monthly frequency of dust source activation for July 2006, derived from (a) SEVIRI BTD colour composite and (b) OMI AI. (Source: Schepanski et al., 2007)

There have been three previous attempts to delimit Saharan dust sources using remote sensing: (1) IDDI (Brooks and Legrand 2000); (2) TOMS (Washington et al., 2003); and (3) Schepanski et al., (2009). These methods have been merged in one map as shown in Figure 2.10. It is clear that the maps outline different source areas, and there is a disagreement, particularly at low concentrations. TOMS and IDDI are closer to each other than to Schepanski et al., (2009), however in some of the the southern part of the Sahara IDDI and Schepanski et al., (2009) did not detect any sources while TOMS recorded many sources In two parts of the central Sahara there is agreement between all techniques; (1) The Bodélé Depression and (2) The area covers western of Mali and southern of Algeria.

In terms of what is the best of these three methods for mapping sources. It is clear that TOMS and IDDI map the sources and the transport of dust from the sources. This is why in Figure 2.10 both methods map large areas. However, Schepanski et al., (2009), maps much smaller areas because only dust sources are mapped, producing a more accurate result.

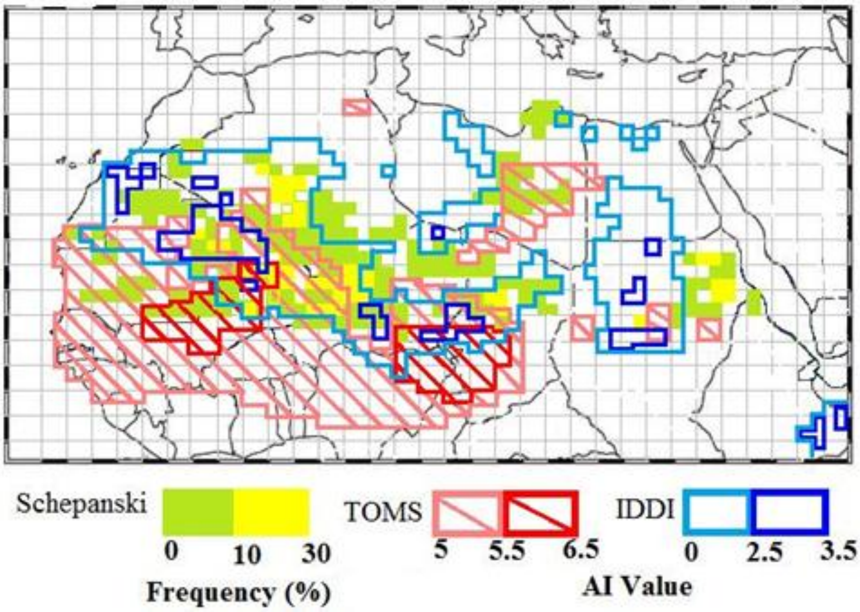


Figure 2.10 Composite of Saharan dust sources maps produced by (1) Schepanski et al., (2009), (2) TOMS Washington et al., (2003), and (3) IDDI Brooks and Legrand (2000).

### 2.5.2 Comparison Between Remote Sensing and Ground Measurements for Mapping Dust

Figure 2.11 shows a comparison between the traditional ground based methods used to map the dust sources and the remote sensing techniques. In general there are disagreements between the remote sensing result and the traditional methods, with the latter showing large areas in the south of the Sahara and the former in the north. However, remarkably there is agreement in the areas where all, or all but one of the methods overlap. These source regions are the Bodélé Depression and the western flanks of the Hoggar Mountains. The Bodélé Depression is a well known and well understood source (e.g. Warren et al., 2007 and Washington et al., 2006), however, the Hoggar Mountains source is poorly understood, and though the general region has often been recognised as a source, the restricted region where all these methods overlap has not been recognised as a premier Saharan source before. This region merits further research.

(1) Traditional methods

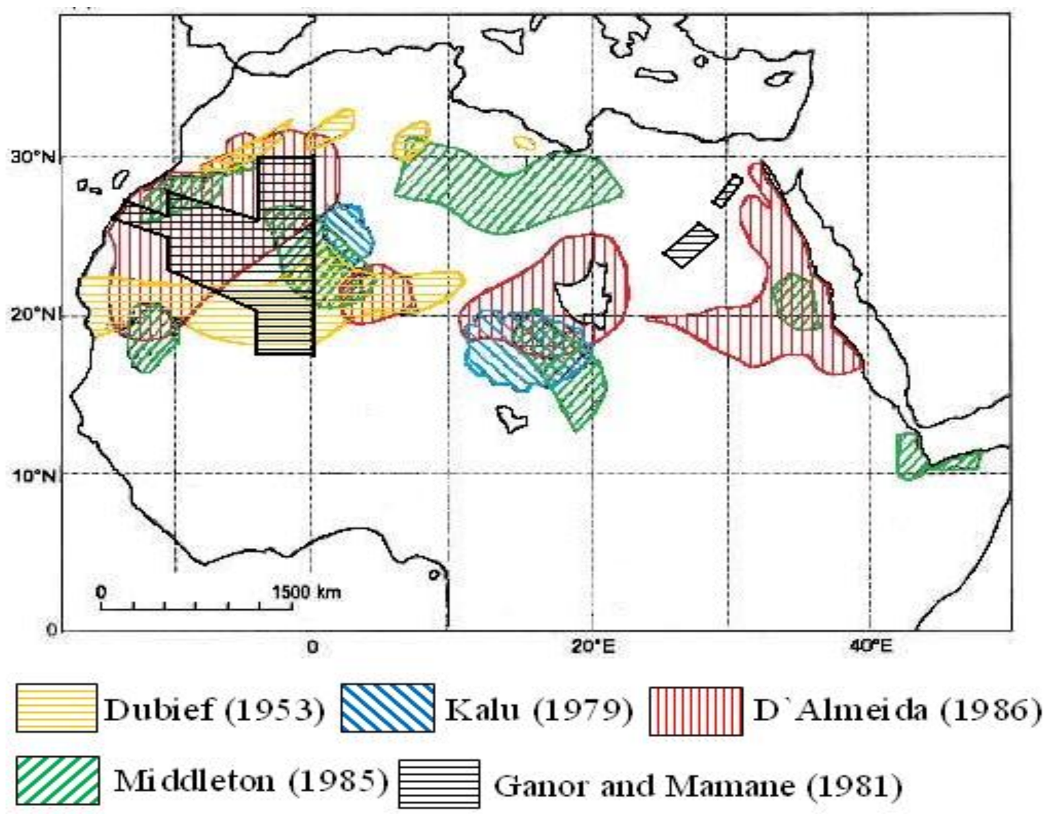


(2) Remote sensing methods

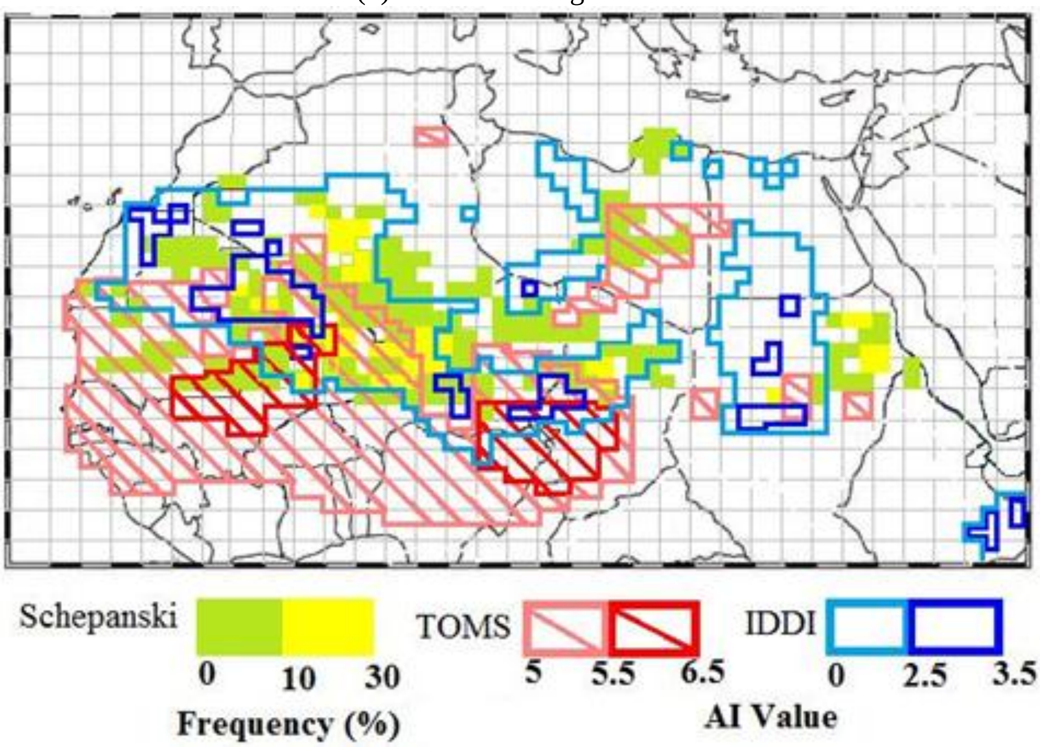


Figure 2.11 Saharan dust sources maps produced by using (1) Traditional methods after (Dubief 1953, Kalu 1979, D'Almeida 1986, Middleton 1985, Ganor and Mamane 1982) (2) Remote sensing methods after (Schepanski 2009, Brooks and Legrand 2000, Washington et al., 2003).

## 2.6 Aims and Objectives

The first aim of this study is to investigate and make comparisons between different techniques used to detect dust using remote sensing. While there are several techniques that can be used to identify desert dust, no comprehensive comparison has been done to evaluate the utility of the different techniques. Here these comparisons are done statistically, graphically, and visually in order to identify which method is most applicable to dust source detection. Five test areas were used during a quantitative comparison of remote sensing methods in order to ensure that the selected technique can perform well over the most common backgrounds of the Sahara.

The objectives of this aim are:

- Outline the environmental effects of dust and the dust cycle.
- Outline the different algorithms for detecting dust storms.
- Outline the remote sensing of dust.
- Select techniques for the comparison.
    - Implement the algorithms over different background of the Sahara using the MODIS data in order to generalize the result over most common background of the Sahara.
- Apply a statistical analysis and validation for the different techniques to find out which of method is most accurate in order to use for the rest of the study.
- Evaluate and select the most accurate cloud mask in order to use for image analysis and visual interpretation to separate dust from cloud.
- Find the best way to present the dust visually.

Limestone is one of the five tested background and chosen to implement the selected technique to evaluate the dust sources because Cyrenaica is dominated by Limestone and it has get easy access to the site for any field work compared to the other tested area. N-E Libya is recognized as one of the main dust sources of the North African. The second aim is to use the optimum technique for dust source detection to evaluate the dust sources in Cyrenaica.

The objectives are to:

- Use the MODIS and SEVIRI to identify the dust sources over Cyrenaica.
- Determine the geomorphology of dust sources in Cyrenaica using Landsat and Google Earth data.

Based on the results of the literature review, this study will quantitatively evaluate five established methods for estimating dust concentration using MODIS data (Ackerman, 1989; Miller, 2003; Handley, 2004; Hansell et al., 2007; Deep Blue, 2006), moreover four new split windows of brightness temperature difference (BTD) have also been used BTD (11 µm-12 µm), BTD (8.6 µm-11 µm), BTD (8.6 µm-12 µm), BTD (3.7 µm-12 µm). We apply the nine selected techniques using MODIS images, investigate each technique and provide statistical, graphical, and visual comparison between them and correlate them with the Aerosol Optical Thickness (AOT) sun-photometer measurements at the AERONET Banizoumbou site, to conclude which technique performs best. We then determine which method provides a good contrast between the dust and background. The most appropriate method is then selected and used to detect the dust over Cyrenaica.

## 2.7 Conclusion

The precise locations of Saharan dust sources are not well known using the ground techniques because each tells a different story about the dust sources apart from two common dust sources in the Bodélé Depression and southern Algeria.

Remote sensing techniques make it possible to locate at least the main sources. The TOMS satellite is good for large scale dust distributions but it has a low spatial resolution and cannot trace dust storms precisely to their sources. Furthermore it detects both emission and transportation of the dust and thus not all anomalies are dust sources. Moreover, the UV bands have difficulty for detecting dust under 1 km altitude (Kubilay et al., 2005).

MODIS (MYD) aerosol product provides more information on dust over water than on land where it fails over bright targets that are common in deserts. The Deep Blue aerosol product has been developed to overcome this problem and holds great promise. However the spatial resolution of both these products is low (10 km), making it difficult to identify the sources of dust. Moreover, Deep Blue is applied to Aqua imagery only though processing is currently under way to apply it to Terra.

The problem with visible techniques is that they do not provide good results over land apart from Deep Blue. Furthermore they cannot be used at night thouth most dust storms activate at day time and only a few activate at night so this is not a major problem.

Brightness temperature split windows are widely used for dust monitoring and have several advantages over the visible wavelengths:

- They can be used during day and night to track the dust.
- Thermal wavelengths can detect dust over the bright areas.

These methods have been shown to be effective at mapping dust sources using both MODIS and SEVIRI.

Techniques that use a combination of visible and thermal bands have portential to identify dust sources because they have the advantage of both wavelengths. However, they have the limitation of the visible wavelengths that they cannot be used at night. The methods have not as yet been used to evaluate dust sources and there is a need to investigate their utility in this regard.

Most of the recent studies that aim to detect dust sources employ thermal bands. The comparison by Baddock et al., (2009) concludes that there is no single method that can be used to detect dust sources over different sources type, because each source can have different mineralogy and most of the techniques used for that comparison influenced by the mineralogy of that source. One of the problems with the study of Baddock et al., (2009) is that it provides a qualitative comparison, a quantitative comparison has not yet been made between these methods. There is a need for such an analysis. This study aims to overcome this problem. To achieve this five techniques were selected for the investigation, the selection being based on using techniques which use visible bands (e.g. Deep Blue (2003)), thermal bands (e.g. Ackerman 1989) and combined bands (e.g. Miller (2003), Hansell et al., (2007), and

(Handley 2004). Moreover, 4 different brightness temperature split windows are tested to find out if any of these provide accurate methods for detecting the dust. However, two of these split windows has not yet investigated. A comparison will be implemented visually, statistically, and graphically by evaluating the techniques using the AERONET data. However, AERONET data is not available all the time for most of the AERONET stations, for that reason the selected years and location for this study are based on the availability of the AERONET data.

Based on the comparison of remote sensing techniques to map the dust sources, the TOMS map shows large areas in Sahara producing dust, however, it is quite difficult to trace the dust sources because of its poor spatial resolution and the fact that the UV is not sensitive to the dust close to their sources. The IDDI technique provides an alternative but has several limitations especially its sensitivity to the water vapour. The Schepanski et al., (2009) method maps sources more precisely by tracking the dust to their sources using the SEVIRI BTD split windows and colour composites. Moreover, due to the high temporal resolution of the SEVIRI data, it allows tracking even the short life time of dust sources. Though Schepanski et al., (2009) provide effective methods of mapping source locations, the method does not identify the nature of the sources, perhaps because the spatial resolution 3 km of the data is not good enough.

Baddock et al., (2009) provide methods of mapping and identifying dust sources using MODIS to locate them and Landsat to identify their nature. A combination of these two methods would provide a comprehensive method for source area identification and characterisation. This thesis aims to achieve this. Therefore a combined Shepanski/Baddock method was developed to identify the dust sources in the north east of Libya with a combination of MODIS, SEVIRI and Landsat ETM data. Northern east Libya was selected as it was identified as a source by Schepanski et al., (2009), but not by any other method, be it from remote sensing or ground based studies. Thus the nature of this potential source has not yet been investigated. Furthermore, the site was readily accessible for field investigation allowing validation of the findings of the remote sensing imagery.

Finally when all the methods of mapping Saharan dust sources are compared there is a vast amount of disagreement, but some agreement, with the Bodélé Depression and the western Hoggar Mountains being sources mapped by all methods, both remote sensing and traditional ones. The nature of the Bodélé Depression source is well understood, however, that of the Hoggar is not. Studying this region would provide a fruitful area of further research.

## 2.8 Structure of Thesis

Following this introduction, this thesis will consist of seven research chapters.

Chapter 1: The literature review, highlighting the different characteristics of dust, its important effects on the global environment and the way it is measured on the ground.

Chapter 2: Provides a literature focussing on remote sensing of dust and the different sensors and techniques are used for mentoring and detecting the dust sources.

Chapter 3: Introduces the methodology for accuracy assessment to evaluate the different techniques used for dust detection.

Chapter 4: Provides the results of this accuracy assessment and decides upon the optimum technique to use for the dust detection in Cyrenaica.

Chapter 5: Introduces the methodology used for detecting and identifying dust sources in Cyrenaica and reviews the geomorphology and geology of the Cyrenaica.

Chapter 6: Presents the dust sources detected in Cyrenaica and their geomorphology.

Chapter 7: Concludes the thesis and suggests further work.

# 3. Methodology for Accuracy Assessment

The aim of this chapter is to go through the steps employed in order to evaluate the nine algorithms used to detect dust sources over five different backgrounds in Sahara. The objectives are:

- Select the most suitable AERONET station.
- Using MODIS data to implement the nine selected algorithms apart from Deep Blue which is NASA product.
- Using sixteen MODIS images determine the correlation between the nine algorithms and the AERONET data.
- Outline four different cloud masks used to determine the most accurate one to implement throughout the rest of the study.
- Evaluate the accuracy of the dust indices using visual interpretation, the M test, and statistical testing.

After reviewing the commonly used techniques to detect dust storms using remote sensing (Chapter 2), nine techniques were selected for accuracy assessment. MODIS data from Aqua and Terra are used to implement the accuracy assessment and the AERONET data is used to validate each method using three types of comparison: statistical, visual, and graphical, as outlined below.

## 3.1 Study Area: The Sahara

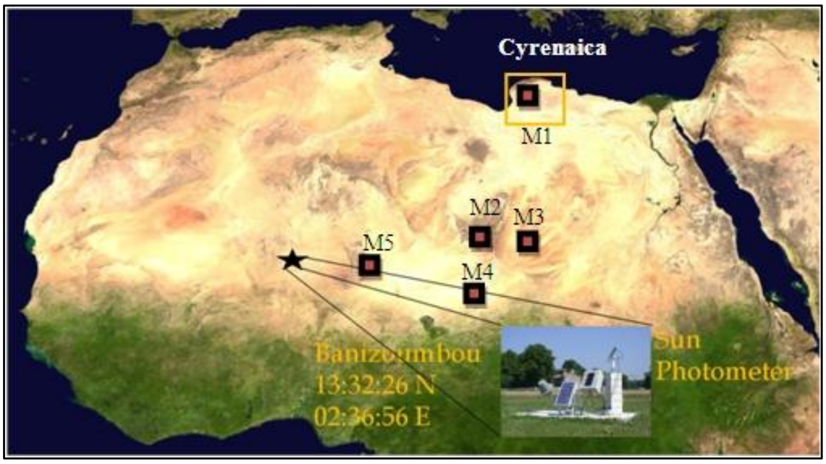


Figure 1.1 MODIS mosaicked Image showing the boundary of the Sahara and the Sun Photometer AERONET site Banizoumbou and the five test areas. M1 is Cyrenaica, M2 is Tibesti Mountain, M3 is an area of sand dunes to the east of Tibesti Mountain, M4 is Bodélé Depression, and M5 is Air Mountains.

The Study area focused on a numbers of regions in the Sahara. First MODIS scenes covering Banizoumbou Niger were used to do the correlation between the techniques and the aerosol optical thickness (AOT) (Figure 1.1). Moreover, the same area was used to test the ability of different types of cloud mask. Another four test areas were used to apply the M test to look at the contrast between the dust and the background (Figure 1.1). The first study area covers Cyrenaica, the second and third study area are in the Tibesti Mountain area in the north west of Chad, the fourth study area is in Bodélé Depression in the south Sahara just south of Tibesti Mountain, and the fifth study area is in the Air Mountains of Niger. After selecting which technique is suitable for detecting the sources of dust, the study will concentrate on Cyrenaica as shown in (Figure 1.1).

To appreciate why it is important to understand dust sources we need to understand the characteristics and the different effects of the dust. Moreover, the dust cycle should be reviewed in order to provide a consolidated background about dust. This is the aim of the following section.

## 3.2 AERONET Data

The AERONET data are used here to select the images were dust can be detected, based on the values of the AOT at the time of image acquisition, and then to do statistical comparison between AOT and the different remote sensing methods. A description of AERONET operations is described in (Chapter 1, Section 1.11). Here we discuss how the data were used.

The Banizoumbou AERONET station level 2.0 were selected for this study because it has full temporal coverage during the years 2006 and 2007, and also has good location for monitoring Saharan dust activity compared with the other stations with similar temporal coverage such as Cape Verde which is close to the coast where it could be affected by water vapour or have more cloud cover. The surficial chemistry of the Banizoumbou AERONET station consistes of soil typical of the Sahel and rich in iron and clay (Shi et al., 2011).


Figure 3.2 MODIS mosaicked Image showing the location of Banizoumbou.

Nine methods have been applied to the sixteen images in order to do the comparisons. This evaluation was based on measurement of the value of the MODIS pixel by calculate the average of 3*3 pixel matrix at the same location of the AERONET station and at the closest time to the Sun-photometer measurements. The MODIS data analysed in this study were collected during dust storms events over the Sahara using Terra and Aqua satellites for the year 2006 and 2007. Sixteen MODIS scenes covering the Banizoumbou AERONET site (Figure 3.2) were chosen, and downloaded from the NASA website http://ladsweb.nascom.nasa.gov/data/search. Only MODIS images was used for the correlation between the AOT and the indices because MODIS has got higher resolution than SEVIRI, the selection of sixteen MODIS images was based on the value of the AOT from the Banizoumbou AERONET station whereby it was possible to decide whether there is dust over the area of interest or not and how much dust there was. It was also possible to exclude smoke and other aerosols by ensuring that only the retrievals for AOT (1020nm) $\geq$ 0.5 are used (Dubovik et al., 2002). Figure 3.3 shows an example of AOT data received from Banizoumbou AERONET site for one year.

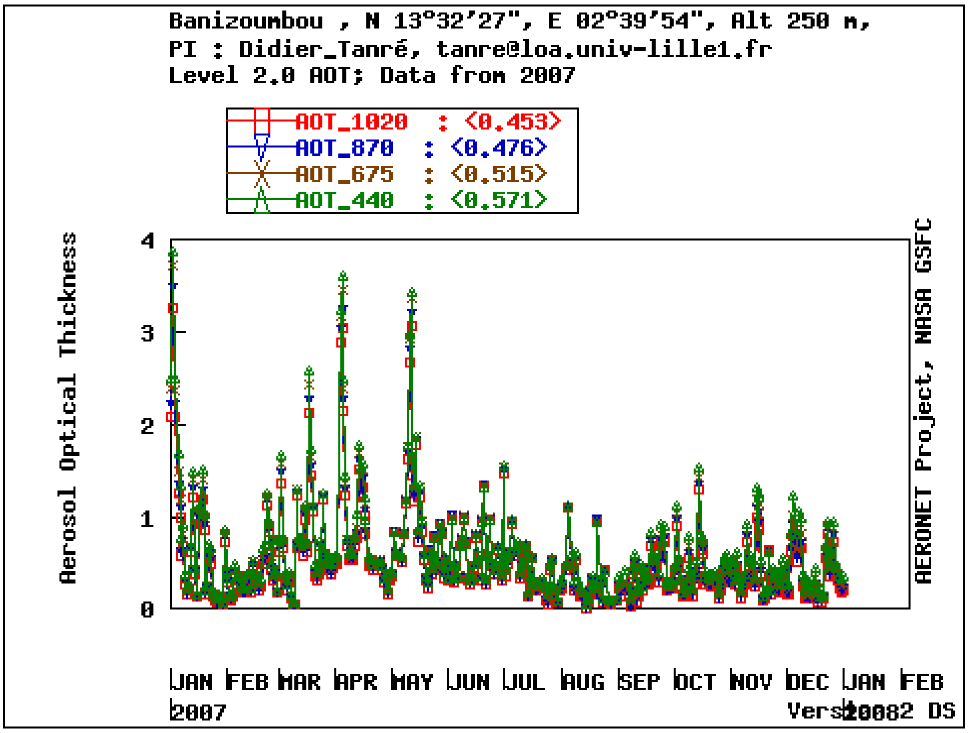


Figure 3.3 AOT Level 2.0 data for clear sky conditions for the year 2007 from Banizoumbou station (at the location N 13˚32′27″, E 02˚39′54″). The altitude of the station is 250m. Four different wavelengths ARE displayed in different colours in the graph. (Source: http://aeronet.gsfc.nasa.gov)

In order to develop a rigorous correlation dataset a range of concentrations of dust needs to be selected. This was achieved by selecting a range of AOT values close to the time of the satellite overpass and then acquiring these images. Data from the AERONET site can be used to achieve this. For example Figure 3.3 can be used to decide which months of the year have different AOT values, in this case it is clearly shown that January and April has the highest AOT during the year of 2007. Through the value of the AOT is an indicator for the presence of aerosols it does not say exactly what type of aerosol is it. The AOT is recorded in four different wavelengths to allow the interpreter to classify the type of aerosol based on the sensitivity of different type of aerosol, we can decide which wavelength we can use, and in our case we have used AOT 1020nm due to its sensitivity to the mineral dust (Dubovik et al., 2002).

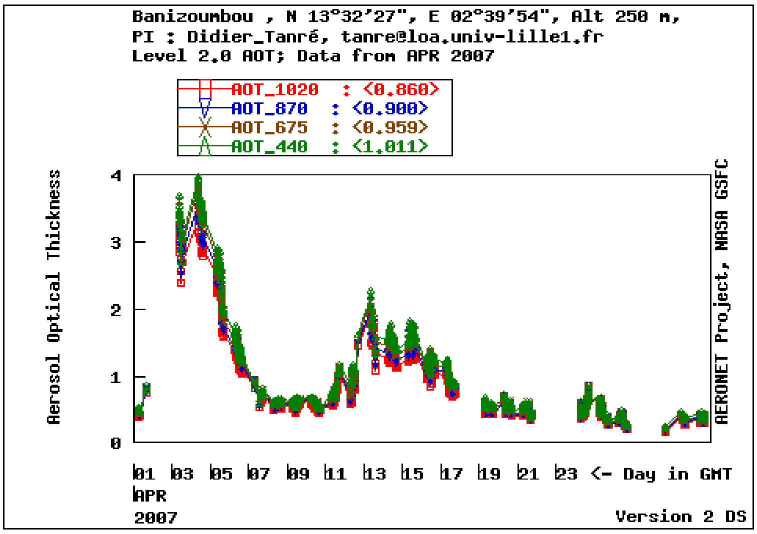


Figure 3.4 AOT Level 2.0 data from April of 2007, the AOT values in the first 5 days of the month have got high values and at the second half of the month the AOT values are less than 0.5. (Source: http://aeronet.gsfc.nasa.gov)

The monthly graph is shown in Figure 3.4 for April. It allows the selection of specific days. The value of AOT is always over 0.5 which indicates that during this month there was always aerosol over this area. However, the AOT value varies from hour to hour depending on the concentration of the dust. Thus we can plot the days were we expecting dust. Figure 3.5 displays the distributions of the AOT during the third of April 2007. The graph shows dust over the study area for most of the day, and the AOT value stayed over 2 from 9 am to 2 pm. Using this information the data from the time of the Terra or Aqua overpass was selected to correlate the AOT with the various indices derived from the MODIS imagery.

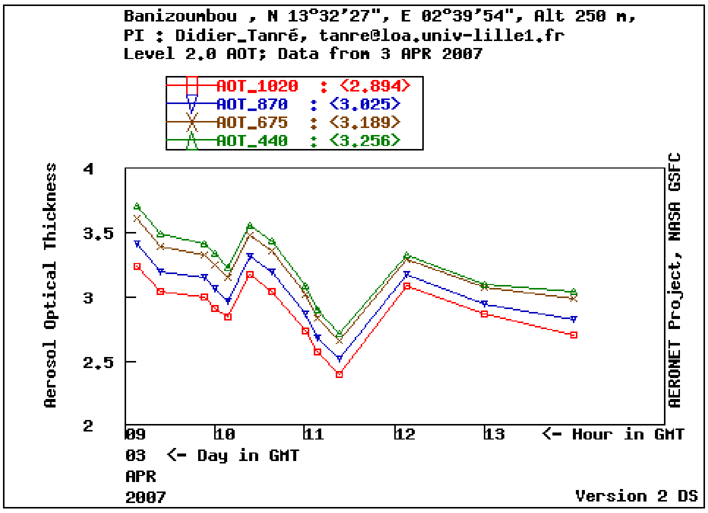


Figure 3.5 AOT Level 2.0 data from April 3rd of 2007, in the morning the AOT value have got the highest value, were at mid of the day the AOT have got the lowest value because the concentration of dust is reduced (Source: http://aeronet.gsfc.nasa.gov).

Table 3.1 lists the sixteen chosen AOT values from 2006 and 2007 for the Banizoumbou AERONET station. The data are pre and post field calibrated, automatically cloud cleared and manually inspected.

Table 3.1 List of Level 2 Quality Assured AOT used in this study at Banizoumbou.

| AOT | Date(dd-mm-yyyy) | Time(hh:mm) | Julian_Day | AOT_1020nm |
|---|---|---|---|---|
| 1 | 01:01:2007 | 09:39 | 1 | 1.809073 |
| 2 | 12:01:2007 | 10:28 | 12 | 0.584544 |
| 3 | 03:04:2007 | 10:38 | 93 | 3.048300 |
| 4 | 05:01:2007 | 12:55 | 5 | 1.222321 |
| 5 | 17:01:2007 | 13:06 | 17 | 0.884955 |
| 6 | 19:01:2007 | 14:15 | 19 | 1.001109 |
| 7 | 03:03:2007 | 14:02 | 62 | 0.526485 |
| 8 | 10:03:2007 | 13:08 | 69 | 1.192865 |
| 9 | 05:04:2007 | 10:23 | 95 | 2.371686 |
| 10 | 06:04:2007 | 11:07 | 96 | 1.166856 |
| 11 | 05:04:2007 | 13:23 | 95 | 2.194388 |
| 12 | 12:03:2006 | 10:07 | 71 | 0.704177 |
| 13 | 12:03:2006 | 13:00 | 71 | 0.683043 |
| 14 | 18:04:2006 | 10:04 | 108 | 1.668942 |
| 15 | 12:12:2006 | 07:52 | 346 | 0.963792 |
| 16 | 29:12:2006 | 12:52 | 363 | 1.028582 |

## 3.3 MODIS Data Retrieval

Based on the AOT listed in Table 3.1, sixteen (Level-1B calibrated radiance) MODIS images are selected from the Atmosphere Archive and Distribution System (LAADS) for the Terra and Aqua platforms at the same date and closest time to the AERONET data for the years 2006 and 2007. The details of the dates of the MODIS images used and the bands employed in the analysis are shows in Tables 3.2, 3.3, and 3.4. The reflectance and emissive radiance was imported for ENVI and IDL software for analysis. Bands 1, 4, and 3 as Red, Green, and Blue (RGB) respectively, were most suitable for visualising the landscape and for the visual comparison of these images.

Table 3.2 Summary of thermal bands used in this study

| Band | Bandwidth | Central Wavelength | Pixel Size | Used Technique |
|---|---|---|---|---|
| 20 | 3.66 µm - 3.84 µm | 3.785 µm | 1 km | Ackerman (1989) / Handley (2004) |
| 29 | 8.40 µm - 8.70 µm | 8.518 µm | 1 km | Hansell et al., (2007) |
| 31 | 10.78 µm - 11.28 µm | 11.017 µm | 1 km | Ackerman(1989)/ Miller(2003)/ Handley(2004) /Hansell et al., (2007) |
| 32 | 11.77 µm - 12.27 µm | 12.032 µm | 1 km | Miller(2003)/ Handley(2004)/ Hansell et al., (2007) |

Table 3.3 Summary of visible bands used in this study

| Band | Bandwidth | Central Wavelength | Pixel Size (m) | Used Technique |
|---|---|---|---|---|
| 1 | 0.620 µm – 0.670 µm | 0.645 µm | 1 km | Miller (2003) |
| 3 | 0.459 µm – 0.479 µm | 0.465 µm | 1 km | Miller (2003) |
| 4 | 0.545 µm – 0.565 µm | 0.553 µm | 1 km | Miller (2003) |
| 8 | 0.405 µm – 0.420 µm | 0.411 µm | 1 km | Hundley |

Table 3.4 Summary of MODIS images used in this study

| Image No. | MODIS Sensor | Date (dd-mm-yyyy) | Time (hh:mm) UTC | Location {UL( lon, lat), LR(lon, lat)] |
|---|---|---|---|---|
| 1 | Terra | 01:01:2007 | 10:10 | UL 02°07’15W, 21°11’36N<br><br>LR 14°30’92E, 04°17’23N |
| 2 | Terra | 12:01:2007 | 09:50 | UL 03°42’44E, 27°06’50N<br><br>LR 20°35’21E, 10°09’55N |
| 3 | Terra | 03:04:2007 | 10:35 | UL 08°10’50W, 21°56’02N<br><br>LR 08°25’27E, 05°01’53N |
| 4 | Aqua | 05:01:2007 | 12:50 | UL 01°14’00W, 25°11’37N<br><br>LR 16°21’04E, 09°54’22N |
| 5 | Aqua | 17:01:2007 | 13:15 | UL 07°31’00W, 25°29’33N<br><br>LR 10°04’23E, 10°16’40N |
| 6 | Aqua | 19:01:2007 | 13:00 | UL 01°40’32W, 15°59’09N<br><br>LR 15°10’55E, 00°43’57N |
| 7 | Aqua | 03:03:2007 | 12:45 | UL 00°20’09W, 26°56’57N<br><br>LR 17°26’37E, 11°48’01N |
| 8 | Aqua | 10:03:2007 | 12:50 | UL 00°30’23W, 22°39’34N<br><br>LR 16°48’33E, 07°22’38N |
| 9 | Terra | 05:04:2007 | 10:25 | UL 06°57’42W, 13°16’58N<br><br>LR 09°42’24E, 03°34’56S |
| 10 | Terra | 06:04:2007 | 11:05 | UL 15°14’46W, 25°07’50N<br><br>LR 01°31’57E, 08°12’21N |
| 11 | Aqua | 05:04:2007 | 13:25 | UL 07°44’37W, 15°37’47N<br><br>LR 09°06’27E, 00°17’41N |
| 12 | Terra | 12:03:2006 | 10:05 | UL 01°58’02W, 14°44’34N<br><br>LR 14°44’26E, 02°13’15S |
| 13 | Aqua | 12:03:2006 | 13:05 | UL 04°38’13W, 21°05’17N<br><br>LR 12°32’54E, 05°48’46N |
| 14 | Terra | 18:04:2006 | 10:20 | UL 03°43’50W, 28°26’33N<br><br>LR 13°12’19E, 11°29’15N |
| 15 | Terra | 12:12:2006 | 10:35 | UL 08°44’43W, 18°54’25N<br><br>LR 07°49’53E, 02°01’08N |
| 16 | Aqua | 29:12:2006 | 12:45 | UL 01°02’11W, 29°22’19N<br><br>LR 17°01’51E, 14°12’00N |

## 3.4 MODIS Data Pre-processing

All MODIS images were downloaded from the NASA website in Level 1B 1km that is calibrated to spectral radiance in watts per square meter per steradian per micron ($Wm^{-2}\ sr^{-1}\ \mu m^{-1}$).

Using the ENVI software the L1B images was geo-referenced using a geographic Lat/Lon projection on the WGS-84 mapping datum. Full size images (approximately 2300 km x 2300 km) were used.

## 3.5 Brightness Temperature

Images were then converted to Brightness temperature (BT). This is a convenient descriptive measure of thermal radiation from the Earth's surface and atmospheric aerosols can be expressed in the form of the temperature of a blackbody emitting an identical amount of radiation at a given wavelength. This procedure requires specification of wavelength interval, direction, and location of the observation. BT may have different values based on the angle of the sensor, bandwidth, and the wavelength (Norman et al., 1995). Equation 3.1 formulates the relation between directional radiance and target brightness temperature for channel i:

$$R_{B,i}(\theta,\phi) = R(T_{B,i}(\theta,\phi)) = \int_{\lambda 1}^{\lambda 2} \frac{f_i(\lambda)C_1}{\pi\lambda^5[\exp(\frac{C_2}{\lambda T_{B,i}(\theta,\phi)})-1]} d\lambda \qquad (3.1)$$

Directional Radiance $R_{B,i}(\theta,\phi)$

Target Brightness Temperature $T_{B,i}(\theta,\phi)$

Wavelength $\lambda$

$\lambda_1$ and $\lambda_2$ are lower and upper wavelengths

$C_1 = 3.7404.10^8\ W\mu^4 m^{-2}$

$C_2 = 14387\mu k$

$f_i(\lambda)$ Is the relative response of the IRT detector between $\lambda_1$ and $\lambda_2$

Using the IDL software the brightness temperature was calculated for emissive bands using inverse Planck function (Wooster and Rothery 1997) as shown below:

$$BT = \left(\frac{hc}{k\lambda}\right)\frac{1}{ln\left(2hc^2\lambda^{-5}L^{-1}+1\right)} \tag{3.2}$$

*Where:*

$L$ = spectral radiance ($Wm^{-2}\ sr^{-1}\ m^{-1}$)

$h$ = Planck's constant (j/s)

$c$ = speed of light in vacuum (m/s)

$k$ = Boltzmann gas constant (j/k)

$\lambda$ = band or detector centre wavelength (m)

$BT$ = temperature in Kelvin (k)

## 3.6 Cloud Masking

A cloud mask is an image based product that gives information on the presence of cloud. Cloud masking is an important step during the image pre-processing and interpretation stage to separate dust from cloud, because some indices do not separate cloud from dust, and in the cases where they do some types of cloud (i.e. cirrus cloud) can be difficult to distinguish from the dust (Ackerman et al., 1998).

Cloud contamination remains a major problem and an important source of error effecting the retrieval of aerosol and surface properties from satellites (Mishchenko et al., 1999). Because the dust is transported horizontally over large distances, it sometimes located as much as 5 km in altitude, which is above the water vapour layer and at this altitude it can produce high reflectance at 1.38 µm which is used to detect cirrus cloud. Moreover dust particles produce emissivity differences between 8.6 µm and 11 µm that create brightness temperature differences similar to those of thin cirrus (Wald et al., 1998).

In order to overcome these problems cloud masks are applied to images. Three cloud masks were tested to select the most accurate one to use in the study as outlined below.

### 3.6.1 The Giglio et al., (2003) Cloud Mask

Clouds masking using Giglio et al., (2003) algorithm was initially developed for the AVHRR- derived Global Fire Product (Giglio et al., 2003). The method uses tests based on a combination of solar reflected radiation and thermal infrared brightness temperatures, classifying pixels as cloudy if they satisfied any of the following tests:

$$\rho_{0.65} + \rho_{0.86} > 0.9 \tag{3.3}$$

$$T_{12} < 265K$$

$$(\rho_{0.65} + \rho_{0.86} > 0.7) \text{ and } (T_{12} < 285K)$$

Where ρ is the reflectance measured (in the specified wavelength) in μm and T is the brightness temperature in Kelvin at the specified wavelength.

### 3.6.2 MODIS Cloud Mask

The MODIS clouds mask algorithm uses radiance from 13 MODIS spectral bands (Table 3.5). This algorithm classifies each pixel as either confident clear, probably clear, cloudy or probably cloudy. The MODIS cloud mask has 1 km and 250m spatial resolution depending on the wavelengths used. The 250m cloud mask is based on the visible wavelengths whereas the 1 km cloud mask is based on the infrared spectral bands (Ackerman et al., 1998).

The cloud mask is then updated using other MODIS products that map phenomena that can be confused with cloud as outlined below:

A maximum likelihood classification initialized from the cloud mask algorithm was used to classify the scenes and clouds, the method tries to analyze data and identify several group of classes and can be described by the following steps:

1- Classify the MODIS measurements using the MODIS cloud mask
2- Calculate the mean vector and covariance matrix for each class
3- Calculate the mean vector and covariance matrix for each class
4- Calculate the distance between the vector of each pixel and all the class mean vectors and assign the pixel to the nearest class
5- Update the class mean vector and covariance matrix off each class

6- Analyze the separability of the classes by merging the pixels were the distance between the pixels is very small and forming new class if the distance between a pixel and its nearest class is very large.

Table 3.5 MODIS bands used for the cloud mask algorithm
(Source: http://modis.gsfc.nasa.gov/about/specifications.php)

| MODIS Bands | Bandwidth (nm) | Central Wavelength (nm) | Pixel Size (m) |
|---|---|---|---|
| 1 | 620 - 670 | 645 | 250 |
| 2 | 841 - 876 | 856 | 250 |
| 5 | 1230 - 1250 | 1241 | 500 |
| 6 | 1628 - 1652 | 1629 | 500 |
| 18 | 931 - 941 | 935 | 1000 |
| 19 | 915 - 965 | 935 | 1000 |
| 20 | 3,660 – 3,840 | 3,785 | 1000 |
| 21 | 3,930 – 3,989 | 3,960 | 1000 |
| 27 | 6,535 – 6,895 | 6,752 | 1000 |
| 29 | 8,400 – 8,700 | 8,518 | 1000 |
| 31 | 10,780 – 11,280 | 11,017 | 1000 |
| 32 | 11,770 – 12,270 | 12,032 | 1000 |
| 35 | 13,785 – 14,085 | 13,907 | 1000 |

1- Determine the pixel is over land or water.
2- Determine the ecosystem type.
3- Determine if pixel is in a sun glint region.
4- Determine if the pixel is in a day or night regime.
5- Retrieve information from snow cover and ice data base.
6- Update snow cover by implementing simple Normalized Difference Snow Index (NDSI).
7- Apply appropriate single field of view (FOV) masking test to insure the FOV of the earth surface is unobstructed by clouds and to insure the FOV is not affected by cloud shadows. .
8- If confidence level is still uncertain, use spatial uniformity tests on 3 x 3 pixel regions. The confidence is based on four level of confidence; clear, probably clear, probably cloudy, cloudy.
9- Check for temporal consistency
10- Update clear-sky radiance

### 3.6.3 Deep Blue Algorithm Cloud Mask

Hsu et al., (2003) used the cloud mask algorithm developed by Ackerman et al., (1998) to screen for cloud pixels. The algorithm is based on spatial variance over a 3 pixels × 3 pixels applied to the radiance at 412 nm using automated texture classification techniques that estimate the confidence of a pixel being cloudy. 412 nm is used because the surface reflectivity at this wavelength is usually dark over land compared to the longer wavelengths thus ensuring more contrast between the cloud free and cloudy pixels. Moreover, the 412 nm wavelength provides a good contrast between thick dust layers and the clouds.

### 3.6.4 The BTD (11 µm-12 µm) Split Window

Differences between two infrared spectral bands have been shown to be useful for detecting clouds (Ackerman, 1997). The difference between BT11 µm and BT12 µm is widely used for cloud detection, for example Kriebel et al., (1988) used (11 µm-12 µm) split-window to detect cirrus cloud from AVHRR data. The BTD (11 µm-12 µm) window gives dust and background a negative value and the clouds a positive value (Ackerman, 1997). For this study BTD (12 µm-11 µm) split-window was thresholded at 0 with positive values assigned to the cloud mask.

## 3.7 Cloud Mask Accuracy Testing

To determine which cloud mask is most accurate, three MODIS images were selected that contained different cloud types. Three hundred points were then randomly distributed over each cloud mask and the presence of cloud evaluated at these point using visual interpretation of MODIS colour composites (Bands 1, 3, and 4 on R, G, and B). The points were defined using the Idrisi random sample programme. The 300 points were classified into three classes using visual interpretation of colour composite imagery:

1- Red class, representing background.

2- Yellow class, representing dust.

3- Green class, representing cloud.

There are three classes were employed in order to test the cloud mask accuracy, as it was noted during image interpretation that some methods misclassified dust as cloud, and thus would perform poorly for the purpose of dust detection. By analysing these three classes this misclassification could be evaluated.

## 3.8 Techniques to Detect Dust Storms

Nine techniques were selected for the evaluation, some of them use combined visible and thermal infrared bands, and the rest use brightness temperature difference split windows as listed below:

- Ackerman (1989).
- Miller (2003).
- Hansell et al., (2007).
- Handley (2004).
- Deep Blue (2003).
- BTD (3.7 μm-12 μm) split window.
- BTD (8.6 μm-11 μm) split window.
- BTD (8.6 μm-12 μm) split window.
- BTD (12 μm-11 μm) split window.

## 3.9 Evaluating the Accuracy of Dust Indices

Three methods were used to evaluate the accuracy of dust indices: (1) visual analysis, (2) the M test that was used to study background effects and (3) other statistical tests that were applied to evaluate the relationship between the AOT and the dust index in question.

### 3.9.1 The M Test

The selected 9 techniques were evaluated to find out which technique can best distinguish between dust and the different backgrounds using the M test. Pereira (1999) argues that visual inspection alone is not an accurate methodology for determining the ability of indices to discriminate between classes. He suggests the M test that uses the differencing of means, and the inclusion of standard deviations as a measure of noise as shown below:

$$M = (\mu_d - \mu_b) / (\sigma_d + \sigma_b) \qquad (3.4)$$

$\mu$ = mean

$\sigma$ = standard deviation

d = dust

b = background

In order to determine the susceptibility of the different methods to different backgrounds the M test was applied over 5 different backgrounds to ensure that the selected technique can perform well over different rock types. The five backgrounds used for this study are: Limestone, Basalt, Diatomite**,** Quartz, and Granite. The reason for choosing these five types of background is because they are common rocks in the Sahara and are located close to the most known sources of dust. In order to allow direct comparison between techniques the result from each technique (dust index) was studied without any image enhancements applied. Details and the result of M test will be described in section (4.3).

### 3.9.2 The Emissivity of the Background

The emissivity of a surface is the ratio of the energy radiated from the surface to energy radiated by blackbody at same temperature and same wavelength. Prata, (1993) discussed the effect of land surface emissivity on satellite measurements and conclude that different surface emissivity can causes a reduction on emitting radiance. Moreover, the anisotropy of emissivity may reduce or increase the total radiance from the surface. Thus, the emissivity of land surface is important factor for determining the thermal radiation of the land surface.

In order to understand why different techniques give different result over different backgrounds how different backgrounds present different results using different dust indices, the emissivity of five tested backgrounds used during this thesis are presented.

There are several factors can control the emissivity of a surface such as water content, chemical composition, structure, roughness, the wavelength, and the view angel of the sensor. Thus these factors those have the potential to affect the various dust indices evaluated in this study. In desert environments perhaps the most important factor is the emissivity of the different rock and sediment types that make up the vast majority of the desert surface. The emissivity of these different backgrounds is studied in order to find out how each of the split windows that were designed to detect dust are affected by the background geology/geomorphology and to compare these findings to those of the M test in order to try and explain the reasons for the different background affects evident in the various dust indices studies here.

### 3.9.2.1 Laboratory Infrared Spectra

There are several mineral spectral emissivity studies that have been conducted in the mid-infrared. Lyon (1964) published spectral emissivity measurements of 98 samples of primarily igneous rocks that were evaluated both petrographically and chemically. Hunt and Salisbury (1974) published reflectance spectra of 85 igneous rocks while Salisbary et al., (1992) presents mineral spectra of different particle size ranges. However, these data are not available digitally.

The ASTER digital spectral library has over 2400 visible and middle infrared spectra of natural and manmade materials. It is a compilation of spectra including data from three spectral libraries: the Johns Hopkins University (JHU), Jet Propulsion Laboratory (JPL), and United State Geological Survey (USGS) Spectral Library. This Aster spectral library was used in this study. Four of the five tested backgrounds are available in ASTER spectral library (Basalt, Limestone, Quartz, and Granite). The emissivity of the Diatomite was measured at the Geography Laboratory of King’s College London Geography Department using a MIDAC M2000 series FTIR spectrometer with a spectral range from 1.5 – 15.4 µm.

Four samples from each background were averaged and used to calculate the emissivity differences in the same manner as the brightness temperature differences are applied to the various dust indices. For the diatomite where there is only one sample and it was used alone.

### 3.9.3 Statistical Testing

The statistical testing is used to provide a strong evaluation of the relationship between AOT and the remote sensing techniques. In order to have different types of tests to support this accuracy assessment the correlation and the Root Mean Square Error (RMS Error) between indices and AOT was calculated.

#### 3.9.3.1 Correlation and Regression

Correlation and linear regression is widely used in geographical research to study relationships between phenomena. Regression gives the equation

$$y= a + b x \tag{3.5}$$

Were y is the predicted value of the dependent variable, x is the value of the independent variable, and (a and b) are regression coefficients. The dependent values are the variable whose values are to be predicted, given values of the independent variable. In our case the dust indices are the dependant variable evaluated to determine how they can predict the independent AOT measurements from the AERONET data.

The $R^2$ value can be used to assess the strength of the relationship between the various dust indices and AOT (Schepanski et al., 2007). The Pearsons product moment correlation coefficient was employed, because the Kolmogorov-Smirnov Test showed that the data was normally distributed as outlined below.

#### 3.9.3.2 Normality Testing

The Kolmogorov-Smirnov test was used to test the normality of the distribution after standardizing the data in order to determine whether a data set is well modeled by a normal distribution. In this case the normality test is used to test how each indices value are distributed over the sixteen selected images. This test used in conjunction with visual examination of the histogram with normal curve superimposed over it. (Ebdon, 1985)

### 3.9.3.3 Standardizing the Data.

The units and range of the dust indices are not same and this can lead to problems in applying both correlation and RMS Error. Thus it is necessary to standardize the indices using the following equation (Ebdon, 1985):

Standardized Variable = $((\sum_{i=n}^{i=1} DustIndex) - \mu) / \sigma$ (3.6)

### 3.9.3.4 Error Bars

The results of the correlation and regression analysis are presented in graph form in (Chapter 4). To aid interpretation error bars have are also displayed. Error bars are used to indicate the error in reported measurements when comparing two quantities. The error (total uncertainty) in AOT measurements from a calibrated field instrument under cloud-free conditions is < 0.0l for wavelength at 1020 nm (Holben, et. al., 1998). The noise equivalent difference temperature for the MODIS thermal bands are 0.05 k (Xiong et al., 2006).

### 3.9.3.5 RMS Error Test

The RMS error is a statistical measure of the difference between each index and the AOT value. The RMS error calculated the difference between the measured and predicted value, is a commonly used method for accuracy assessment and is calculated using the following formula.

RMS = $\sqrt{\mu(\sum_{i=n}^{i=1} AOT - \sum_{i=n}^{i=1} DustIndex)^2}$ (3.7)

# 4. Results for Accuracy Assessment

The aim of this chapter is to display the results of the steps outlined in Chapter 3 in order to evaluate between nine algorithms to detect dust sources over five different backgrounds in Sahara. The objectives are

- Outline the results and the comparison between four cloud masks used and to select the most accurate one to implement in the rest of the study.
- Evaluating the accuracy of the dust indices results using visual comparison.
- Evaluating the accuracy of the dust indices results using M test for five different backgrounds.
- Evaluate the emissivity of the background material.
- Evaluate the accuracy of the algorithms statistically by comparison to aeronet data.
- Evaluate different colour composites that can be used to display the dust sources.

The results of applying the different methods outlined in chapter three are outlined below.

## 4.1 Cloud Mask Test Accuracy Assessment

The four cloud mask described in Section 3.5 was first applied to the MODIS images. Three MODIS images are selected for the cloud mask test in order to evaluate the accuracy between the four selected cloud mask to select which of these cloud masks has got the highest percentage for masking cloud as cloud rather than background or dust. Three hundred points were randomly distributed over each tested MODIS colour composite image in order to classify the classes based on the visual interpretation. Then, the result of these classes interpretation was plotted over the result from applies these four tested cloud mask on the MODIS image. Three classes are selected for the cloud mask test; the first call is green and that is representing the cloud, the second class is yellow and that is representing dust, and the third class is red and that is representing the background. The accuracies of each tested image will represented and discussed separately after each tested image using overall agreement and the Kappa coefficient K (Foody 2002).

The first tested MODIS image is dated 17/1/2007 by the MODIS Aqua sensor, cloud in white is clearly visible in the north west corner of the image, the dust appears in light grey and is found in the southern part of the image, the north east corner of the image shows the Tassili Mountains in the south eastern part of Algeria, this part of the image is dark and clear from the dust.

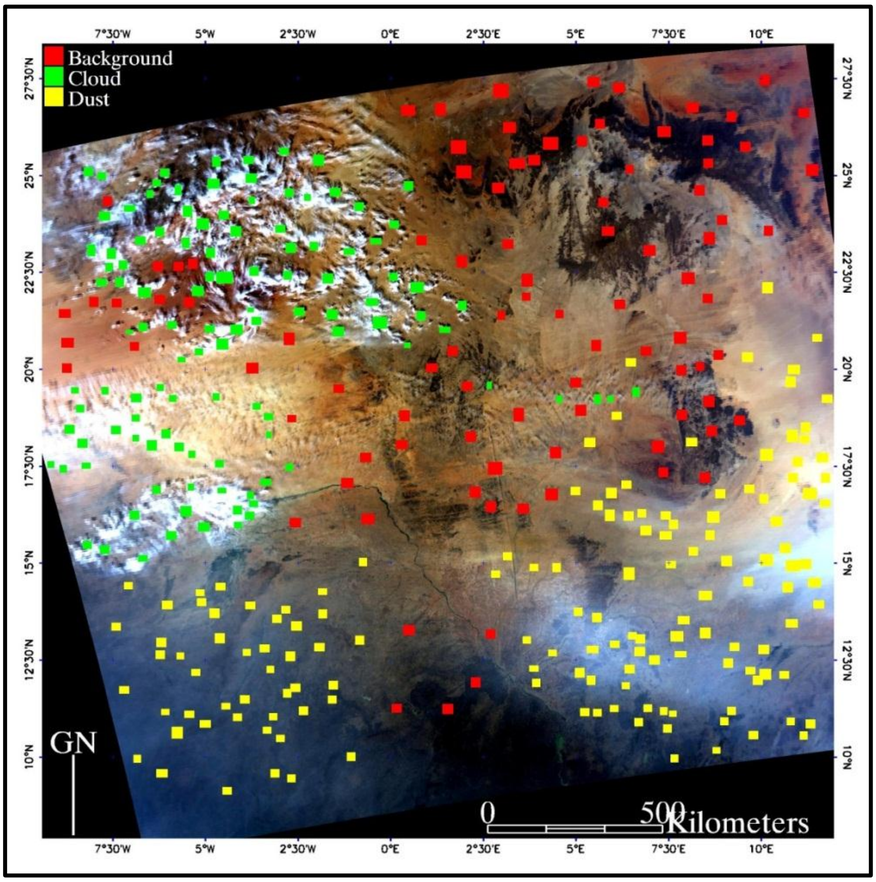


Figure 4.1 True colour composite image dated 17/01/2007 acquired at 13:15 local time by the MODIS Aqua sensor over Sahara (located within latitude 9.44° N – 27.26° N, and longitude 9.9° W – 11.52° E). Pixel resolution is 1km and image time was 13:15 local time. In this figure red points represent the background, the yellow points represent the dust, and the green points represent the cloud.

The cloud masks in Figure 4.2 clearly mask the majority of the cloud with different accuracies as shown in Table 4.1. Some cloud masks (i.e. the MODIS cloud mask) miss-classify significant amounts of dust as cloud and some of the background as dust as it shown in Table 4.1 and Figure 4.2. The Kappa (K) coefficient shows that the accuracy varies between the different cloud masks. MODIS cloud mask has got the lowest (K) and the overall agreement was low compared to the other tested cloud mask. The Giglio et al., (2003) cloud mask has got the highest agreement (K) and the overall agreement is very high as shown in Table 4.1. Most of the cloud masks have masked the north western corner cloud of the image well. The southern part of the image has been misclassified as cloud only by the BTD (11 µm-12 µm) split window and the Deep Blue algorithm cloud masks. BTD (11 µm-12 µm) and Deep Blue have got similar (K) values of agreement for cloud that has been classified as cloud and a similar percentage for miss-classifying the cloud as either dust or background, however the methods less accurate than the Giglio et al., (2003) cloud mask.

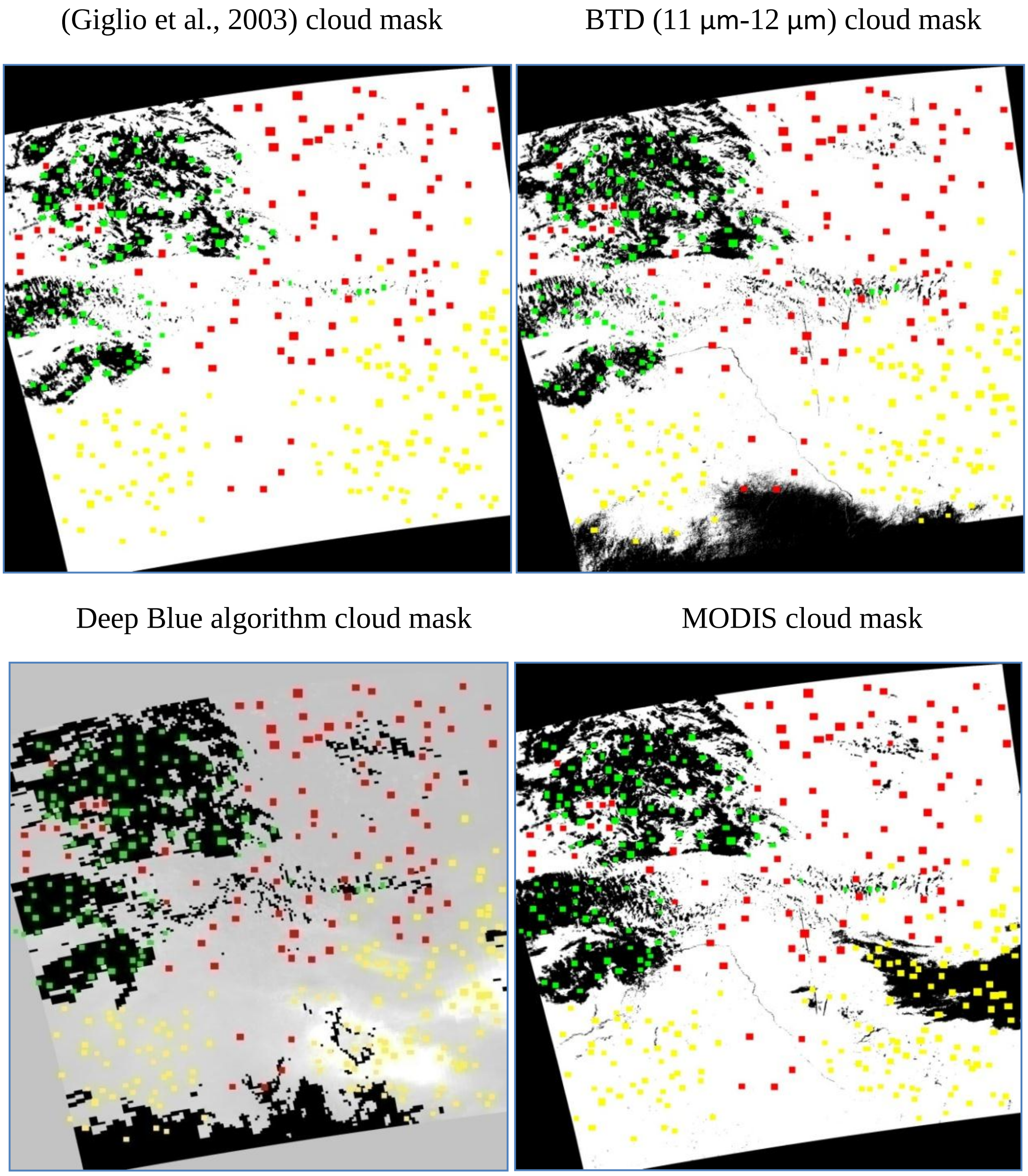


Figure 4.2 The result achieved from apply the four different cloud masks on the image of Figure 4.1.

Table 4.1 Accuracy of cloud masks for the MODIS image dated 17/01/2007 using confusion matrix.

| (Giglio et al., 2003) | Cloud | Dust | Background | Tatal | Producer Accuracy | |
|---|---|---|---|---|---|---|
| Cloud | 80 | 0 | 0 | 80 | 100% | |
| Dust | 0 | 120 | 0 | 120 | 100% | |
| Background | 3 | 0 | 97 | 100 | 97% | |
| Total | 83 | 120 | 97 | 300 total point | | |
| User Accuracy | 86% | 100% | 100% | Overall agreement 96.7% | | K=0.98 |

| BTD (11 µm-12 µm) | Cloud | Dust | Background | Tatal | Producer Accuracy | |
|---|---|---|---|---|---|---|
| Cloud | 75 | 9 | 3 | 87 | 86% | |
| Dust | 0 | 111 | 0 | 111 | 100% | |
| Background | 8 | 0 | 94 | 102 | 92% | |
| Total | 83 | 120 | 97 | 300 total point | | |
| User Accuracy | 90% | 92.5% | 97% | Overall agreement 93% | | K=0.89 |

| Deep Blue algorithm | Cloud | Dust | Background | Tatal | Producer Accuracy | |
|---|---|---|---|---|---|---|
| Cloud | 73 | 10 | 5 | 88 | 83% | |
| Dust | 0 | 110 | 0 | 110 | 100% | |
| Background | 10 | 0 | 92 | 102 | 90% | |
| Total | 83 | 120 | 97 | 300 total point | | |
| User Accuracy | 88% | 91.6% | 94.8% | Overall agreement 91.2% | | K=0.87 |

| MODIS | Cloud | Dust | Background | Tatal | Producer Accuracy | |
|---|---|---|---|---|---|---|
| Cloud | 81 | 30 | 7 | 118 | 68.6% | |
| Dust | 0 | 90 | 0 | 90 | 100% | |
| Background | 2 | 0 | 90 | 102 | 97% | |
| Total | 83 | 120 | 97 | 300 total point | | |
| User Accuracy | 90% | 92.5% | 97% | Overall agreement 88.6% | | K=0.80 |

The cloud masks where also applied to the MODIS scene over the centre of Sahara as shown in Figure 4.3 where cloud is visible in the center of the image and dust is clearly shown in the image blowing from the Bodélé Depression in Chad in the south-eastern part of the image. The northern part of the image shows the sand dunes of the Morzuq Basin in the south east of Libya and the Ahaggar Mountains in the south eastern part of Algeria, the extreme south of the image is darker than the rest of the image due to the appearance of the vegetation in the Sahel, moreover a dust haze is present in the south west of the image. The cloud masks (Figure 4.4) again mask the majority of the cloud, but with a different accuracy as it shown in Table 4.2. The MODIS cloud mask again has got the lowest (K) value due to miss classifying large amount of dust as cloud.

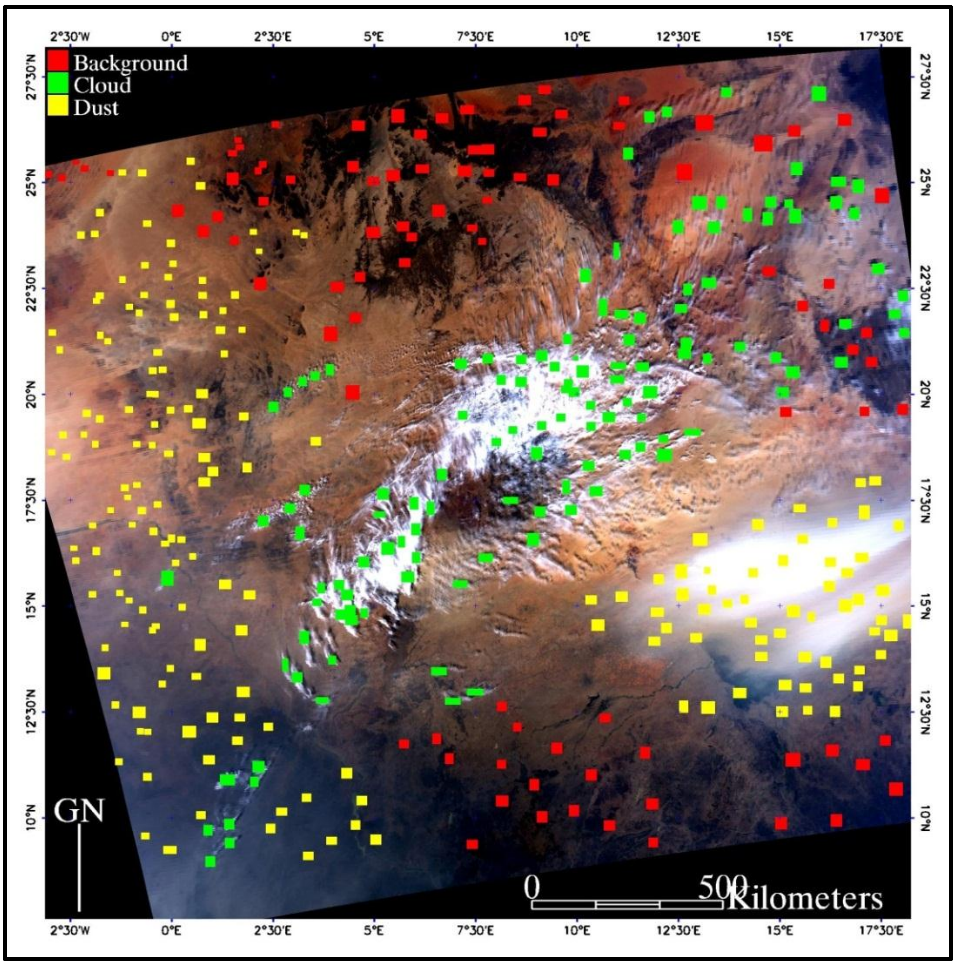


Figure 4.3 True colour composite image bands (1,4,3) dated 05/01/2007 acquired by the MODIS Aqua sensor over Sahara (located within latitude 7.45° N – 26.03° N, and longitude 3.15° W – 18.30° E). Pixel resolution is 1km and image time was acquired at 12:50 local time. In this figure red points represent the background, the yellow points represent the dust, and the green points represent the cloud.

As in the previous image the Giglio et al., (2003) cloud mask achieved the highest agreement (K=0.96) were the BTD (11 μm-12 μm) and Deep Blue cloud masks both has got a much lower scores (K=0.71) and the MODIS cloud mask has the lowest agreement (K=0.64) due to significant amount of dust being miss-classifyed as cloud (Table 4.2). The poor accuracy of the MODIS cloud mask results from the fact that the vast majority of dust over the Bodélé Depression in Chad was miss-classified as cloud by the MODIS cloud mask algorithm.

Giglio et al., (2003) cloud mask | BTD (11 μm-12 μm) cloud mask

Deep Blue algorithm cloud mask | MODIS cloud mask

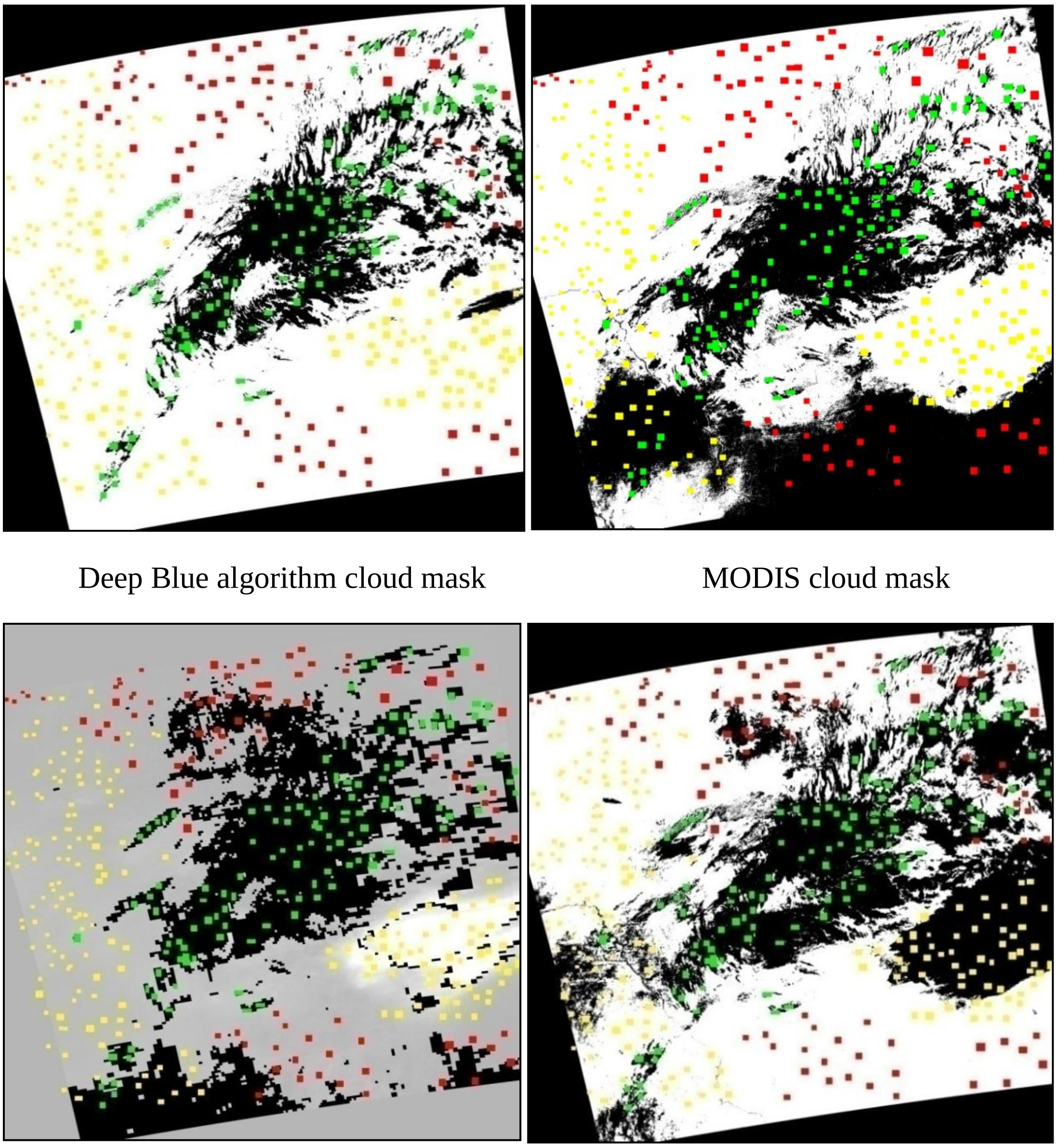

Figure 4.4 The results achieved from apply the four different cloud masks on the image of Figure 4.3.

Table 4.2 Accuracy of cloud masks for the MODIS image dated 05/01/2007 using confusion matrix.

| (Giglio et al., 2003) | Cloud | Dust | Background | Tatal | Producer Accuracy |
|---|---|---|---|---|---|
| Cloud | 113 | 2 | 2 | 117 | 96.5% |
| Dust | 3 | 89 | 0 | 92 | 96.7% |
| Background | 0 | 0 | 91 | 91 | 100% |
| Total | 116 | 91 | 93 | 300 total point | |
| User Accuracy | 97.4% | 97.8 | 97.8 | Overall agreement 97.7% k=0.96 | |

| BTD (11 µm-12 µm) | Cloud | Dust | Background | Tatal | Producer Accuracy |
|---|---|---|---|---|---|
| Cloud | 116 | 28 | 27 | 171 | 67.8% |
| Dust | 0 | 63 | 0 | 63 | 100% |
| Background | 0 | 0 | 66 | 66 | 66% |
| Total | 116 | 91 | 93 | 300 total point | |
| User Accuracy | 100% | 69.2 | 71% | Overall agreement 79% | K=0.71 |

| Deep Blue algorithm | Cloud | Dust | Background | Tatal | Producer Accuracy |
|---|---|---|---|---|---|
| Cloud | 112 | 20 | 30 | 162 | 69.1% |
| Dust | 2 | 71 | 0 | 73 | 97.2% |
| Background | 2 | 0 | 63 | 65 | 97% |
| Total | 116 | 91 | 93 | 300 total point | |
| User Accuracy | 96.5% | 78% | 67.7% | Overall agreement 84.2% | k=0.71 |

| MODIS | Cloud | Dust | Background | Tatal | Producer Accuracy |
|---|---|---|---|---|---|
| Cloud | 115 | 48 | 20 | 183 | 62.8% |
| Dust | 0 | 43 | 0 | 43 | 100% |
| Background | 1 | 0 | 73 | 74 | 98.6% |
| Total | 116 | 91 | 93 | 300 total point | |
| User Accuracy | 99.1% | 47.2% | 78.4% | Overall agreement 81% | k=0.64 |

The third and final image is shown in Figure 4.5. On the north side of the image is Tamanrasset in the Ahaggar Mountains of southern of Algeria, the southern side of the image is darker than the north side due to the vegetation on the southern cost of the African continent and the black part of the image which is in the south western corner of the image is the Gulf of Guinea. Cloud in white is clearly visible in the south western corner of the scene. Dust is clearly shown in the image blowing from the east part of the image. The cloud masks shown in Figure 4.6 again mask the majority of the cloud with different level of accuracy as it shown in Table 4.3. All methods perform worse on this image compared to the other test results as is shown in Table 4.3. The MODIS cloud mask again has got the lowest (K=0.70) followed by BTD (11 µm-12 µm) (K=0.77).

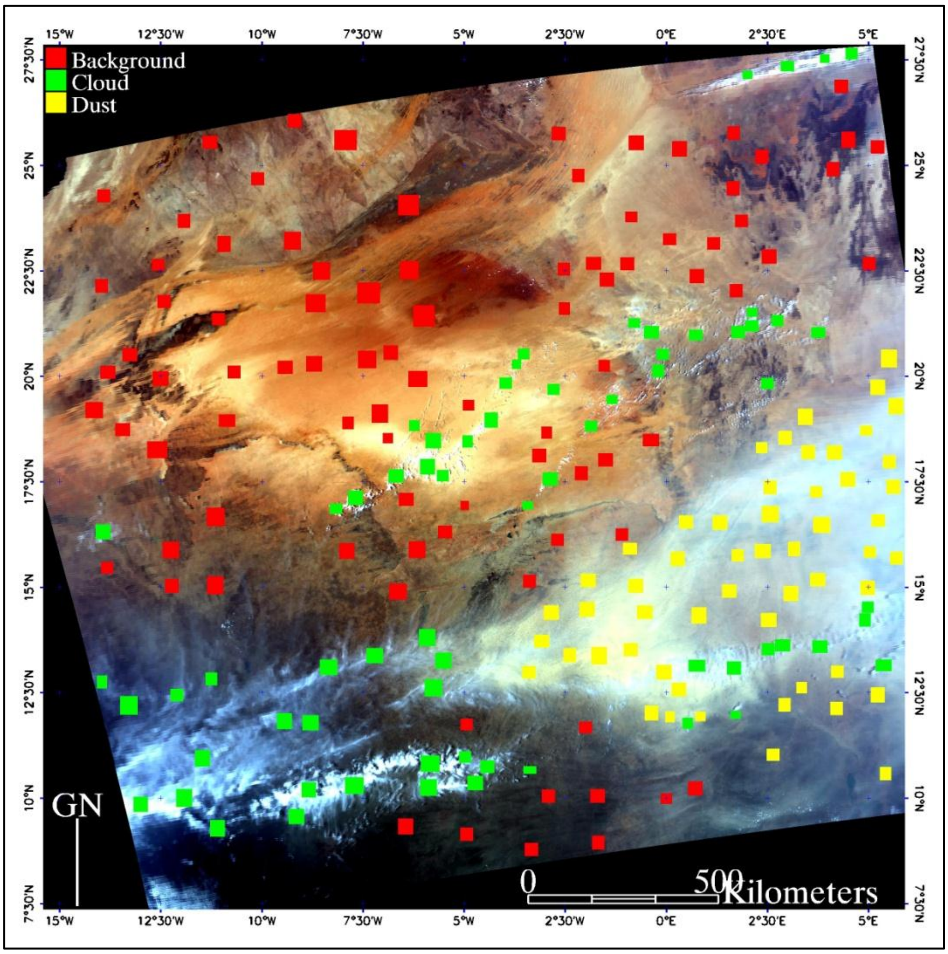


Figure 4.5 True colour composite image bands (1,4,3) dated 03/04/2007 acquired by the MODIS Aqua sensor over Sahara (latitude 7.30° N – 25.45° N, and longitude 15.20° W – 5.38° E). Pixel resolution is 1km and image time was 13:40 local time. Cloud (in white) is clearly visible in the south west corner of the image. Red points represent the background, the yellow points represent the dust, and the green points represent the cloud.

Giglio et al., (2003) cloud mask again has the highest agreement (K=0.89) in this case but lowest agreement compared with the previous two tested images. The Deep Blue cloud mask has good agreement (K=0.87) in this tested image and is close to the Giglio et al., (2003) method (Table 4.3). The MODIS cloud mask again miss-classifies the dust as cloud.

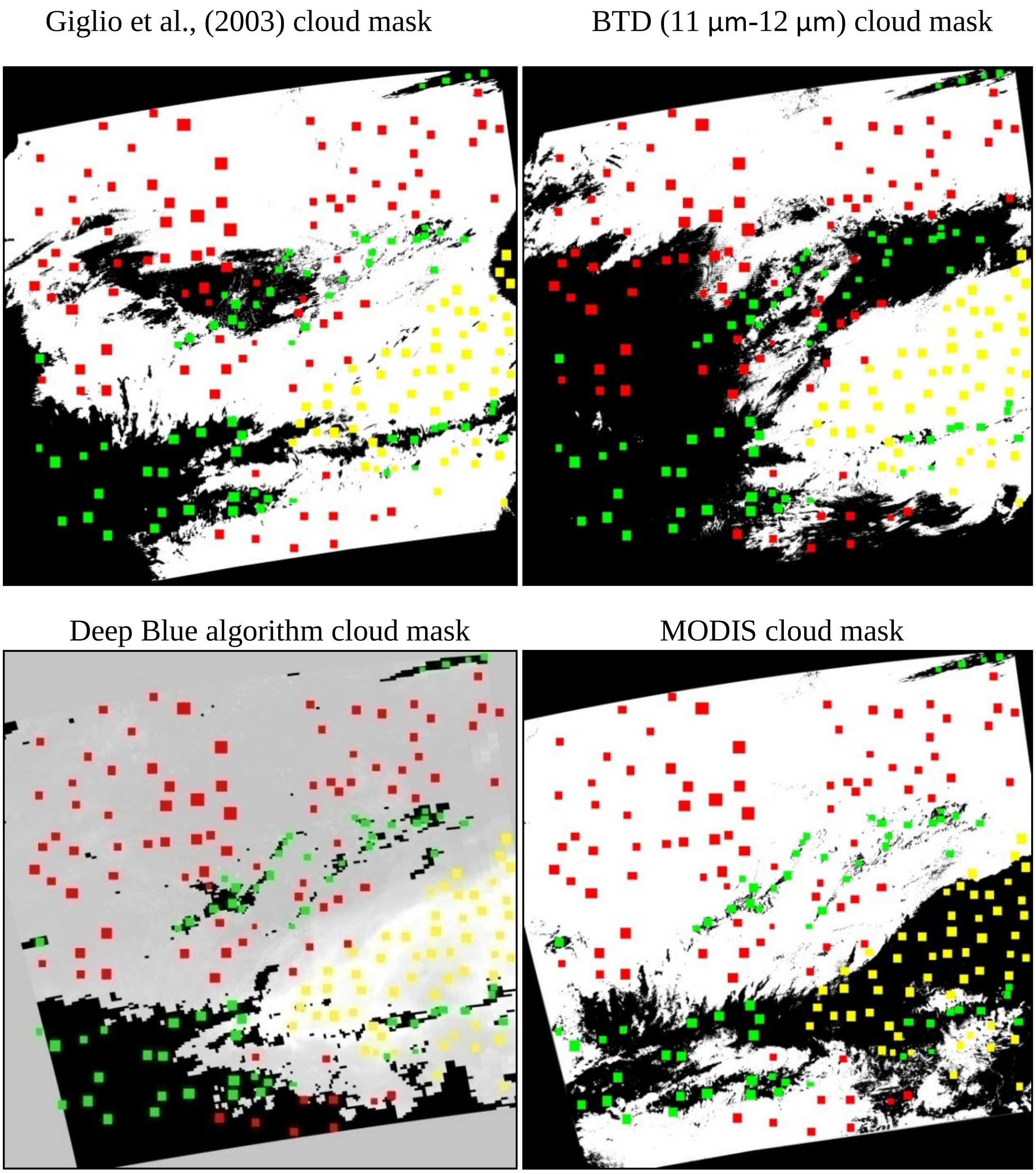


Figure 4.6 The results achieved from apply the four different cloud masks on the image of Figure 4.5.

Table 4.3 Accuracy of cloud masks for the MODIS image dated 03/04/2007 using confusion matrix.

| Giglio | Cloud | Dust | Background | Tatal | Producer Accuracy | |
|---|---|---|---|---|---|---|
| Cloud | 91 | 8 | 11 | 110 | 82.7% | |
| Dust | 0 | 77 | 0 | 77 | 100% | |
| Background | 2 | 0 | 111 | 113 | 98.2% | |
| Total | 93 | 85 | 122 | 300 total point | | |
| User Accuracy | 97.8% | 90.5% | 91% | Overall agreement 93.3% | | k=0.89 |

| BTD (11 µm-12 µm) | Cloud | Dust | Background | Tatal | Producer Accuracy | |
|---|---|---|---|---|---|---|
| Cloud | 85 | 3 | 35 | 123 | 69.1% | |
| Dust | 8 | 82 | 0 | 90 | 91.1% | |
| Background | 0 | 0 | 87 | 87 | 100% | |
| Total | 93 | 85 | 122 | 300 total point | | |
| User Accuracy | 91.3% | 96.4% | 71.3% | Overall agreement 86.5% | | k=0.77 |

| Deep Blue algorithm | Cloud | Dust | Background | Tatal | Producer Accuracy | |
|---|---|---|---|---|---|---|
| Cloud | 83 | 4 | 10 | 97 | 85.5% | |
| Dust | 3 | 81 | 0 | 84 | 96.4% | |
| Background | 7 | 0 | 112 | 119 | 94.1% | |
| Total | 93 | 85 | 122 | 300 total point | | |
| User Accuracy | 89.2% | 96.4% | 94.2% | Overall agreement 92.6% | | k=0.87 |

| MODIS | Cloud | Dust | Background | Tatal | Producer Accuracy | |
|---|---|---|---|---|---|---|
| Cloud | 88 | 48 | 4 | 140 | 62.8% | |
| Dust | 2 | 37 | 0 | 39 | 94.8% | |
| Background | 3 | 0 | 118 | 121 | 97.5% | |
| Total | 93 | 85 | 122 | 300 total point | | |
| User Accuracy | 94.6% | 56.4% | 96.7% | Overall agreement 83.8% | | k=0.70 |

From the results it is clear that the Giglio et al., (2003) cloud mask has the highest agreement in general for masking the actual cloud as cloud and the lowest percentage for miss-classifying the clouds as either dust or background based on the three tested MODIS images. However the Giglio et al., (2003) method still sometimes removes data relating to dust as is clearly noticed in the Bodélé Depression. The MODIS cloud mask has the lowest accuracy because most of the dust was miss classified as cloud especially over the Bodélé Depression**.** Thus the (Giglio et al., 2003) cloud mask will be used in the rest of the study.

## 4.2 Visual Interpretation of Results and Comparison

After the nine selected techniques were applied over the sixteen selected MODIS images, two MODIS image were chosen for the visual comparison; the Air Mountains (Figure 4.10) and the Bodélé Depression (Figure 4.9) because different type o clouds can be seen in these two images. The visual comparison was done over the test areas were the source of dust can be clearly identified. All of the index results were displayed without image enhancement to allow visual comparison between the techniques and are presented after applying the (Giglio et al., 2003) cloud mask. Most of the techniques performed well visually in the first test image (Air Mountains; Figure 4.10), because the background is dark and the dust are lighter. Thus, dust can be distinguished easily from the background due to the high contrast between the dust and the background. However, for bright backgrounds, such as the Bodélé Depression, dust can be confused with background in some cases as the visible bands have difficulty distinguishing between the dust and the background when the surface is bright surface.

The first test image for the visual comparison is from MODIS Aqua sensor dated 17/1/2007. The test area will focus over Air Mountain. The dust sources are located south east of the Air Mountains. The colour composite image shows the dust passing south of the Air Mountain.

**4.7(A)**

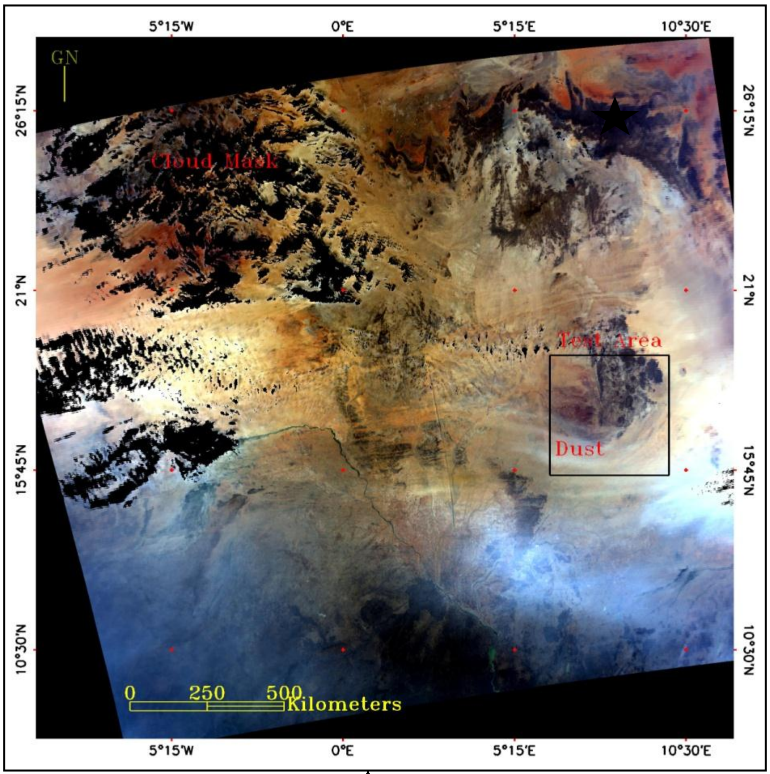


4.7 (B) Test Area (Dust)


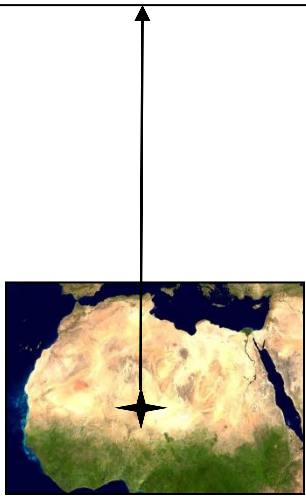

4.7 (C) Test Area (No dust)

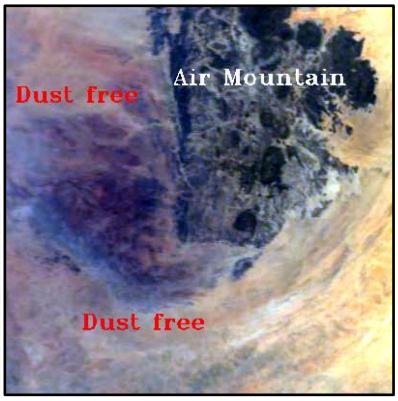


Figure 4.7 (A&B) True colour composite of a dust storm imaged on 17/01/2007 by the MODIS Aqua sensor over the Air Mountain(latitude 9.44° N – 27.26° N, and longitude 9.9° W – 11.52° E). The pixel resolution is 1km and image time was acquired at 13:15 hrs local time. The test area has been bordered by black rectangle and is shown in B. Figure 4.7 (C) shows a dust free image of the same area from Terra sensor acquired over the Air Mountain on 03/06/2009 at 09:45 hrs local time.

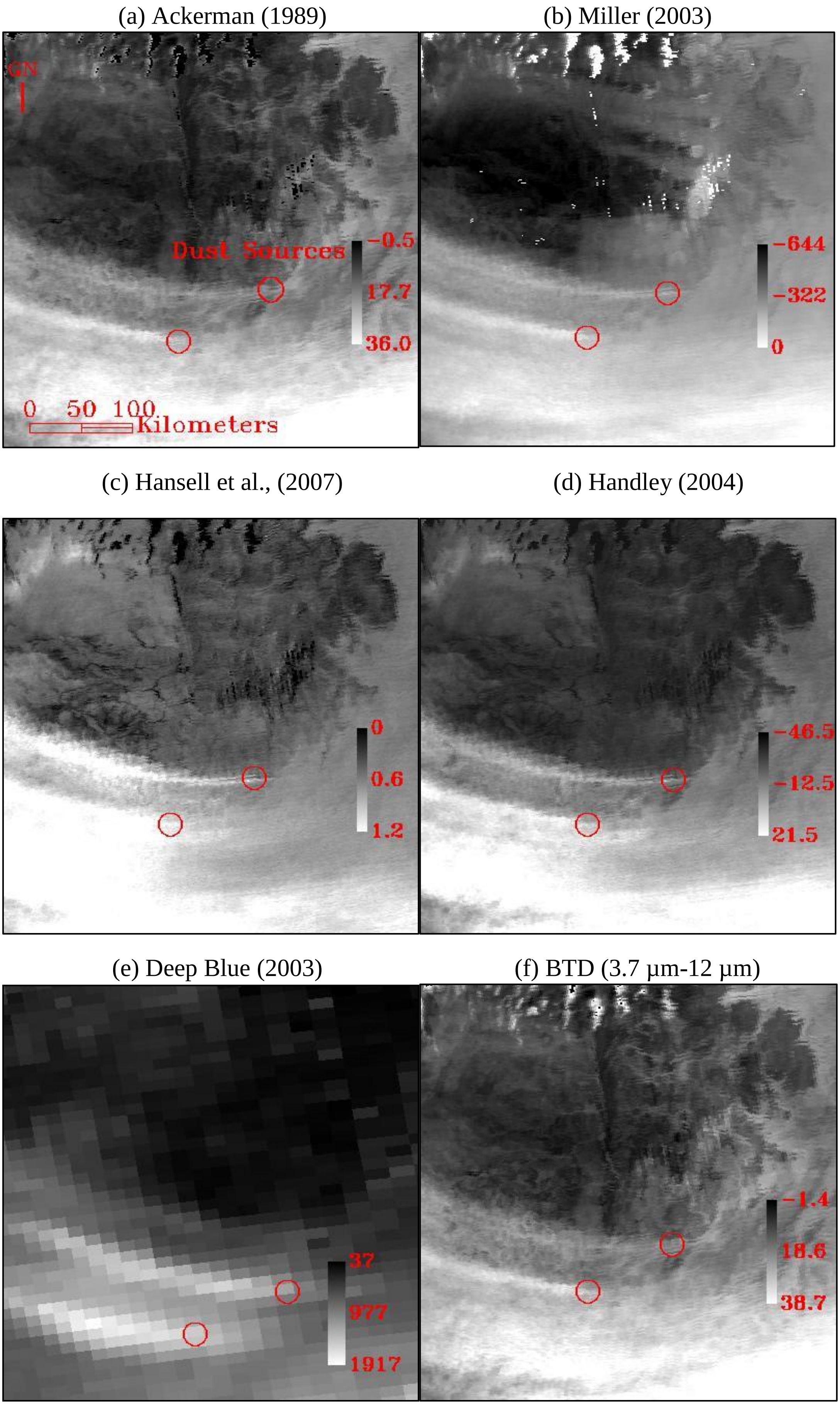
(a) Ackerman (1989)
(b) Miller (2003)
GN
Dust Sources
-0.5
17.7
36.0
0 50 100 Kilometers
-644
-322
0
(c) Hansell et al., (2007)
(d) Handley (2004)
0
0.6
1.2
-46.5
-12.5
21.5
(e) Deep Blue (2003)
(f) BTD (3.7 µm-12 µm)
37
977
1917
-1.4
18.6
38.7

(g)BTD (8.6 μm-11 μm)

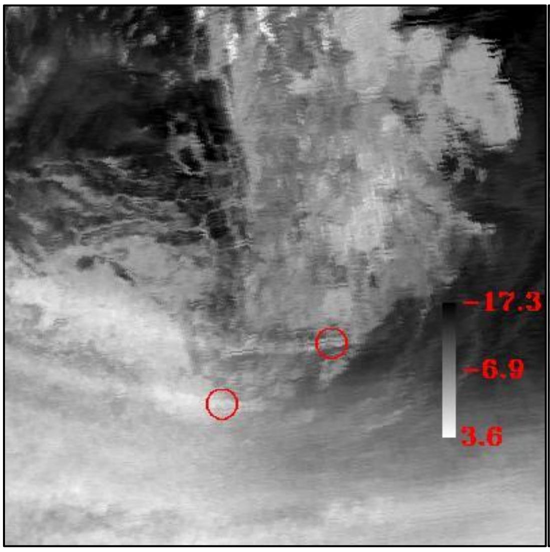


(h) BTD (8.6 μm-12 μm)

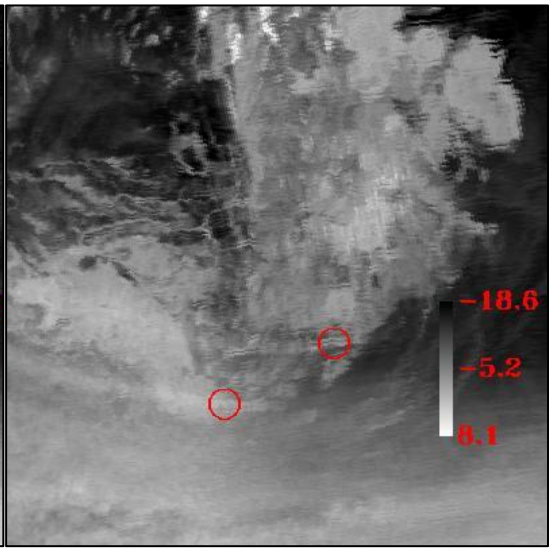


(i) BTD (12 μm-11 μm)

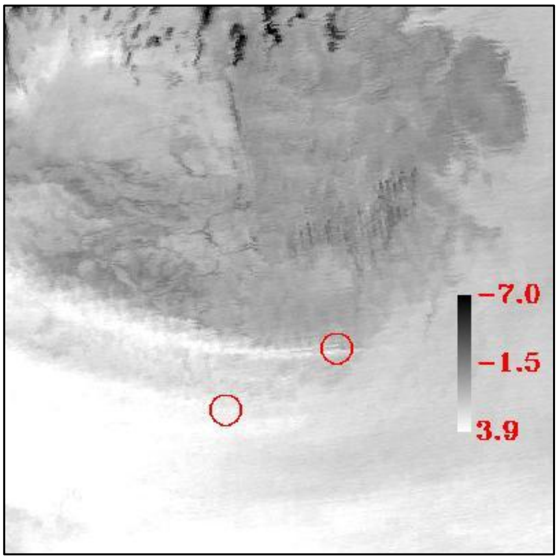


Figure 4.8 Results from applying the nine selected techniques to the image of Figure 4.7 (A). Miller index is used as a reference image and the other indices used Miller sources and displayed over their dust indices. The main sources of dust have been circled in red in order to allow comparison between the ability of each technique to locate the source of dust visually.

Figure 4.8 shows the ability of each dust index to trace the source of the dust from the Air Mountains region. All of the dust indices have been applied on the same MODIS image with a 1km spatial resolution apart from the Deep Blue product that has 10km spatial resolution. Deep Blue (2003) has low background affects and good contrast between dust and background, though the low spatial resolution makes it hard to precisely identify dust sources. The BTD (12 μm-11 μm), Hansell et al., (2007), Handley (2004) Ackerman (1989) and BTD (3.7 µm-12 µm) shows similar visual results to each other but they have been affected by the background more than Deep Blue. The BTD (8.6 µm-11 µm) and BTD (8.6 µm-12 µm) indices have very strong background effects and little contrast between dust and background in the source areas.

The red circles in Figure 4.8 show the two main dust sources detected from the Miller dust index and displayed over all the dust indices in order to distinguish between the ability of each dust indices to detect the dust sources. The Miller dust index is used as reference because visually it appears to show the individual dust sources well. Not all the tested indices match the two dust sources detected by Miller and that can display the ability of the different indices to identify exact location, clearly shows in Figure 4.8 detecting dust sources and varies between the indices. Deep Blue is the worst in this case because the dust source comes from small area and the low pixel resolution (10 km) of Deep Blue make it difficult to identify the source. BTD (12 µm-11 µm), BTD (8.6 µm-11 µm), and BTD (8.6 µm-12 µm) shows also poor result by observing high values over the mountains area make it difficult to distinguish the dust from the background.

The second test image for the visual comparison is from MODIS Terra sensor dated 12/1/2007. The test area is the Bodélé Depression because it is one of the most important dust sources in the world (Warren et al., 2007). The colour composite image clearly shows the dust generated from the Bodélé Depression, the dust free image show the diatomite.

**4.9(A)**

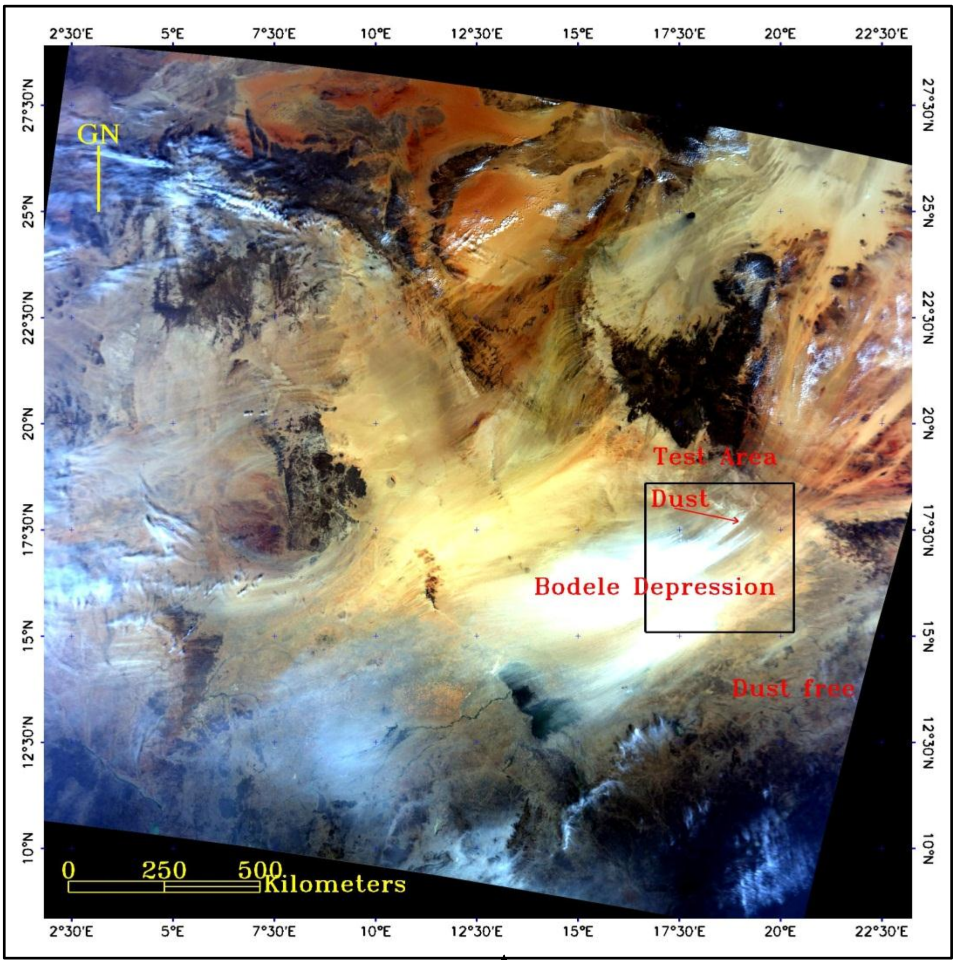


4.9(B) Test Area (Dust)

4.9(C) Test Area (No dust)

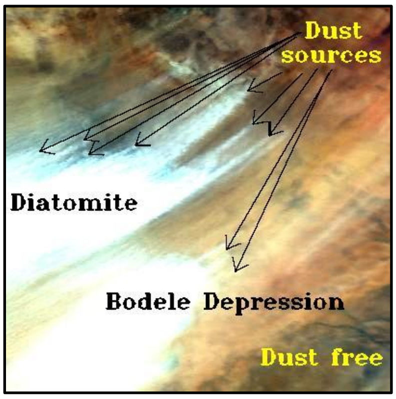


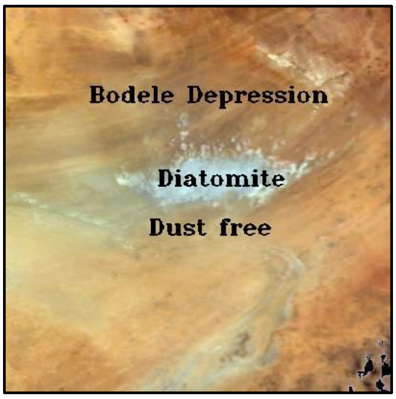


Figure 4.9 (A&B) True colour composite of a dust storms imaged on 12/01/2007 by the MODIS Terra sensor over the Bodélé Depression (latitude 9.44° N – 27.26° N, and longitude 9.9° W – 11.52° E). Pixel resolution is 1km and image time was 09:50 hrs local time. Cloud (in white) is clearly visible in the south of the scene. The test area has been bordered by black rectangle and is shown in figure B. Figure 4.9 (C) shows a dust free image from Terra sensor over the Bodélé Depression acquired on 03/06/2009 at 09:45 hrs local time over the same area of Figure 4.9 (B).

(a) Ackerman (1989)

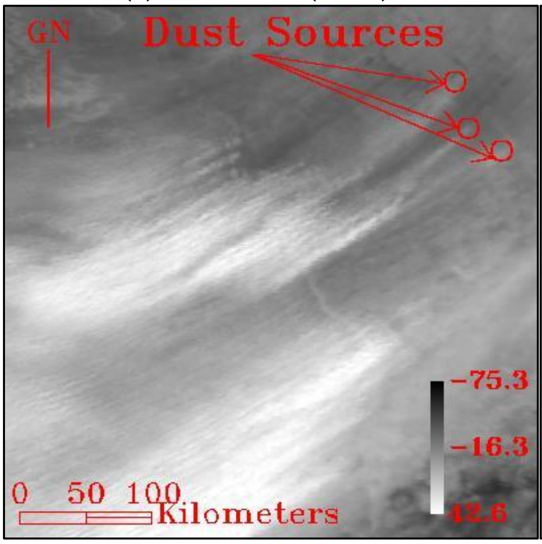


(b) Miller (2003)

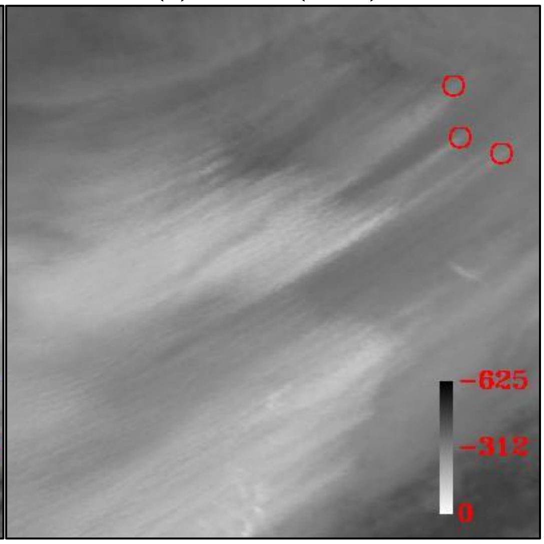


(c) Hansell et al., (2007)

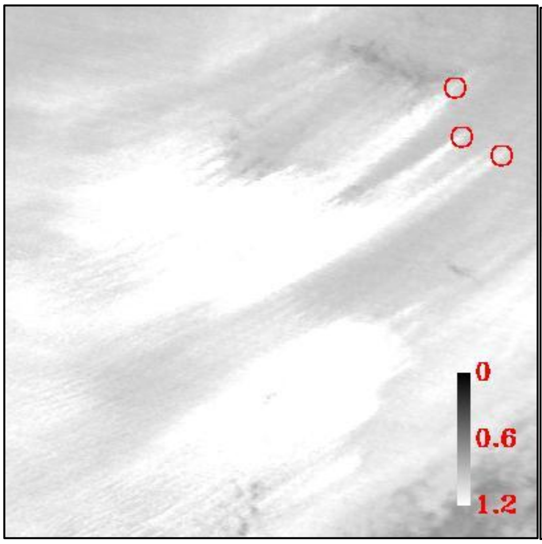


(d) Handley (2004)

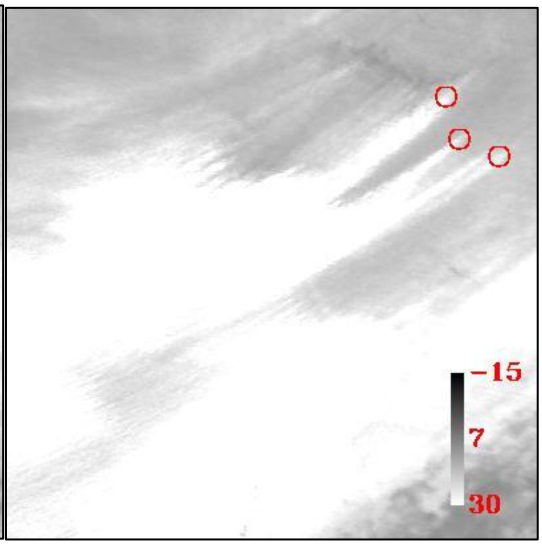


(e) Deep Blue (2003)

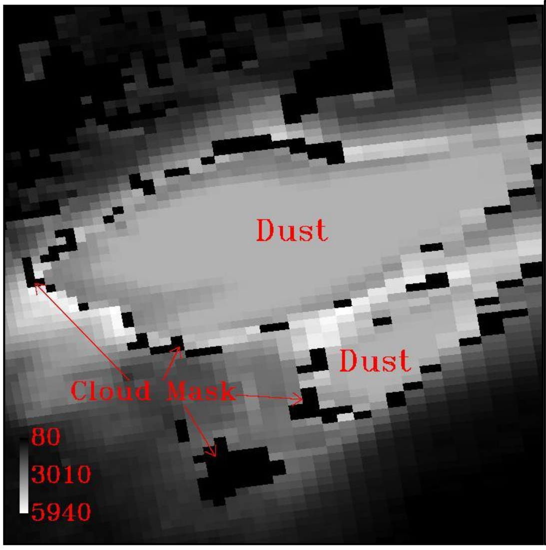


(f) BTD (3.7 µm-12 µm)

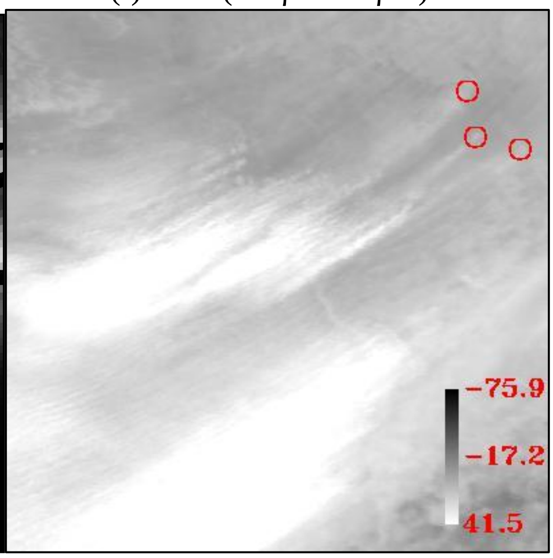

(g) BTD (8.6 µm-11 µm)

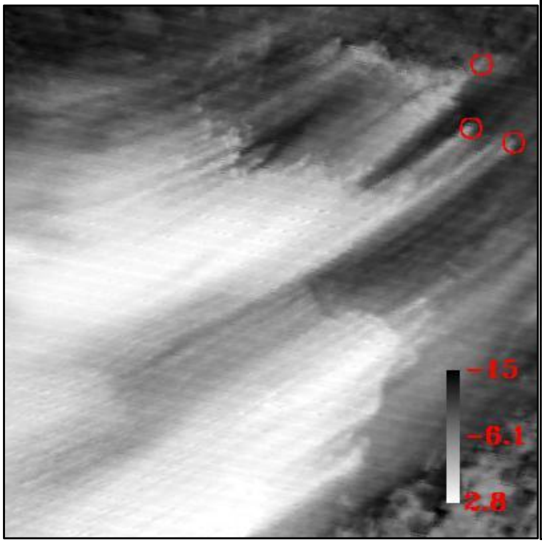


(h) BTD (8.6 µm-12 µm)

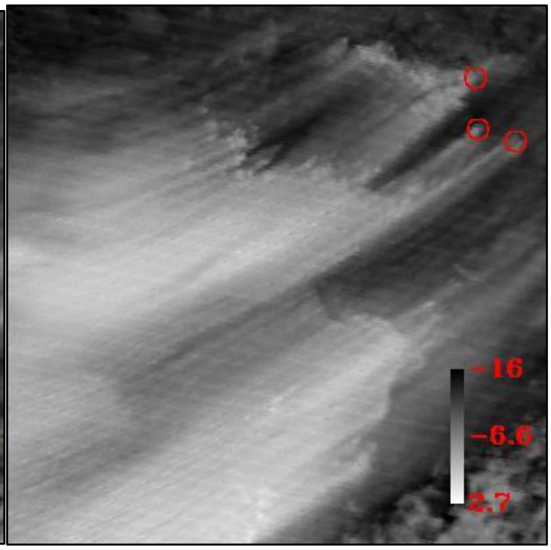


(i) BTD (12 µm-11 µm)

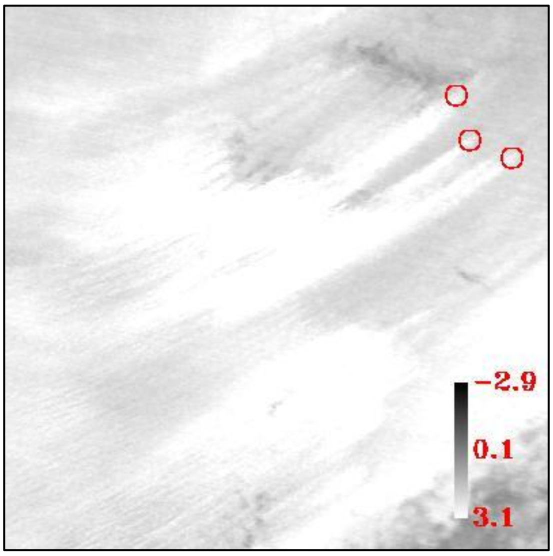


Figure 4.10 Results from applying the nine selected techniques to the image of Figure 4.9 (A). The sources of three prominent dust sources have been circled in red in order to allow comparison between the ability of each technique to locate the source of dust visually.

Figure 4.10 shows the result of each dust indices from the Bodélé Depression. The red dots in Figure 4.10 show three dust sources detected from the Ackerman dust index and displayed over all the dust indices in order to distinguish between the ability of each dust indices to detect the dust sources. The Ackerman dust index is used as reference for the red dots because visually it appears most clearly to show the individual dust sources. For this image the cloud mask has not worked very well and it has not been used because it has masked areas of high dust concentrations as cloud. To trace the source of the dust Hansell et al., (2007), Handley (2004), and BTD (12 µm-11 µm) are very similar and dust sources can be detected clearly and present the best result visually because the diatomite is dark and the dust bright. Deep Blue (2003) again shows poor contrast between the dust and the background and it is not possible to see many of the dust sources and some dust pixels at the edges of the dust storms have been misclassified as cloud, Ackerman (1989), Miller (2003), BTD (3.7 µm-12 µm) BTD (8.6 µm-11 µm) and BTD (8.6 µm-12 µm) show reasonable results in distinguishing the majority of the background from the dust, but both diatomite and dust produce bright index values making it hard to determine the exact location of the sources.

Two types of background were dominant in this visual comparison: Diatomite in the Bodélé Depression and Granite, in the Air Mountains. In general, from the two test areas as displayed in Figure 4.7 and 4.9 most of the tested methods vary in their performance over both backgrounds. Deep Blue (2003) is poor visually over both test areas for monitoring the dust and it is quite difficult to trace the dust sources especially the single dust plumes generated from small sources due to the low pixel resolution (10km) compared to the rest of the indices (1km). Miller (2003) shows reasonable results in both areas but exhibits some background effects over both Granite and Diatomite. Hansell et al., (2007), Handley (2004) and BTD (12 µm-11 µm) shows good result visually for both granite and diatomite, followed by Ackerman (1989) and BTD (3.7 µm-12 µm) with more background affects in both areas. BTD (8.6 µm-11 µm) and BTD (8.6 µm-12 µm) provide reasonably good results visually over diatomite but very poor results over granite where tracing the dust sources is difficult due to the strong background effects which make it hard to identify some backgrounds from dust.

This visual comparison shows that background has a large effect on the utility of each index for dust source detection, however, this qualitative comparison itself it is not enough to decide between different types of dust detection techniques, for that reason these results are evaluated with the M test that tests the ability of each dust indices to distinguish the dust from the background.

## 4.3 The M Test Results

The M test has been employed over five different types of background: Limestone in Cyrenaica, Basalt in the Tibesti Mountains of Chad, Diatomite in the Bodélé Depression of Chad, Granite in the Air Mountains of Niger, and Sand to the east of the Tibesti Mountains in Chad. These five different backgrounds are examples of commonly exposed rocks and sediments in the Sahara. All of the MODIS images for these areas were acquired by the Terra and Aqua platforms. We have used one image to implement M for each test area by selecting images that show dust and dust free areas over the selected background. In the case of the Bodélé Depression test area we have used two images, one with dust and the second dust free, as it was difficult to find a single image were some dust was deflating from the diatomite and some of the diatomite was free of dust. In order to ensure that the interpretation of the dust free area was correct, a dust free image of each site was acquired and used for the display and interpretation only. All the dust indices are implemented in all test areas to see the influence of each technique on the tested background. The two areas used for the M test are highlighted by two squares on the used images.

M value $\geq 1$ indicate good ability to distinguish between the dust and background, if the M value is $< 1$ the contrast between the dust and background is low. The median and range of M has been calculated in order to find out how the M test of each tested techniques work over the five different backgrounds. The median indicates that all the tested techniques has got M value greater than 1 (Table 4.4), which indicates that all of these techniques can provide good contrast between the dust and the background. However, some methods have very high values and thus perform much better than others. Discussion of the results involves discussing the visual interpretation of all of the used images, and then discussing the result of the M test. Moreover, the histograms of the image containing are plotted next to each dust index in order to visualise the separation between the dust and the background. The (Giglio et al., 2003) cloud mask has been used for the visual display of all images apart from Deep Blue. However, in the Diatomite M test the cloud mask has been removed because it masks out some dust over the tested area.

The emissivity of the four used MODIS thermal bands over the five tested background will be discussed and displayed after the M test for each background in order to try and understand why the background effects happen.

### 4.3.1 Limestone Background in Cyrenaica

The first image used for the test is Limestone from Cyrenaica (Figure 4.11). The MODIS image was collected by the Terra satellite on the 26/10/2007 at 09:05 hrs local time (Figure 4.11 A&B) and shows a dust storm generated from the south of study area towards the Mediterranean Sea. Figure 4.11 (C) shows MODIS image collected by Aqua satellite on the 10/02/2006 at 11:20 hrs local time, no dust can be seen in the image. The test area has been shifted a little bit on the Deep Blue image in order to avoid the cloud mask which covers part of the test area. The geology of the test area is limestone with marl and clay intercalations and with minor gypsum. Outcrops of these rocks appear as bright colours in the image. Vegetation is common in the wetter regions in the north of the image providing a darker background. The dust is shown in Figure 4.11 (B), and the free dust background in Figure 4.11 (C). The Limestone which is bright makes it more difficult to distinguish between the dust and the background compared to the north of the image was the background is vegetation.

4.11(A)

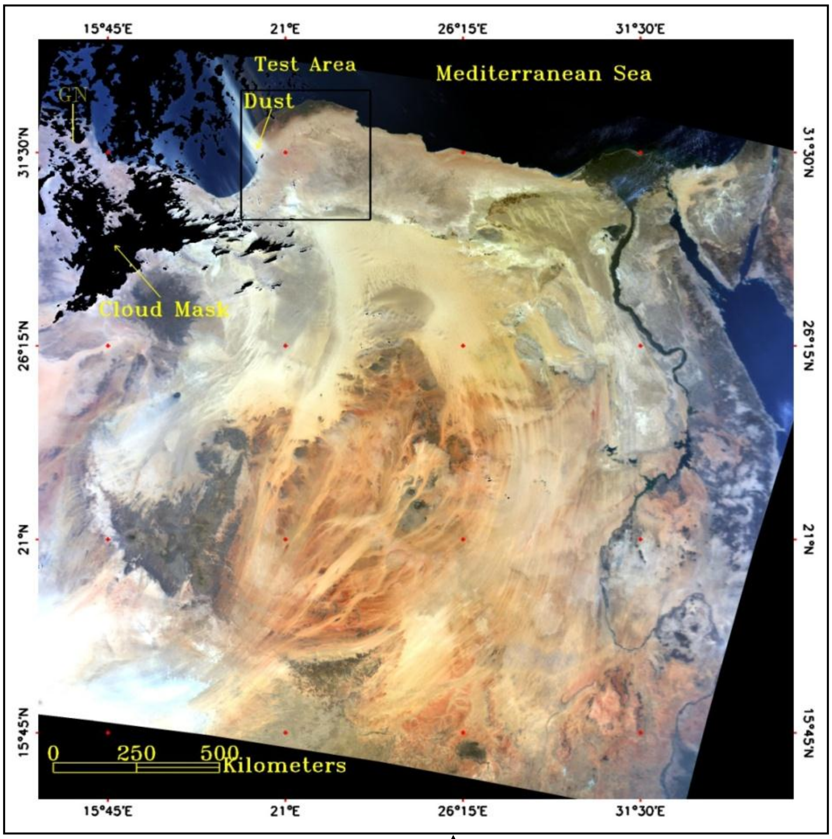


4.11 (B) Test Area (Dust)

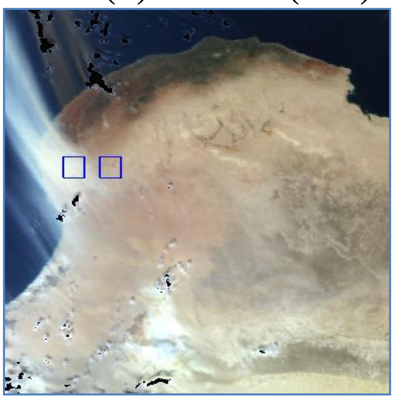

4.11(C) Test Area (No dust)

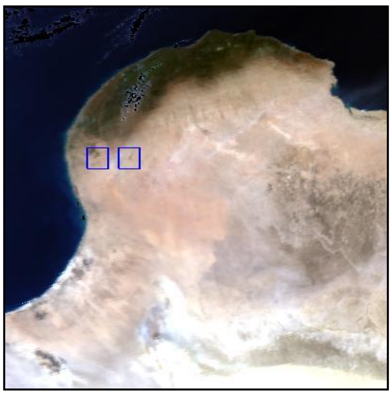

Figure 4.11 (A&B) True colour composite of a dust storm imaged on 26/10/2007 by the MODIS Terra sensor over Cyrenaica (latitude 29.30° N – 33.06° N, and longitude 19.45° E – 23.41° E). Pixel resolution is 1km and image time was acquired at 09:05 hrs local time. (C) True colour composite of MODIS imaged on 10/02/2006 by the MODIS Aqua sensor, image time was 11:20 hrs local time. The two squares in Figure (B&C) represent the M test areas.

Figure 4.12 shows the 9 dust indices applied over Cyrenaica, Libya, with the M results shown in Table 4.4. Ackerman (1989), BTD (3.7 µm-12 µm) and Miller (2003) show the best results visually for detecting the dust and have the ability to trace the dust back to the sources with the lowest background effects, the histograms of these indices shows good separation between the background mode and the dust mode, the M test results agree with the visual result and indicates good contrast between the dust and the background. Deep Blue (2003) is difficult to interpret due to the presence of the cloud mask over most of the test area including much of the area where dust is detected in other mages, the histogram spectra of Deep Blue (2003) does not shows good separation between the background mode and the dust mode because the dust appears in only a small area due to the poor accuracy of the cloud mask. However, M test shows the highest result for Deep Blue (2003) because the M test done over small area were the poor cloud mask has no effects in the M test result but it has in the visual result, thus the mean of Deep Blue will provide a good separation between the dust and the background. BTD (8.6 µm-11 µm) and BTD (8.6 µm-12 µm) also shows reasonable result. However, it is quite difficult to distinguish between the dust and the background and difficult to trace the dust sources. The histograms of these indices show small separation between the background mode and the dust mode.

Hansell et al., (2007), Handley (2004), and BTD (12 µm-11 µm) have got low contrast between the dust and the background and it is difficult to distinguish between the dust and the background and dust sources cannot be readily interpreted, the histogram of these indices shows one spread out (Platykurtic) mode and in the case of Handley (2004) the separation is very small, the M test result of these indices shows the lowest M value agreeing visual interpretation.

Ackerman (1989)

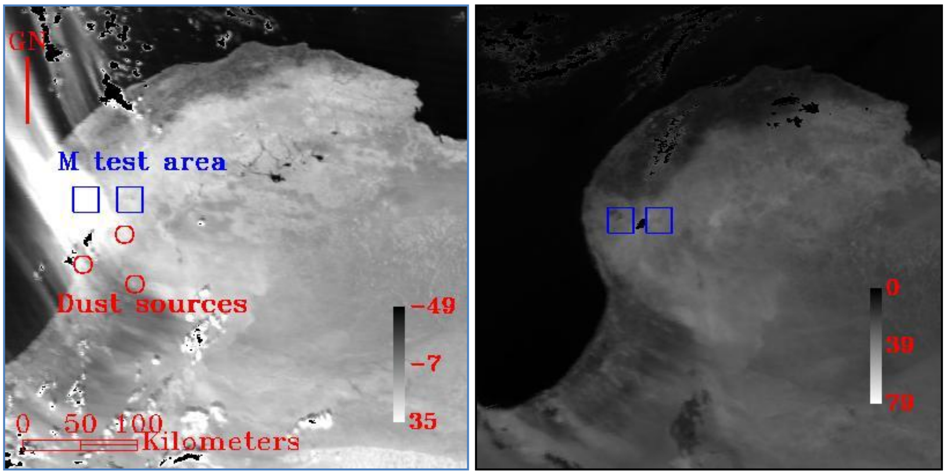


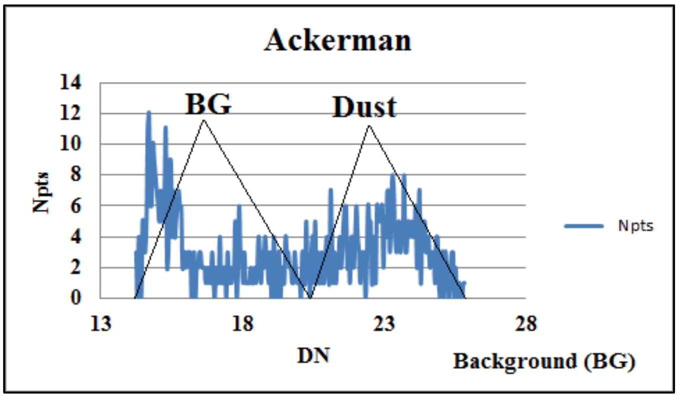


Miller (2003)

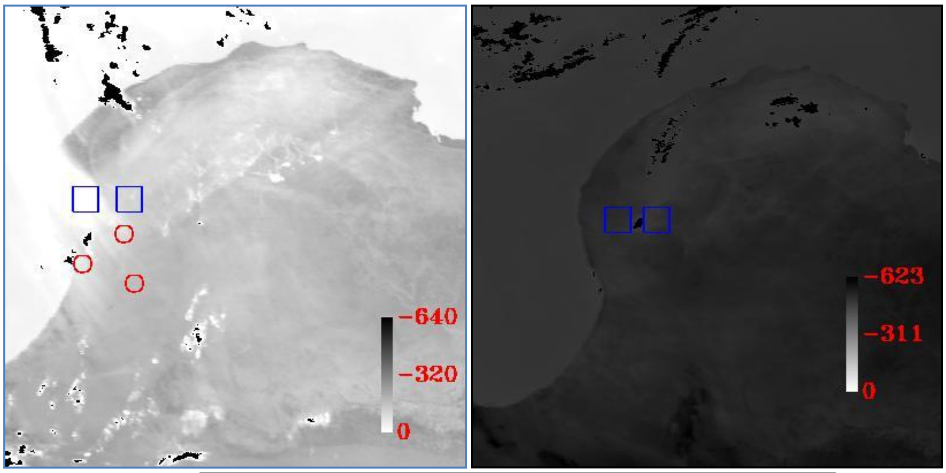


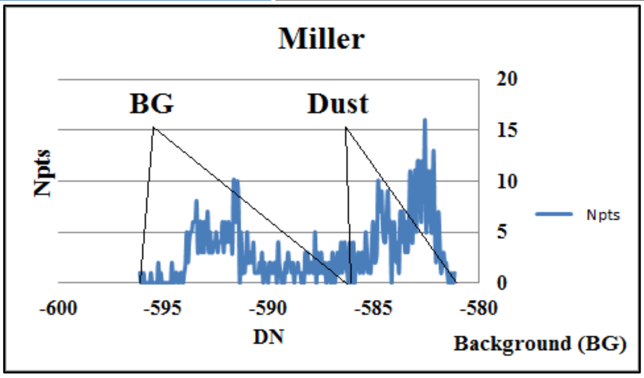

Hansell et al., (2007)

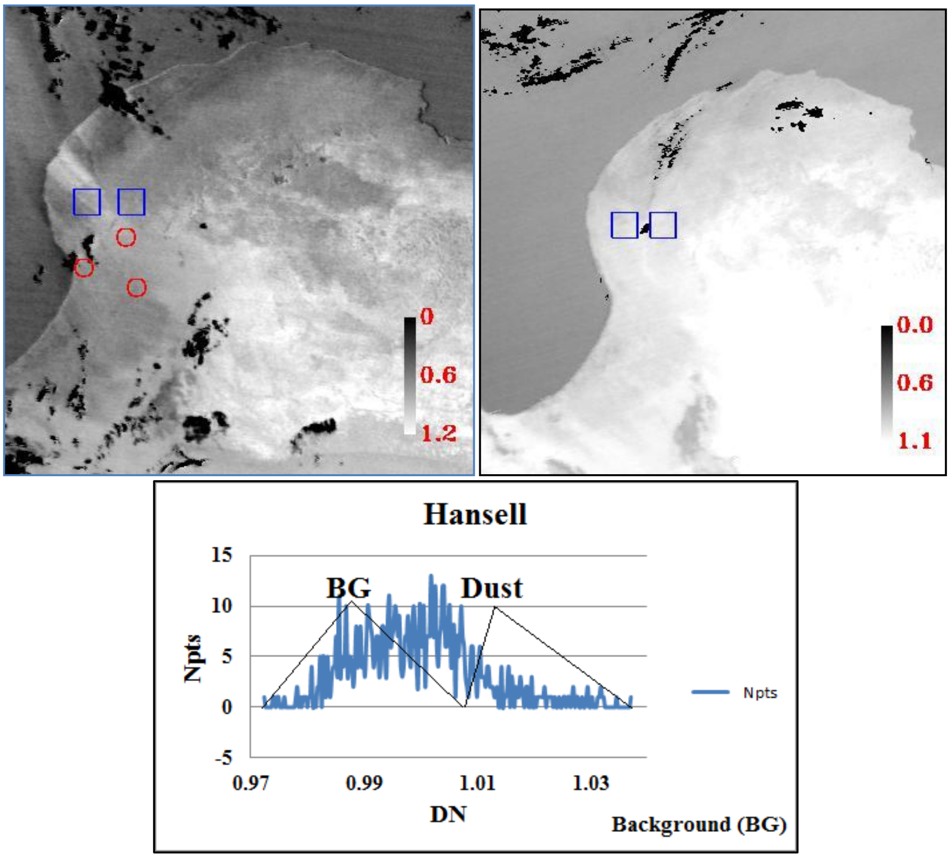


Handley (2004)

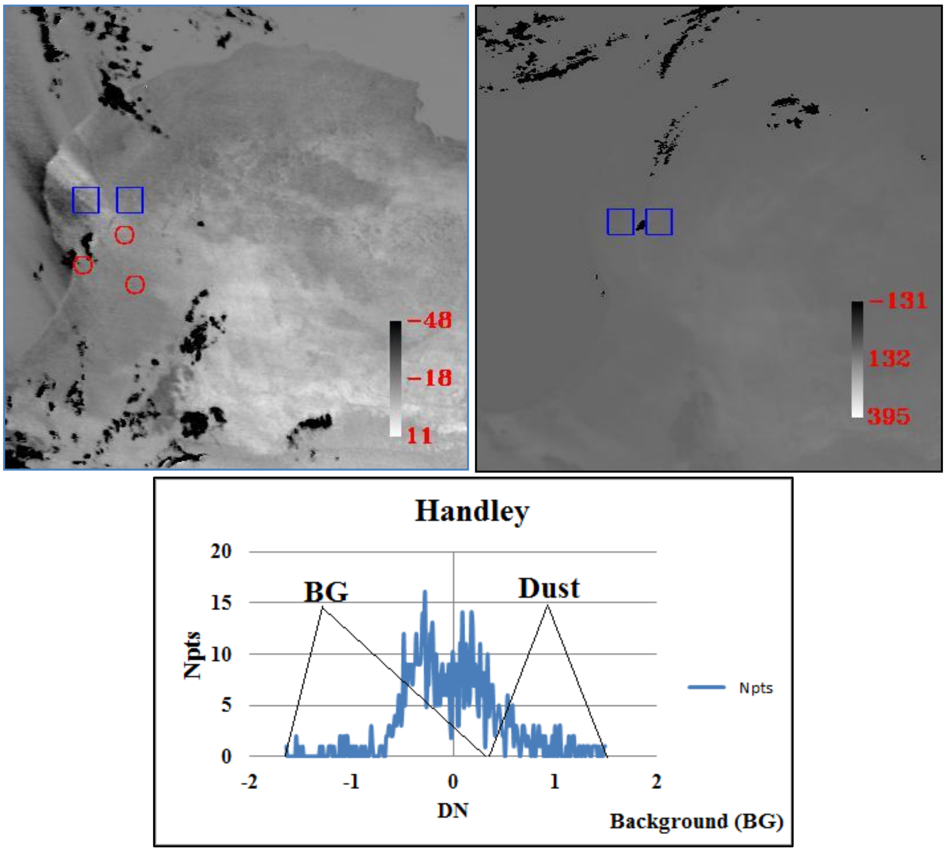

Deep Blue (2003)

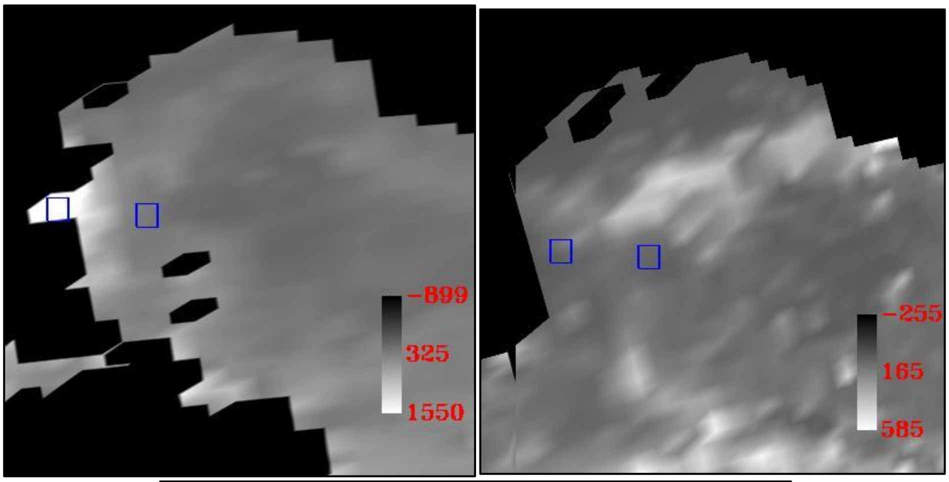


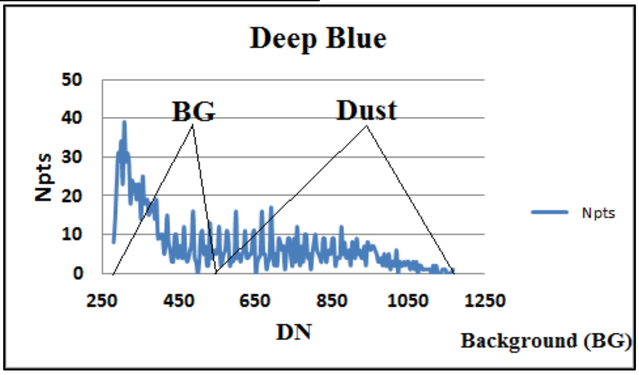


BTD (3.7 µm-12 µm)

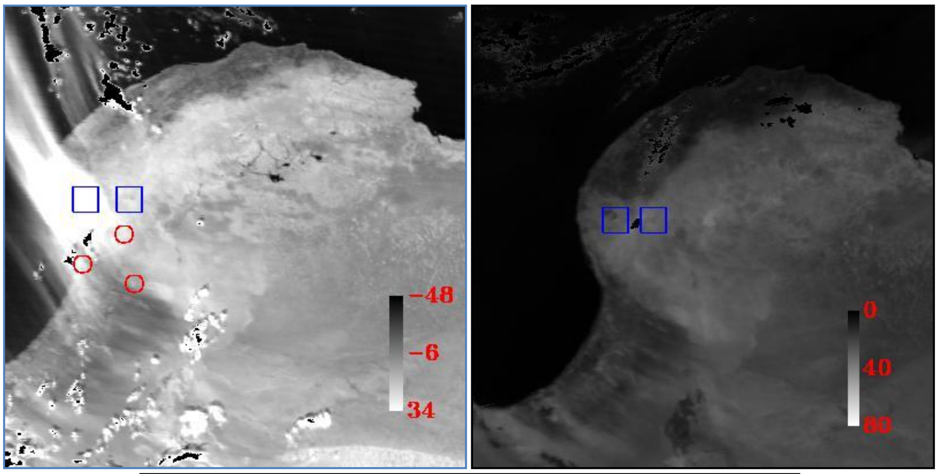


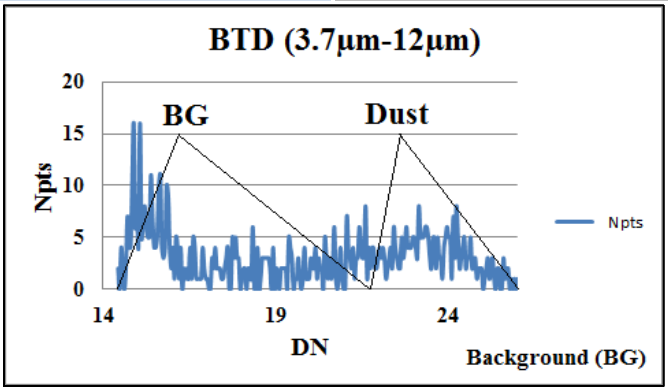

BTD (8.6 µm-11 µm)

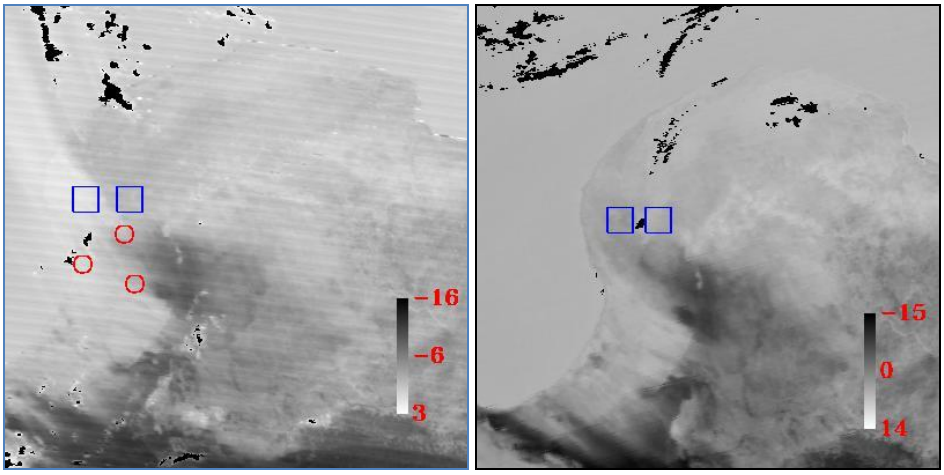


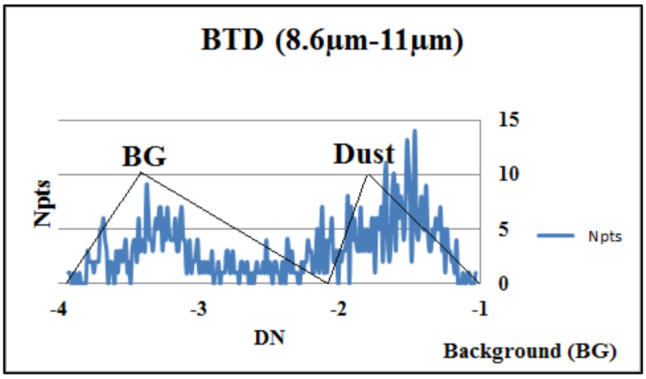


BTD (8.6 µm-12 µm)

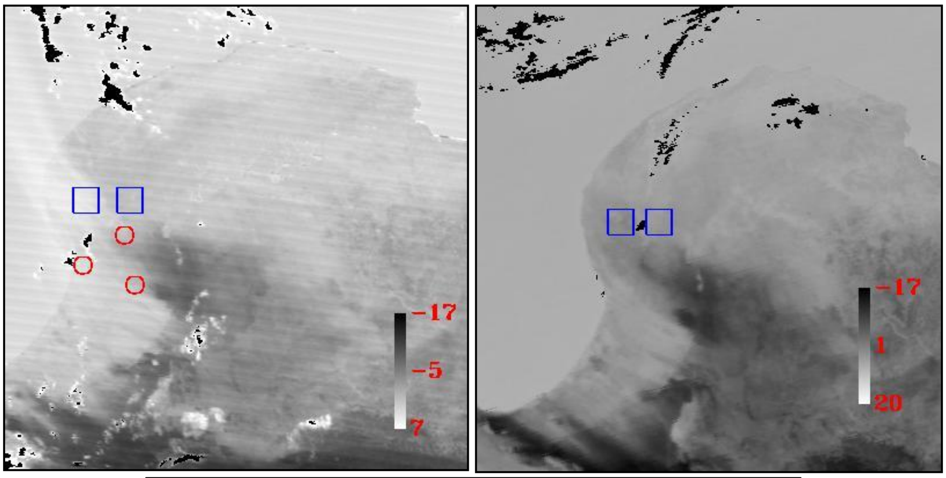


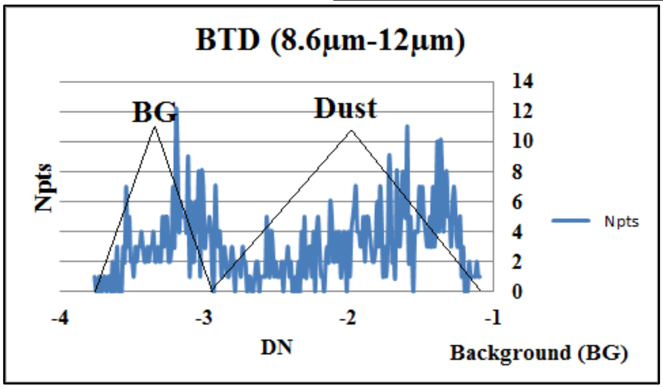

BTD (12 µm-11 µm)

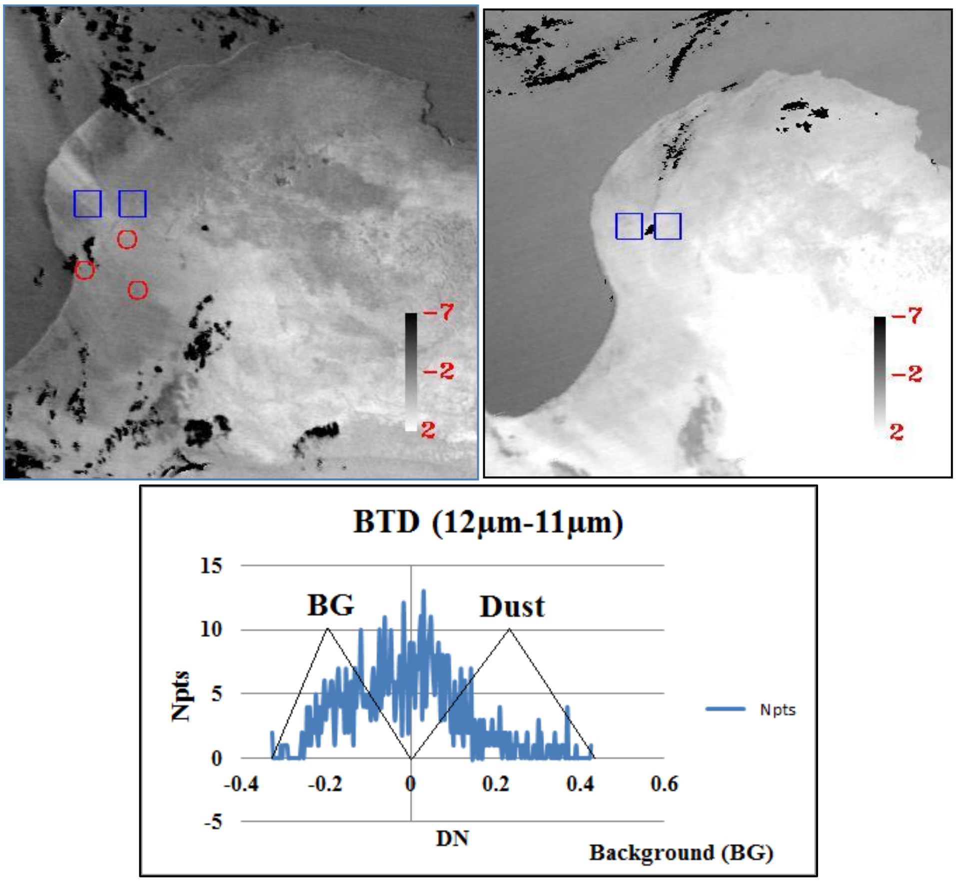


Figure 4.12 Result of applying the M test to the nine selected techniques for the image of Figure 4.11. The M test area has been highlighted by blue squares. The red dots show some of the expected dust sources.

The free dust image used to show what the test area of the dust image looks like compared to the no dust image and to see if there is any background influence for the indices were there is no dust over the test areas. Most of the indices show no dust in the dust free image apart from Hansell, BTD (12 µm-11 µm) and Deep Blue here it is quite difficult to interpret because there is considerable variation over the tested background.

When looking at Table 4.4 in general the M value for Limestone has the lowest values compared to the other tested backgrounds. This could be because; (1) the limestone background is bright, but not quite as bright as the dust, (2) the concentration of the tested dust blown from the limestone at that area is less than the dust blown from the other areas.

Table 4.4 Result of M test from five different backgrounds using MODIS images

| Background / Techniques | M (Limestone) (Bengasi) | M (Basalt) (Tibesti Mountain) | M (Quartz) (Sand dune) | M (Granite) (Air Mountain) | M (Diatomite) (Bodélé depression) | Median | Range |
|---|---|---|---|---|---|---|---|
| Ackerman (1989) | **1.55** | **5.53** | **3.24** | **1.74** | **3.03** | 3.03 | 3.98 |
| Miller (2003) | **1.80** | **6.37** | **5.29** | **2.79** | **2.29** | 2.79 | 4.57 |
| Hansell et al., (2007) | 0.22 | **8.64** | **1.65** | **3.33** | **3.49** | 3.33 | 8.42 |
| Handley (2004) | 0.25 | **8.29** | **1.68** | **2.64** | **3.72** | 2.64 | 8.04 |
| Deep Blue (2003) | **1.67** | **8.99** | **8.87** | **11.20** | **4.91** | 8.87 | 7.32 |
| BTD (3.7 µm-12 µm) | **1.56** | **5.05** | **2.40** | **1.61** | **2.56** | 2.4 | 3.19 |
| BTD (8.6 µm-11 µm) | **1.42** | **4.12** | **4.09** | 0.27 | 0.96 | 1.42 | 3.85 |
| BTD (8.6 µm-12 µm) | **1.41** | **3.04** | **3.49** | 0.17 | 0.90 | 1.41 | 3.32 |
| BTD (12 µm-11 µm) | 0.16 | **9.27** | **1.58** | **3.38** | **3.39** | 3.38 | 9.11 |

## 4.3.2 Basalt Background of the Tibesti Mountains

The second image is from MODIS Aqua sensor acquired on 24/02/2006 over Tibesti Mountain in northern Chad and southern Libya. Tibesti Mountains consist of inactive volcanoes apart from the Pic Tousside area which is potentially active. The Tibesti Mountains are the highest mountains in the Sahara, the highest peak being Emi Koussi at 3,415 m. The geology of the two Tibesti test areas is Basalt. The first test area of the image is covered by dust, which appears bright (Figure 4.13 B) due to the influence of the dust. The second test area to the south is free of dust and much darker because the Basalt background absorbs radiation in all wavelengths, as is confirmed in the dust free image (Figure 4.13 C).

4.13 (A)

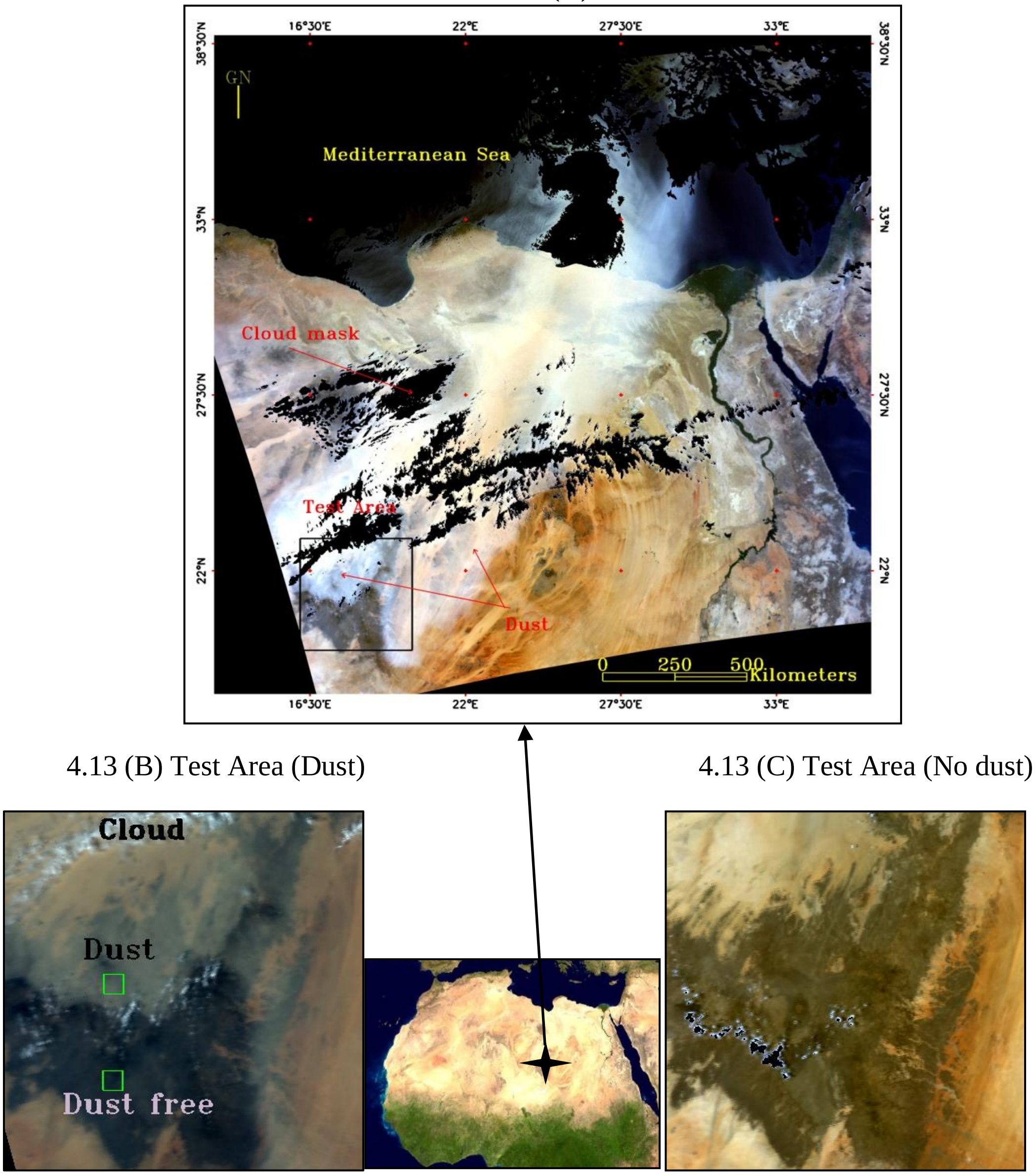


Figure 4.13 (A&B) True colour composite of a dust storms imaged on 24/02/2006 by the MODIS Aqua sensor over Tibesti Mountain (within latitude 19.11° N – 23.33° N, and longitude 15.39° E – 20.51° E). Pixel resolution is 1km and the image time was acquired at 11:30 hrs local time. (B) The first test area is located over the dust 11 whereas the dust free test area is located to the south of the dust. (C) A dust free image of the same area acquired on the 26/10/2007 by the MODIS Terra sensor at 09:05 hrs local time.

Figure 4.14 shows the results of the 9 dust indices applied over Tibesti Mountains. Visually BTD (12 µm-11 µm), Hansell et al., (2007) and Handley (2004) show good contrast between the basalt background and the dust, and the histogram of these indices shows good separation between the background mode and the dust mode, furthermore the M test result agrees with the visual result and indicates good contrast between the dust and the background. Ackerman (1989), BTD (3.7 µm-12 µm), and Miller (2003) are similar and show less contrast than the above listed techniques but still a reasonable contrast, the histogram of these indices shows the less separation background mode and the dust mode than the previous indices but still the visual result is reasonable and the M test result agrees with the visual result and indicates reasonable contrast between the dust and the background. BTD (8.6 µm-11 µm) and BTD (8.6 µm-12 µm) are the worst visually with no contrast between the dust and the background especially for (8.6 µm-12 µm) where the dust cannot be seen at all. The histogram spectra of BTD (8.6 µm-11 µm) index shows the background mode and the dust mode but the separation between the two modes is very narrow and thus poor contrast between the dust and the background. BTD (8.6 µm-12 µm) is the worst visually and that is clearly shown in the dust histogram. The M test result agrees with the visual result and indicates poor contrast between the dust and the background.

The highest background effects are noticed visually for BTD (8.6 µm-11 µm) and BTD (8.6 µm-12 µm), both of which are very good at mapping the presence of basalts but not dust. Moreover, Deep Blue (2003) shows good contrast between the basalt background and the dust but as usual with doubt concerning the accuracy of the cloud mask. Evaluation of the free dust images indicates that most of the tested indices show no dust over the tested background. However, Deep Blue (2003), BTD (8.6 µm-11 µm), and BTD (8.6 µm-12 µm) shows high values in the dust free images providing similar values to the dust image and thus detecting dust when it is not actually there.

The M test results have on average got the highest value over the basalt background than any other indicating that any of them would be good for detecting dust over basalt terrain, presumably because dust is bright and basalt is very dark, particularly when compared to the Limestone. This does not agree with the visual interpretation and the evaluation of the histograms which suggests that some methods perform very badly. The reasons for this discrepancy are unclear.

Ackerman (1989)

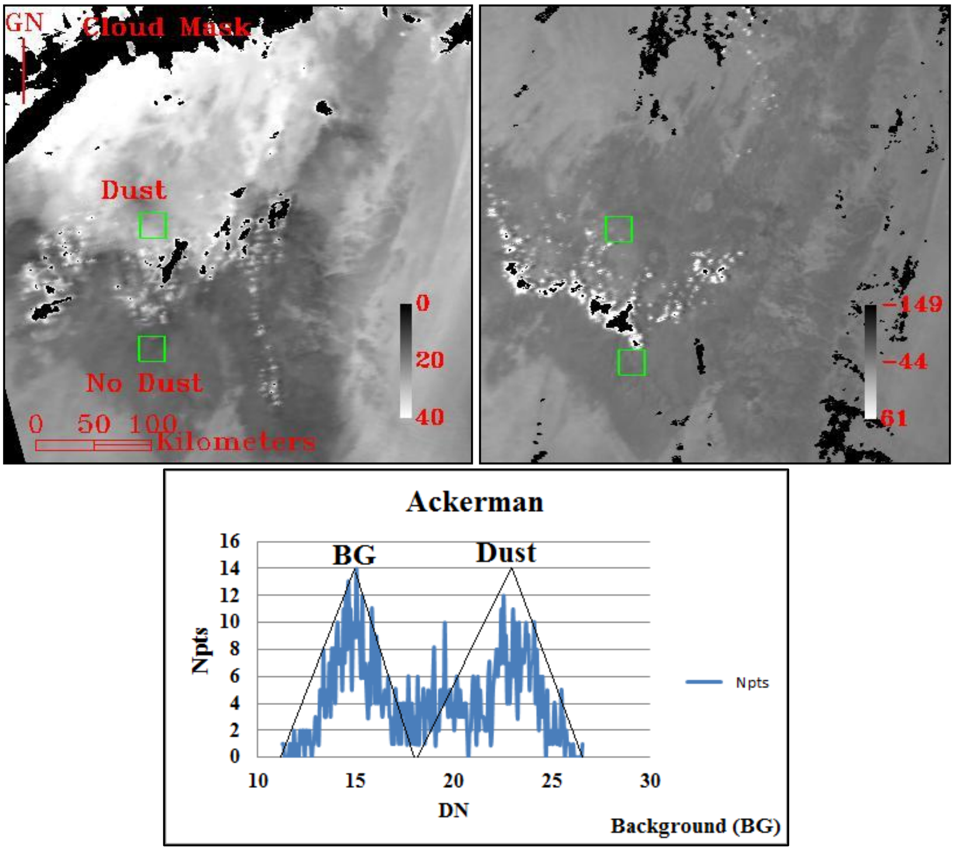


Miller (2003)

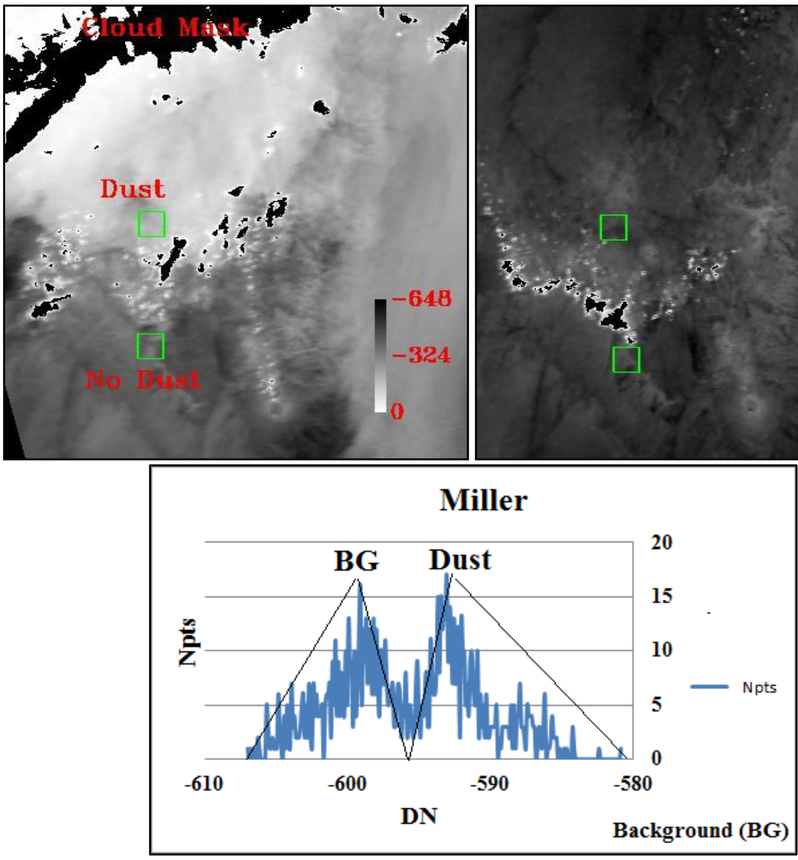

Hansell et al., (2007)

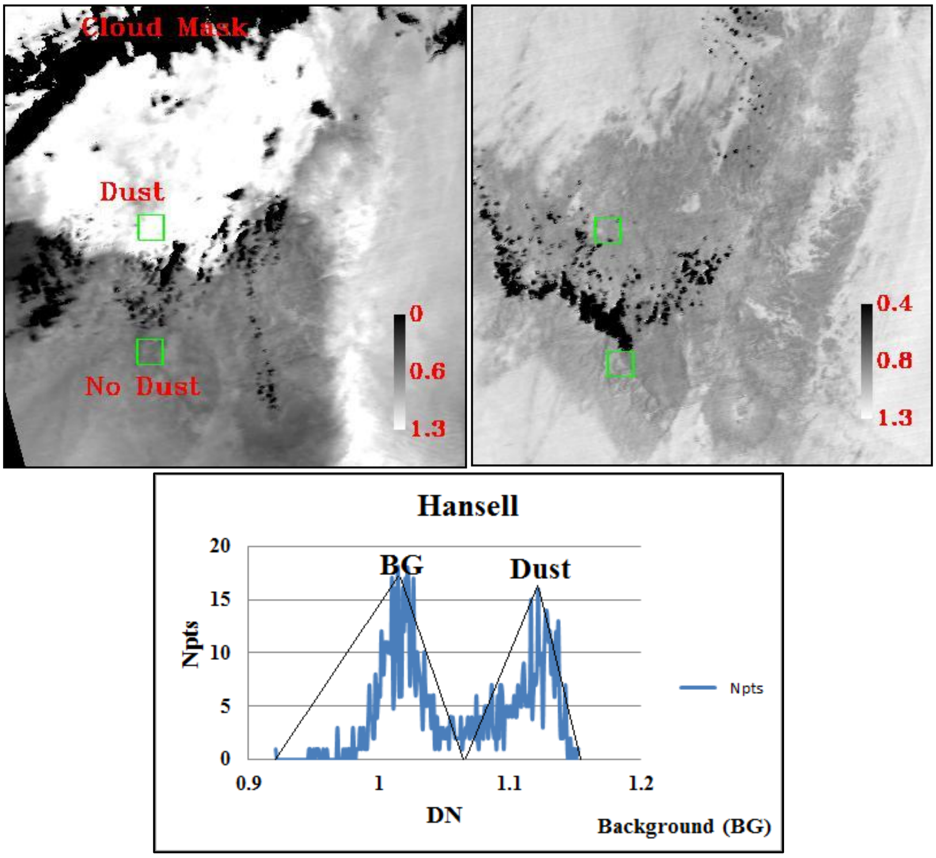


Handley (2004)

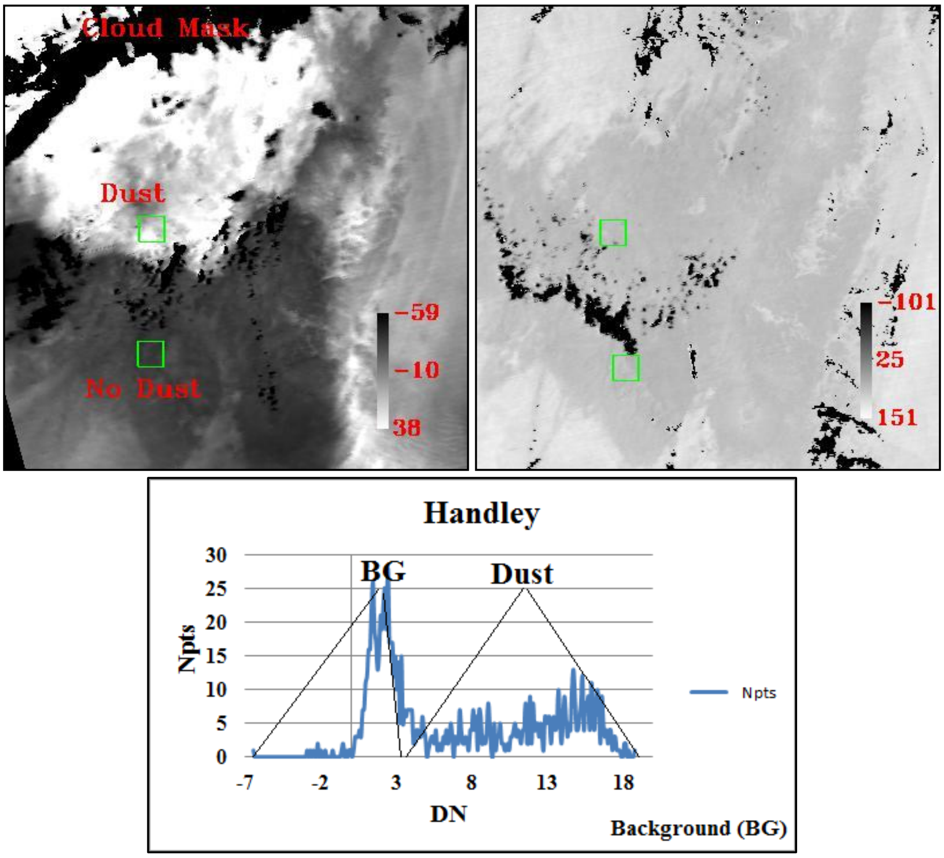

Deep Blue

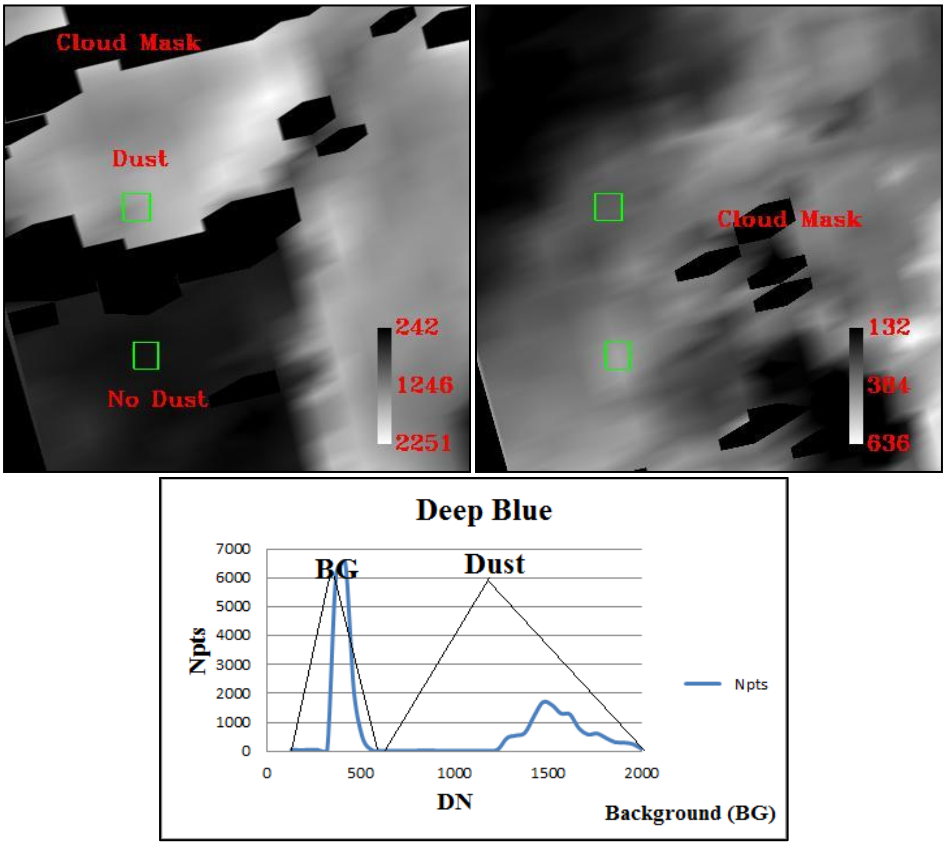


BTD (3.7 µm-12 µm)

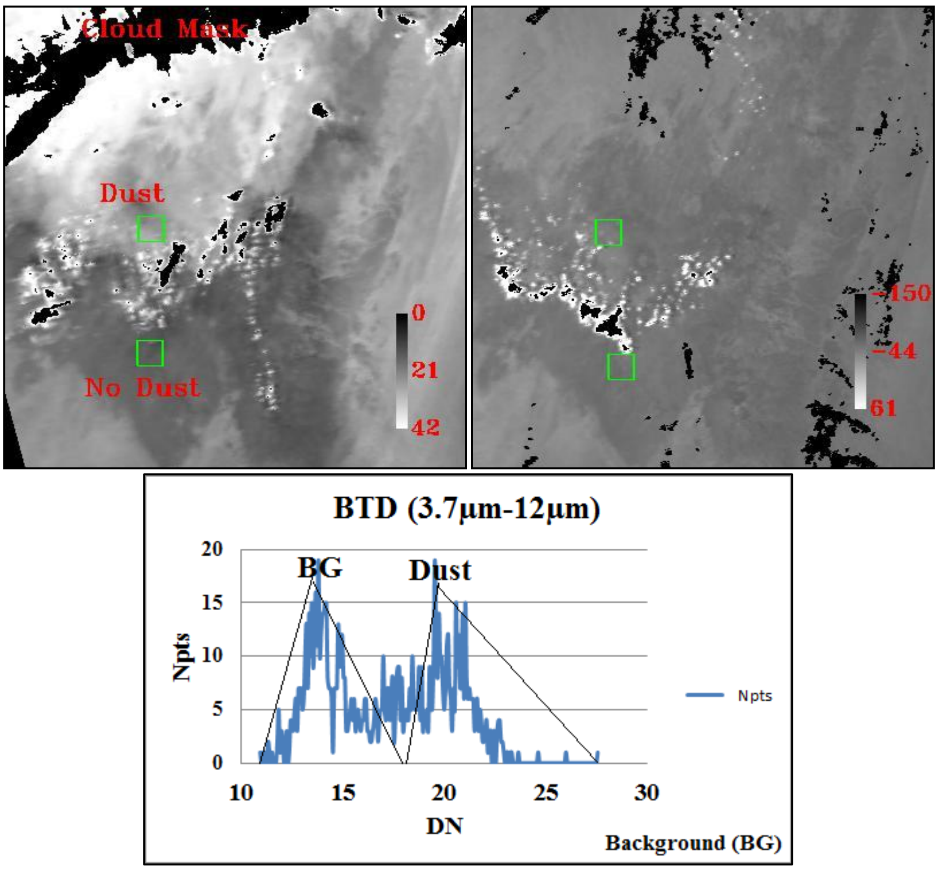

BTD (8.6 µm-11 µm)

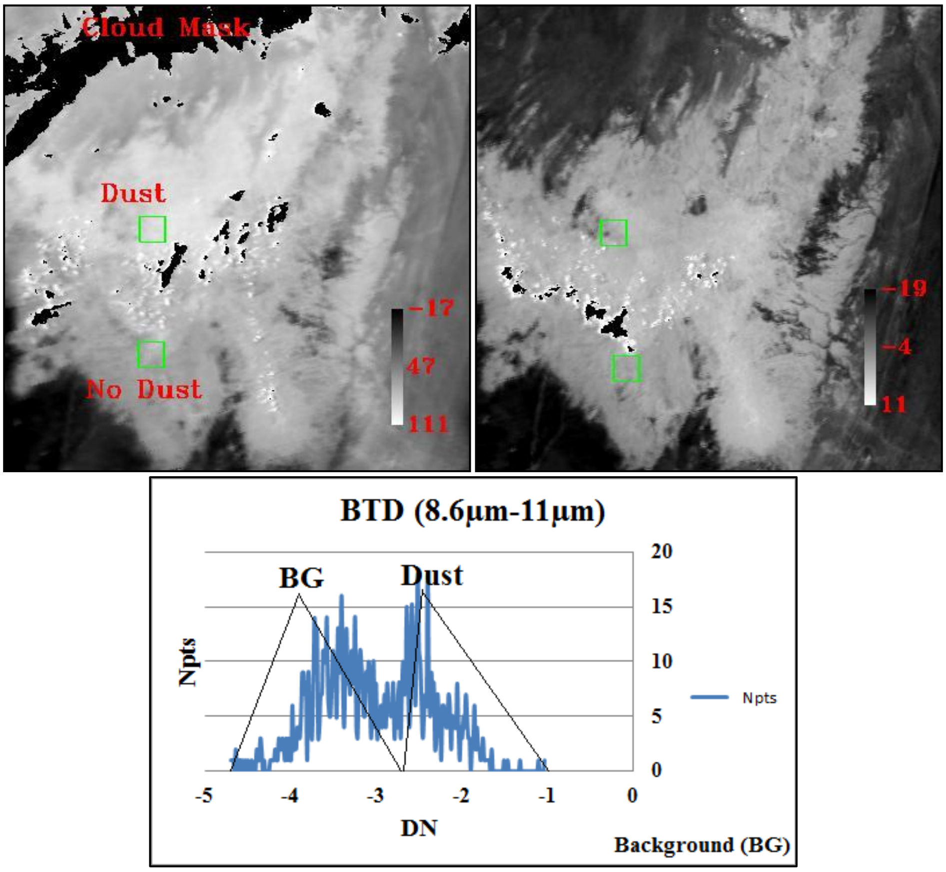


BTD (8.6 µm-12 µm)

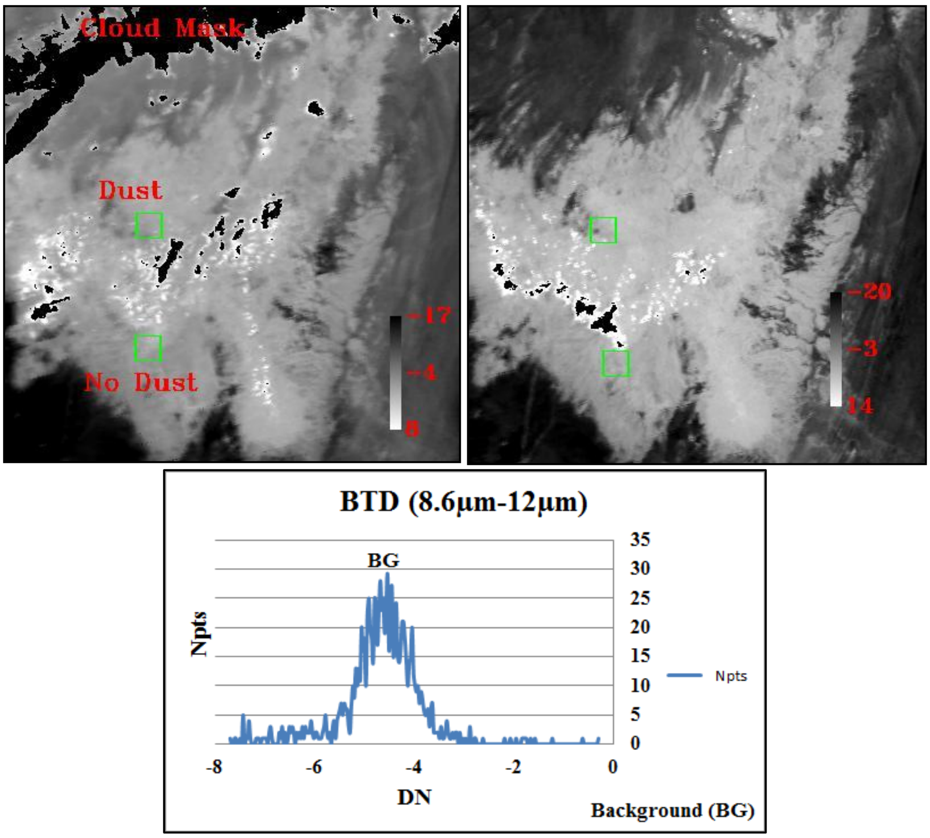

BTD (12 μm-11 μm)

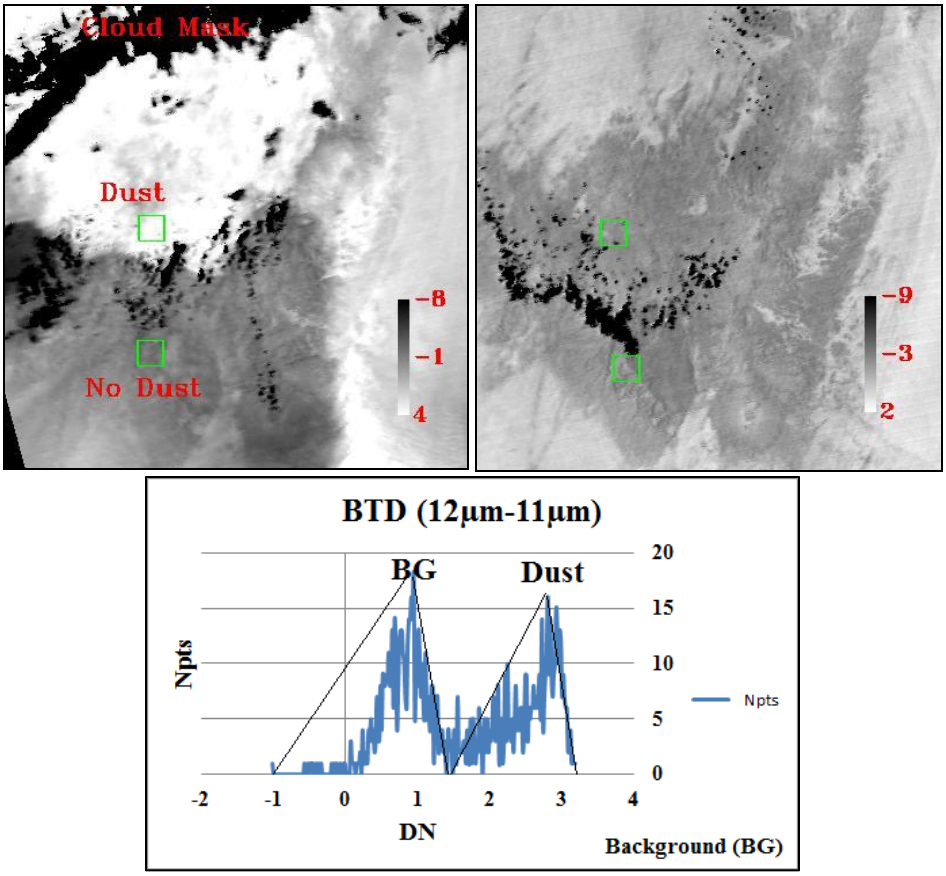


Figure 4.14 Result of applying the M test to the nine selected techniques for the image of Figure 4.13. The M test area has been highlighted by blue squares. The red dots show some of the expected dust sources.

### 4.3.3 Quartz Sand Background East of the Tibesti Mountains

The fourth image tested is over sand dunes east of the Tibesti Mountains acquired on 24/02/2006 by the MODIS Aqua sensor (Figure 4.15 A&B). The mineralogy/landforms of the two test areas are quartz sand dunes and sand sheets. In the first test area (Figure 4.15 A&B) the sand dunes are covered by dust which appears as a light grey in the image. In the second test area the sand dunes appear darker because there is no dust (Figure 4.15 C).The dust free image of the same area was acquired on the 26/10/2007 by the MODIS Terra sensor at 09:05 hrs local time.

4.15 (A)

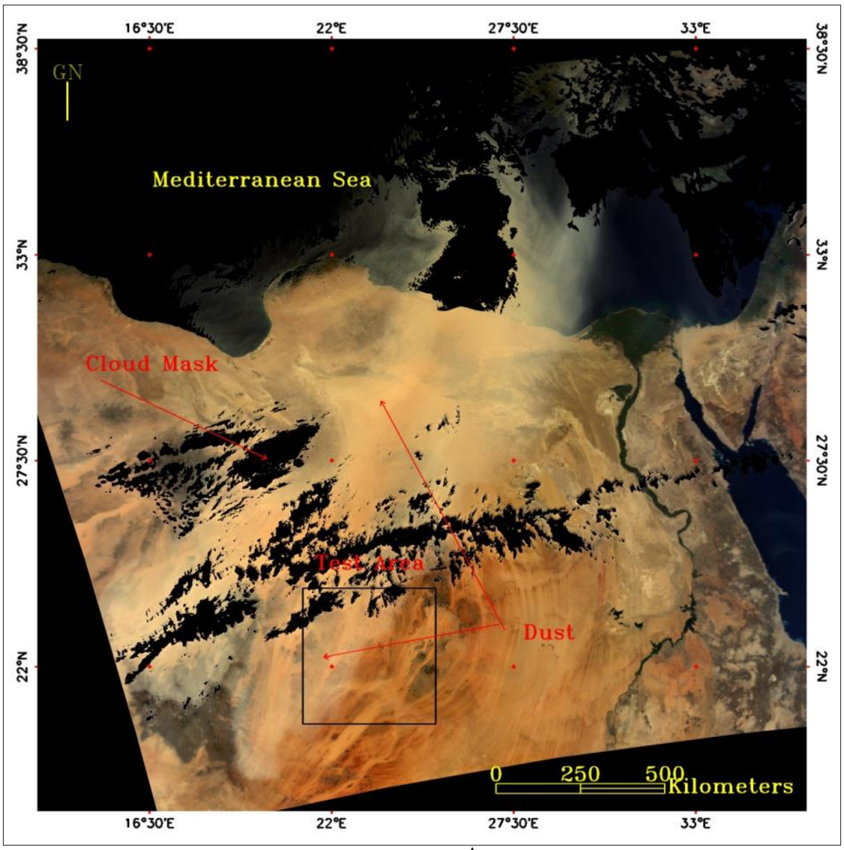


4.15 (B)

4.15 (C)

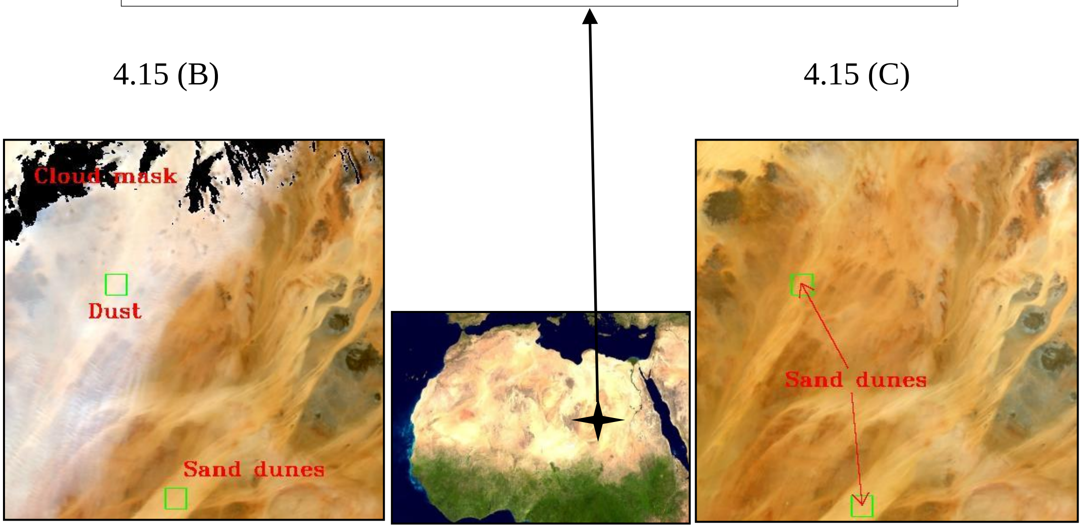


Figure 4.15 (A&B) True colour composite of a dust storms imaged on 24/02/2006 by the MODIS Aqua sensor over eastern Tibesti Mountain (latitude 19.11° N – 23.33° N, and longitude 15.39° E – 20.51° E). Pixel resolution is 1km and image time was acquired at 11:30 hrs local time. The test areas have been bordered by green rectangle. (C) The second test area is a dust free image of the same area acquired on the 26/10/2007 by the MODIS Terra sensor at 09:05 hrs local time. The background of this test area is quartz which appears bright in the image.

Figure 4.16 shows the results of the 9 dust indices applied over quartz sand located eastern of Tibesti Mountains.

Deep Blue (2003) provides the best result visually providing a good contrast between the dust and the background and the histogram shows good separation between the background mode and the dust mode, the M test result agrees with this and indicates high contrast between the dust and the background. Miller (2003) is also shows good results visually and the histogram shows good separation between the two modes, further more the M test has got the second highest M value after Deep Blue. BTD (8.6 µm-11 µm) and BTD (8.6 µm-12 µm) shows large background effects over different parts of the image. However, in the M test area the distinction between the dust and the quartz is reasonably good and the histogram shows reasonable separation between the background mode and the dust mode, the M test result agree with the visual result and indicates good contrast between the dust and the background. Ackerman (1989), and BTD (3.7 µm-12 µm) show similar results though the dust can be distinguished from the background less well than with the above listed techniques, the histogram shows clearly the dust and the background modes but with less separation between the background mode and the dust mode, the M test result agree with the visual result and indicates fair contrast between the dust and the background. Hansell et al., (2007) and BTD (12 µm-11 µm) shows low contrast compared to the above mentioned techniques and the histogram shows small separation between the dust and the background modes and that is in agreement with the M test were these two techniques have got the lowest M value. Handley (2004) looks good visually and the histogram clearly displays the dust and the background mode with reasonable separation between the two modes. However, the M test does not show a high M value, though it is higher than Hansell et al., (2007) and BTD (12 µm-11 µm).

The dust free image shows that Hansell et al., (2007) and BTD (12 µm-11 µm) shave high values in the dust free dust image which are similar to the values in the dusty image and can potentially cause false positive identification of dust. Moreover, Deep Blue shows variation over the tested background in the dust free dust image which is makes it quite difficult to say if there is dust being detected or no.

Ackerman (1989)

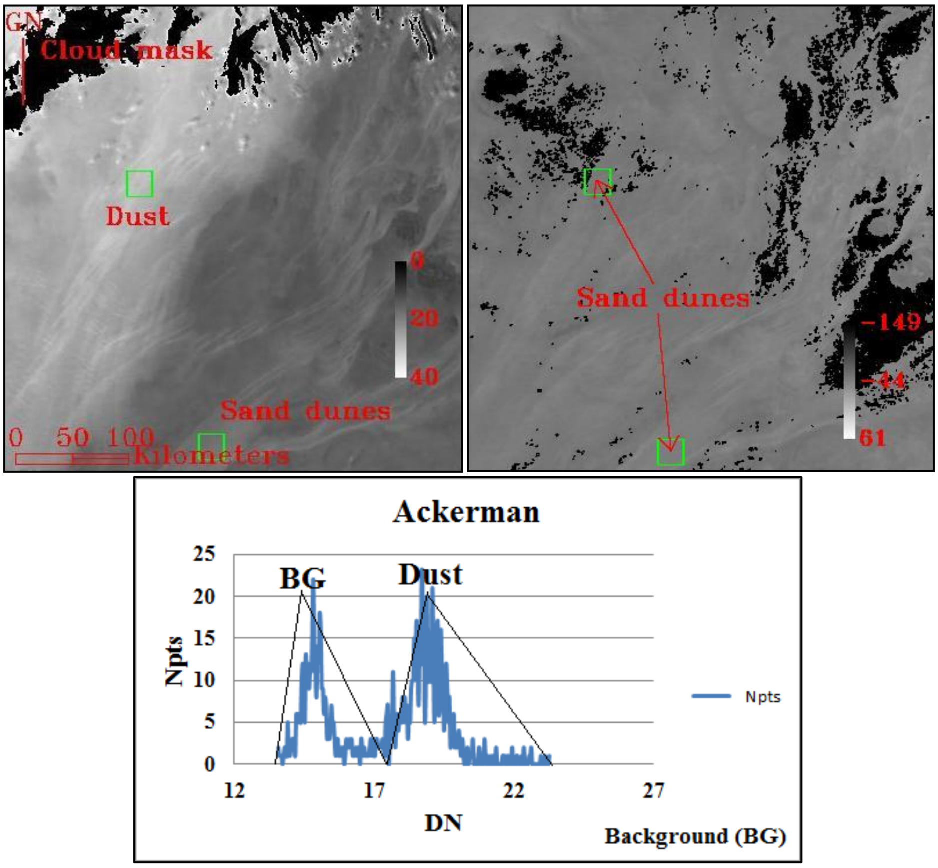


Miller (2003)

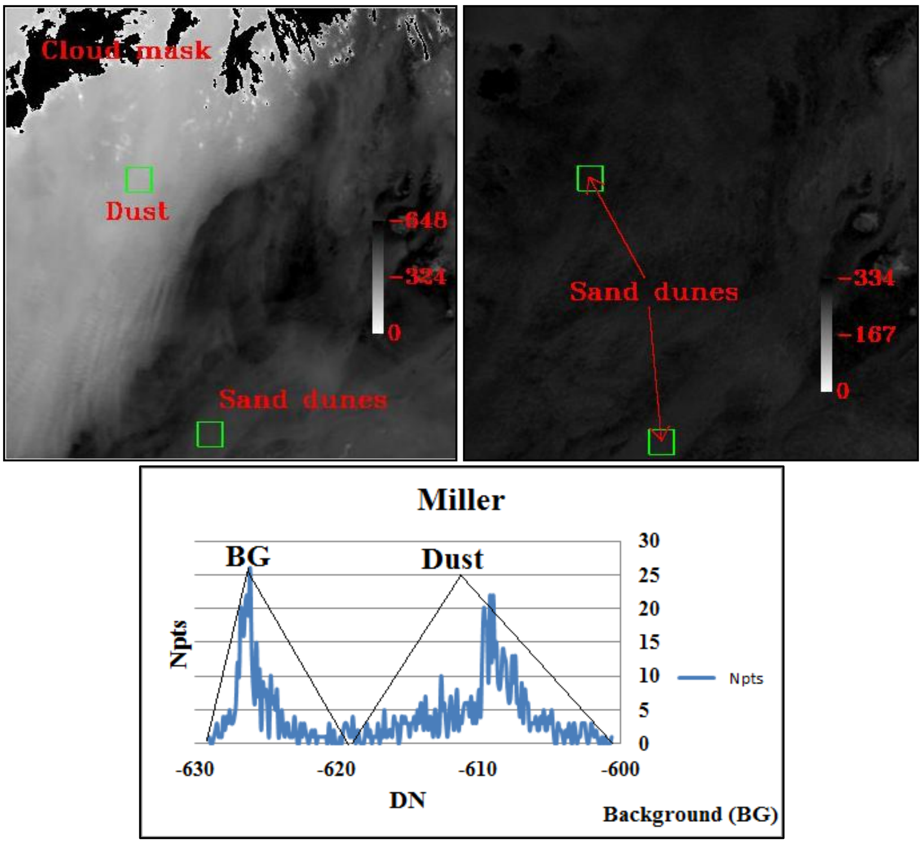

Hansell et al., (2007)

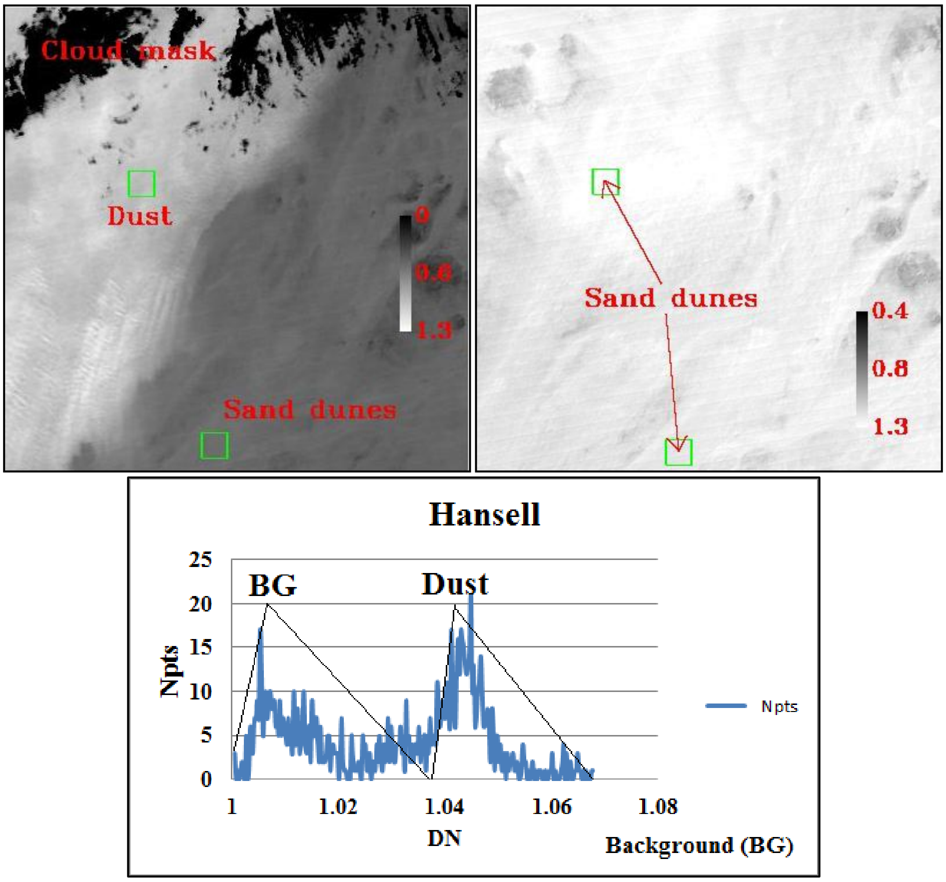


Handley (2004)

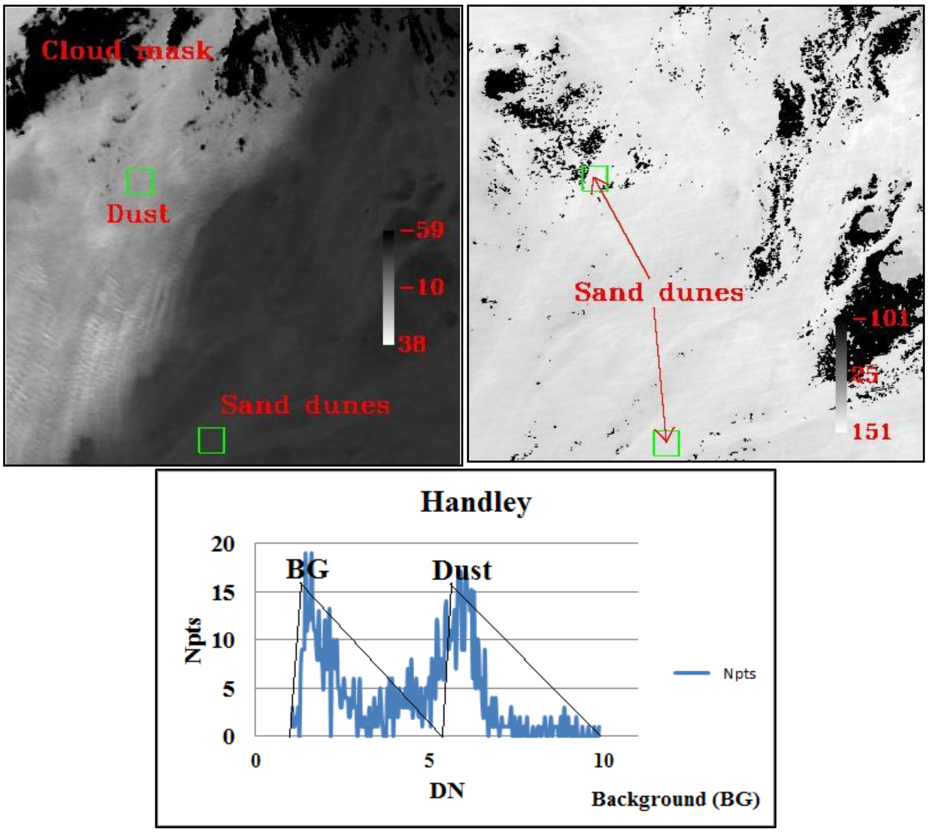

Deep Blue

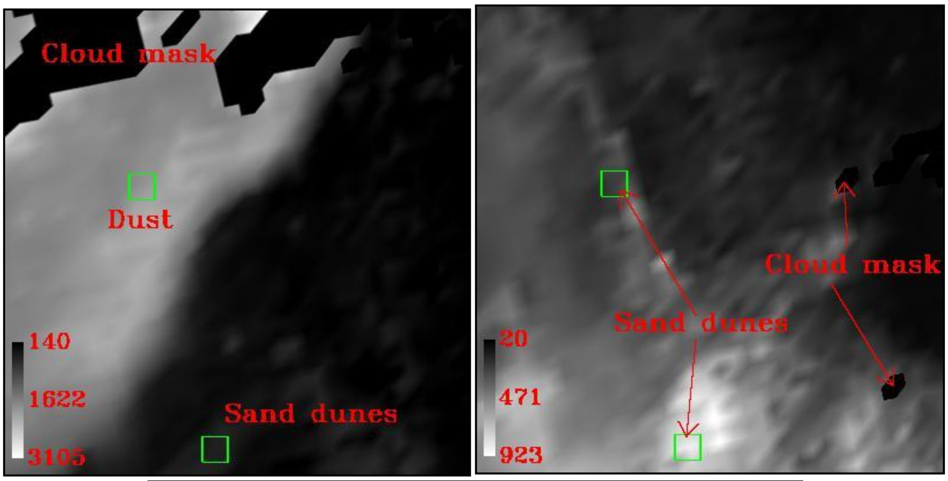


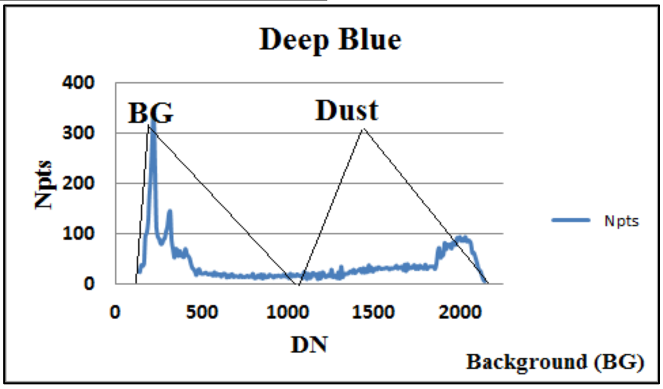


BTD (3.7 µm-12 µm)

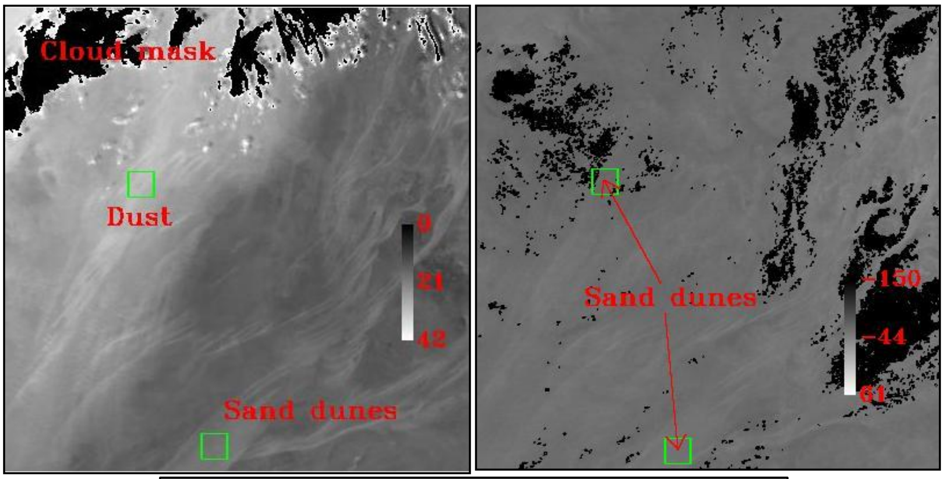


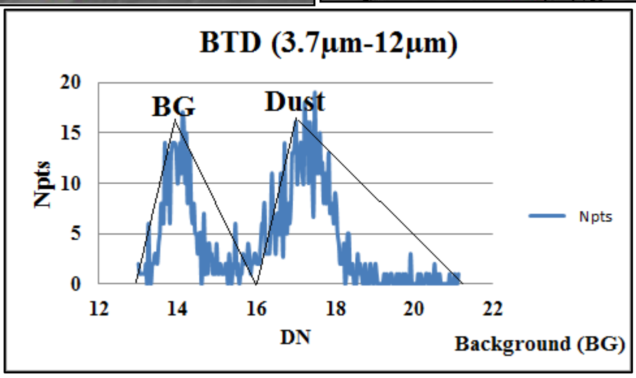

BTD (8.6 µm-11 µm)

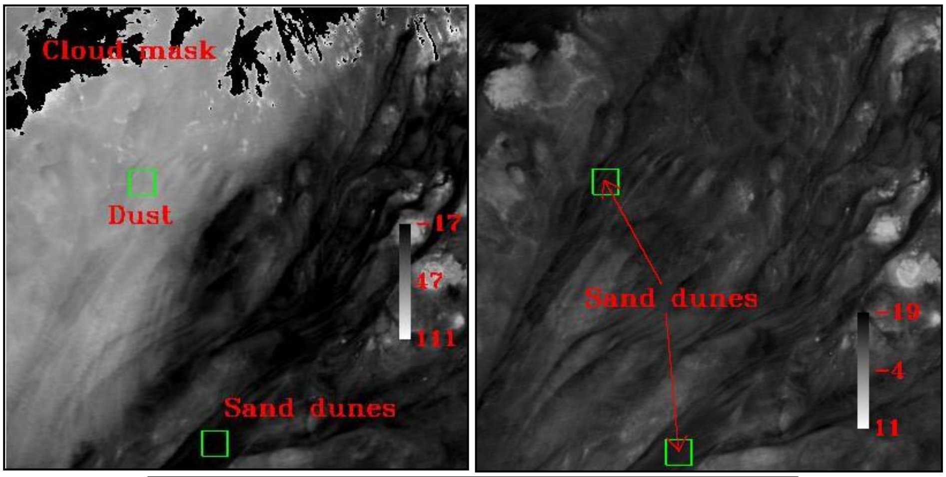


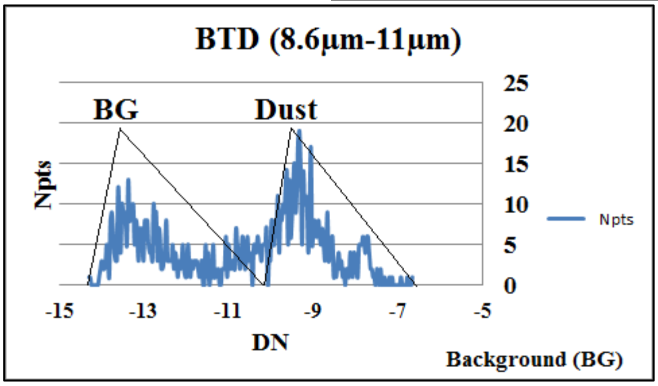


BTD (8.6 µm-12 µm)

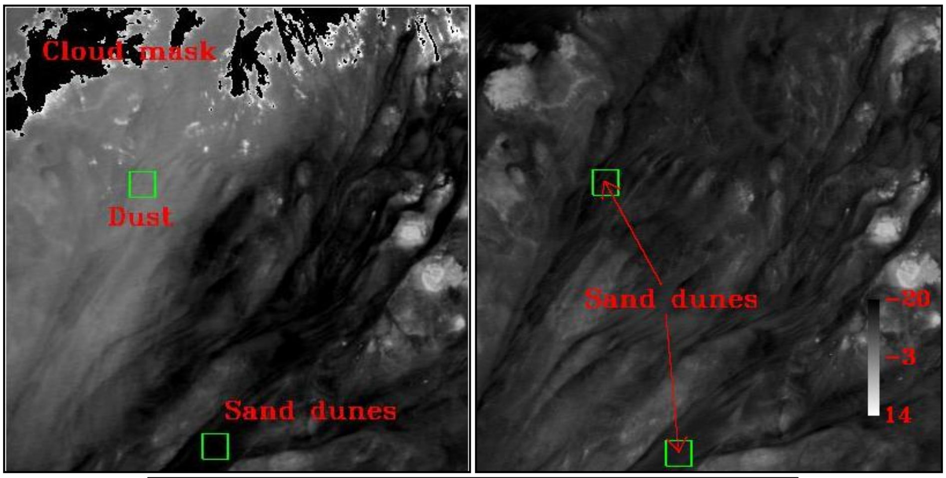


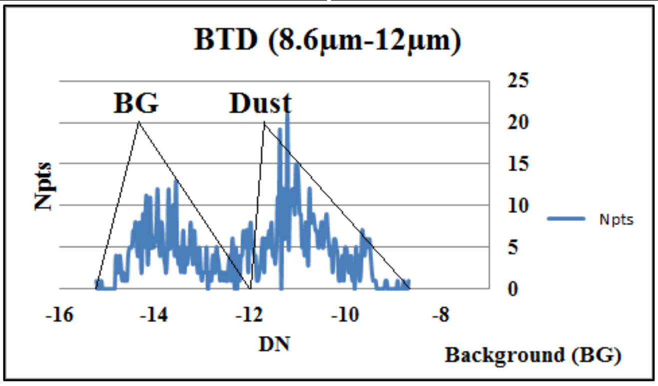

BTD (12 µm-11 µm)

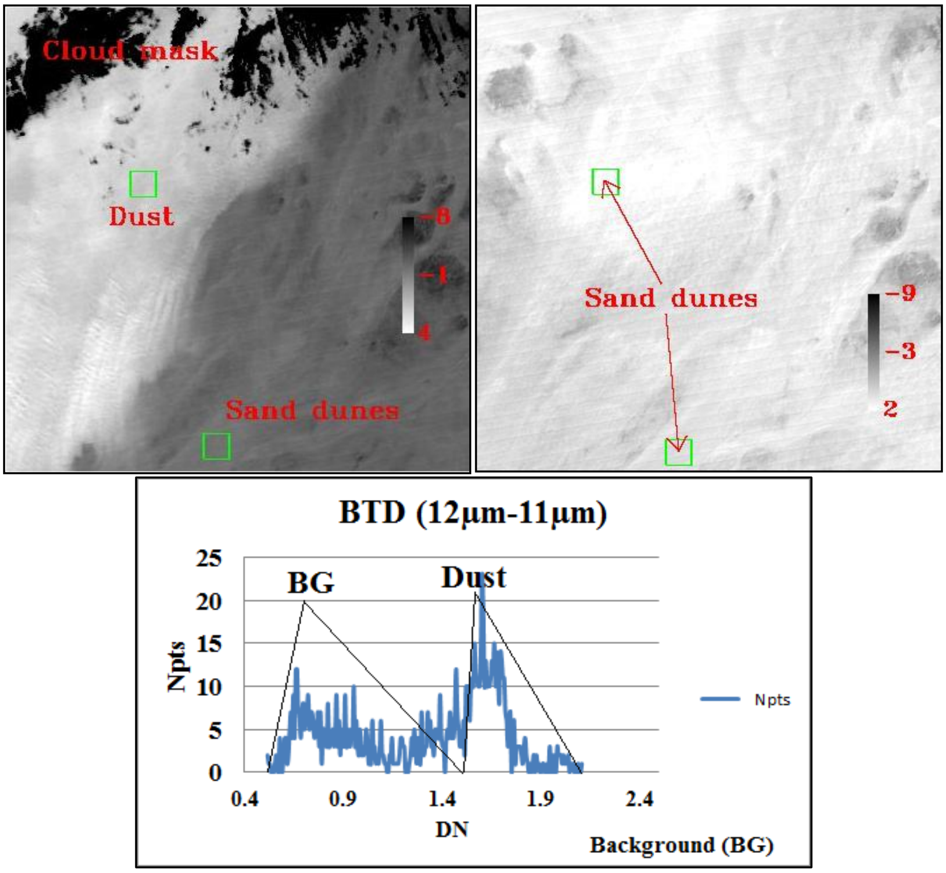


Figure 4.16 Result of applying the M test to the nine selected techniques for the image of Figure 4.15. The M test area has been highlighted by blue squares.

### 4.3.4 Granite Background of the Air Mountains

The fifth image was acquired over the Air Mountain in the Centre of Niger from the MODIS Aqua sensor on 12/01/2007. The geology of the Air Mountains is granite. The test areas of the dusty image are shown in Figure 4.17 (B) and for the dust free image in Figure 4.17 (C).

4.17(A)

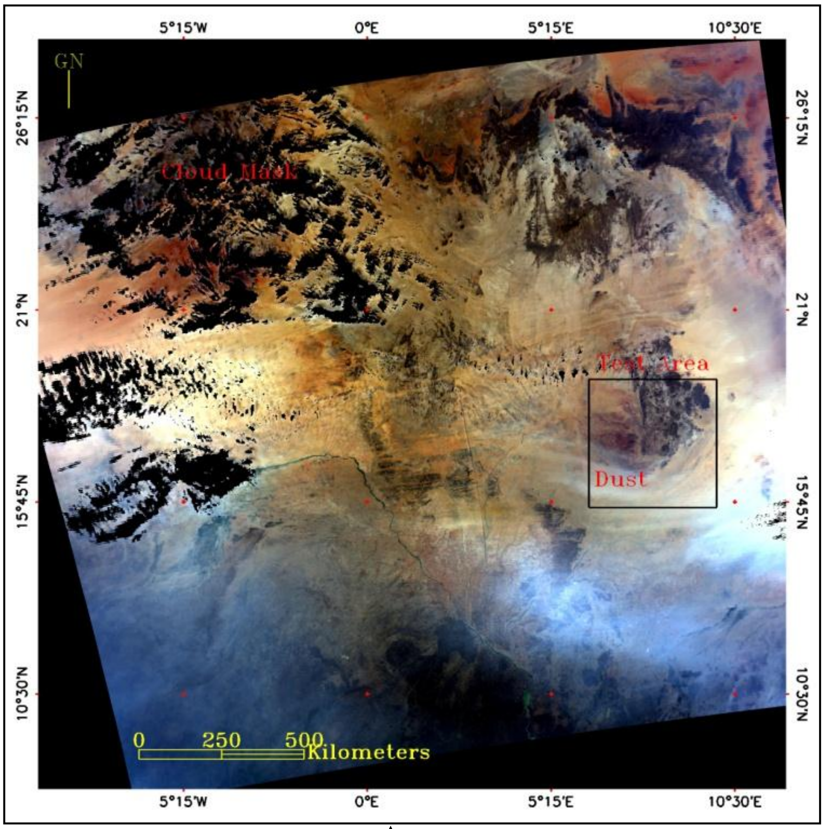


4.17(B)

4.17(C)

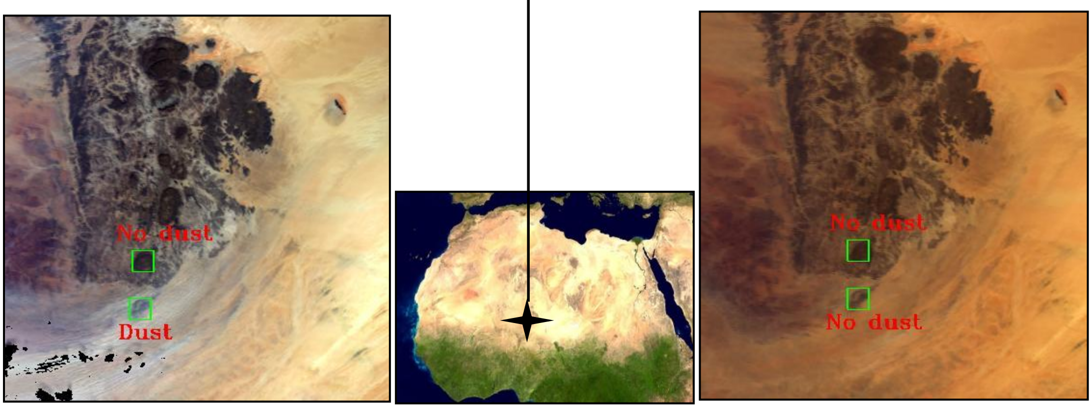


Figure 4.17 (A) True colour composite image by the MODIS Aqua sensor acquired over the Air Mountain (latitude 15.35° N – 19.10° N, and longitude 6.52° E – 10.40° E) dated 12/01/2007 and acquired at 13:15 hrs local time. Pixel resolution is 1km. (B) shows zoom on the test area of the image in Figure 4.17 (A). Pixel resolution is 1km and image time was acquired at 13:15 hrs local time. The test area has been bordered by black rectangle. Figure 4.17 (C) shows dust free image from Terra sensor over the same area of the Air Mountain acquired on 03/06/2009 at 09:45 hrs local time.

Figure 4.18 shows the 9 dust indices applied over the Air Mountains, BTD (12 µm-11 µm) and Hansell et al., (2007) show the best contrast visually and the histogram shows good separation between the background mode and the dust mode, the M test also suggests high contrast. Handley (2004) and Miller (2003) also shows good contrast between and the histogram shows good separation as does the M test. Ackerman (1989), and BTD (3.7 μm-12 μm) have reasonable contrast, the histogram shows good separation between dust and background but there are high background effects compared the previous indices perhaps indicating why these methods have got lower M values compared to the previous indices, The BTD (8.6 μm-11 μm) and BTD (8.6 μm-12 μm) are the worst visually and there is no contrast between the dust and the background and no dust sources can be detected, the histogram spectra of these indices shows only one mode with no separation between the background and the dust, the M test result also and indicates poor contrast between the dust and the background.. Deep Blue (2003) visually shows poor contrast between the dust and the background, moreover, the histogram has multiple modes suggesting complex background effects while the M test suggests very high contrast in the image where there is no dust some dust activity can be seen suggesting a poor performance over granite under low dust conditions.

The dust free image shows no dust over the granite for most of the techniques apart from Hansell et al., (2007), Handley (2004), and BTD (12 μm-11 μm) were there are bright area which is can be misclassified as dust.

Ackerman (1989)

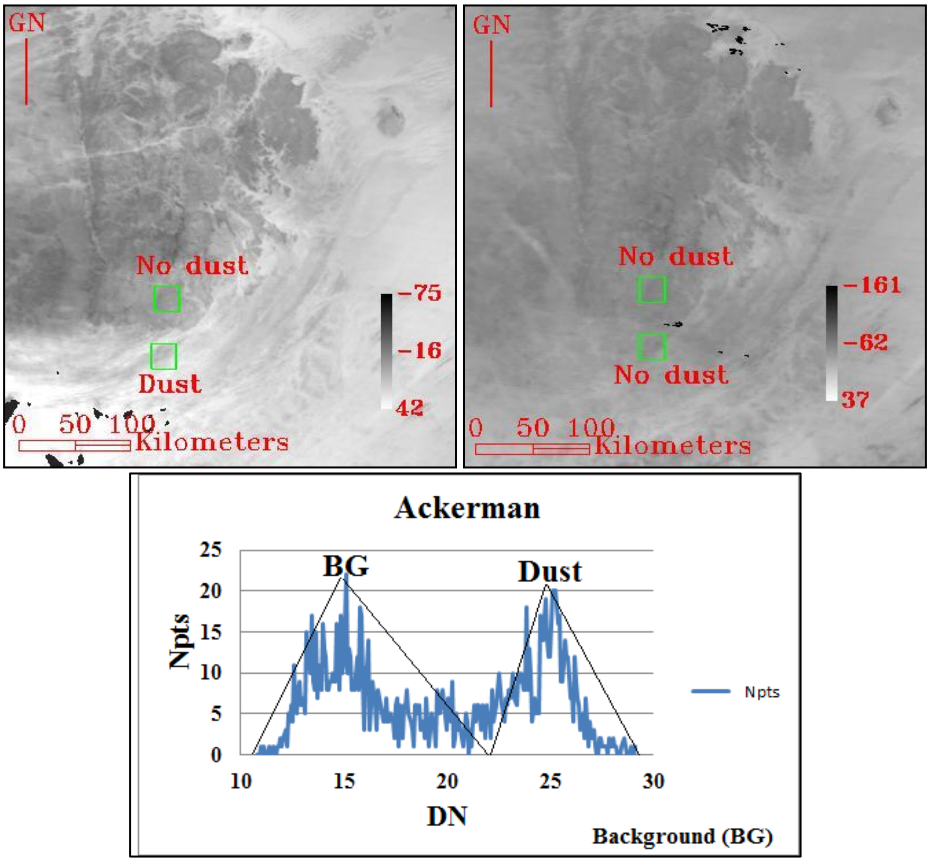


Miller (2003)

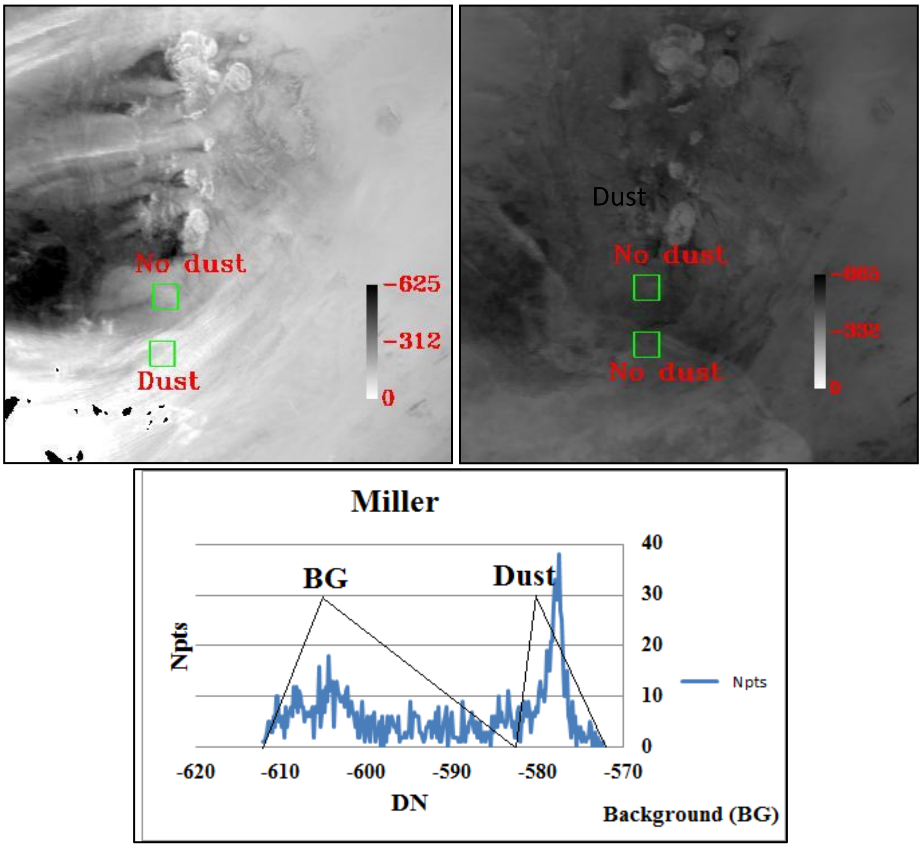

Hansell et al., (2007)

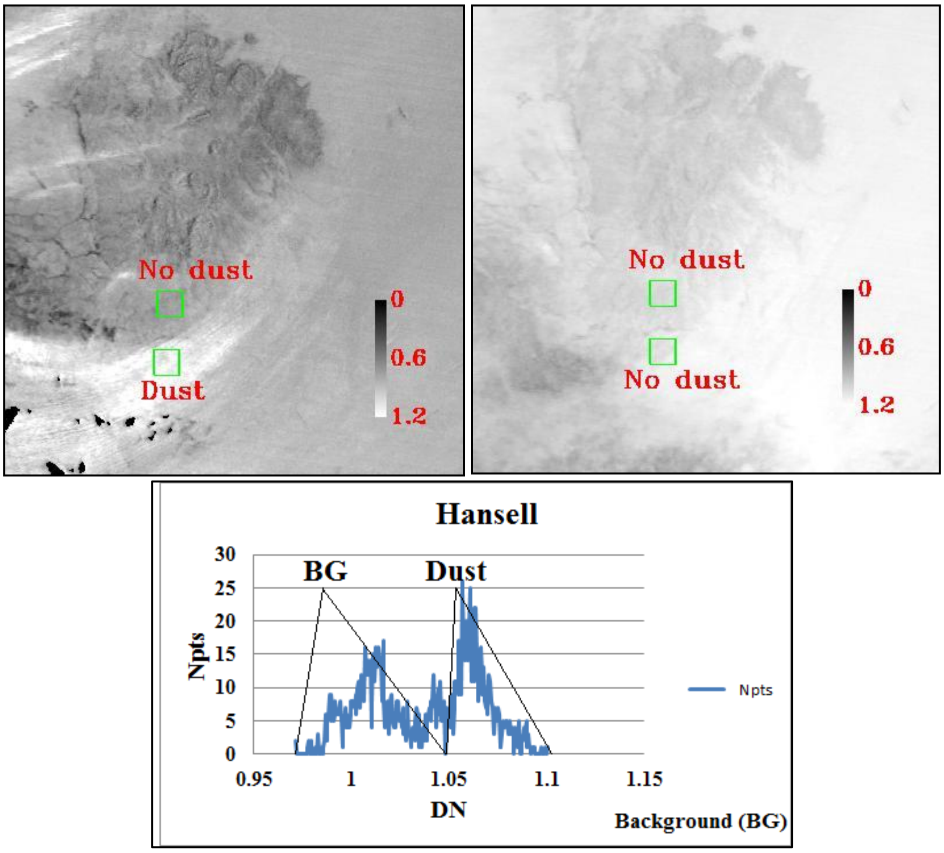


Handley (2004)

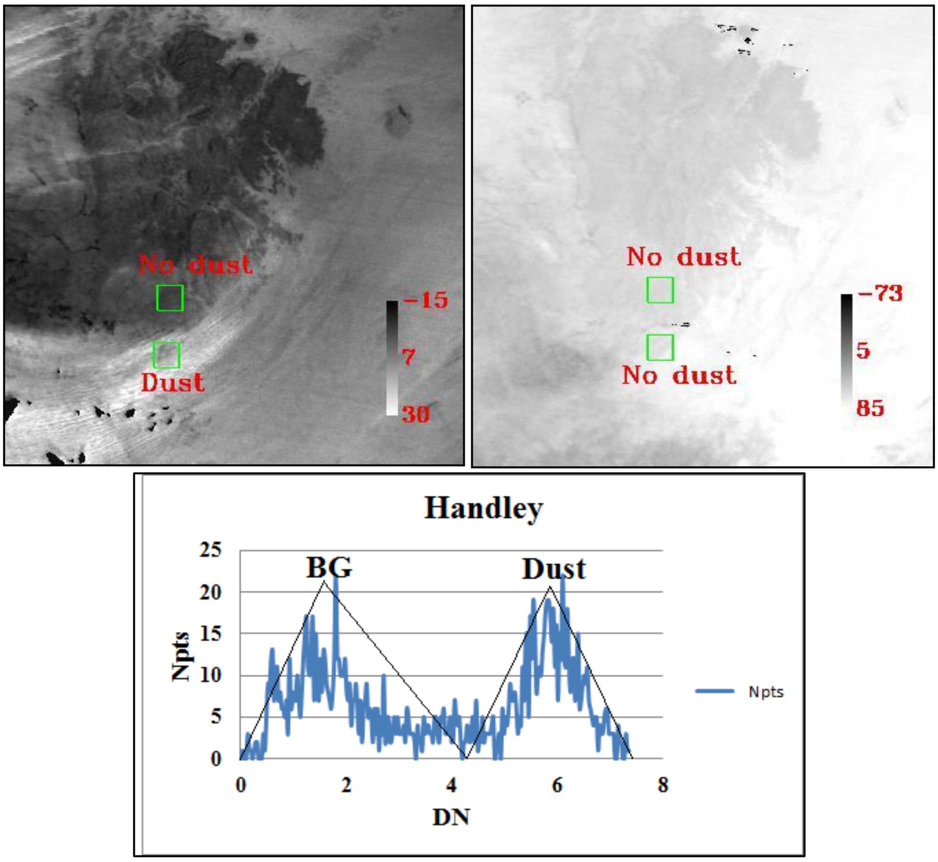

Deep Blue (2003)

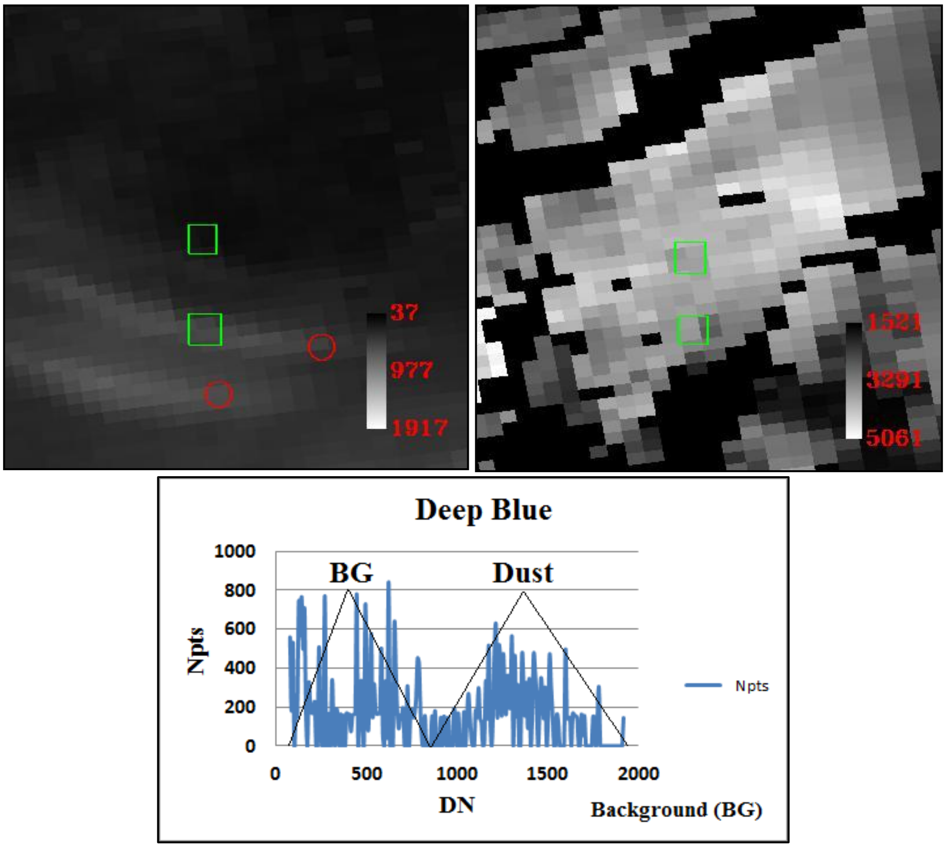


BTD (3.7 µm-12 µm)

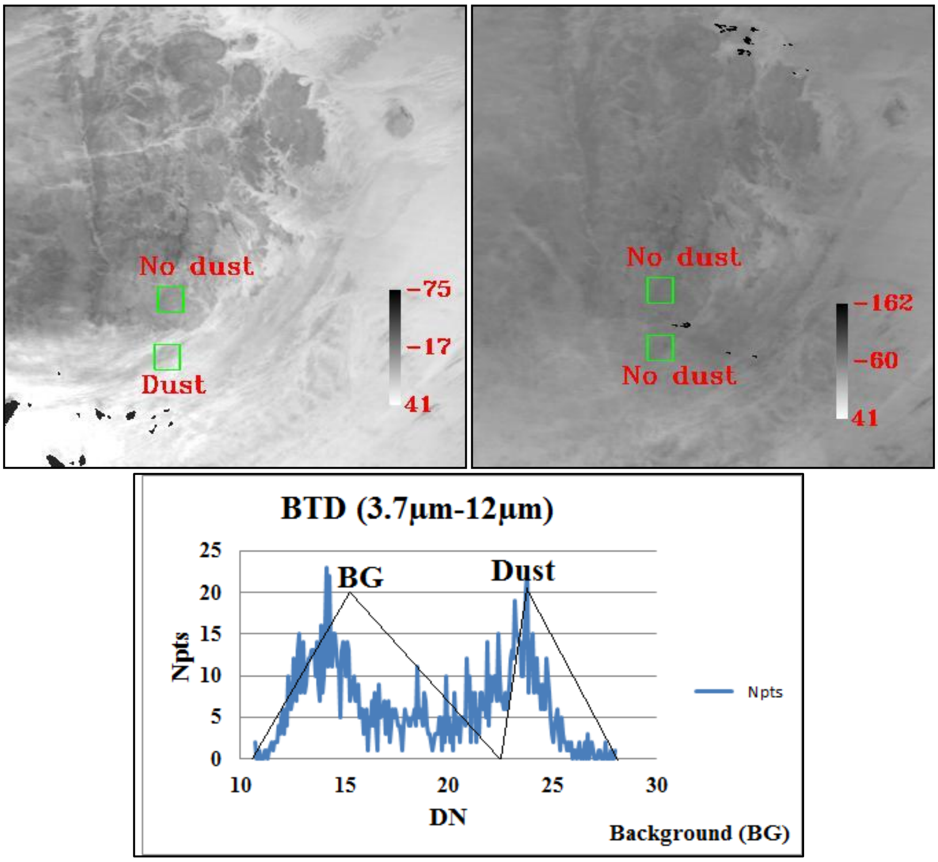

BTD (8.6 µm-11 µm)

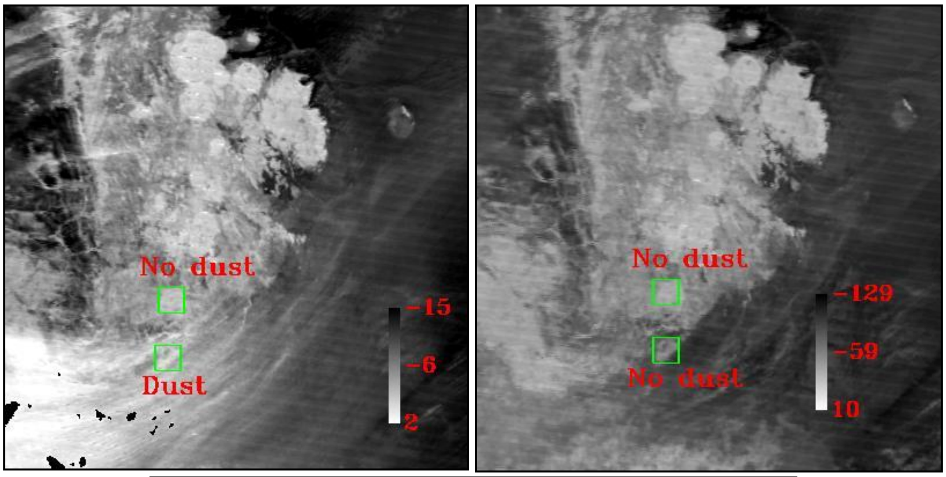


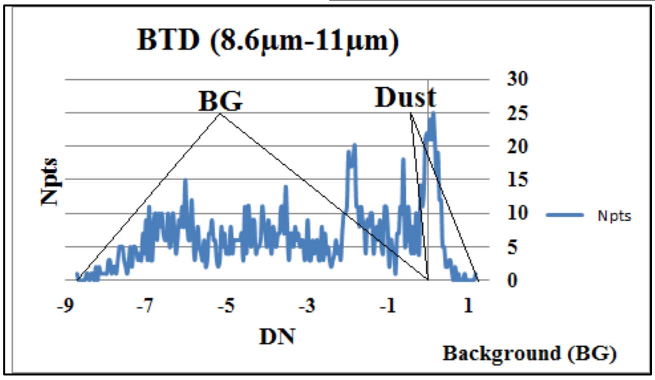


BTD (8.6 µm-12 µm)

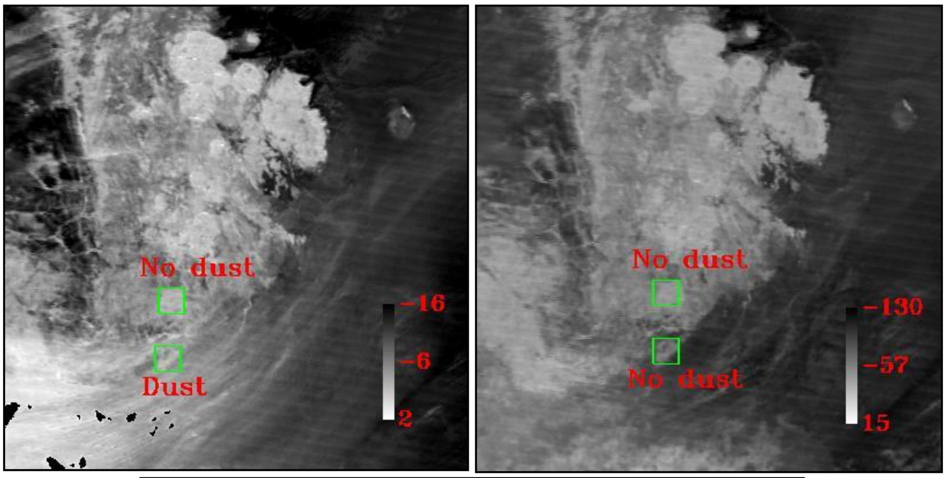


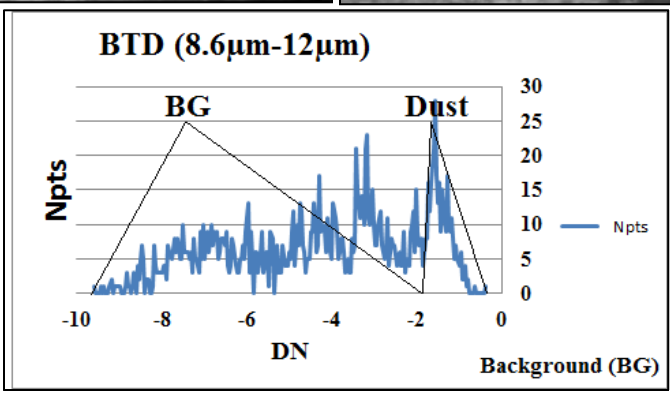

BTD (12 µm-11 µm)

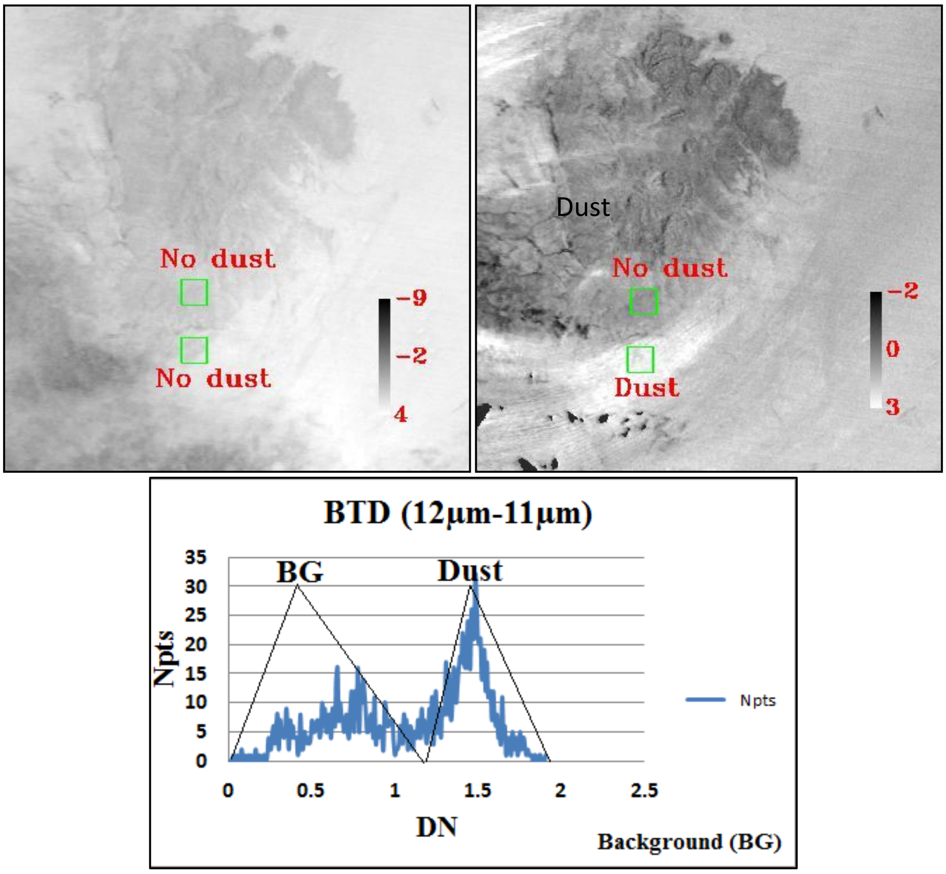


Figure 4.18 Result of applying the M test to the nine selected techniques for the image of Figure 4.17. The M test area has been highlighted by green squares.

### 4.3.5 Diatomite Background of the Bodélé Depression

The third image used for the test was acquired over Bodélé Depression, Chad in order to study the effect of a bright diatomite background. Bodélé Depression is the lowest point in the Chad Basin, and is recognized as the world dustiest place, having an average about 100 dust days per year (Warren et al., 2007). Diatomite paleo-lake sediments exposed at the surface of the depression are the source material for the dust. Two MODIS images were used to calculate M due to difficulty in finding images with diatomite areas covered by dust and the other part of the same image with diatomite clear from dust. The first image used for this test is dated 12/01/2007 were dust can be seen blowing from the Bodélé Depression (Figure 4.19 A&B), the second image is dated 3/06/2009 were no dust activity can be seen in the image. The diatomite appears bright in the image, as shows in Figure 4.19 (C).

4.19(A)

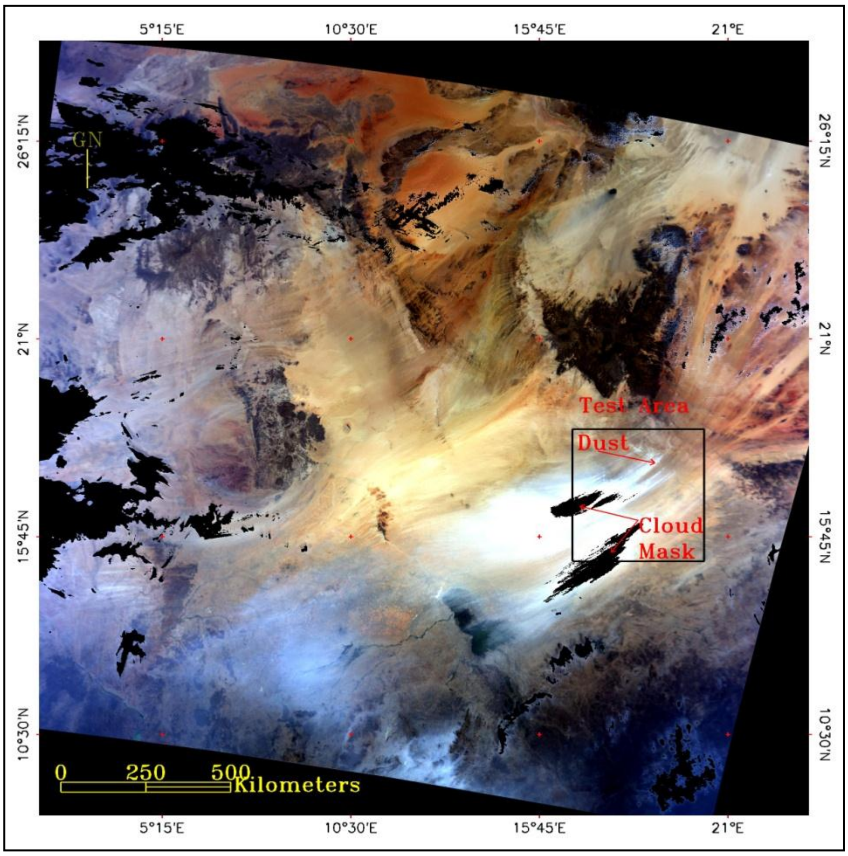


4.19(B) Dust

4.19(C) No dust

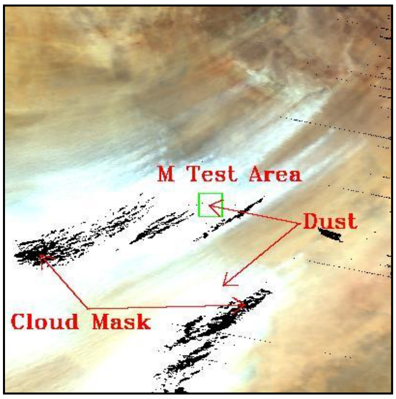


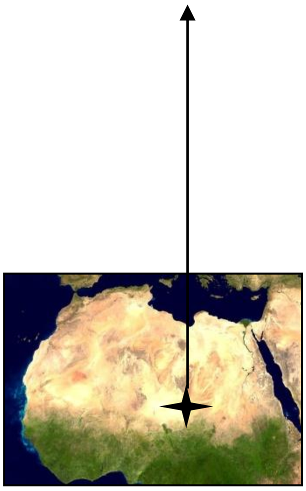

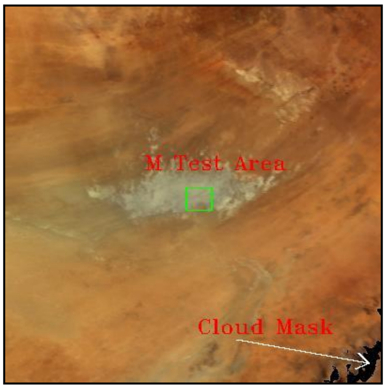


Figure 4.19 (A&B) True colour composite image by the MODIS Terra sensor over Bodélé Depression (latitude 15.07° N – 18.43° N, and longitude 15.53° E – 19.38° E) acquired on 12/01/2007 at 09:50 hrs local time. The pixel resolution is 1km. Figure 4.19 (C) shows free dust image from Terra sensor over the Bodélé Depression acquired on 03/06/2009 at 09:45 hrs local time over the same area of Figure 4.19 (B). The green square represent the M test area.

Figure 4.20 shows the spatial structure of the 9 dust indices applied over Bodélé Depression**.** The M result is shown in Table 4.4. It is clear that the cloud mask is being confused with high concentrations of dust in this image. BTD (8.6 µm-11 µm) and BTD (8.6 µm-12 µm) detect diatomite as dust in the dust free image. BTD (12 µm-11 µm), Handley (2004), and Hansell et al., (2007) also detect dust in the dust free image. However, these methods are detecting a different background material. The former methods provide high values over diatomite whilst the latter methods do so over the non diatomaceous areas.

The histogram of BTD (8.6 µm-11 µm) and BTD (8.6 µm-12 µm) shows good separation between the background mode and the dust mode, however, the diatomite is included in the dust mode, with the non diatomite dominant background forming the mode with the lower values, but the M test indicates low contrast between the dust and the background, thus backing up this interpretation. The histogram s of BTD (12 µm-11 µm), Handley (2004), and Hansell et al., (2007) shows quite good separation between the dust mode and the background mode. The best results visually are Ackerman (1989), Miller (2003), and BTD (3.7 µm-12 µm), all have the ability to clearly define the dust sources and no dust can be seen in the free dust image. The histogram spectra shows good separation between the background mode and the dust mode and the M test result generally agrees with the visual result and indicates reasonable contrast between the dust and the background. However, Miller (2003) shows some stripes of dust on the free dust image which in fact is part of the geology of the area and not dust. Visually Deep Blue (2003) shows low contrast between the dust and the background, and as usual has difficulty in identifying the dust sources and the edge pixels of the dust are masked by the cloud mask. The histogram of Deep Blue (2003) shows limited separation between the background and the dust and difficult to identify the dust mode and the background mode because of a lot of high frequency noize between them. However, the M test d indicates high contrast between the dust and the background. The dust free image shows result similar to the granite, no dust is detected over the diatomite for most of the techniques apart from BTD (8.6 µm-11 µm), BTD (8.6 µm-12 µm), and Deep Blue were there are high values appear on the diatomite. There is bright area with high values appears just south of the Bodélé Depression and that is confirmed by all of the indices in different concentration, however, BTD (12 µm-11 µm), Handley (2004), and Hansell et al., (2007) shows that area has got high values compared to the other and probably it is dust passing over that area.

Ackerman (1989)

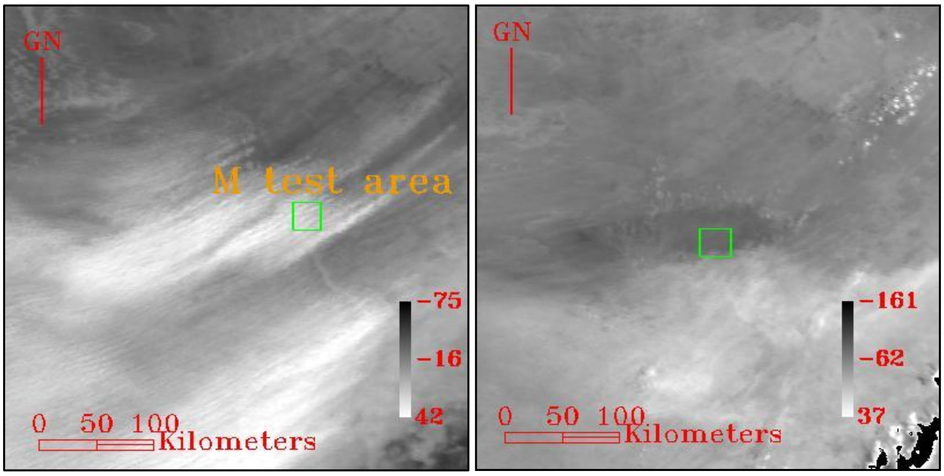


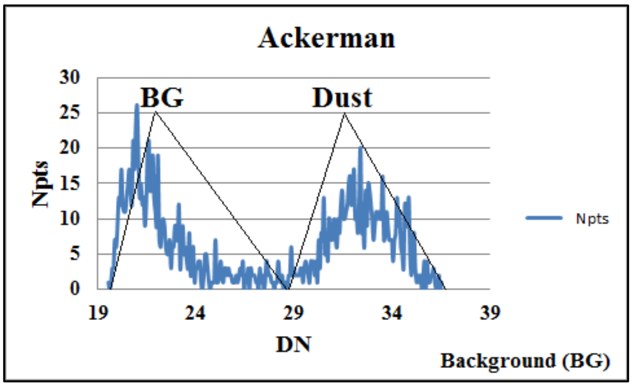


Miller (2003)

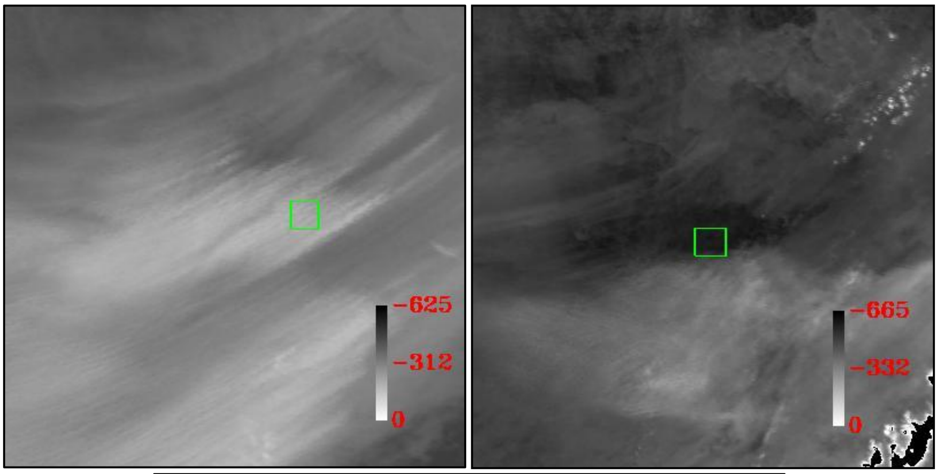


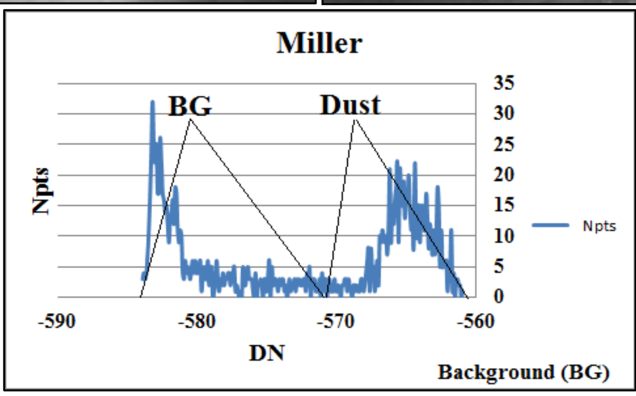

Hansell et al., (2007)

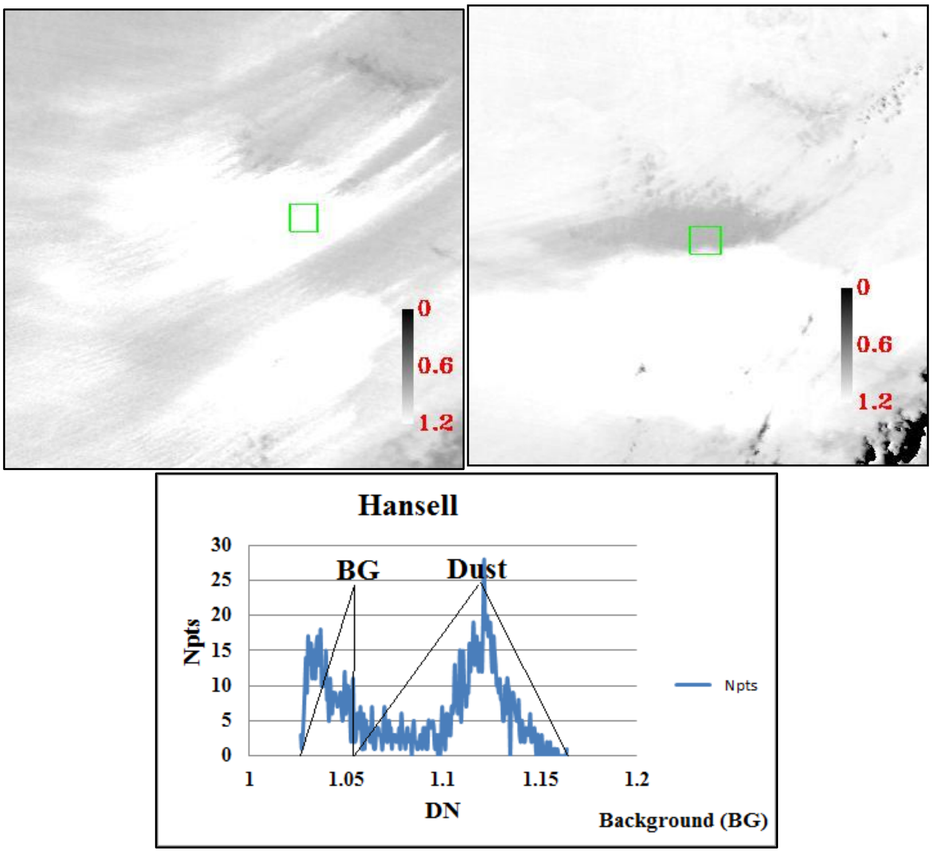


Handley (2004)

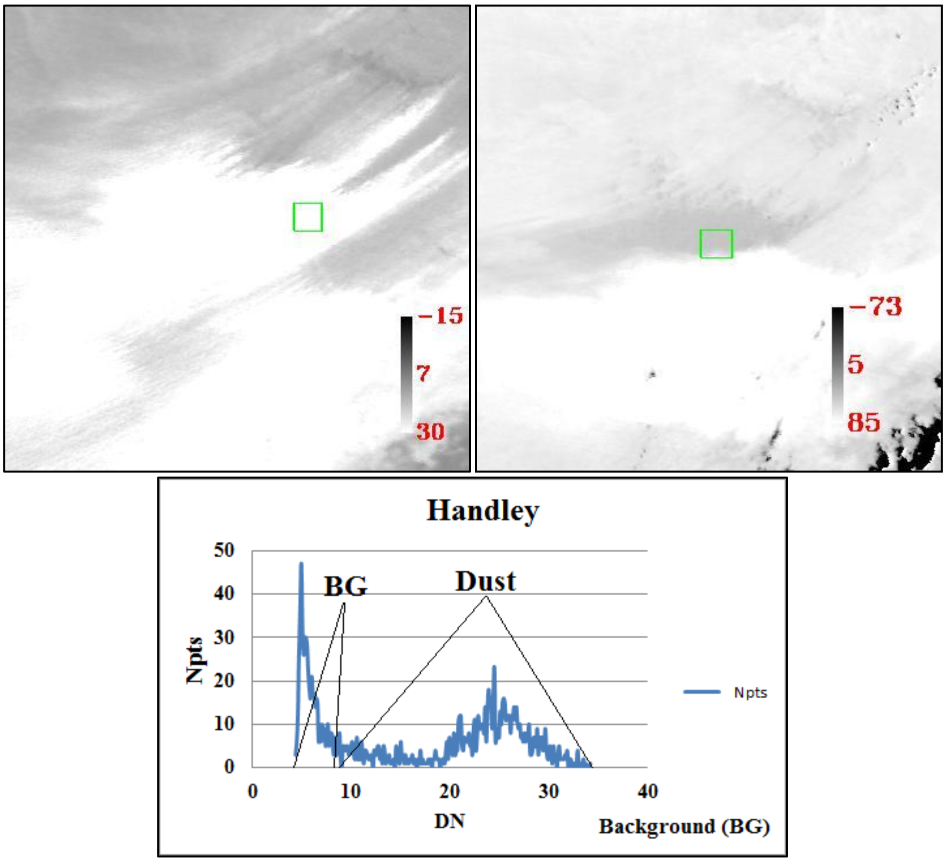

Deep Blue (2003)

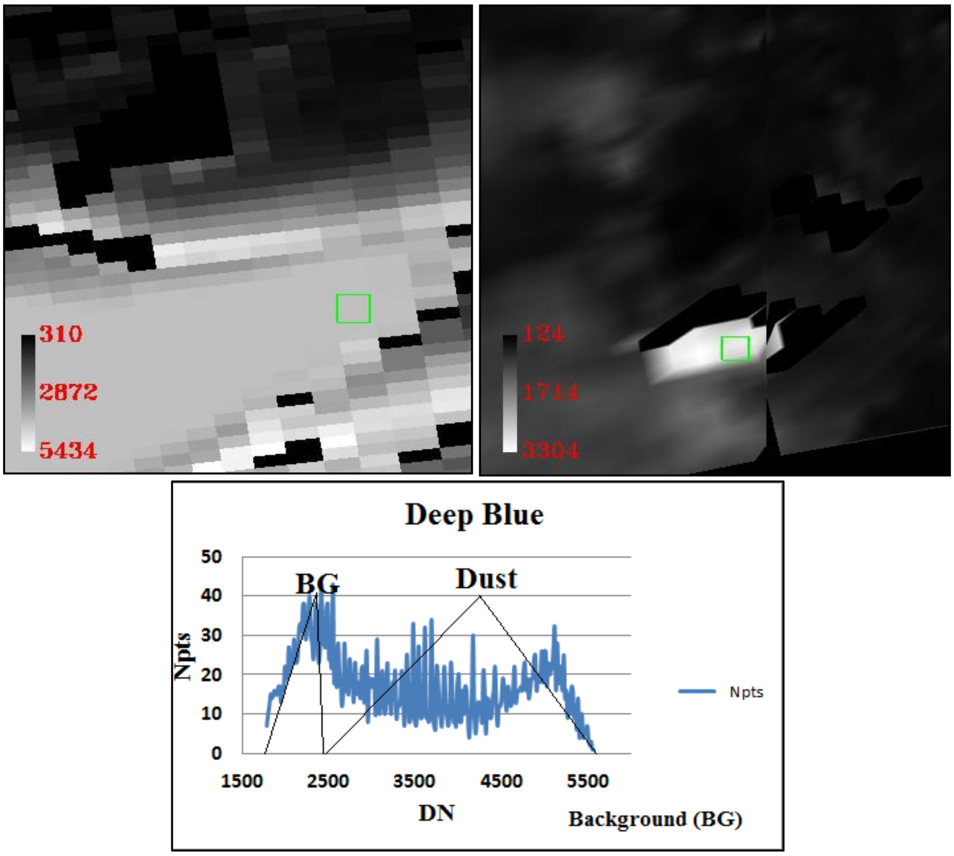


BTD (3.7 µm-12 µm)

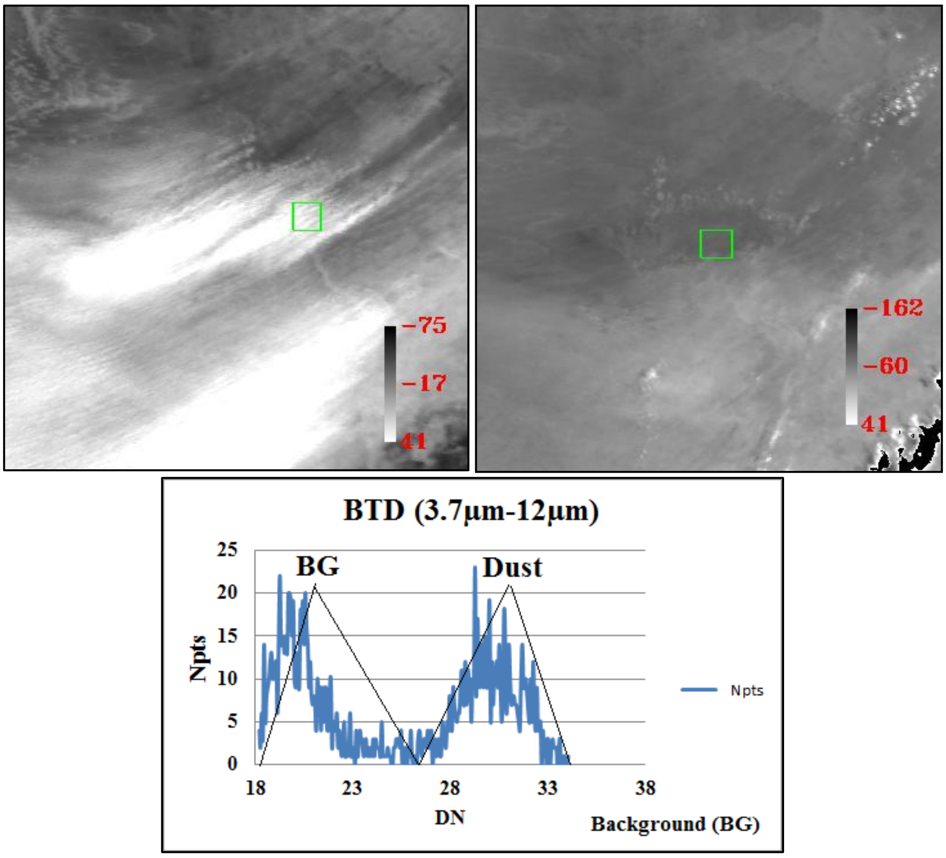

BTD (8.6 µm-11 µm)

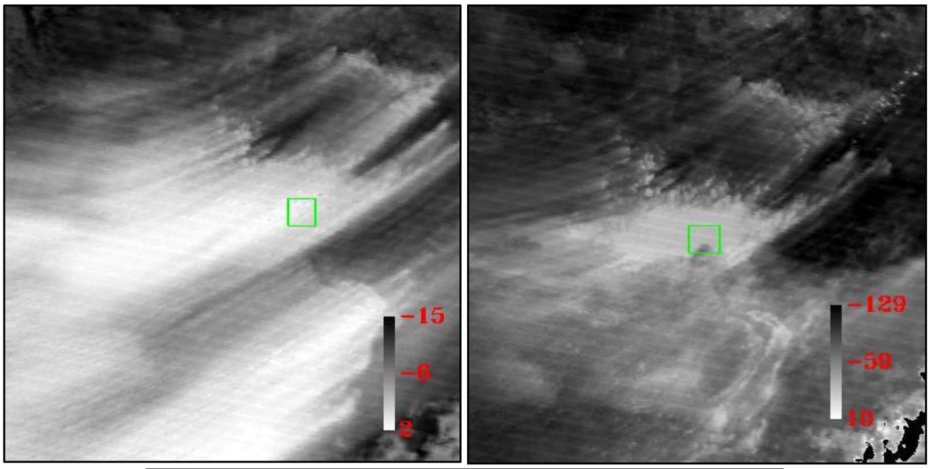


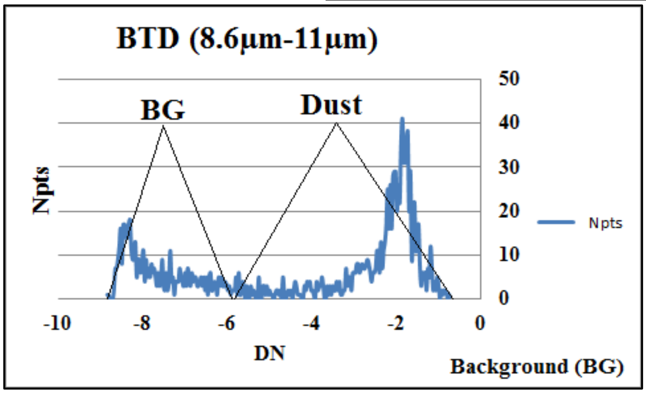


BTD (8.6 µm-12 µm)

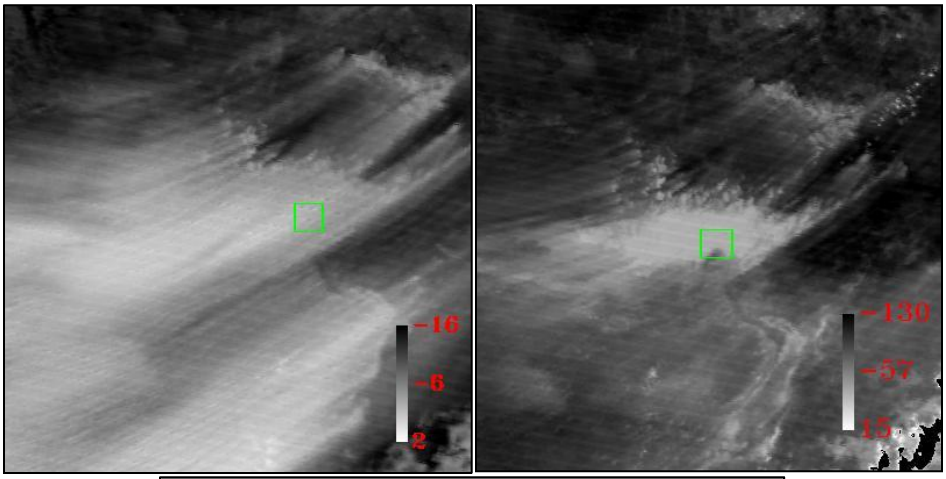


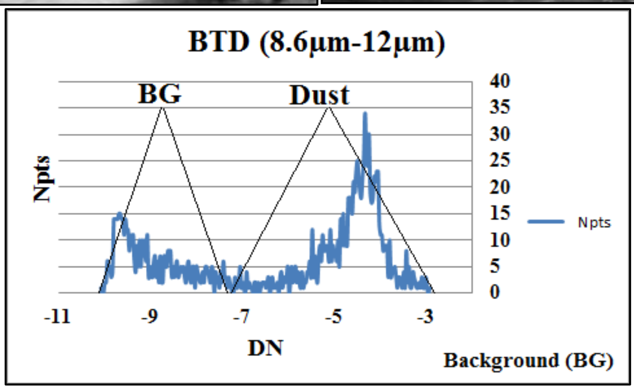

BTD (12 µm-11 µm)

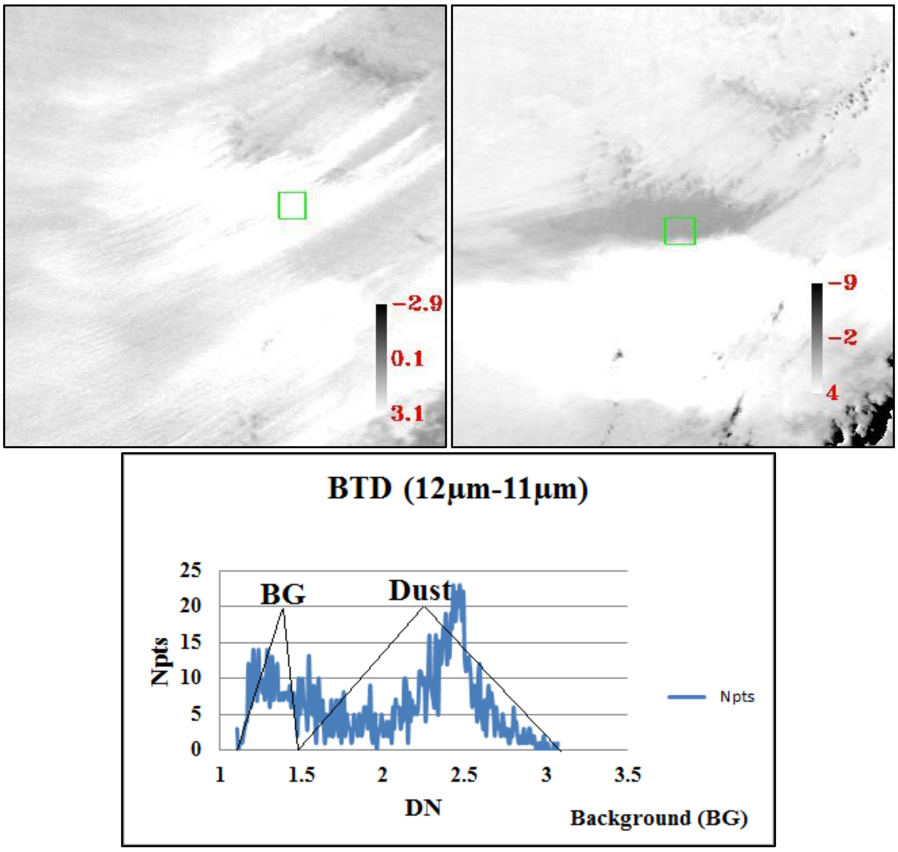


Figure 4.20 Result of applying the M test to the nine selected techniques for the image of Figure 4.19. The M test area has been highlighted by blue squares. The red dots show some of the expected dust sources. Due to difficult to identify area with dust and without dust over the same background in the same image another image has used showing no dust activity over the same area as it shown in Figure 4.19(C). The green square in this image represents the M test area.

### 4.3.6 Causes of Background Effects

Surface emissivity is a measure of inherent efficiency of the surface in converting heat energy into radiant energy above the surface (Sobrino et al., 2001). Land surface emissivity is critical for determining the thermal radiation of the land surface (Caselles et al., 1995). There are several factors can control the emissivity of a surface such as water content, chemical composition, structure, roughness, the wavelength, and the view angel of the sensor (Snyder et al., 1998). Thus these factors are those that have the potential to affect the background in the various dust indices evaluated in this study. In desert environments perhaps the most important factor is the emissivity of the different rock and sediment types that make up the vast majority of the desert surfaces.

Without fieldwork it is hard to determine which of these factors are affecting the different methods. However, in the case of the chemical composition it is possible to look at the spectra of these background materials in order to interpret why each technique gives different results over different backgrounds.

#### 4.3.6.1 The Emissivity of Background Materials

The emissivity of four samples of the different background materials were is selected from the ASTER spectral library (Clarke et al., 1993) is plotted in Figures 4.18. In order to see the emissivity in the MODIS used bands they have been plotted on the spectra, furthermore the emissivity differences for the different split windows employed in this study are also shown, large differences indicate potential geological background effects.

The emissivity of limestone is shown in Figure 4.21 (A). In general the difference in the emissivity at the MODIS wavelengths is relatively small. This is shown by the small differences in emissivity for the different emissivity difference (ED) split windows (Figure 4.21 A). These were calculated after averaging the four spectra of each mineral. Thus the difference in the emissivity of the Limestone at different wavelengths appears to induce no major background affects at the MODIS wavelengths employed here and the observed background effects must be due to other factors.

The emissivity spectra of the four samples of basalt selected from the ASTER spectral library are plotted in Figure 4.21 (B). In general the difference in the emissivity at the used wavelengths is relatively small and similar to limestone, as shown by the small differences in emissivity for the different split windows (Figure 4.21 B). Thus the difference in the emissivity of the Limestone at appears to induce no major background affects at the MODIS wavelengths employed here and other explanations for the background effects are needed.

The emissivity spectra of the four samples of quartz selected from the ASTER spectral library are plotted in Figure 4.21 (C). For the quartz the difference in the emissivity at the ED (8.6 μm-11 μm) and ED (8.6 μm-12 μm) is almost zero and that is agree with the visual result and the M test were the distinguish between the dust and the quartz is clearly displayed. However, the emissivity difference for ED (3.7 µm-11 µm) and ED (3.7 µm-12 µm) is relatively high compared to the rest of ED's and that can potentially explain why they have not got strong contrast between the dust and the sand dunes. Furthermore, this is in agreement with the M test were the contrast between the dust and background is small compared to BTD (8.6 µm-11 µm) and BTD (8.6 µm-12 µm). In contrast ED (12 µm-11 µm) is almost zero but significant background effects are evident. And seem to be due to other factors as the case of the limestone. The emissivity spectra of the four samples of granite selected from the ASTER spectral library are plotted in Figure 4.21 (D) The difference in the emissivity at the ED (3.7 µm-11 µm) and ED (3.7 µm-12 µm) are relatively small. For ED (3.7 µm-11 µm) and ED (3.7 µm-12 µm) the difference in emissivity is almost zero and this agrees with the visual result and the M test were the distinction between the dust and the quartz is clearly displayed.

The emissivity difference for ED (8.6 µm-11 µm) and ED (8.6 µm-12 µm) is relatively high compared to the rest of ED's and could be why they have not got strong contrast between the dust and the sand. This result is in agreement with that of the M test were the contrast between the dust and background is small. Finally, the ED for ED (12 µm-11 µm) is almost zero and the visual result and M test is agreed with this.

The emissivity of diatomite is not provided in the ASTER spectral library. It was thus was measured in King's College London Geography Department using a MIDAC M2000 series FTIR spectrometer with a spectral range from 1.5–15.4 µm. The spectra were acquired using the methods developed by Smith (2008). The emissivity of one sample of Peruvian diatomite is plotted in Figure 4.21 (E). In general the difference in emissivity between the bands is relatively small and appears to induce no major background affects at the MODIS wavelengths employed here and these background effects must be due to other factors.

This analysis of emissivity spectra shows that background effects due to changes in the chemistry of rocks and sediments only explains a small part of the variation seen in the imagery and thus other factors must be at work. These factors can control the emissivity of a surface such as water content; chemical composition, structure, roughness, the wavelength, and the view angel of the sensor include and require further study.

a) Emissivity of the Limestone

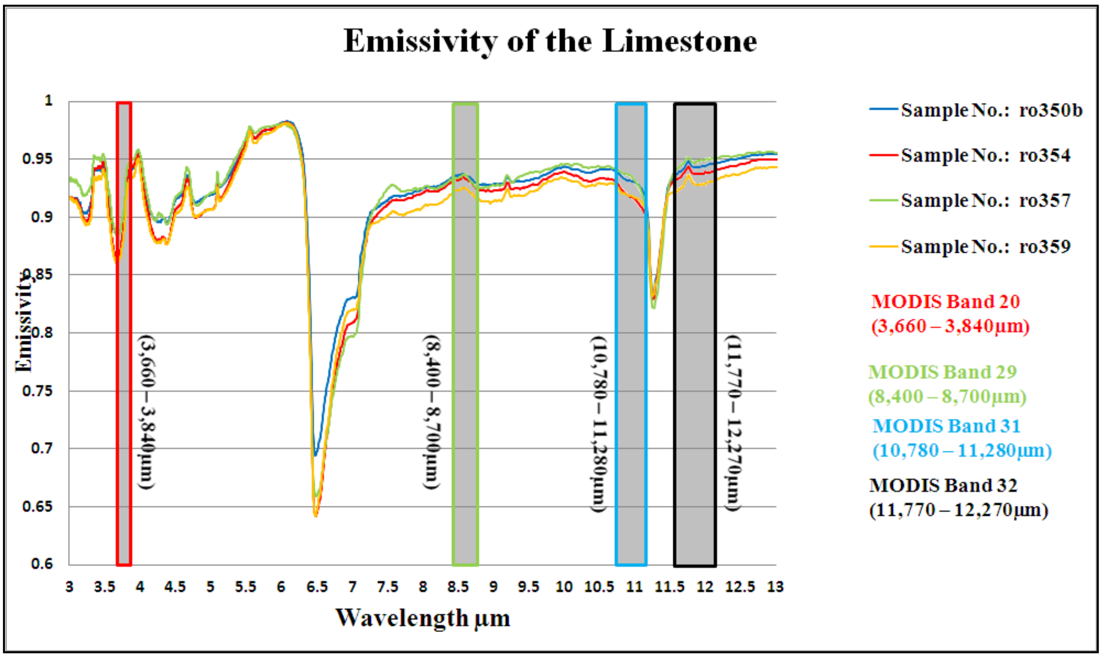


b) Emissivity of the Basalt

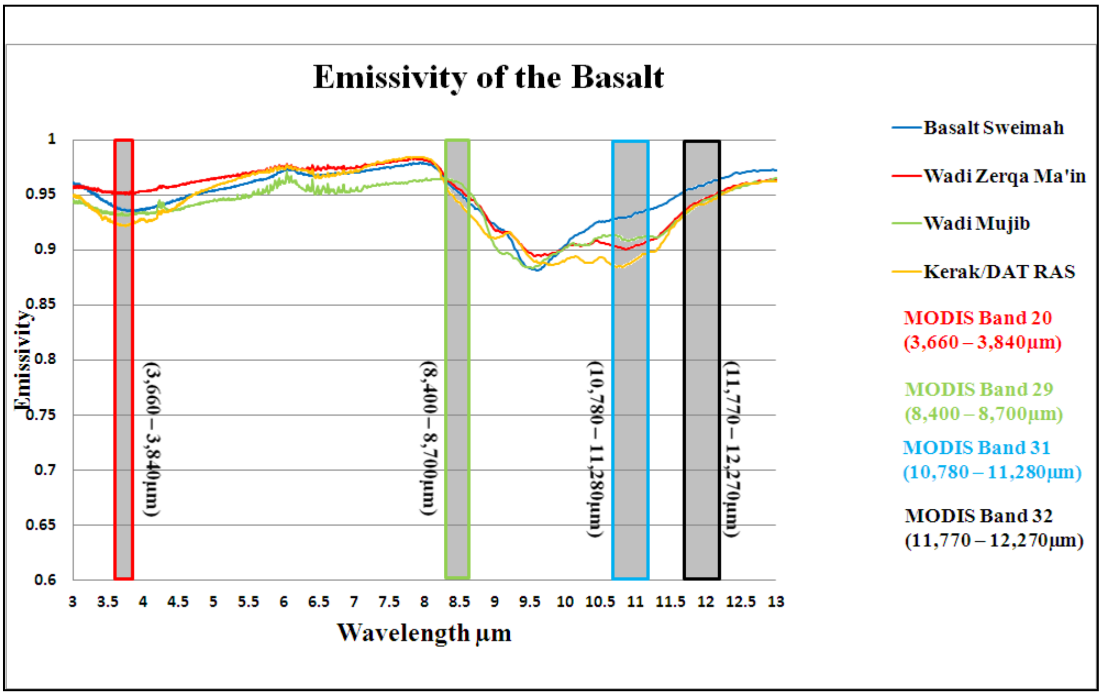

c) Emissivity of the Quartz

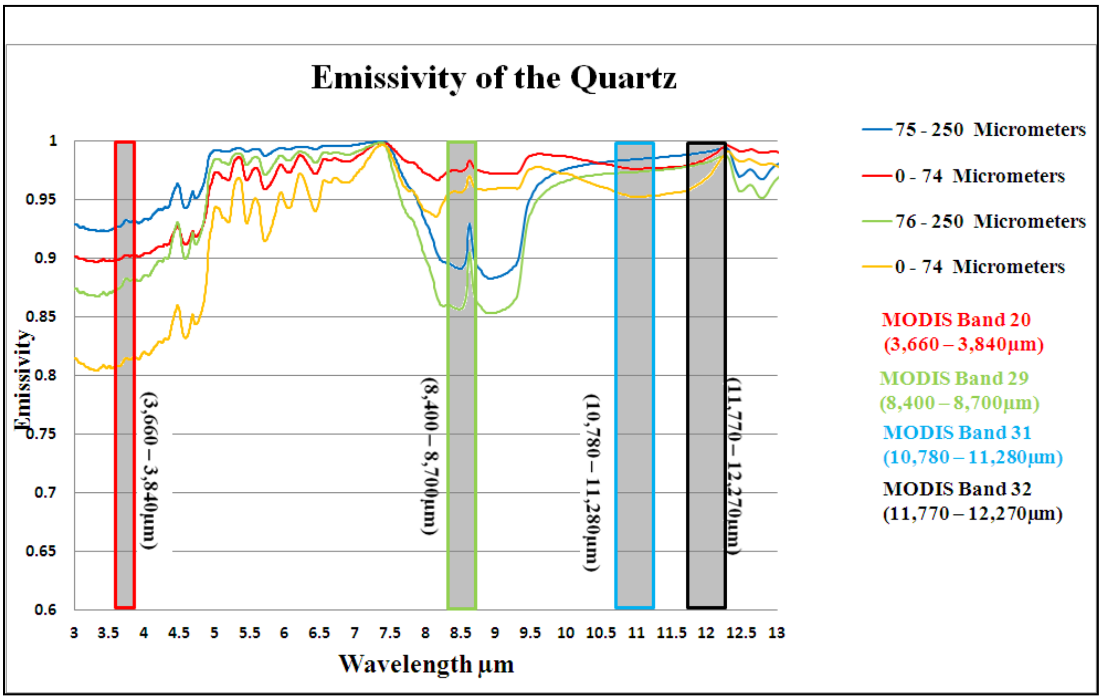


d) Emissivity of the Granite

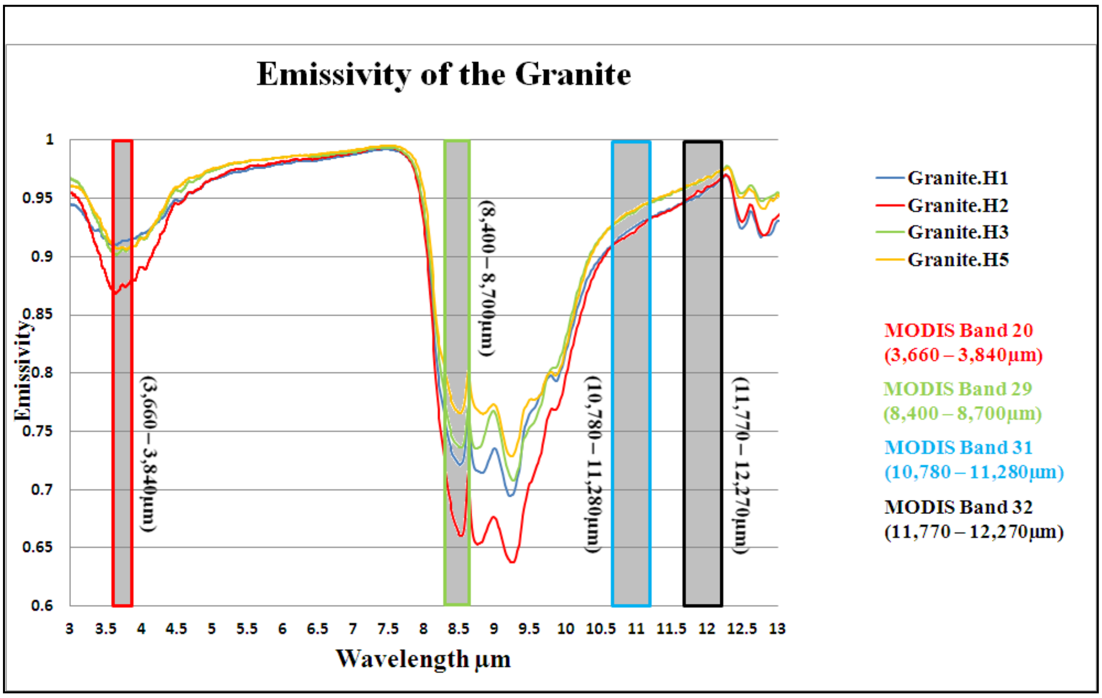

e) Emissivity of the Diatomite

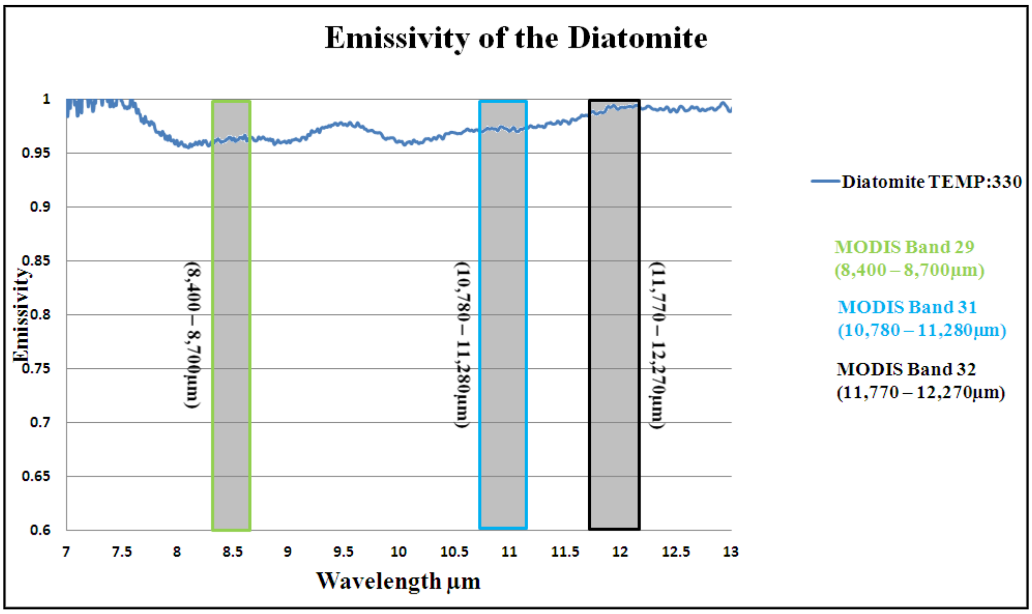


Figure 4.21 Emissivity from 3 to 14 µm of five backgrounds used during this study are displayed her. (a) Four samples of limestone, (b) Four samples of basalt, (c) Four samples of quartz (d) Four samples of granite, and (e) One sample of diatomite. The bandwidth for four used bands from MODIS is plotted on the graph.

In general the emissivity difference was small over all the tested background (Table 4.5) a part from Quartz BTD (3.7 µm-11 µm), BTD (3.7 µm-12 µm) and Granite BTD (8.6 µm-11 µm), BTD (8.6 µm-12 µm) where it was relatively high compared to the other split windows BTD. The correlation between the M test results and the emissivity difference for the five BTD split windows over five tested background show no correlation (Figure 4.22). Thus, the change in the emissivity difference caused by changes in the chemistry of the background does not appear to be the main factor causing the observed background effects.

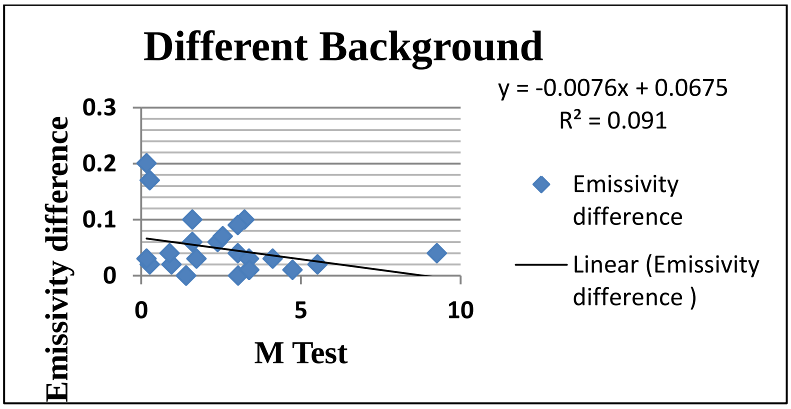


Figure 4.22 Regression between the M test and the emissivity difference for the five tested background.

Table 4.5 Emissivity difference and M test calculated using BTD for five different backgrounds

| Background | BTD | M test | Emissivity difference |
|---|---|---|---|
| Limestone | BTD (3.7 μm-11 μm) | 3.03 | 0.04 |
| Limestone | BTD (3.7 μm-12 μm) | 2.4 | 0.06 |
| Limestone | BTD (8.6 μm-11 μm) | 1.42 | 0.00 |
| Limestone | BTD (8.6 μm-12 μm) | 1.41 | 0.00 |
| Limestone | BTD (11 μm-12 μm) | 3.38 | 0.01 |
| Diatomite | BTD (3.7 μm-11 μm) | 3.03 | 0.09 |
| Diatomite | BTD (3.7 μm-12 μm) | 2.56 | 0.07 |
| Diatomite | BTD (8.6 μm-11 μm) | 0.96 | 0.02 |
| Diatomite | BTD (8.6 μm-12 μm) | 0.90 | 0.04 |
| Diatomite | BTD (11 μm-12 μm) | 3.39 | 0.01 |
| Basalt | BTD (3.7 μm-11 μm) | 5.53 | 0.02 |
| Basalt | BTD (3.7 μm-12 μm) | 4.75 | 0.01 |
| Basalt | BTD (8.6 μm-11 μm) | 4.12 | 0.03 |
| Basalt | BTD (8.6 μm-12 μm) | 3.04 | 0.00 |
| Basalt | BTD (11 μm-12 μm) | 9.27 | 0.04 |
| Quartz | BTD (3.7 μm-11 μm) | 3.24 | 0.10 |
| Quartz | BTD (3.7 μm-12 μm) | 1.61 | 0.10 |
| Quartz | BTD (8.6 μm-11 μm) | 0.27 | 0.02 |
| Quartz | BTD (8.6 μm-12 μm) | 0.17 | 0.03 |
| Quartz | BTD (11 μm-12 μm) | 3.38 | 0.01 |
| Granite | BTD (3.7 μm-11 μm) | 1.74 | 0.03 |
| Granite | BTD (3.7 μm-12 μm) | 1.61 | 0.06 |
| Granite | BTD (8.6 μm-11 μm) | 0.27 | 0.17 |
| Granite | BTD (8.6 μm-12 μm) | 0.17 | 0.20 |
| Granite | BTD (11 μm-12 μm) | 3.38 | 0.03 |

## 4.4 Statistical Results

Table 4.6 shows the results of the statistical tests that were applied to each index and its corresponding AOT. By considering a single site background effects are constant and the ability of the indices to measure dust concentration is evaluated.

The RMS error measures the difference between each index and the AERONET AOT value (Table 4.6). Deep Blue (2003) has got 28% error and that matches very well the result achieved by Hsu et al., (2003) who shows that the aerosol optical thickness derived from the Deep Blue algorithm are within 20% to 30% of the AOT derived from different sun-photometer stations from the AERONET. The error of the other methods is considerably higher, Ackerman (1989), BTD (8.6 µm-11 µm), BTD (8.6 µm-11 µm), BTD (3.7 µm-12 µm) have got ~50% error. Hansell et al., (2007), Handley (2004), and BTD (12 µm-11 µm) exhibit a very big error (~100%).

The P-value of the KST test indicates that the dust indices and the AOT from the AERONET are all normally distributed (Table 4.6) all of the P-values of the tested techniques are less than 5% thus the data is not different from a cumulative normal distribution with 95% confidence.

Table 4.6 Statistical test results from analysis of the sixteen MODIS images

| **Techniques** | P-value of KST | RMS | $R^2$ | SLOPE |
|---|---|---|---|---|
| Ackerman (1989) | 0.64 | 0.53 | 0.714 | 0.8451 |
| Miller (2003) | 0.96 | 0.69 | 0.556 | 0.7458 |
| Hansell et al., (2007) | 0.91 | 1.46 | 0.022 | 0.1493 |
| Handley (2004) | 0.82 | 1.27 | 0.018 | 0.1365 |
| Deep Blue (2003) | 0.55 | 0.28 | 0.913 | 0.9556 |
| BTD (3.7 µm-12 µm) | 0.24 | 0.56 | 0.687 | 0.8288 |
| BTD (8.6 µm-11 µm) | 0.75 | 0.51 | 0.735 | 0.8578 |
| BTD (8.6 µm-12 µm) | 0.60 | 0.55 | 0.699 | 0.8362 |
| BTD (11 µm-12 µm) | 0.74 | 1.49 | 0.0366 | 0.1914 |

KST: Kolmogorov-Smirnov Test
RMS: Root Mean Square Error

The correlation between each of the nine selected techniques and the AOT values at the Banizoumbou station has also been calculated to determine the strength of the relationship between each dust index and AOT (Table 4.6). The scatter grams are shown in Figure 4.23. Table 4.6 also summarizes the slope of the relationships between the two variables in order to see if the rate of change between them is similar as the dust concentration increases.

Ackerman (1989)

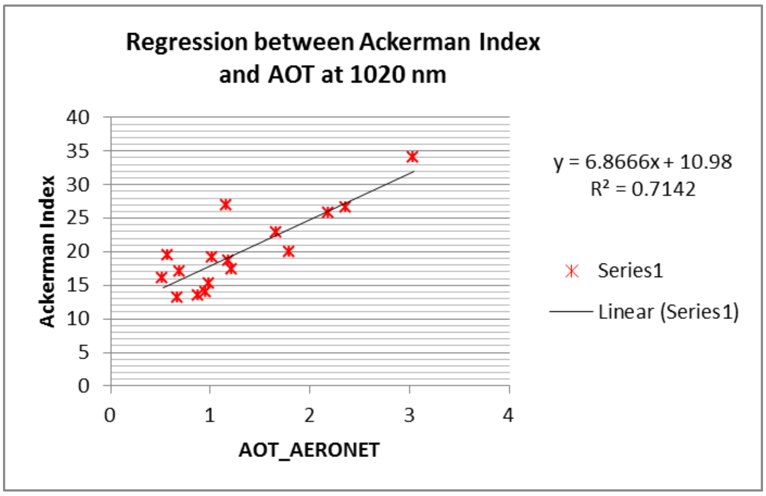


Miller (2003)

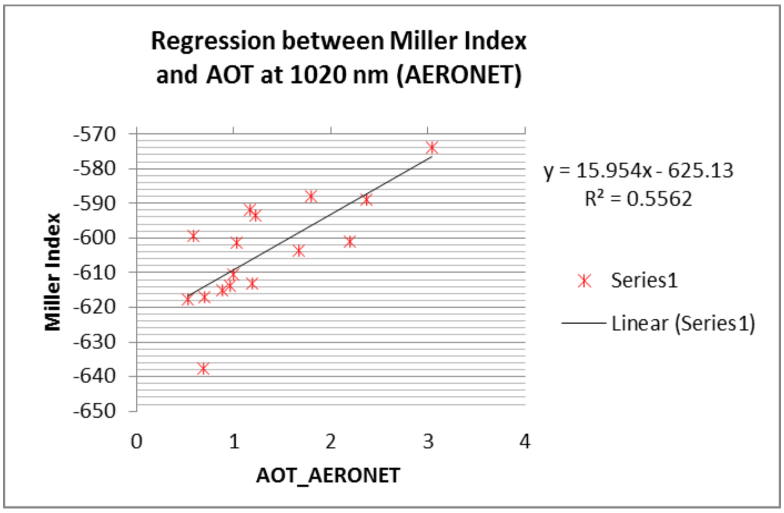


Hansell et al., (2007)

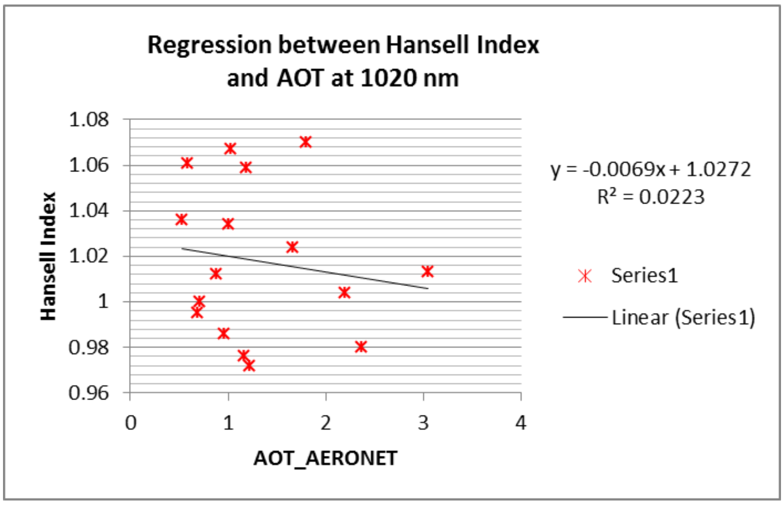

Handley (2004)

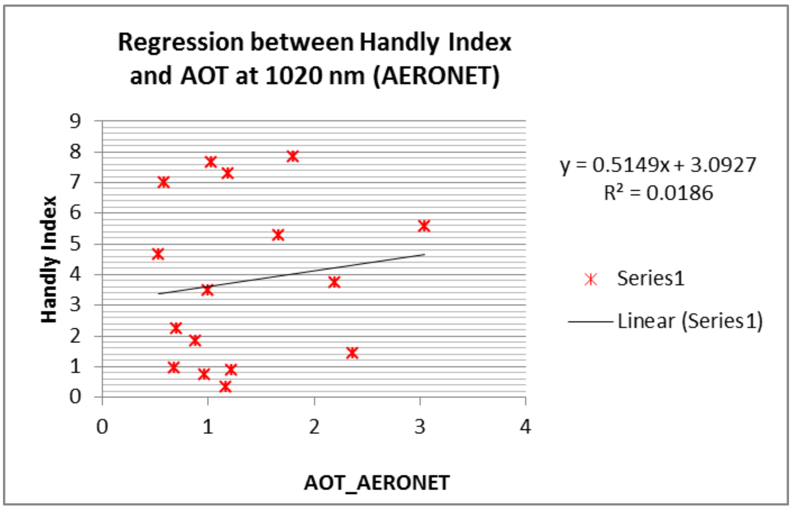


Deep Blue (2003)

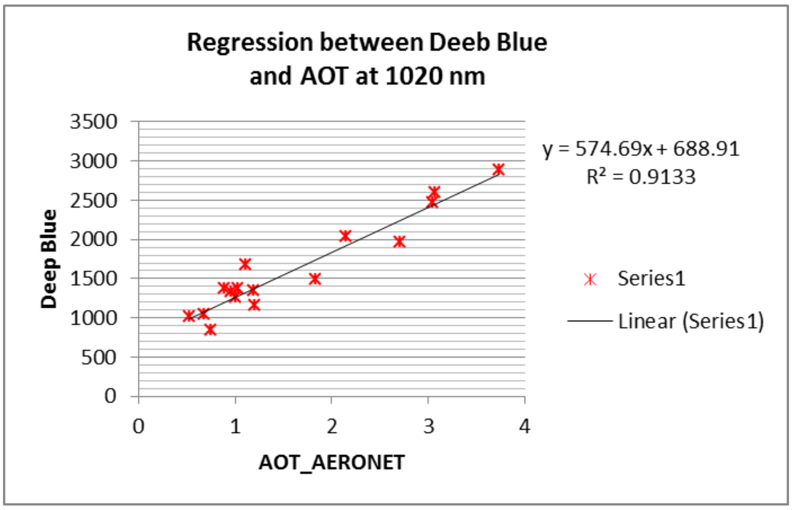


BTD (3.7 µm-12 µm)

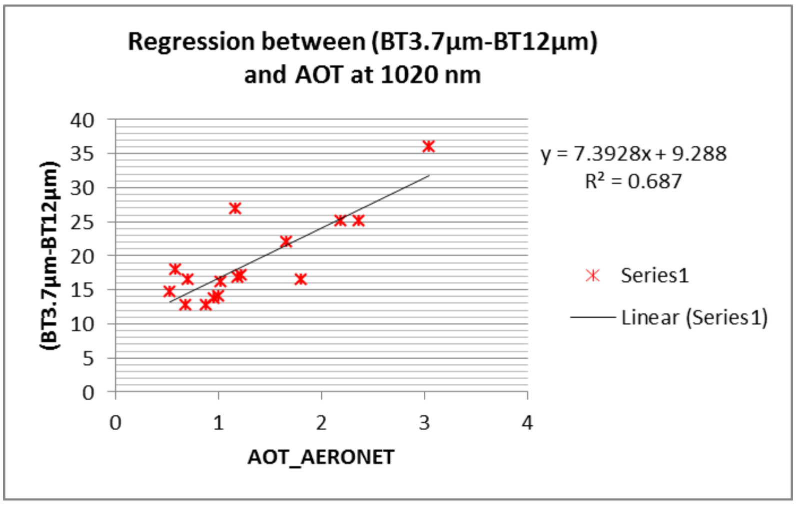

BTD (8.6 µm-11 µm)

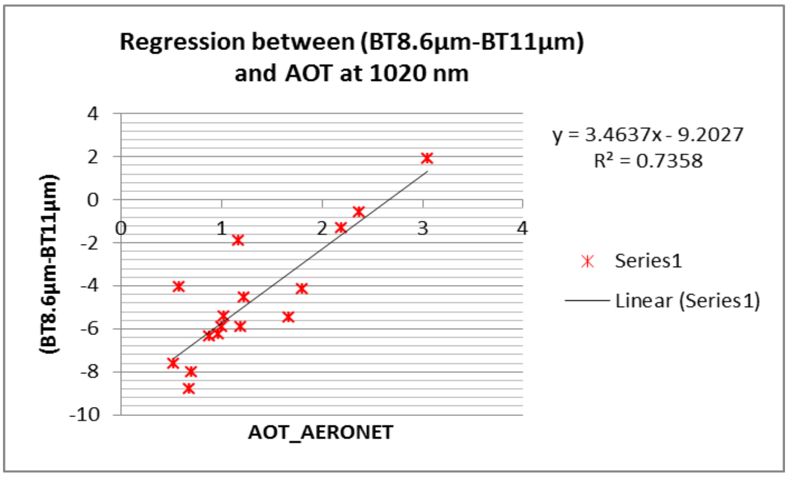


BTD (8.6 µm-12 µm)

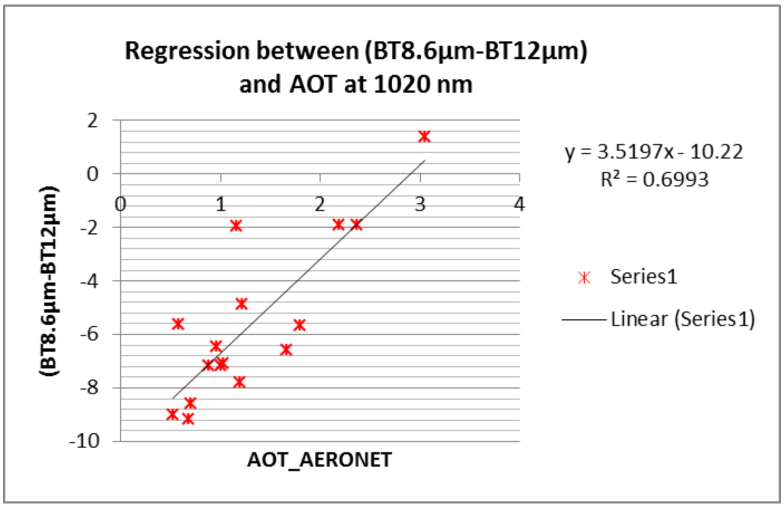


BTD (12 µm-11 µm)

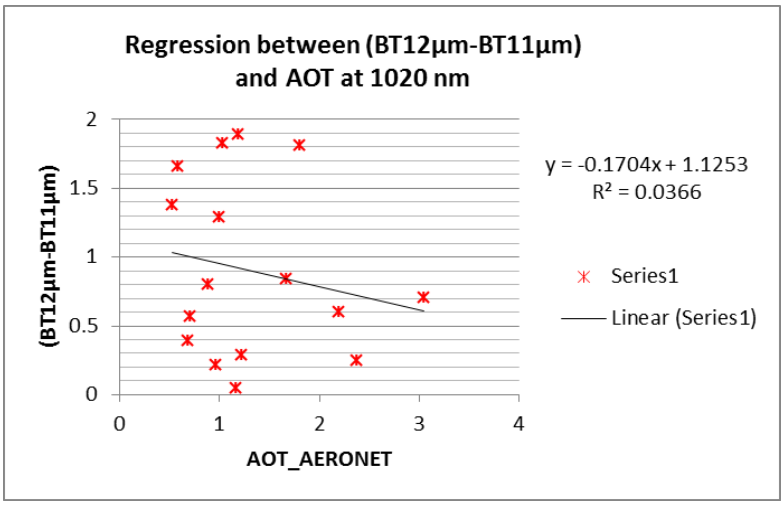


Figure 4.23 Regression between the nine dust indices calculated from the sixteen MODIS images and the AOT from the Banizoumbou AERONET station.

Deep Blue (2003) has got the highest correlation with the AOT ($R^2$ =0.91). Hsu et al., (2003) also found the AOT of Deep Blue and the AOT from the AERONET shows good agreement, however they do not provide the $R^2$ value. BTD (8.6 µm-11 µm), Ackerman (1989), BTD (8.6 µm-12 µm), and BTD (3.7 µm-12 µm) have got similar correlation to each other with $R^2$ values of ~0.7. Miller (2003) has got a slightly lower correlation $R^2$ =0.55. However, Hansell et al., (2007), Handley (2004), and BTD (12 µm-11 µm) have no correlation with the AOT values. Table 4.6 shows that there is very good agreement between RMS, $R^2$ and slope. Based on that agreement, Deep Blue (2003) is the highest in the rank followed by BTD (8.6 µm-11 µm)**.** Ackerman (1989) is in the third place and BTD (8.6 µm-12 µm), BTD (3.7 µm-12 µm), and Miller (2003) are listed in the fourth, fifth and sixth respectively.

Handley (2004), Hansell et al., (2007), and BTD (12 µm-11 µm) are in the bottom of the list and no significant correspondence can be noted statistically between the values of these indices and the AOT.

The reason for the poor correlation for Hansell et al., (2007) and Handley (2004) appears to be because both of the techniques have used the BTD (12 µm-11 µm) split window. It is shown in Table 4.6 that the BTD (12 µm-11 µm) split window exhibits the lowest correlation. The Miller (2003) method also uses the BTD (12 µm-11 µm) split window but weights it and the weight of the window is not strong when added to the other parameters employed in his approach. In contrast as Hansell et al., (2007) and Handley (2004) have divided and multiplied the BTD (12 µm-11 µm) split window in their techniques and this gives quite a strong weight to the result and appears to be the main cause of their poor performance.

## 4.5 Evaluating Different Colour Composites

Colour composites are useful for detecting dust and have been developed for SEVIRI data as reviewed in chapter 2, section 2.3.3.2.9. Such a method of depicting dust in imagery has the potential to be useful for dust source mapping and may be better than looking at a single grey scale image of an index. The SEVIRI colour composite employs BTD (12 µm-11 µm) on the red colour gun as a way of depicting the cloud, BTD (11 µm-8.6 µm) on the green colour gun in order to detect dust and the 11 micron band on the blue colour gun to detect the cirrus cloud. In order to test its usefulness of this approach all the dust indexes evaluated in this thesis are combined into the colour composite by displaying them on the green band that is used to depict dust over Cyrenaica (Figure 4.24).

The resultant image is then interpreted in order to assess their utility for mapping dust sources (Figure 4.25).

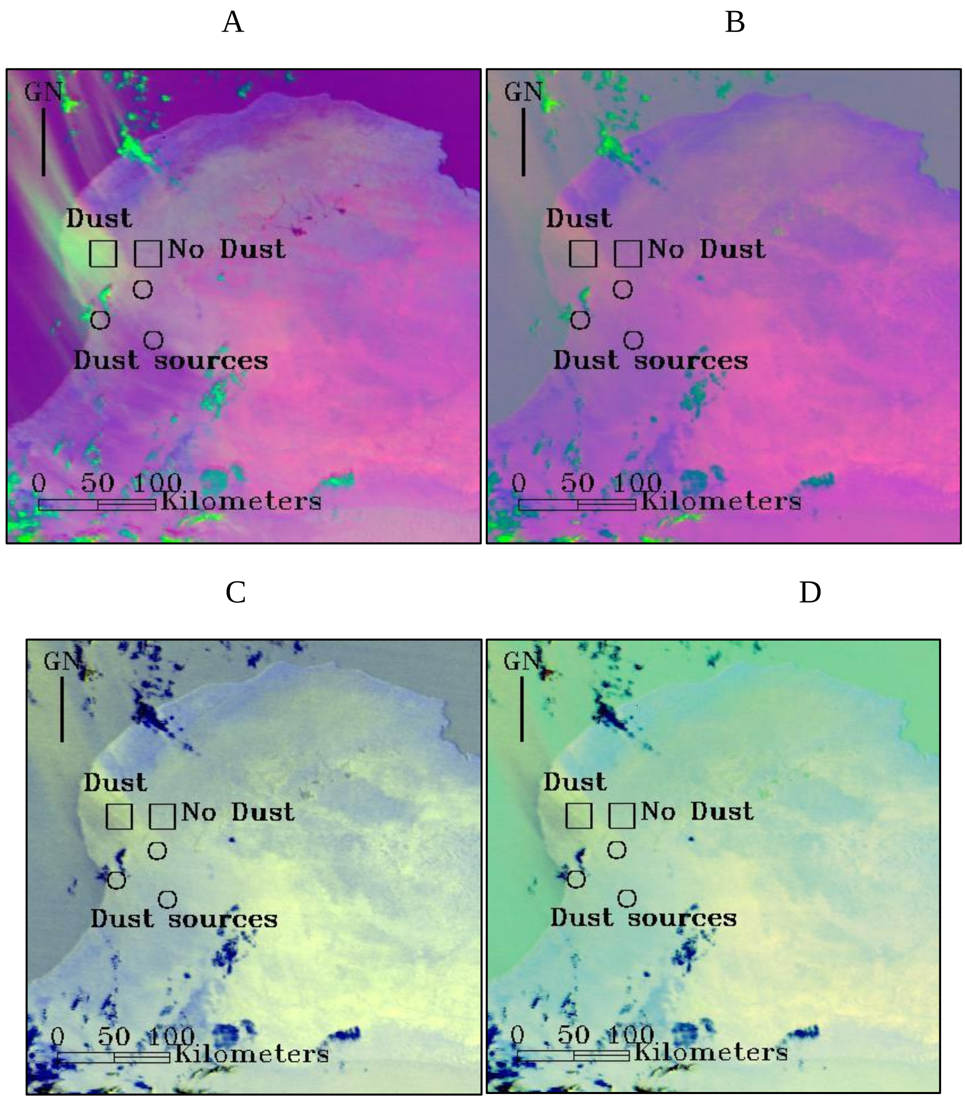

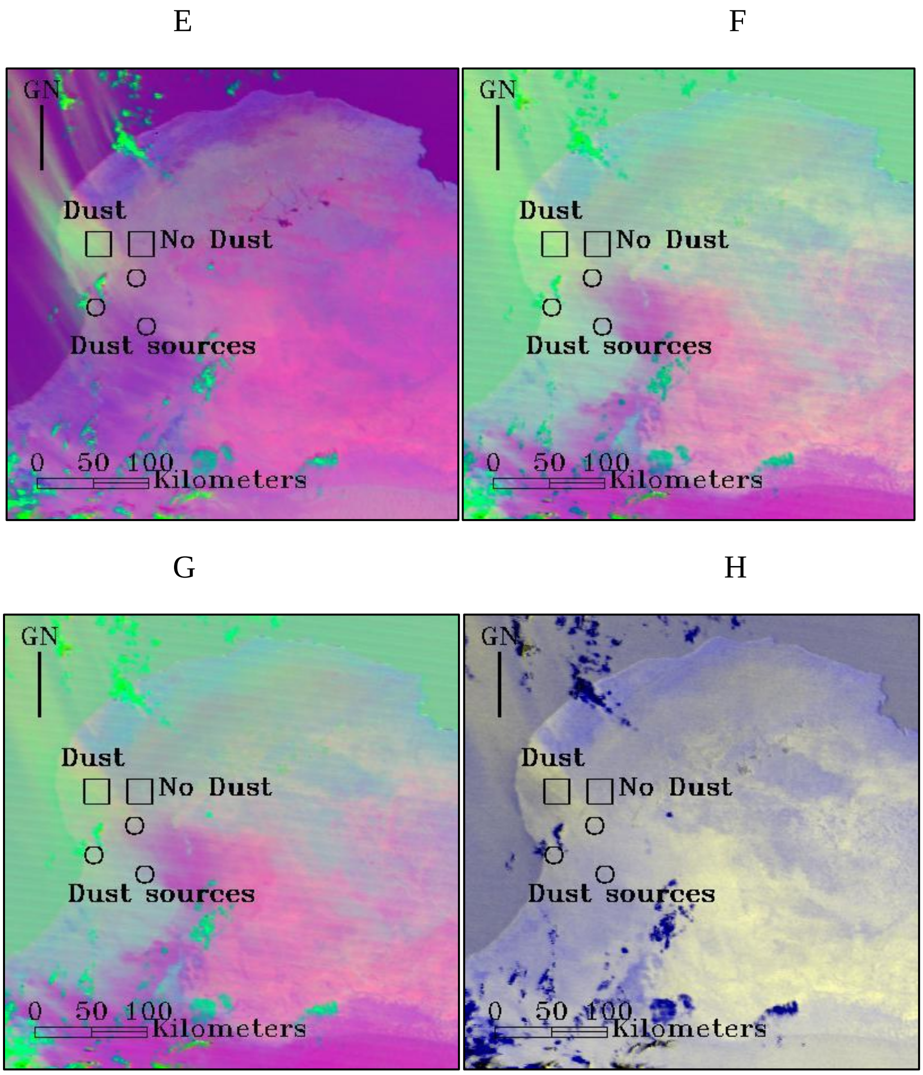


Figure 4.24 Presentation of SEVIRI colour composite type images using MODIS data. The SEVIRI colour composite (RGB) differ by replacing G band which is sensitive to the dust with (A) Ackerman, (B) Miller, (C) Hansell, (D), Handly, (E), BTD (3.7 µm-12 µm), (F) BTD (8.6 µm-11 µm), (G) BTD (8.6 µm-12 µm), and (H) BTD (12 µm-11 µm).over Cyrenaica.

Ackerman and BTD (3.7 µm-12 µm) shows the best colour composite result and quite similar to the SEVIRI colour composite result. The SEVIRI colour composite (RGB) scheme is used after replacing the G band by the eight tested indices in order to test the ability of the tested dust indices to detect dust using the SEVIRI colour composite. The Deep Blue is not used her because it has different pixel resolution and cannot be combined with the other data.

After selecting Ackerman to detect the dust sources over Cyrenaica, we tested the ability of the Ackermann (1989) split window to identify dust in the SEVIRI colour composites over different backgrounds. The five MODIS images used for M test were employed in this regard. Figure 4.25 show the SEVIRI colour composite in general gives better contrast between the dust and the background than the modified colour composite for all but one of the study areas. However replacing the green band with Ackerman (1989) over Limestone background improves the contrast between the dust and the background compared to the SEVIRI colour composite. Thus it is clear that the optimum method for each type of background can be used in a SEVIRI type colour composite to help map the location of dust sources.

R: 12 µm-11 µm, G: 11 µm-8.5 µm, B: 11 µm    R: 12 µm-11 µm, G: Ackerman, B: 11 µm

A

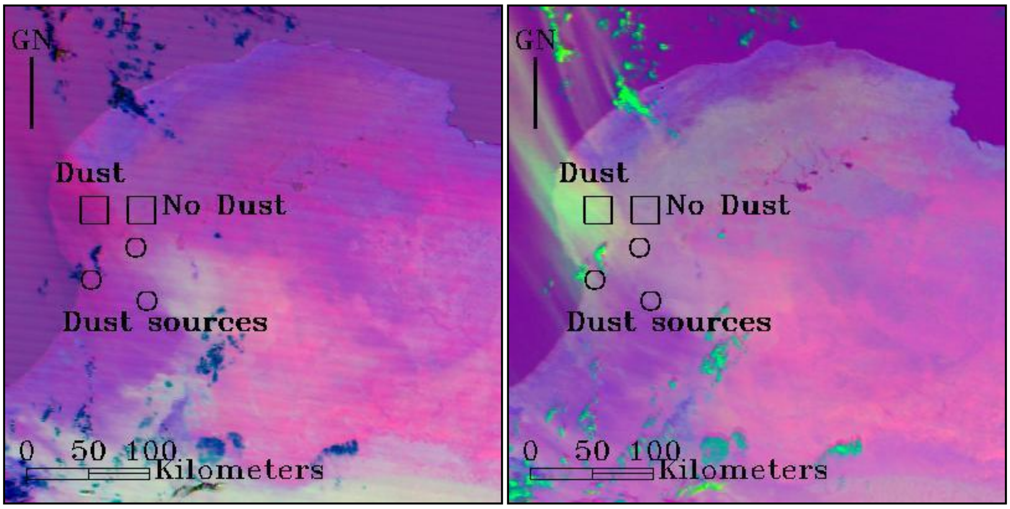


B

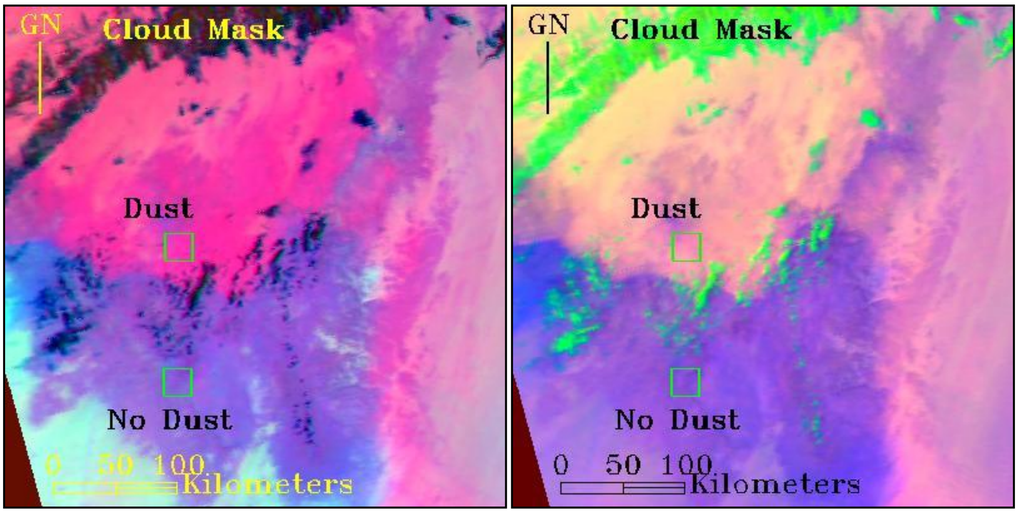

C

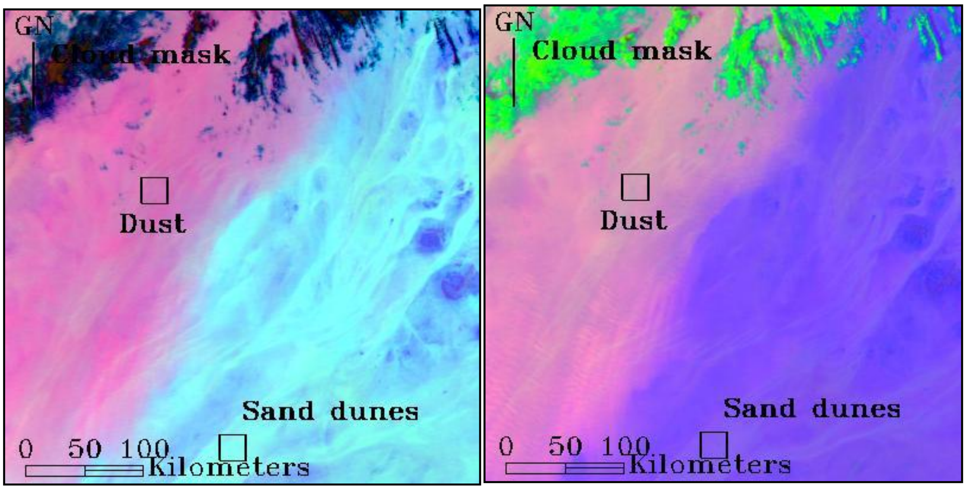


D

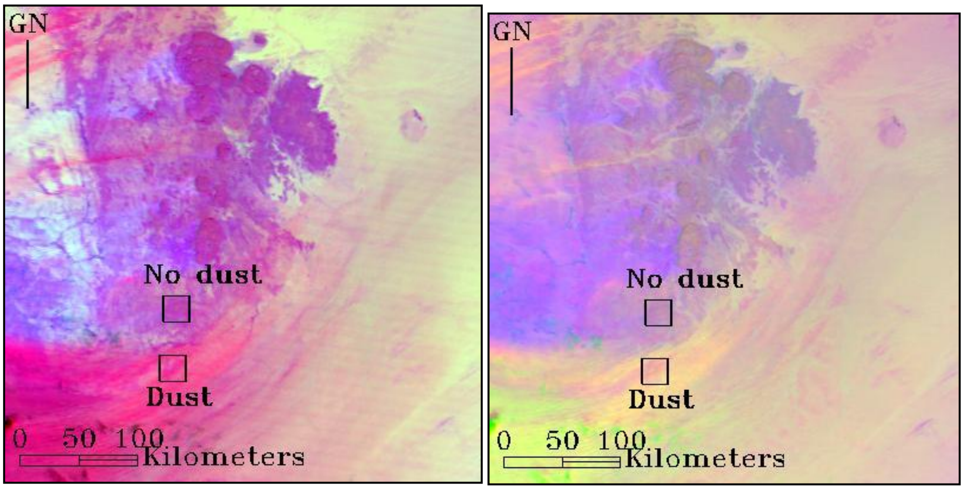


E

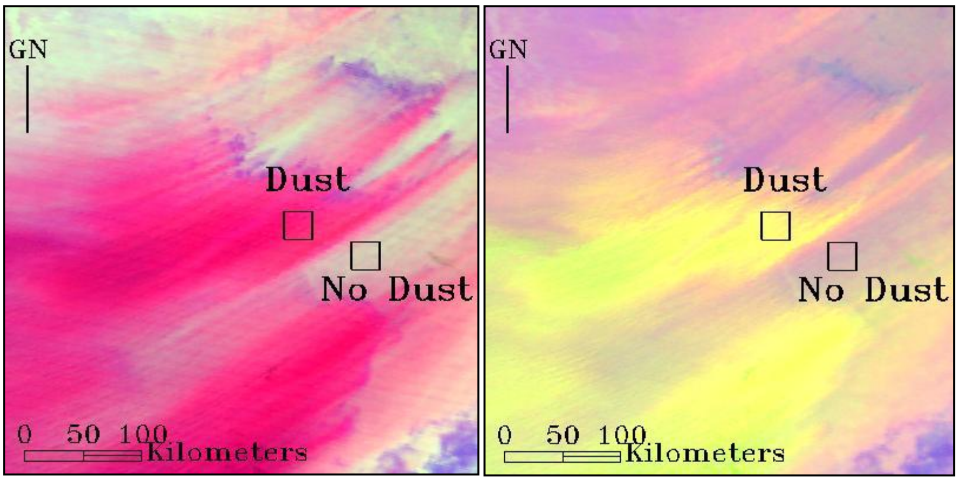


Figure 4.25 Presentation of SEVIRI colour composite type images using MODIS data. The SEVIRI colour composite (RGB) differ by replacing G band which is sensitive to the dust with Ackerman (1989) over five tested backgrounds. (A) Limestone, (B) Basalt, (C) Quartz (D) Granite, and (E) Diatomite.

## 4.6 Discussion and Conclusion

Visual analysis of the different dust indices suggests that they exhibit different performances in different regions. These discrepancies appear to be related to the different geological and geomorphologic background materials and specifically the way they absorb and reflect visible and infrared radiation. These background effects were evaluated by implementing the M statistic.

The median of the M test over five different types of background (Table 4.4) indicates that Deep Blue (2003) exhibits the most contrast followed by Miller (2003). Ackerman (1989), BTD (3.7 µm-12 µm) Handley (2004), Hansell et al., (2007), and BTD (12 µm-11 µm) that have all got similar mean values and perform reasonably well. However, BTD (8.6 µm-11 µm) and BTD (8.6 µm-12 µm) have got a low median M statistic and thus seem to perform poorly over most backgrounds. Notwithstanding this the type of background was found to have a significant effect on the utility of the different indices in different areas. The M test was high in general over the Basalt and the Quartz, presumably because both are dark, absorbing the most of radiation and only a small amount radiation is reflected back to the space. In contrast the dust layer is much brighter than the background and so can be easily detected. Over light backgrounds such as limestone the M statistic was much lower for all indices because both the background and the dust were bright.

The dust index histograms generally agree with M and the visual interpretation, showing two distinct modes with good separation when contrast is high and commonly a single mode when it is low. Deep Blue shows the high contrast over all backgrounds according to the M value, however, visual interpretation of the imagery is usually extremely difficult and due to the low spatial dust sources are rarely evident. Furthermore, deep blue seems to detect dust in dust free imagery.

Other methods show more variations over different backgrounds. Over the Limestone background, Ackerman (1989) is the best method to detect the dust. Over the basalt background, BTD (12 µm-11 µm) is the best method. Miller (2003) has got the best result over the quartz background. BTD (12 µm-11 µm) is the best method over the granite. Ackerman (1989) is the best method to detect the dust over the diatomite background.

The visual result of the free dust images from applying the 9 techniques over 5 tested background indicate that Handley (2004), Hansell et al., (2007), and BTD (12 µm-11 µm) shows high values over all the tested background apart from the basalt background. However, BTD (8.6 µm-11 µm) and BTD (8.6 µm-12 µm) shows high values over all the tested background apart from the quartz background. Deep Blue (2003) also has got high values over most of the tested background in the dust free image. Furthermore, Ackerman (1989), Miller (2003), and BTD (3.7 µm-12 µm) perform well over the free dust images supporting the use of these techniques.

In order to understand and interpret the M test results, the emissivity of the five different tested backgrounds where presented and discussed. In general the similarity between the emissivity difference for the five tested BTD split windows and the M test was negligible indicating that the emissivity difference does not explain the M test result and other factors need to be evaluated.

The statistical analysis of the relationship between these indices and AOT suggested that Deep Blue has got the highest correlation $R^2 = 0.91$ and support by the result from Hsu et al., (2003) were the AOT of Deep Blue and the AOT from the AERONET shows good agreement.

When the results of M and the statistical comparison to AOT are compared to each other it is evident that Deep Blue (2003) performs well in both the statistical and M analysis. However, it visual interpretation shows it is no good for detecting dust sources, primarily because of the low spatial resolution and the poor accuracy of the cloud mask which usually masks out most of the dust. The rest of the techniques are not as good in terms of correlation with AOT and contrast but many clearly show dust sources over most backgrounds. BTD (8.6 µm-11 µm) and BTD (8.6 µm-12 µm) are the second and the fourth best according to the statistical comparison with AOT, $R^2 = 0.73$ and $R^2 = 0.69$ respectively. However the M results and visual results disagree with the $R^2$ results. Indeed those methods that on average have good contrast with the background appear to have the lowest correlation with AOT and vice versa. This indicates that some methods are good at discriminating dust from background but not the amount of dust, whilst others are good at determining dust concentrations. For example Handley (2004) and Hansell et al., (2007) have not got any significant statistical relationships to AOT, however their mean M test was in the middle compared to the other techniques, BTD (12 µm-11 µm) has got very low correlation and RMS but the mean M test result is good, being the third highest on average being brought down by the low contrast over Limestone and the Quartz.

Some methods offer a compromise. Ackerman (1989) is in third position according to the statistical results and has got the fourth position according to the mean M result. BTD (3.7 µm-12 µm) is in the fifth level statistically and in the seventh level in the M test. Miller (2003) is in the sixth level statistically with $R^2$=0.5 but the mean of the M test is high providing the second highest result after Deep Blue.

In summary it is evident that there is a variable relationship between these indices and AOT as well as their ability to work over different backgrounds. Deep Blue performs well in both cases but has a low spatial resolution and thus is not very good for defining dust point sources. Furthermore, the cloud mask applied to Deep Blue performs poorly, consistently masking out dust instead of cloud. For these reasons it cannot be used to define dust sources.  The only method with similar high average values of M is BTD (11 µm-12 µm), Handley and Hansell. Ironically these methods have the lowest correlations and highest RMS error, suggesting that though they may be good for detecting dust by discriminating it from the background, but increasing values of the index are not well related to higher dust concentrations. Finally some methods offer a compromise solution with a reasonable ability to detect dust over most backgrounds and quite good correlations with AOT

This suggests that if the aim of a research project is to both detect sources and monitor concentrations then specific methods need to be applied to specific backgrounds, such as Ackerman or Miller over Limestone backgrounds. However, if the research needs to look over large areas that contain different backgrounds then a compromise method is needed and a good option here would be BTD (8.6 µm-11 µm).

Ackerman (1989) provides a good tradeoff between contrast with the background and accuracy of dust detection. It has got the third highest correlation ($R^2$ = 0.71) after Deep Blue ($R^2$ = 0.91) and BTD (8.6 µm-11 µm) ($R^2$=0.73) and visually provides reasonable contrast between the dust and the background over most of the tested backgrounds, and is particularly good over limestone. Thus the technique will be used in the following chapter to evaluate the dust sources over Cyrenaica 2008 is Ackerman (1989) is this region has a predominantly limestone background.

The colour composite comparison using MODIS data based on similar to SEVIRI colour composite (RGB) done by replacing the G band by the tested techniques apart from Deep Blue, shows Ackerman has got the best colour composite result and quite similar to SEVIRI colour composite. Moreover, Ackerman colour composite is tested over all tested background and provides good result.

# 5. Evaluating Dust Sources in Cyrenaica: Background and Methods

## 5.1 Aims and Objectives

Cyrenaica north east of Libya is selected to use the methods found to be effective in Chapter 4 to evaluate the dust sources. No previous study have provided detailed information about the nature of the dust sources in Cyrenaica that has been recently recognized by Schepanski et al., (2007).

The objectives of this chapter are to:

- Provide a geological and geomorphologic review of the area
- Evaluate the Ackerman (1989) method for detecting dust sources in Cyrenaica
- Integrate SEVIRI with MODIS data to evaluate their synergy and ability to enhance the detection of dust.
- Use high resolution images to determine the geomorphology and landuse of the sources identified by SEVIRI and MODIS. This will be achieved using Landsat ETM colour composites and NDVI, the Shuttle Radar Topography Mission (SRTM) digital elevation model (DEM) and Google Earth.
- Analyze the geomorphology and grain size of selected dust sources in the field

The region of North east of Libya chosen for study is shown in Figure 5.1 and covers 160,000 km$^2$. It is selected because Schepanski et al., (2007) showed that N-E Libya is important source of dust, however, no other study has ever suggested that it is (Chapter 1) and thus the source requires investigation as does the nature of any sources detected. Finally parts of the region could be accessed for site survey and collection for some samples.

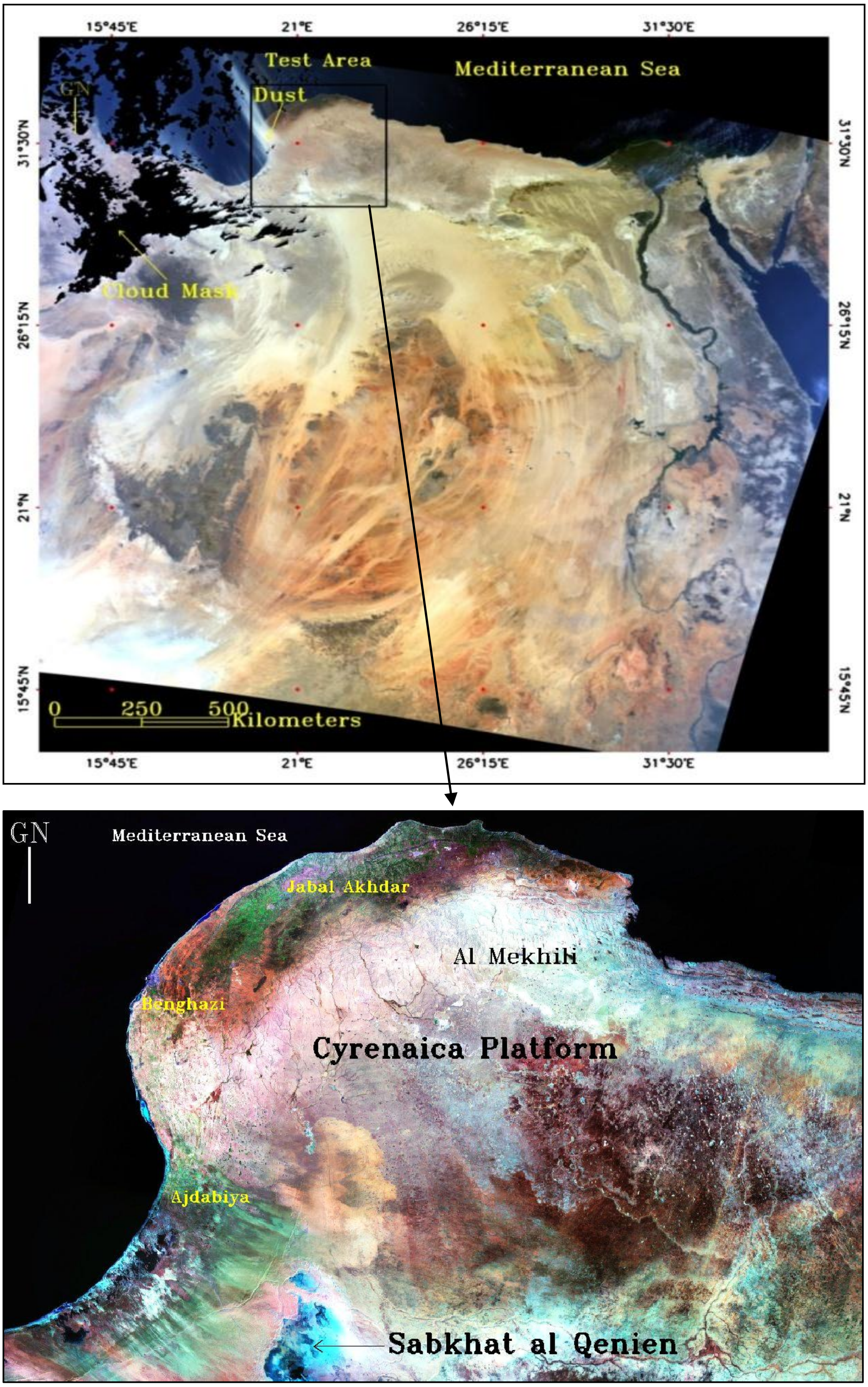


Figure 5.1(A) True colour composite of a dust storm imaged on 26/10/2007 by the MODIS Terra sensor over N E Libya. (B) Landsat image colour composite bands (1,3,4) shows the territory of Cyrenaica.

## 5.2 Geomorphology and Climate of Cyrenaica

The main topographical features of Cyrenaica are shown in Figure 5.2. As can be seen from that map, the only area of high relief is Jabal Akhdar which is occupies the most northern part of the NE Libya and spreads from Benghazi to Derna about 250km in length rising in some places to an altitude of 880 m above sea level. It falls off southwards to 100 m just 90 km inland. The change in the altitude is associated with a steep gradient in climatic, ecological and geomorphological conditions from Mediterranean vegetation in the north to the desert vegetation in the south.

Cyrenaican climate has marked seasonal variations influenced by both the Mediterranean Sea and the desert. The average temperature in the north of Cyrenaica is range from 27 to 32 ºC in summer and during winter is ranges from 12 to 20 ºC. Cyrenaica experiences a marked variation in rainfall. The northern coast and mountains annually receive as much as 400-500 mm of rainfall but this rapidly decreases along the southern flanks of Jabal Akhdar, declining to less than 50 mm in the Sahara Desert in the south of the study area. However, once every five to six years or so there is pronounced drought sometimes lasting for two successive seasons.

On the Northern and eastern flanks of Jabal Akhdar McBurney (1955) noted two escarpments (Figure 5.2). The lower escarpment runs for over 400km between Ras-Etin east of Derna in the east. The upper escarpment is shorter and runs almost continuously for about 300km between Ras-Etin east of Derna to El-Abiar in the west. However, the SRTM DEM (Figure 5.3) shows that the escarpments are both longer and more numerous McBurney (1955) recognized. El Hawat et al., (2005) shows that these escarpments are past fault controlled shorelines and this view is supported by the digital elevation model. He located a quarry at Farzugha that revealed both these attributes. Figure 5.4 shows the DEM of western Cyrenaica, and the beach ridge shorelines located at Farzugha, Figure 5.4 (B) shows photo of a quarry at Farzugha taken by El Hawat et al., (2005) that display beach deposits in the foreground and a back wall that is a normal fault that cuts through the Oligocene and Lower Miocene successions. The wave cut platform in the foreground is thought to have formed during the Pleistocene.

The DEM (Figure 5.3) shows that there are at least ten shoreline escarpments on the Benghazi coastal plain running from north to south. The eastern five of these are clearly shown in the south of the image buried under a large fan formed by a large river that flows from Jabal Akhdar and cuts through the first escarpment debouching onto the much smaller upfaulted beaches that from the coastal plain. Some of these escarpments exhibit beach ridges that are suggestive of a coastal origin. Thus it appears that the Cyrenaican costal plain consists of upfaulted beaches overlain in places by alluvium derived from the rivers that drain Jabal Akndar.

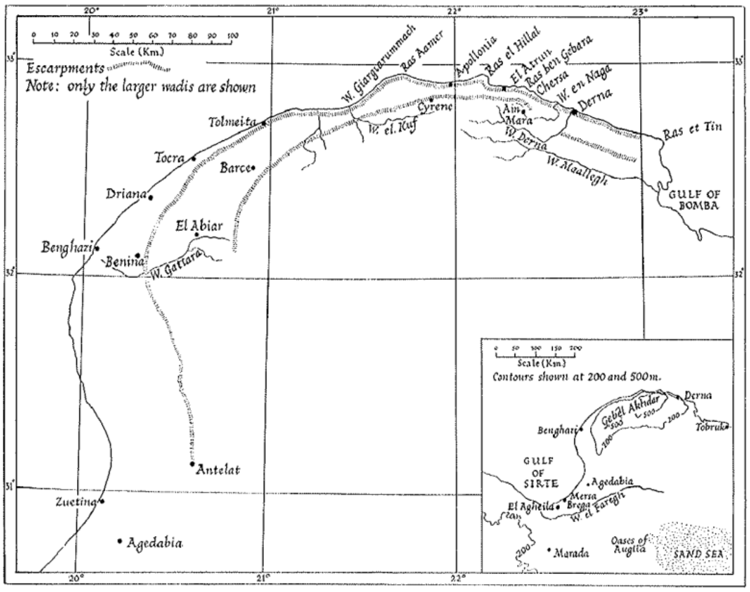


Figure 5.2 Map of Cyrenaica, showing position of the Jabal Akhdar. (Source: McBurney 1955)

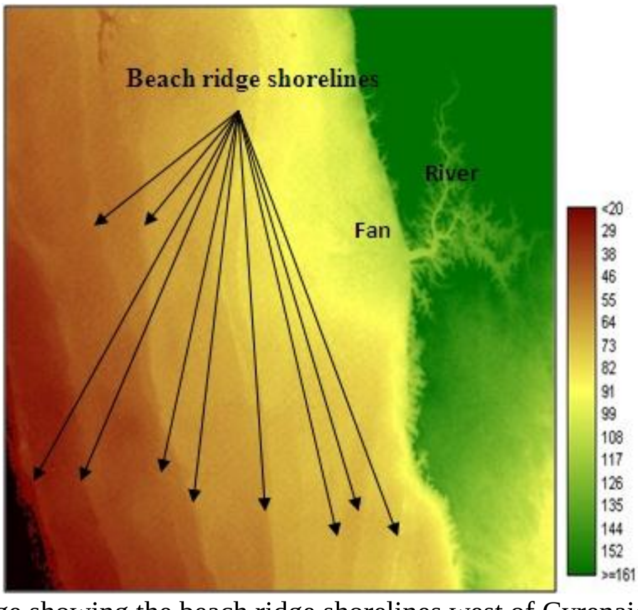


Figure 5.3 DEM image showing the beach ridge shorelines west of Cyrenaica. There are ten clear beach ridge shorelines.

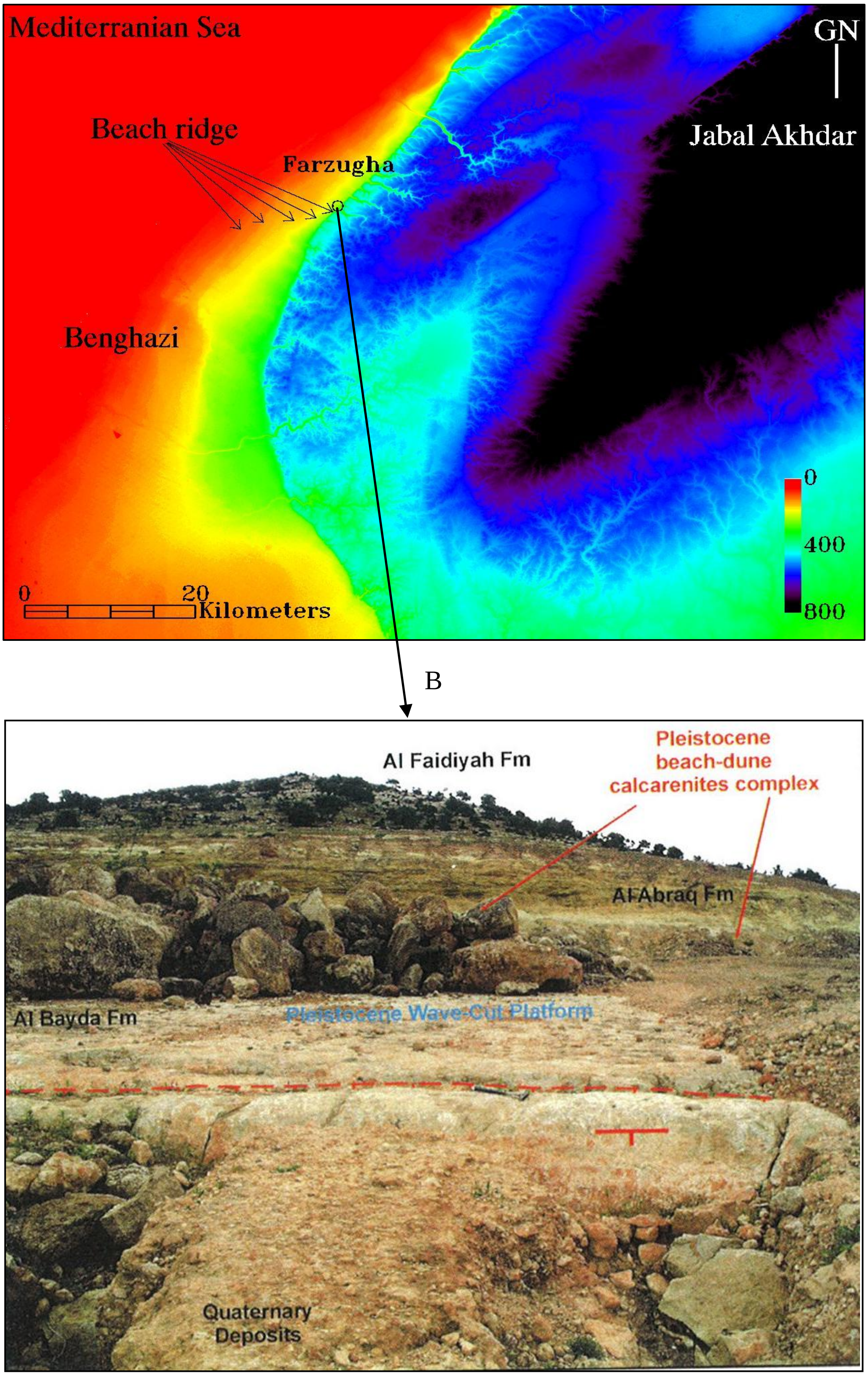


Figure 5.4 (A) DEM image showing the beach ridge shorelines west of Cyrenaica. (B) Beach ridge at Farzugha north east of Benghazi. (Source: El Hawat et al., 2005)

The geomorphology of southern Cyrenaica is evident in the satellite image (Figure 5.5) and the DEM (Figure 5.6). A series of rivers flowing off Jabal Akhdar onto the plains to the south Sahara platform (Figure 5.7 A, B, C, D), most of these rivers terminate in small closed basins that contain fans and lakes. The DEM (Figure 5.7 E, F, G) shows that the lakes in eastern Cyrenaica are larger than those in the west.

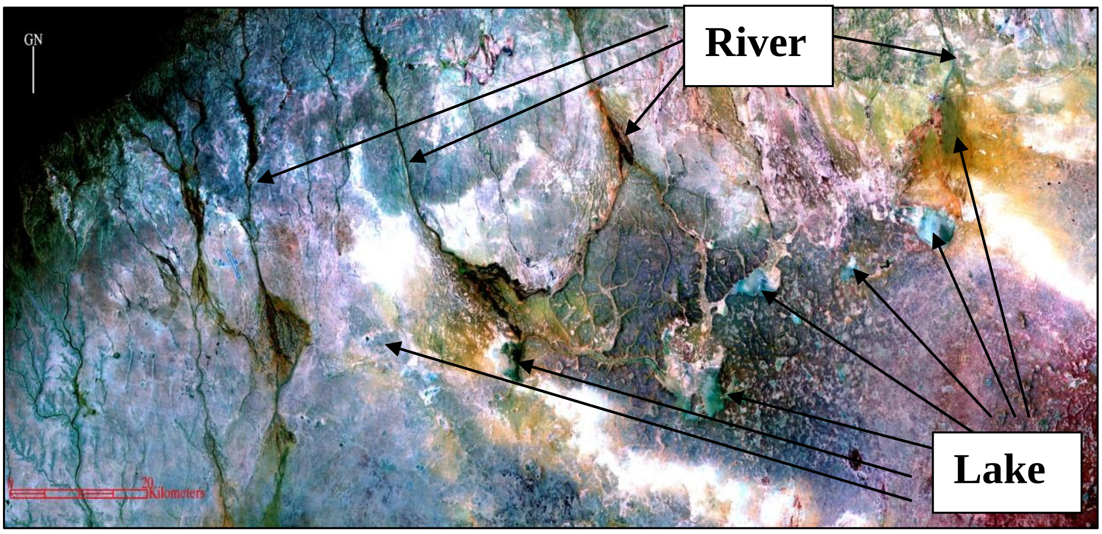


Figure 5.5 3D Landsat image of Cyrenaica, showing the location of the river channels that flow down from Jabal Akhdar and terminate in lakes located on the margin of the Cyrenaica platform.

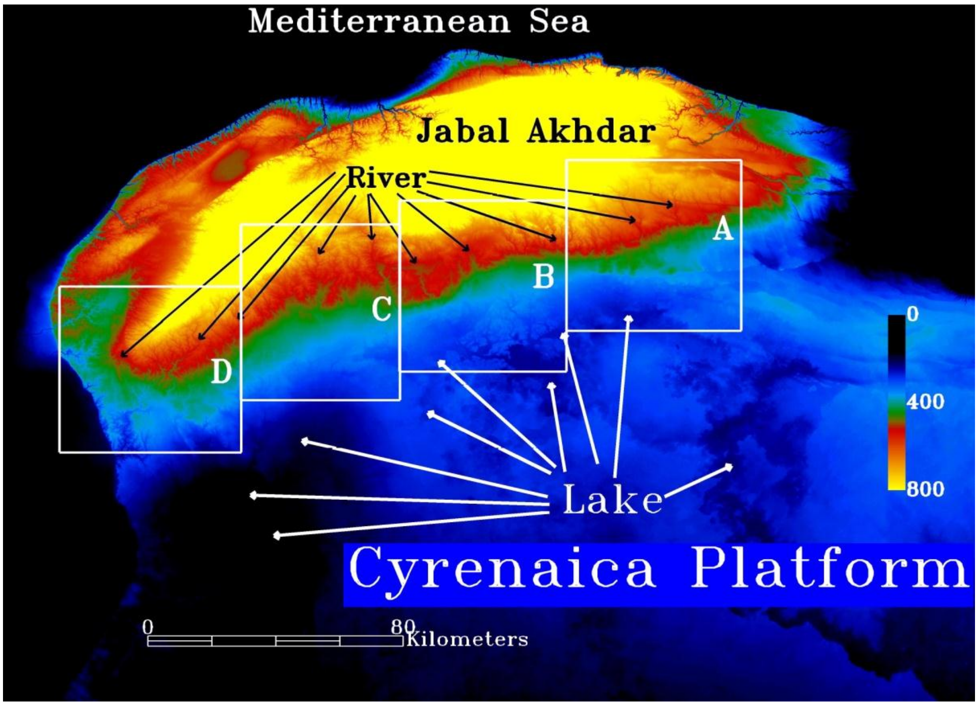


Figure 5.6 DEM Map showing general views of rivers flow off along the Jabal Akhdar and the Lakes where the water flow terminates. Regions A to D are shown in the following figure.

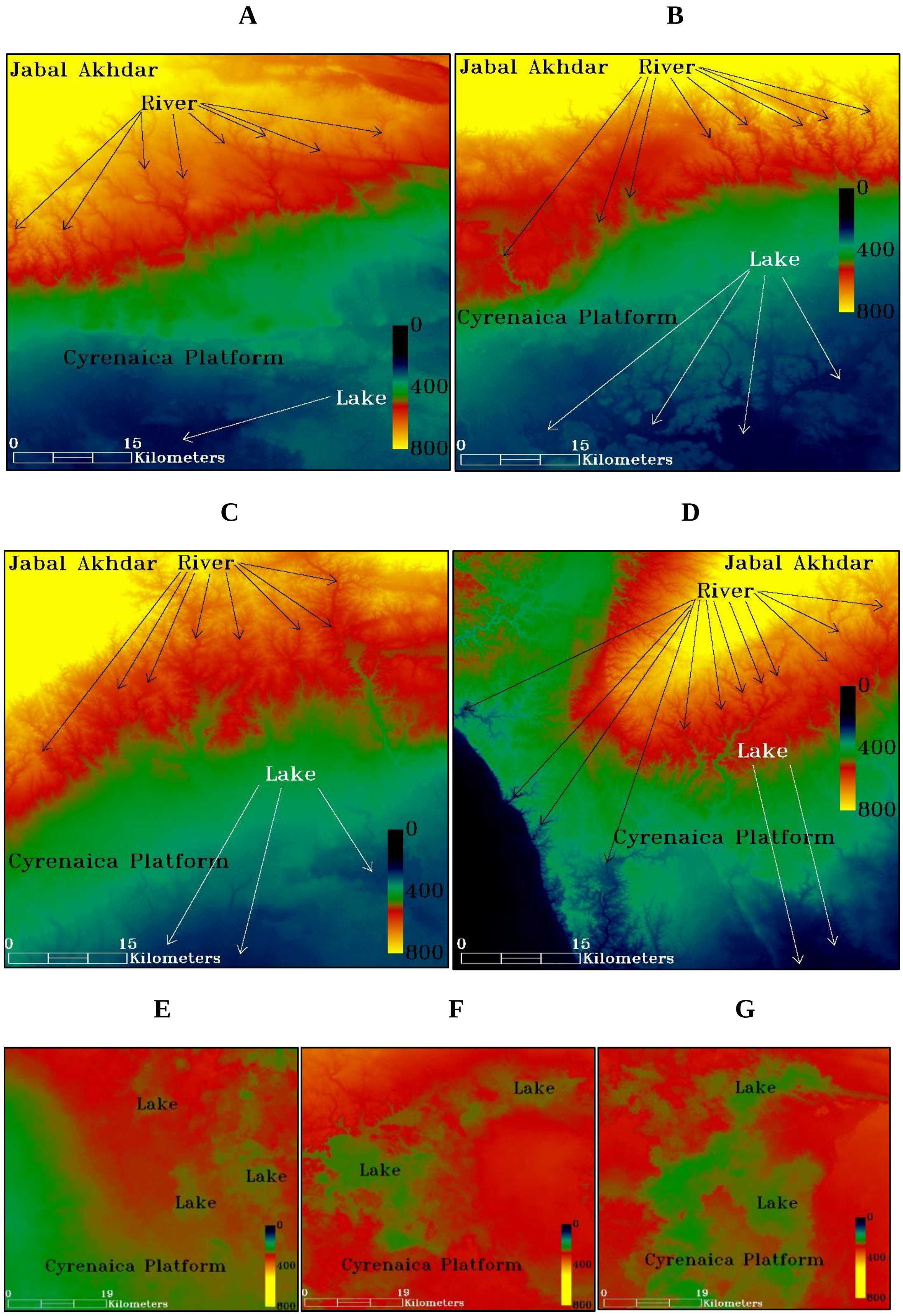


Figure 5.7 Detailed DEM images of Figure 5.4 showing the rivers that flow off Jabal Akhdar (A, B, C and D) and the lakes where the water terminates (E, F, and G).

## 5.3 Geology of Cyrenaica

### 5.3.1 Geological Development of Jabal Akhdar

The geological history of the study area goes a long way to explaining the geomorphology of the region. During the Upper Cretaceous and Tertiary Cyrenaica was a marine basin, and sediments, mostly limestone with subordinate dolomites and marls built up in the region that is now Jabal Akhdar, Jabal Akhdar is separated from Saharan Platform to the south through deep seated faults with an east-west alignment (Röhlich 1978). Jabal Akhdar has always been the mobile part and the Sahara Platform the stable part. The Jabal Akhdar formed due to compression between the Mediterranean platform and the fixed Sahara Platform. Since the middle Miocene there has been an uplift of at least 750m. Before that the Jabal Akhdar region was characterized by a series of marine transgressions and regressions that gave rise to the thick sequence of predominantly limestone sediments that we see today.

The first episode of compression was in the Santonian when an anticlinorium was uparched to the north of the fault system that defines the northern margins of the Cyrenaica Platform. This large complex arch, which forms the nucleus of contemporary Jabal Akhdar, emerged as an island, the central part of which was subsequently deeply eroded by some hundreds of meters. A renewed marine transgression occurred during the Campanian, continued through the Paleocene with deposition in a neritic and bathyal environment and this ended with an early Eocene uplift of another broad anticlinorium, again aligned along a northeast to southwest trend (Röhlich 1978). A large area of present northeast Libya emerged from under the sea at this time and the strata of the preceding sedimentary cycle were entirely eroded from the highest parts of this tectonic arch.

A renewed marine transgression occurred during the Early and Middle Eocene depositing finely textured, occasionally cherty, bituminous limestone, suggesting a rather deep marine environmental (Röhlich 1978). These strata are absent from the southern slope of Jabal Akhdar, evidence that sub aerial exposure occurred in the southern part of the Jabal Akhdar during Eocene times.

From the Oligocene to the Lower Miocene regressions and transgressions of shallow marine waters repeatedly occurred across the region of Jabal Akhdar and the Sahara

Platform depositing mostly limestone (Röhlich 1978). The final uparching of Jabal Akhdar occurred from the Middle Miocene. The exposed surface of the predominantly Eocene, Oligocene and Miocene limestone strata formed a flat elongated arch divided into subsidiary domes and swales. The shape of this complex arch roughly corresponds to the present gross geomorphology of Jabal Akhdar (Figure 5.8 and 5.9).

The topographic evolution on the northern slope of Jabal Akhdar has been influenced by marine erosion. The two broad terraces mentioned by McBurney were successively sculptured by marine encroachment (Röhlich 1978). The upper terrace has no young marine sediments and it is probable that it was formed by marine erosion during the Pliocene. Distortion of this terrace surface from the horizontal records the younger tectonic movements, which have shaped the present mountains architecture. The presence of littoral sediments of Quaternary age on the lower, coastal terrace confirms its age as well as its marine erosional origin (Röhlich 1978).

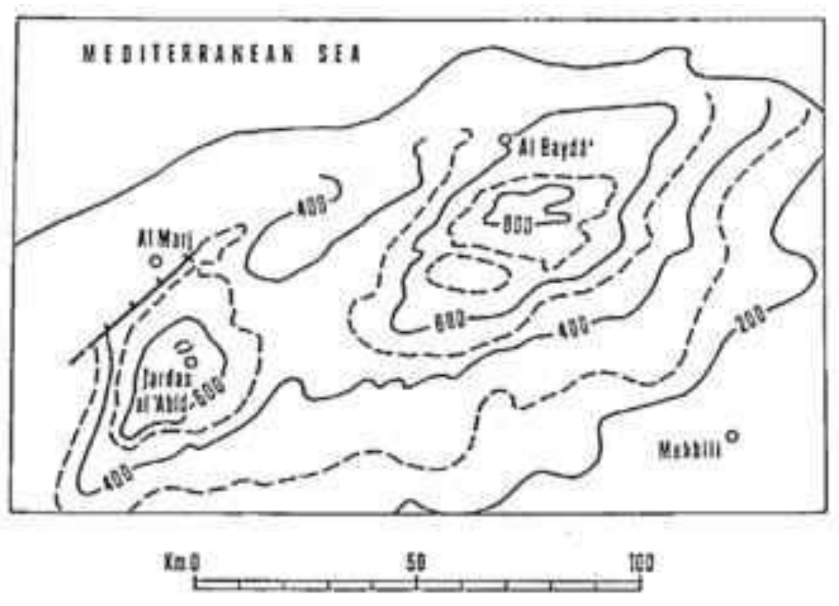


Figure 5.8 Structural map of the Oligocene base (100m stratoisohypses). (Source: Röhlich 1978)

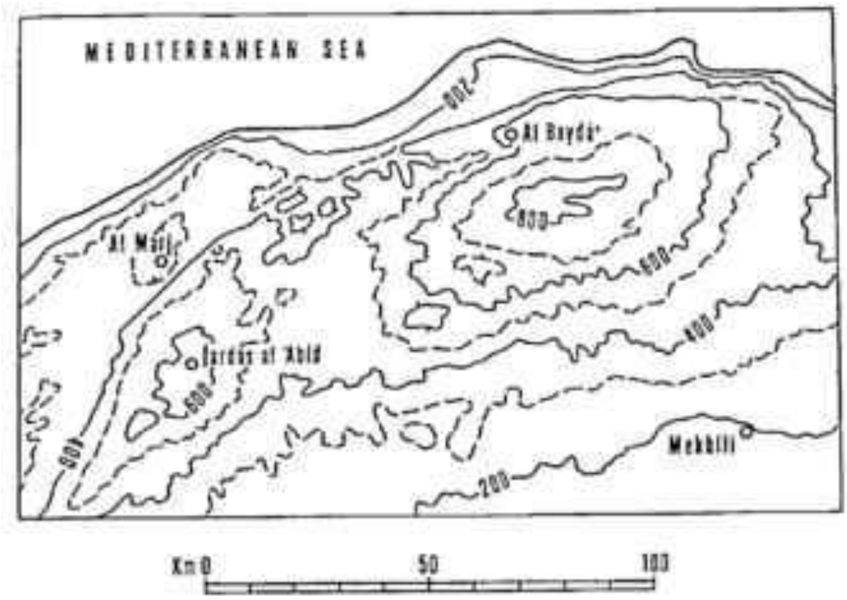


Figure 5.9 Generalized contour lines of the present surface. (Source: Röhlich 1978)

The drainage system of Jabal Akhdar, though roughly radial because of the simple uparched geomorphology, has both an asymmetrical density distribution and an occasionally irregular configuration departing from the radial pattern that would be expected from rivers draining a dome. The asymmetry consists of the more intense and deeply incised dissection on the northern coastal slope. This is the result of steep topographic slope, marine erosive sculpturing, structural complexity and an orographically influenced higher average rainfall (Röhlich 1978). The current drainage alignments may also have been influenced by jointing and solution cavity development within the widespread carbonate rocks in the Miocene.

The rivers that flows off the southern flanks of the Jabal terminate in fans and paleo-lakes within small basins formed along the fault zone that separates it from the Sahara Platform.

### 5.3.2 Geological Development of Sahara Platform and Sabkhat al Qenien

The Sahara platform to the south of the Jabal Akhdar is covered in marine limestone deposited in the numerous marine incursions outlined above. Satellite imagery shows that it is covered in many small depressions, probably formed by the collapse of Late

Miocene solution cavities and subsequently filled by small paleo-lakes (Figure 5.10). To the south of this is the Sirte Basin and Sabkhat al Qenien (Figure 5.11), a large paleo-lake in the lowest point of the basin. Drake et al., (2008) suggest that the topography of the region was controlled by rifting in the Sirte Basin that was centred along the NNW-SSE trending structural axis of Ajdabiya Trough.

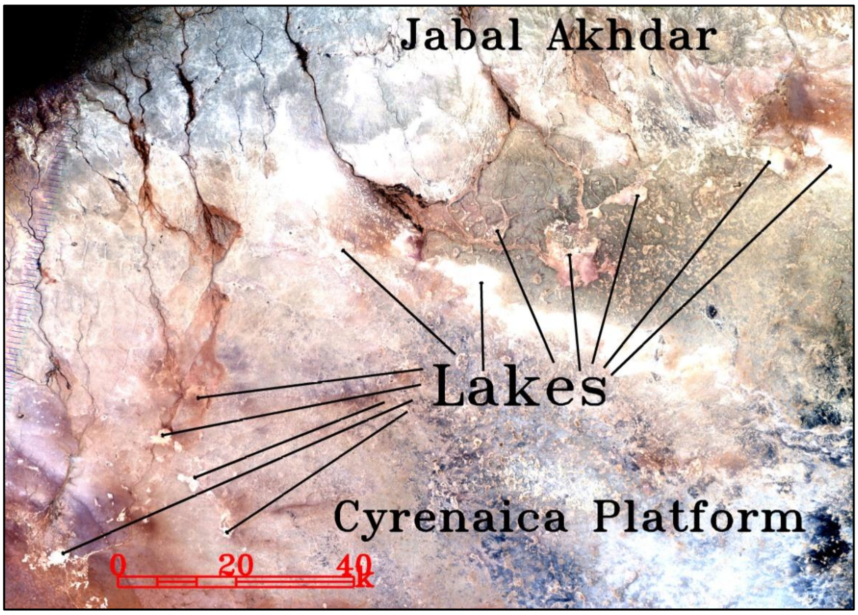


Figure 5.10 Landsat image colour composite bands (1,3, 4) of Cyrenaica, showing the location of the river channels flows down from Jabal Akhdar and terminated at lakes located in Cyrenaica platform.

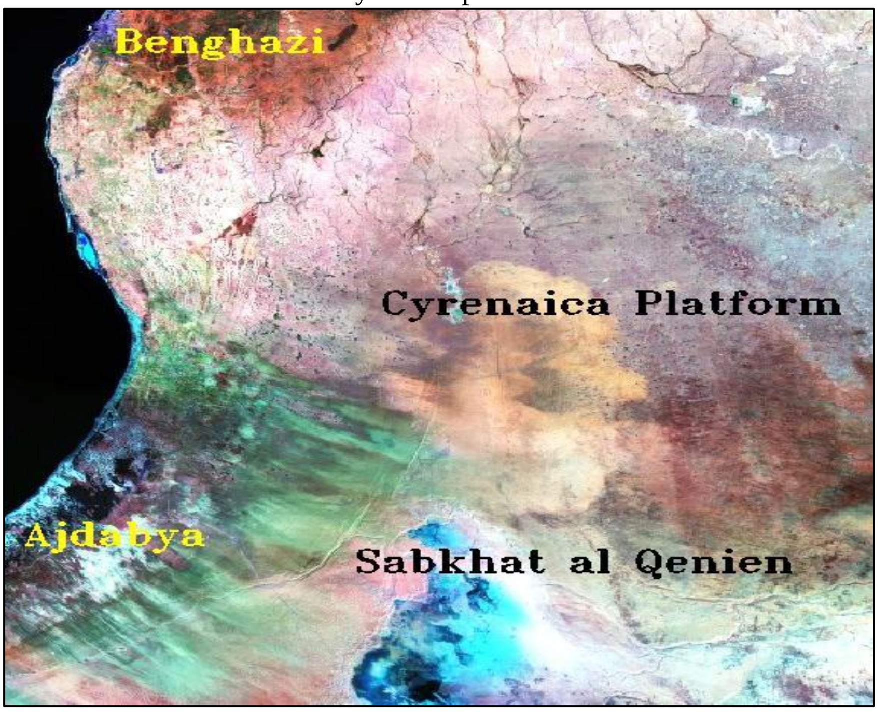


Figure 5.11 Landsat image colour composite bands (1,3, 4) of Cyrenaica, showing the location of the Sabkhat al Qenien.

Drake et al., (2008) suggest how Sabkhat al Qenien was formed (Figure 5.12). During the Lower Pliocene the Mediterranean Sea encroached into the Gulf of Sirte (Figure 5.12 A). During the Upper Pliocene long shore drift brought sediments eroded from Cyrenaica into the Gulf of Sirte forming a bar that started to develop across the mouth of the gulf (Figure 5.12 B). By the Pleistocene the Gulf of Sirte had been completely cut off by the bar formed thus forming the Sabkhat behind the bar (Figure 5.12 C). The lake that formed in this region during Saharan humid periods was fed by rivers emanating from the central Sahara and attained a maximum are of 42,000 km² (Drake et al., 2008). The region is currently a dry paleo-lake that is fed by saline groundwater and producing a thin saline crust underlain by saline mud.

A

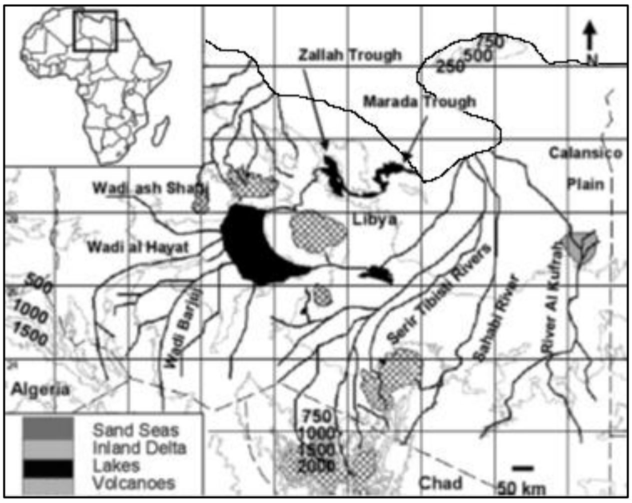


B

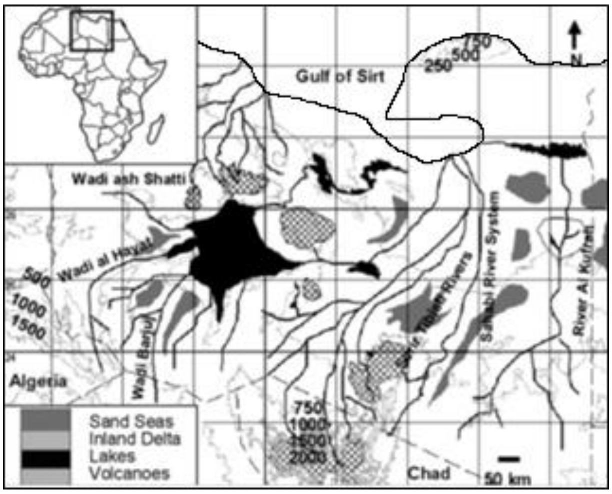


C

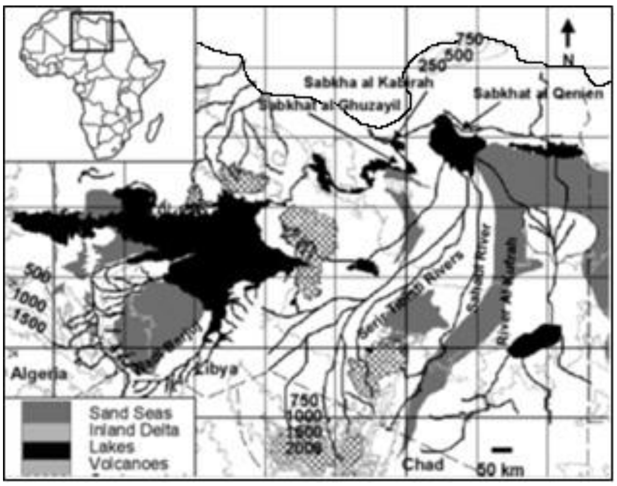


Figure 5.12 Map showing the three period of time passed over Libya and how the Sabkhat al Qenien has been formed. A. Lower Pliocene, B. Upper Pliocene, and C. Pleistocene. (Source: Drake et al., 2008)

## 5.4 Methods for Dust Source Detection

In this chapter we present, implement and evaluate a dust source detection and evaluation methodology in Cyrenaica that uses the MODIS dust detection methods that chapter 4 found to be appropriate and integrates them with data from SEVIRI to provide a better temporal resolution and Landsat/Google Earth to provide a better spatial resolution. These methods are outlined below. The methodology was applied to the region for the year January to December 2008.

### 5.4.1 Integrating MODIS and SEVIRI Data

Based on the results of chapter 4 the Ackerman (1989) method was selected to use for detecting dust sources using MODIS data and this was employed using a 'SEVIRI' style colour composite. Using combination of same bandwidth from MODIS and SEVIRI to detect dust sources has not been used before. The reason for employing this combination of sensors is; (1) MODIS data is good for tracing the dust to their sources because of the high spatial resolution. (2) SEVIRI data is good to follow the trajectory of the dust storm MODIS detects, to determine the life time of dust storm and can be used to find the climatological cause of dust storm because of the high temporal resolution and large area coverage.

### 5.4.2 MODIS Terra and Aqua

To insure detecting as many dust storms generated from N E Libya as possible, both MODIS Terra and Aqua imagery were downloaded for each day of 2008 and tested using the Ackerman 1989 technique to select the images shows dust. The first step was to filter out the images where no dust can be seen or the images that had so much cloud cover most of the test area that no dust could be seen beneath the cloud. The second step was use the selected images to work out if that dust which can be seen in the image is generated from the test area or is just crossing over and that can be done by tracing back each individual dust storms if it is possible, if it is not SEVIRI data can be used for further investigation because of its high temporal resolution.

### 5.4.3 SEVIRI

The SEVIRI data has been used during this study for two purposes; (1) To insure the MODIS data does not miss any single dust storms even it has short life time and it may happen during the time which is out of the MODIS Terra and Aqua passing time. (2) The SEVIRI data has the possibility to determine the life time of each dust storm, its trajectory and climatological cause.

### 5.4.4 Colour Composite

The SEVIRI colours composite were employed in both MODIS and SEVIRI analysis (see section 2.3.3.2.9 for more details). However, the green band of the colour composite (which is related to the dust detection) was changed to the Ackerman (1989) technique, providing the following SEVIRI colour composite.

R= BTD 12.0μm - 10.8μm

G= BTD 11μm - 3.7μm (Ackerman 1989)

B= 10.8μm channel.

## 5.5 Method for Understanding Dust Sources Characteristics

In order to understand the geomorphology and landuse of the dust source areas it was necessary to use high resolution data such as Landsat and Google Earth and digital elevation models.

### 5.5.1 Landsat Geomorphologic and Landuse Mapping

The location of each identified dust source was plotted on mosaiced Landsat TM images covering the test area using a colour composite display employing bands 7,4,2 on red, green and blue respectively. Two types of Landsat imagery were used. 1) A mosaic Landsat image before 2003 to avoid the striping problem on Landsat

TM images that has occurred since 2003 because of the failure of the scan liner corrector. 2) To determine the nature of the sites at the time of image acquisition Landsat ETM data was downloaded even though it suffered this striping problem. Two adjacent Landsat images per month were enough to cover the parts of the test area that produced dust during 2008.

Some of the lakes were found to be subjected to flooding during early 2008. In order to monitor the change of the lakes from wet to dry, Landsat imagery covering all of the lakes in the test area was downloaded and presented.

### 5.5.2Vegetation Mapping Using NDVI

The Normalized Difference Vegetation Index (NDVI) was used to evaluate the vegetation in the vicinity of the dust sources. NDVI is a simple indicator to vegetation cover and is calculated for as follows:

$$NDVI = \frac{(\mathrm{NIR-RED})}{(\mathrm{NIR+RED})} \qquad (5.1)$$

RED stands for the spectral reflectance measurement acquired in the red region, and NIR for the near-infrared. By design, the NDVI varies between -1.0 and +1.0.

### 5.5.3 Digital Elevation Model (DEM) Analysis

The SRTM 90m pixel resolution DEM of the study is was used to view the topography and the geomorphology of the sources in order to help find determine what landform the detected sources came from.

### 5.5.4 Google Earth

Google Earth has got higher resolution images than Landsat TM acquired from different satellites such as Digital Globe, Geo Eye-1, Ikonos, and SPOT 5 (Figure 5.13). Google Earth is used to display high resolution images of the detected dust sources and thus potentially find further information on the nature of the sources. Two scales were used for this study; the first one is 5 km scale in order to see the area surrounding the dust source and the second one is 1km scale in order to see the source in a more detailed. Because the dust sources being evaluated are based on interpretation of a MODIS pixel that represents 1km on ground, the central point of the MODIS pixel is plotted on the Google Earth as is the a 1km square polygon in order to represent the pixel and help identify any geomorphological or landuse variability within the source area. This 1km square polygon is plotted on the small scale images only (1 km).


Figure 5.13 Google Earth map shows the entire region of Cyrenaica and the dust sources detected during 2008. (Source: Google Earth)

## 5.6Field Evaluation

In order to understand the characteristics of a dust source and the mechanisms that produce dust, it was necessary to know the size fraction of the sediments both in their natural state and when they have been eroded. A fan and paleo-lake dust source site was visited by Nick Drake in near El Mekhili in April 2008. Samples were collected from both landforms and digital photos of sample sites were taken. The samples were analysed for grain size by Robyn Inglis (University of Cambridge) as part of her PhD degree and she has kindly provided the results.

### 5.6.1 Grain Size Analysis

The samples were analyzed by taking a lump of sediment approx. 1-5g and placing it in the bottom of the test tube. Each tube was topped up with 4.4% sodium pyrophosphate, whirl mixed and left overnight. The samples were then centrifuged at 3500 rpm for 13 minutes. The liquid was decanted off, and each tube was topped up with 4.4% sodium pyrophosphate and stirred with a glass rod.

After further stirring, the sample was mixed on a whirl mixer to create a vortex. It was checked that all the sample was moving freely and not stuck to the bottom. A few drops of the sample were added to the sample beaker of the Malvern Mastersizer 2000 with a pipette from the sample whilst in a vortex with the ultrasonic probe switched on. Analysis of the sample proceeded when the correct value was maintained for 6 seconds. The sample was measured 3 times for 10 seconds each and an average curve calculated from these curves. The sample was left in the machine until a satisfactory, consistent curve was obtained.

Once a reading had been taken, the Malvern was rinsed with clean water and obscuration checked, before adding the next sample. The results of the grain size analysis are described in the following chapter.

# 6. Evaluating Dust Sources in Cyrenaica; Results

In order to evaluate the dust sources in Cyrenaica the year of 2008 was selected because during that year part of the test area experienced heavy rain, briefly filling up the ephemeral lakes, whilst the other part was much drier. This allowed evaluation of how the meteorological conditions of the area affected the different types of dust source.

All of the dust sources were detected using MODIS and SEVIRI data. SEVIRI has a poorer spatial resolution but has coverage every 15 minutes sometimes allowing diffuse dust sources to be traced back to their source but also providing information on the duration of the dust storm, the direction it was moving in, and when this information was combined with a knowledge of Saharan climatology it was possible to estimate the cause for the dust storm. The sources were then investigated using Landsat images on a monthly base in order to evaluate the geomorphology and land use of the dust sources in more detail. However, there are some months when the Landsat images were not available due to the presence of cloud cover, so when this was the case the dust sources have been mapped using the closest months image. The Landsat imagery is displayed as colour composites using bands 7, 4 and 2 on the red green and blue colour guns. The Normalized Difference Vegetation Index (NDVI) was also calculated from the imagery in order to look at the relationship between vegetation cover and deflation. The Shuttle Radar Topography Mission (SRTM) 90 m digital elevation model of the region was displayed in conjunction with the Landsat colour composites to provide 3D information in order to help interpretation of the landforms. DEM images were displayed both in frames adjacent to the Landsat imagery and as orthographic displays. When higher resolution imagery was required, Google earth was employed. The interpretation and the classification of the dust sources detected at Cyrenaica are displayed in Table 6.1. The dust sources detected at Cyrenaica are from six different Landforms. The interpretation is done based on the characteristic of the Landform at the dust sources as outlined in Table 6.1.

Table 6.1 Type of landforms and landuse of dust sources in Cyrenaica (Bullard et al., 2008).

| Landform | Characteristic |
|---|---|
| Alluvial Fan | Fan shape, covered in river channels, the channels diverge. |
| Alluvial Plain | Flat surface covered in river channels (commonly braided and running east-west) and beach ridge shorelines (running north-south). |
| Lake | Flat surface, found at the bottom of depression, devoid vegetation, bright surface. |
| River | Found at base of valley, long and thin, sometimes braided |
| Agriculture | Regular shaped patches of vegetation. |
| Multiple Landforms | More than one landform/landuse exists at the dust source. |

## 6.1 Example of How Dust Sources are Detected

After the comparison between the nine techniques (Chapter 4) Ackerman (1989) was selected to evaluate the dust sources using SEVIRI and MODIS data to create a 'SEVIRI style' colour composite. A prominent series of dust storms detected over Cyrenaica on 16$^{th}$ July 2008 is displayed in Figure 6.1 to show how the dust sources are detected using this MODIS and SEVIRI images. Moreover, the nine tested techniques in chapter 4 have been applied to the selected image to support the selection of methods chosen in chapter 4. The dust storm detected over Cyrenaica on 16$^{th}$ July 2008 was the strongest and longest dust storm detected in the region in that year. The red circles show the dust sources detected over Cyrenaica using the Ackerman (1989) colour composite. Figure 6.1 clearly shows that the Ackerman method works well in Cyrenaica and that when combined in a colour composite it provides an improvement in dust source detection over the traditional SEVIRI colour composite.

(A) 16 July 2008 MODIS Image RGB

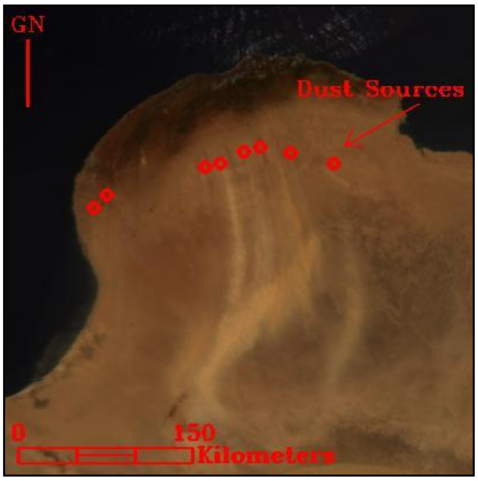


(B) Ackerman 1989

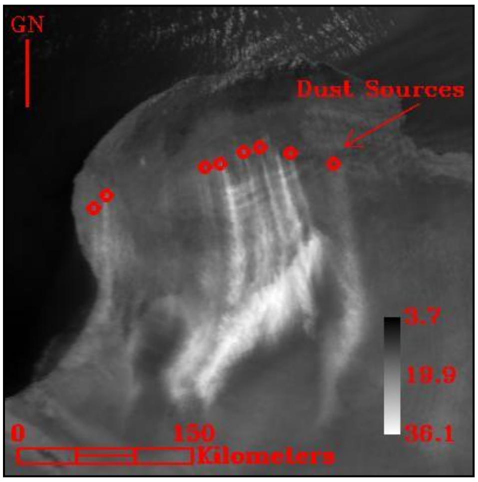


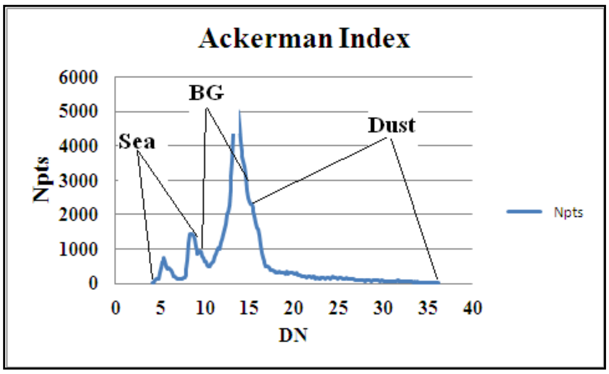


(C) Miller (2003)

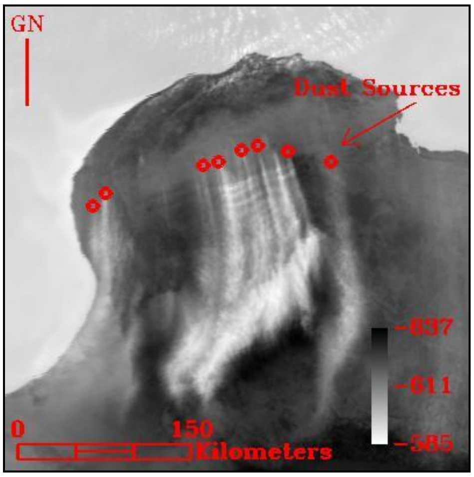


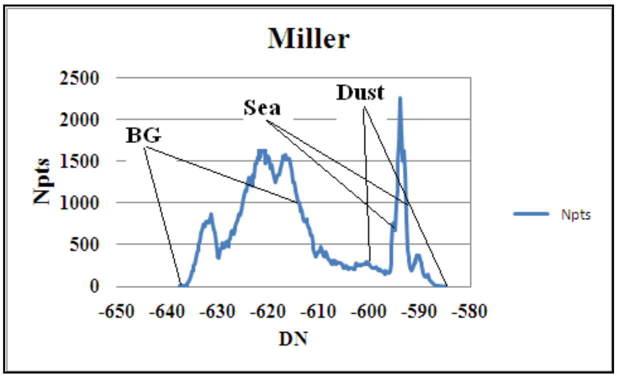

(D) Hansell et al (2007)

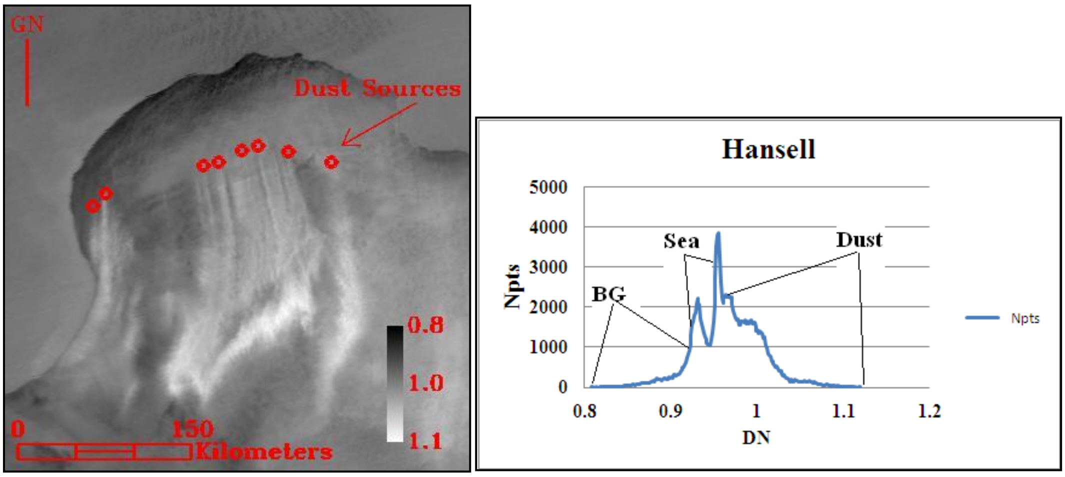


(E) Handley (2004)

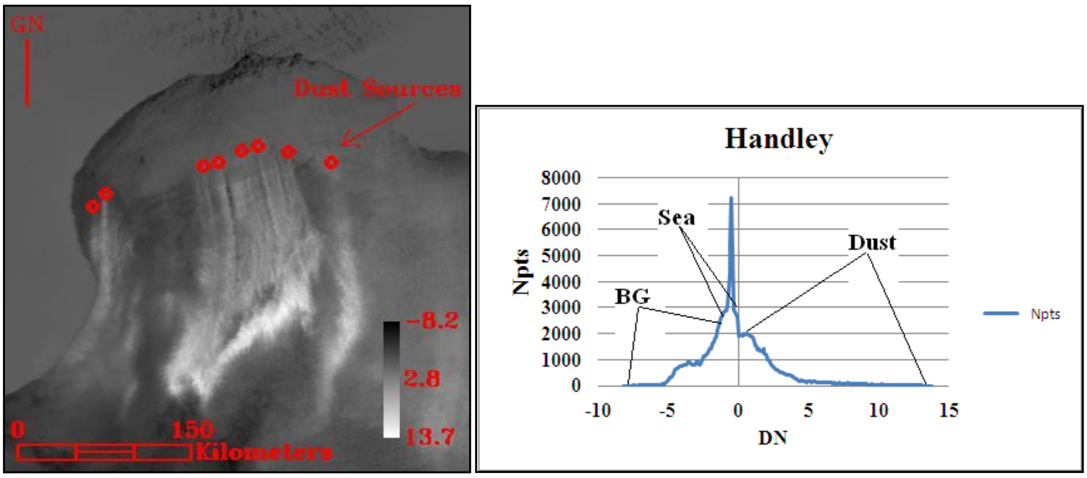


(F) Deep Blue (2003)

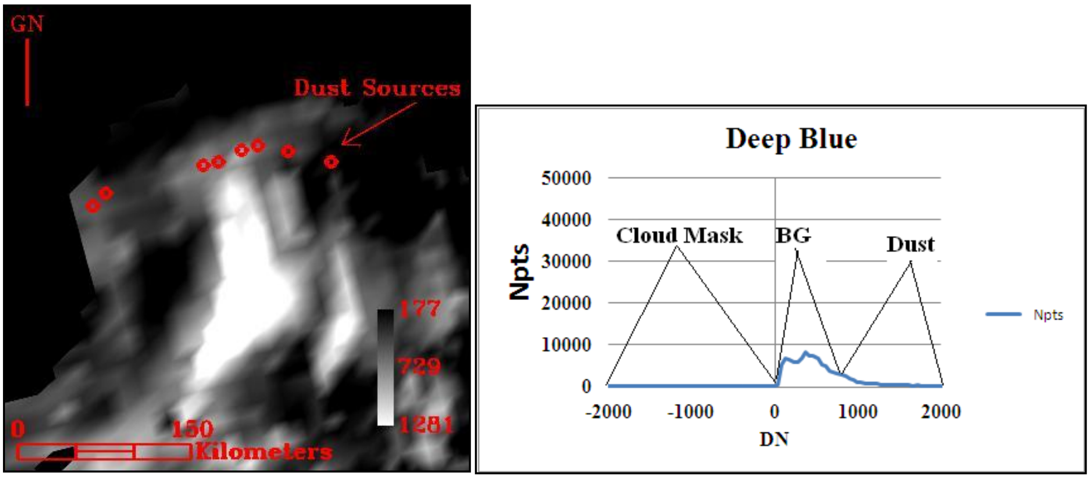

(G) BTD (3.7µm-12µm)

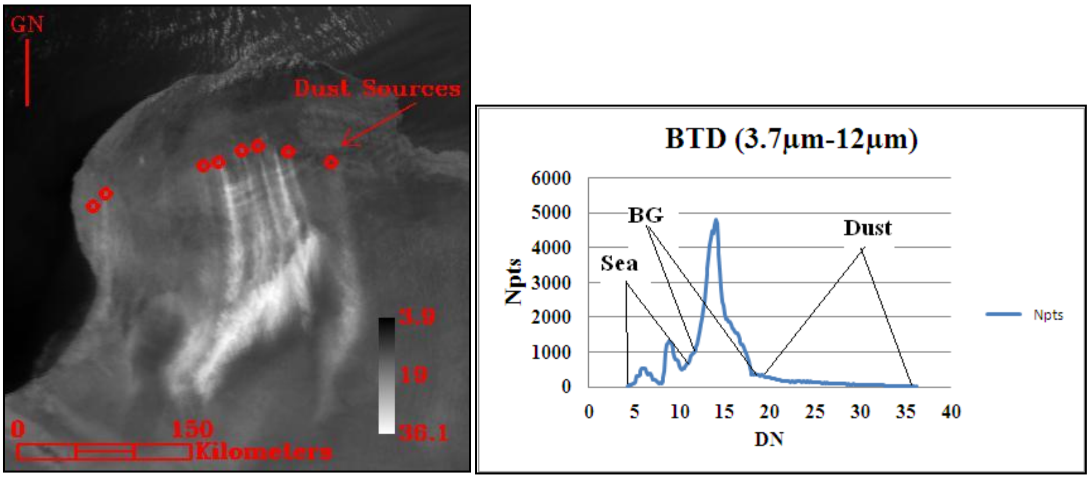


(H) BTD (8.6µm-11µm)

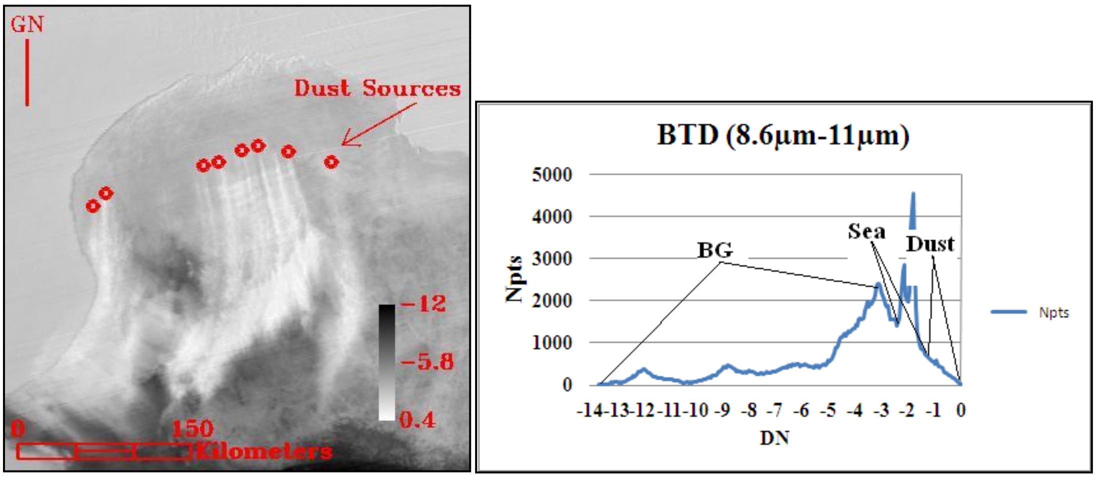


(I) BTD (8.6µm-12µm)

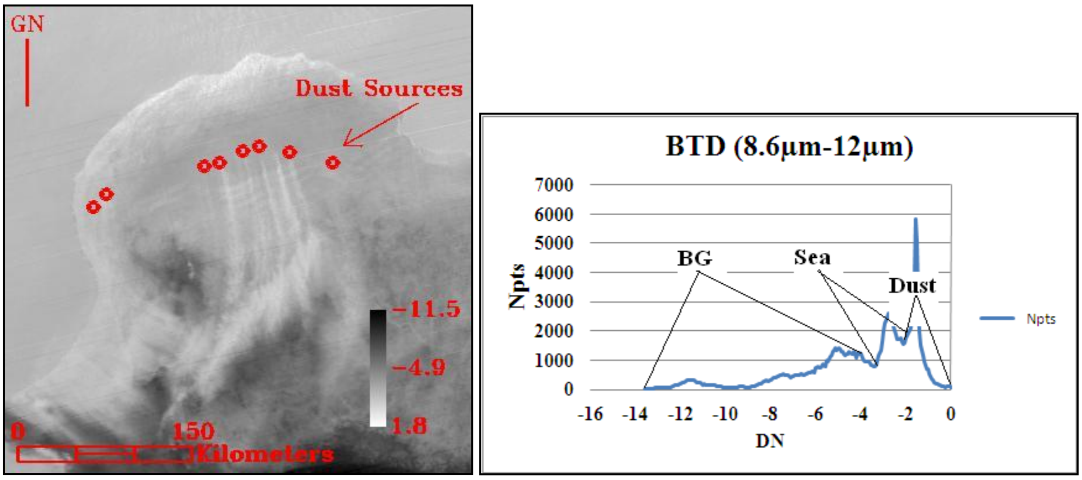

(J) BTD (12µm-11µm)

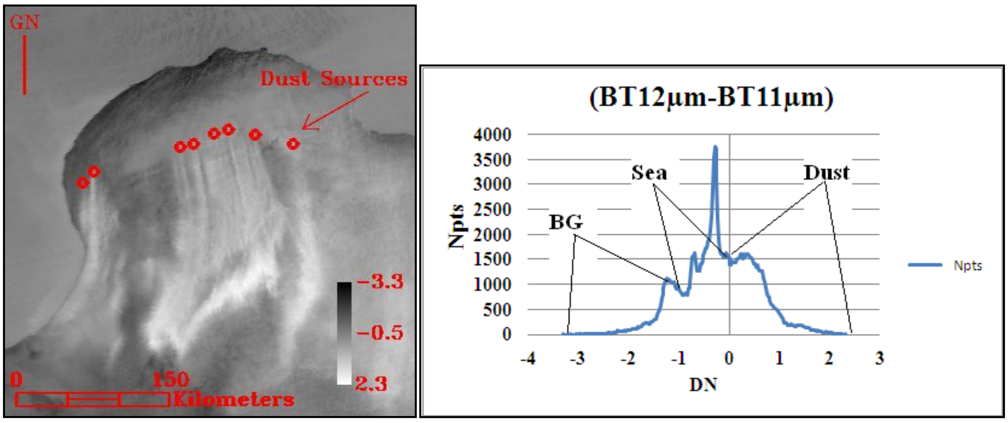


(K) MODIS colour composite

R: 12µm-11µm
G: 11µm-8.5µm
B: 11µm

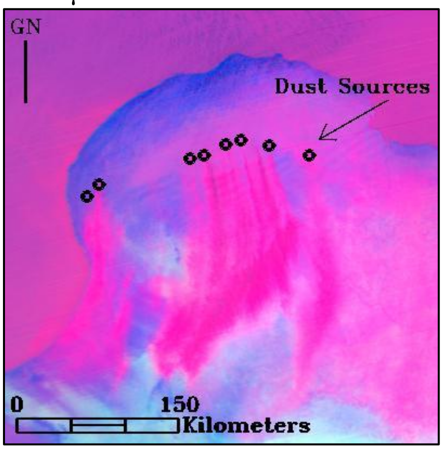


(L) MODIS colour composite

R: 12µm-11µm
G: Ackerman (1989)
B: 11µm

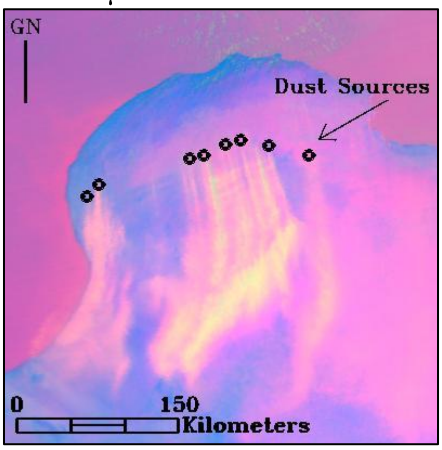


**(M) SEVIRI**

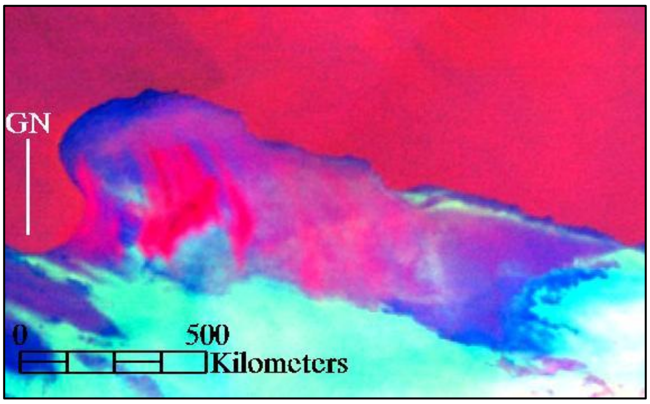


Figure 6.1 Comparison of the ability of each technique to distinguished between the dust and the background. (A) MODIS colour composite. (B-J) Result of applying the nine selected techniques to the MODIS Aqua sensor over Cyrenaica to the image dated 16/07/2008. (K) MODIS data to create a traditional SEVIRI colour composite. (L) MODIS data to create a traditional SEVIRI colour composite with Ackerman (1989). (M) SEVIRI data colour composites. The red circles show the detected dust sources.

## 6.2 Dust Source Climatology From SEVIRI Imagery

The SEVIRI images have been used in conjunction with MODIS images for the dust sources detection, however, time series of images can also be used to illustrate the duration, direction, and synoptic climatology of the dust storms and using this information infer the cause of each dust storm (Table 6.2). This is possible because SEVIRI data has 15 minutes temporal resolution making it possible to find out the direction by a creating movie for all dust storms and thus being able to tell when start and finish, where they come from, where they go, the cloud systems associated with the storms, and which direction the dust storms takes.

The majority of the dust storms in Cyrenaica started at 8:00 am and end at 14:00 pm. However, the largest two dust storms detected during 14$^{th}$ of May and the 16$^{th}$ of July started at 6:00 am and end at 16:00 pm. The highest percentage of the dust storms (70%) are caused by anticyclone conditions and the dust goes northwards and north-east towards the Middle East and Southern Europe. Israelevich et al. (2003) documented that some of the dust that reaches Israel comes from Libya, and it is probably Cyrenaican dust. Ganor et al. (1991) also recorded 23 heavy dust storms in Israel over 20 years that originally come from North Africa, much of this is probably Cyrenaican dust. The other 30% of dust storms are caused by the Haramattan travel southwards over the Sahara. This wind develops within the lower troposphere with surface air flowing from the North African high pressure south-westward towards the lower pressure zone over the Atlantic Ocean in the Gulf of Guinea (Kalu, 1979). None of the ground based methods for detecting dust outlined in chapter 1 has recognized Cyrenaica as an important Saharan dust source, particularly for dust travelling northwards towards Europe. However, Schepanski et al (2009) recognizes Cyrenaica as a significant Saharan dust source and this work confirms that view.

Schepanski et al (2009) found 65% of the dust sources activity (March 2006 to February 2008) occurs during local morning hours 6:00 am to 9:00 am UTC caused by Low Level Jet (LLJ). In this study 70% of the dust sources activity (March 2008 to November 2008) occurs during local morning hours, it starts at (7:00-8:30 am) but that end at different times, 50% of the 70% ends at mid day (11:00-12:30 am) UTC and are caused by Anticyclone and the other 50% ends between 14:00-16:30 am UTC and are caused by Haramattan.

Table 6.2 Dust storms detected over Cyrenaica during year 2008 using SEVIRI

| No. | Date | Life Time | Direction | Cause |
|---|---|---|---|---|
| 1 | 11 March | 09:30 to 14:00 | NW-SE | Harmattan |
| 2 | 13 March | 11:30 to 13:00 | South-North | Anticyclone |
| 3 | 25 March | 08:30 to 14:00 | South-North | Anticyclone |
| 4 | 20 April | 08:00 to 14:00 | South-North | Anticyclone |
| 5 | 21 April | 08:00 to 14:00 | South-North | Anticyclone |
| 6 | 22 April | 10:00 to 13:00 | South-North | Anticyclone |
| 7 | 14 May | 08:00 to 16:00 | NW-SE | Harmattan |
| 8 | 18 May | 08:00 to 12:00 | South-North | Anticyclone |
| 9 | 03 June | 08:30 to 11:30 | South-North | Anticyclone |
| 10 | 07 June | 08:00 to 16:00 | South-North | Anticyclone |
| 11 | 13 June | 12:00 to 12:30 | South-North | Anticyclone |
| 12 | 23 June | 08:00 to 14:00 | NW-SE | Harmattan |
| 13 | 29 June | 12:30 to 14:30 | North -South | Harmattan |
| 14 | 16 July | 07:30 to 16:00 | North -South | Harmattan |
| 15 | 01 October | 07:00 to 11:00 | South-North | Anticyclone |
| 16 | 02 October | 07:00 to 11:00 | South-North | Anticyclone |
| 17 | 28 November | 08:30 to 11:30 | South-North | Anticyclone |

**Percentage: 70% Anticyclone and 30% Harmattan.**

## 6.3 Describing the Dust Sources

Figure 6.2 and Table 6.3 shows the dust sources detected during 2008. Fifty three dust storms in total were detected, 46 of these could be traced back to their source, and the other 7 dust storms had no obvious source, presumably as dust had mixed with cloud at the dust sources area which make it difficult to identify the dust sources using either MODIS or SEVIRI, or because the dust cloud had been transported from outside the study area. These storms were termed ‘diffuse dust storms’.

The Cyrenaica is covered by two Landsat scenes, one centred on Benghazi and one on Jabal Akhdar. The Cyrenaica test area was divided into these two regions. This was done in order to avoid confusion as both regions were not viewed at the same time by Landsat because some Landsat scenes exhibit high cloud cover in one region and were cloud free in the other. Figure 6.2 shown the mosaic of these two scenes with the two regions marked. Only six months of Landsat data were useable because of cloud cover; these were; January, February, April, June, July, and August.

The first region is Benghazi, this region is divided in to two sub-regions (south of Benghazi covering 360km² and north of Benghazi covering 360km²). The second region is south of Jabal Akhdar (Green Mountain) covering 17,500km². The south of Jabal Akhdar region is divided in to three sub regions (A, B, and C) in order to view the geomorphology of the dust sources in detail.

Each source is defined by a 1km square which represents the actual pixel size of the MODIS pixel. When more than one landform was found in a pixel it was not possible to decide on the nature of the source and the source was termed 'multiple landform' in Table 6.3.

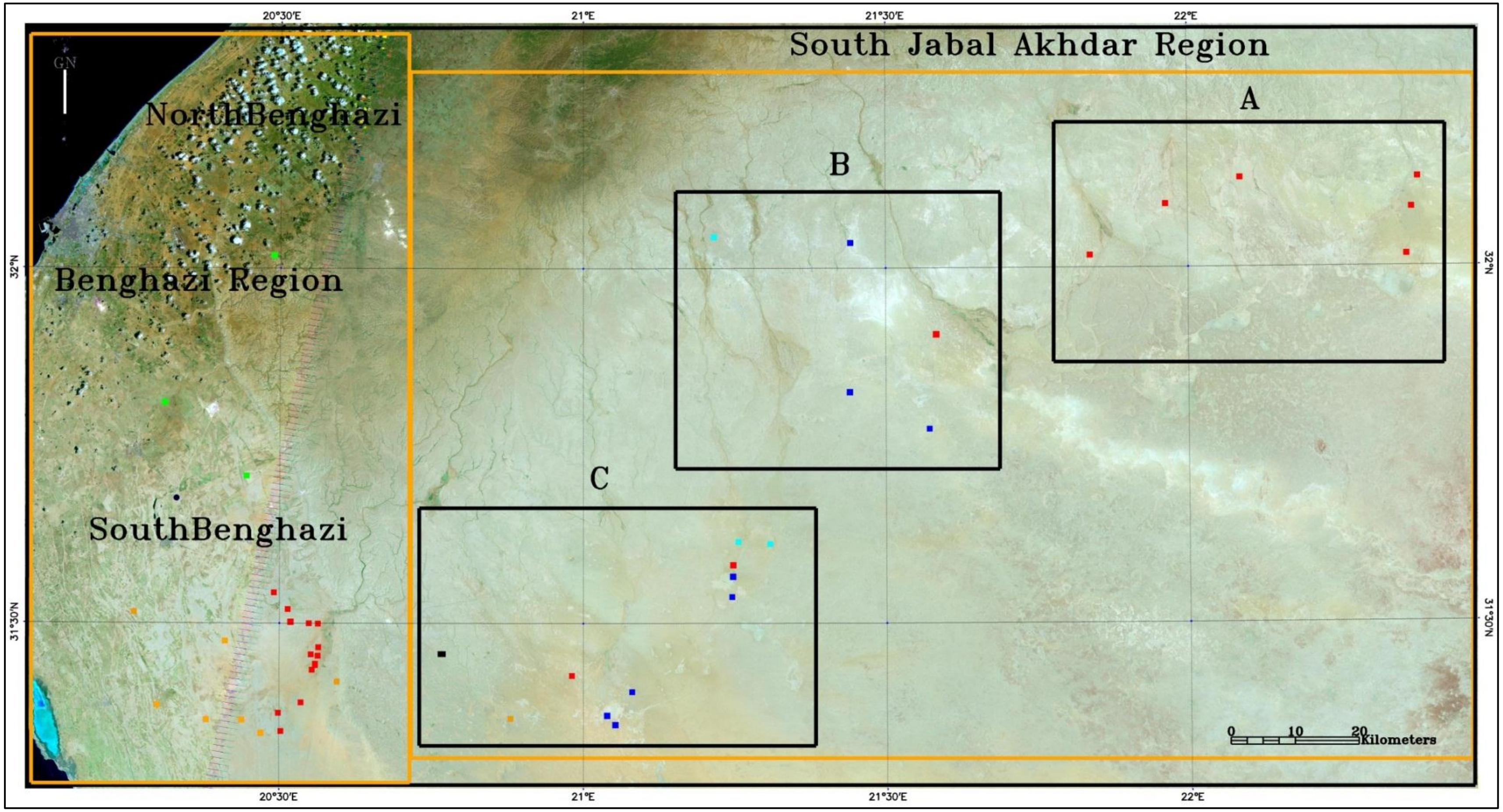


**Dust Sources:** Alluvial Fan Lake River Alluvial Plain Agriculture Multiple Landform

Figure 6.2 Mosaic for two Landsat image showing the two test regions and the 46 dust sources detected in Cyrenaica 2008. Each source type been mapped in different colour as shown in the map key. The study area is divided to two regions; Benghazi region and South of Jabal Akhdar region. Benghazi region is divided to two sub regions; (North Benghazi, South Benghazi) and South of Jabal Akhdar region is divided to three sub regions (A, B, and C).

Table 6.3 listed the 53 dust sources detected in 2008. Each dust source is presented individually showing the date of the dust source, source type, location in Lat & Lon, the duration of the dust storm, the direction, and the estimated cause for the dust storm.

During the following sections, two dust sources from each class of dust source outlined in Table 6.3 will be described in detail and the rest will shown in the appendix. We will start with the southern Jabal Akhdar region where twenty two dust sources are detected. This region is divided in to three sub regions, sub regions A, B and C. Sub-region A has six dust sources, the source detected from alluvial fan on the 25$^{th}$ March will be described in this chapter and the rest are presented in the appendix. Sub-region B has five dust sources, and the source detected from a river on the 16$^{th}$ July will be described here and the rest presented in the appendix. Sub-region C has eleven dust sources, two dust sources detected from a lake the 18$^{th}$ of May and one from river on the 13$^{th}$ of March will be described in this chapter and the rest will be presented in the appendix.

Following this the Benghazi region will presented. The region is divided in to two sub regions; the first sub region is south of Benghazi and has twenty two dust sources, two dust sources detected from alluvial fan on the 11$^{th}$ and 13$^{th}$ of March, and one from an alluvial plain on the 20$^{th}$ of April will be described in this chapter and the rest will be presented in the appendix.

Table 6.3 Dust sources detected over Cyrenaica during year 2008

| No. | Date | Source Type | Location/Lat | Location/Lon | Life Time | Direction | Cause |
|---|---|---|---|---|---|---|---|
| 1 | 11 March | Alluvial Plain | 31°25'17.43"N | 20°49'16.43"E | 09:30 to 15:00 | West-East | Anticyclone |
| 2 | 11 March | Alluvial Fan | 31°30'42.21"N | 20°29'28.37"E | 09:30 to 15:00 | West-East | Anticyclone |
| 3 | 13 March | Alluvial Fan | 32°8'23.44"N | 22°18'39.51"E | 11:30 to 13:00 | NW-SE | Anticyclone |
| 4 | 13 March | Alluvial Fan | 31°28'55.81"N | 20°55'19.99"E | 11:30 to 13:00 | NW-SE | Anticyclone |
| 5 | 13 March | River | 31°40'16.89"N | 21°11'43.52"E | 11:30 to 13:00 | NW-SE | Anticyclone |
| 6 | 13 March | Alluvial Fan | 31°28'23.35"N | 20°32'6.71"E | 09:00 to 15:00 | NW-SE | Anticyclone |
| 7 | 21 March | Diffused dust sources | | | | | |
| 8 | 24 March | Diffused dust sources | | | | | |
| 9 | 25 March | Alluvial Fan | 32°4'25.85"N | 22°18'7.97"E | 08:30 to 15:00 | NW-SE | Anticyclone |
| 10 | 25 March | River | 31°40'4.93"N | 21°14'50.25"E | 08:30 to 15:00 | NW-SE | Anticyclone |
| 11 | 25 March | Alluvial Fan | 31°29'48.77"N | 20°29'56.06"E | 08:30 to 15:00 | NW-SE | Anticyclone |
| 12 | 25 March | Lake | 31°49'48.65"N | 21°30'43.58"E | 08:30 to 15:00 | NW-SE | Anticyclone |
| 13 | 27 March | Diffused dust sources | | | | | |
| 14 | 19 April | Diffused dust sources | | | | | |

| | | | | | | | |
|---|---|---|---|---|---|---|---|
| 15 | 20 April | Alluvial Fan | 31°29'25.30"N | 20°29'38.82"E | 08:00 to 14:00 | South-North | Anticyclone |
| 16 | 20 April | Alluvial Plain | 31°34'17.69"N | 20°12'1.97"E | 08:00 to 14:00 | South-North | Anticyclone |
| 17 | 21 April | Alluvial Plain | 31°25'11.10"N | 20°19'8.57"E | 08:00 to 14:00 | South-North | Anticyclone |
| 18 | 21 April | Alluvial Fan | 31°25'43.55"N | 20°26'20.74"E | 08:00 to 14:00 | South-North | Anticyclone |
| 19 | 21 April | Multiple landforms | 31°30'44.62"N | 20°42'34.35"E | 08:00 to 14:00 | South-North | Anticyclone |
| 20 | 21 April | Lake | 31°35'36.73"N | 21°11'6.40"E | 08:00 to 14:00 | South-North | Anticyclone |
| 21 | 21 April | Alluvial Fan | 31°31'17.08"N | 20°30'15.06"E | 08:00 to 14:00 | South-North | Anticyclone |
| 22 | 22 April | Lake | 31°27'35.31"N | 21°1'15.37"E | 10:00 to 13:00 | South-North | Anticyclone |
| 23 | 14 May | Alluvial Plain | 31°26'25.58"N | 20°14'20.03"E | 08:00 to 16:00 | NW-SE | Harmattan |
| 24 | 14 May | Alluvial Plain | 31°31'50.42"N | 20°21'3.73"E | 08:00 to 16:00 | NW-SE | Harmattan |
| 25 | 14 May | Alluvial Fan | 31°34'32.83"N | 20°27'10.73"E | 08:00 to 16:00 | NW-SE | Harmattan |
| 26 | 14 May | Lake | 31°24'48.12"N | 20°59'35.84"E | 08:00 to 16:00 | NW-SE | Harmattan |
| 27 | 14 May | Alluvial Fan | 31°38'20.22"N | 21°11'13.14"E | 08:00 to 16:00 | NW-SE | Harmattan |
| 28 | 14 May | Lake | 31°52'57.29"N | 21°22'50.45"E | 08:00 to 16:00 | NW-SE | Harmattan |
| 29 | 14 May | Alluvial Fan | 31°57'49.64"N | 21°31'24.25"E | 08:00 to 16:00 | NW-SE | Harmattan |
| 30 | 17 May | Diffused dust sources | | | | | |

| | | | | | | | |
|---|---|---|---|---|---|---|---|
| 31 | 18 May | Lake | 31°25'36.73"N | 20°58'47.13"E | 08:00 to 12:00 | South-North | Anticyclone |
| 32 | 18 May | Alluvial Fan | 31°26'41.64"N | 20°28'32.34"E | 08:00 to 12:00 | South-North | Anticyclone |
| 33 | 18 May | Lake | 31°37'13.24"N | 21°10'55.62"E | 08:00 to 12:00 | South-North | Anticyclone |
| 34 | 03 June | Alluvial Fan | 31°33'20.64"N | 20°29'21.60"E | 08:30 to 11:30 | South-North | Anticyclone |
| 35 | 07 June | Alluvial Plain | 31°25'13.01"N | 20°22'41.00"E | 08:00 to 17:30 | South-North | Anticyclone |
| 36 | 07 June | Alluvial Fan | 31°33'19.47"N | 20°30'12.48"E | 08:00 to 17:30 | South-North | Anticyclone |
| 37 | 7 June | Alluvial Fan | 31°35'57.10"N | 20°25'52.88"E | 08:30 to 11:30 | South-North | Anticyclone |
| 38 | 11 June | Diffused dust sources | | | | | |
| 39 | 13 June | Agriculture | 32°4'28.04"N | 20°25'46.23"E | 12:00 to 12:30 | South-North | Anticyclone |
| 40 | 23 June | Alluvial Fan | 31°30'36.44"N | 20°30'12.65"E | 08:00 to 14:00 | NW-SE | Harmattan |
| 41 | 29 June | Alluvial Fan | 31°24'15.47"N | 20°26'32.52"E | 12:30 to 15:30 | North -South | Harmattan |
| 42 | 16 July | Alluvial Fan | 32°10'56.68"N | 22°19'17.50"E | 06:30 to 16:00 | North -South | Harmattan |
| 43 | 16 July | Alluvial Fan | 32°10'56.68"N | 22° 1'37.92"E | 06:30 to 16:00 | North -South | Harmattan |
| 44 | 16 July | Alluvial Fan | 32° 8'46.96"N | 21°54'9.63"E | 06:30 to 16:00 | North -South | Harmattan |
| 45 | 16 July | Alluvial Fan | 32° 4'27.47"N | 21°46'41.34"E | 06:30 to 16:00 | North -South | Harmattan |
| 46 | 16 July | Lake | 32° 5'32.34"N | 21°22'54.99"E | 06:30 to 16:00 | North -South | Harmattan |

| | | | | | | | |
|---|---|---|---|---|---|---|---|
| 47 | 16 July | River | 32° 6'4.76"N | 21° 8'19.94"E | 06:30 to 16:00 | North -South | Harmattan |
| 48 | 16 July | Alluvial Fan | 31°29'51.56"N | 20°29'56.26"E | 06:30 to 16:00 | North -South | Harmattan |
| 49 | 16 July | Agriculture | 31°52'1.45"N | 20°14'58.38"E | 06:30 to 16:00 | North -South | Harmattan |
| 50 | 24 Sept. | Diffused dust sources | | | | | |
| 51 | 01 Oct. | Agriculture | 31°45'52.47"N | 20°23'7.26"E | 07:00 to 11:00 | South-North | Anticyclone |
| 52 | 02 Oct. | Alluvial Plain | 31°24'5.09"N | 20°24'34.32"E | 07:00 to 11:00 | South-North | Anticyclone |
| 53 | 28 Nov. | Alluvial Fan | 31°33'30.34"N | 20°27'29.91"E | 08:30 to 11:30 | South-North | Anticyclone |

**Percentage: 45% Alluvial Fan 15% Lake 13% Alluvial Plain 6% Agriculture 6% River 2% Multiple landforms 13% Diffuse**

## 6.4 Dust Sources Detected From Southern Jabal Akhdar

Twenty two dust sources were detected in Southern Jabal Akhdar region during 2008 as shown in (Figure 6.2), this represents 42% of dust sources detected during 2008. In south of Jabal Akhdar region seven channels flows down from the mountain and end in alluvial fans and lakes; as can be seen in the Figure 6.3. The largest two lakes are located in the eastern half part of the image in sub-region A (the Al Mekhili paleo-lake). However, there are two small lakes located in the western half of the image in sub-region C. Sub-region B is dominated by alluvial fans.

A

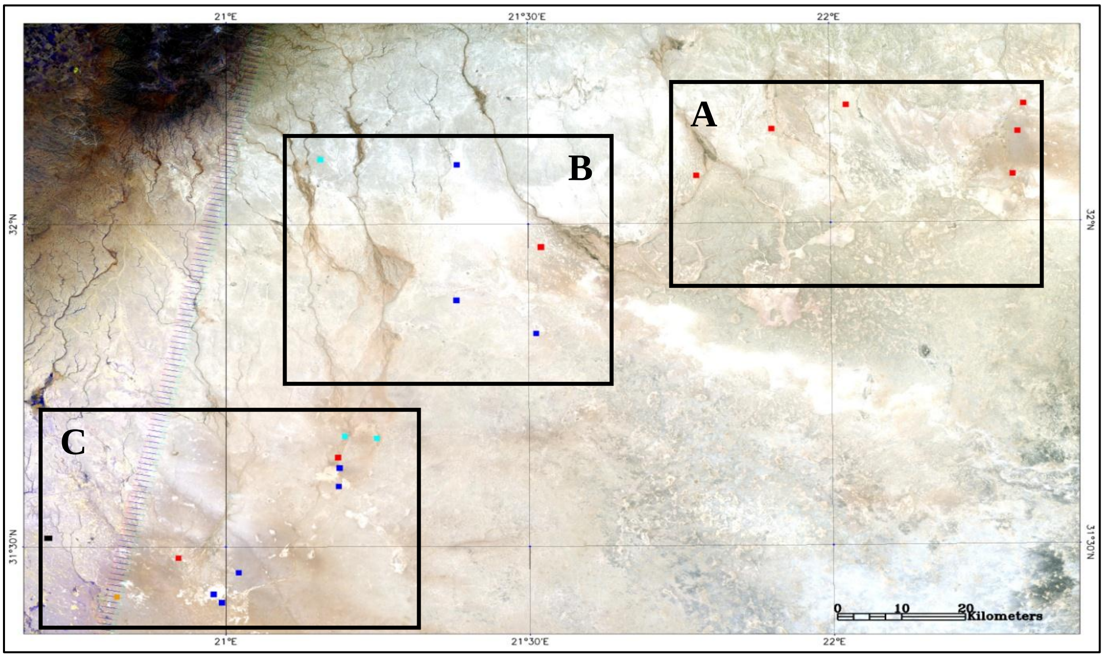


**Dust Sources: Fan Lake River Alluvial Plain Multiple Landform**

B

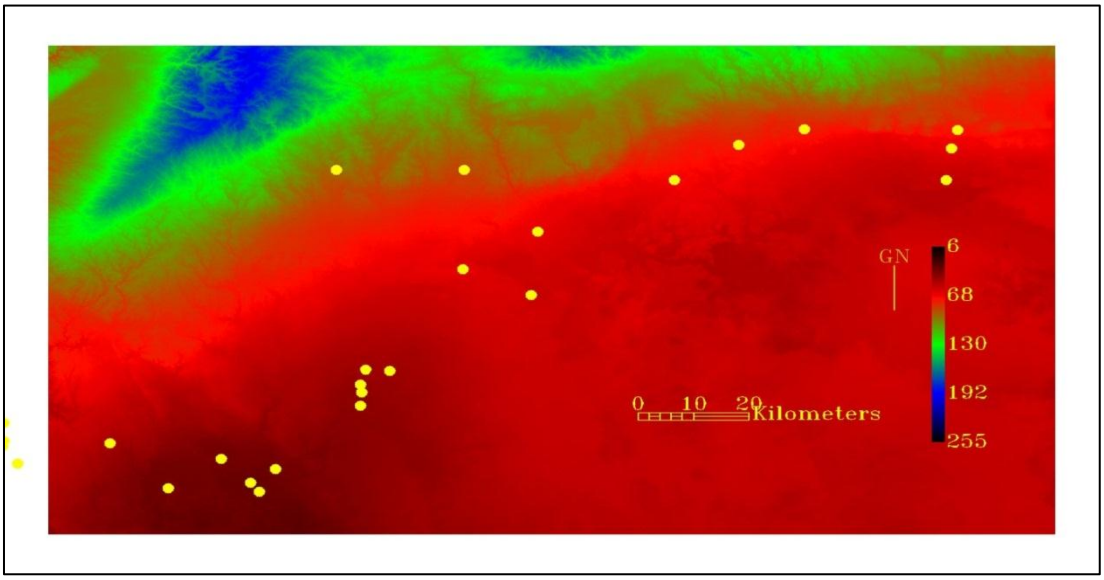


Figure 6.3 (A) Landsat image shows south of Jabal Akhdar region. The region is divided to three sub regions (A,B,C). Dust sources detected are mapped on the image. Each source type been mapped in different colour as shown in the map key. (B) DEM covering the same area, the dust sources plotted in the DEM image in yellow colour.

### 6.4.1 Dust Sources Detected From Southern Jabal Akhdar Sub-Region A

There are six dust sources detected at sub-region A, all from alluvial fans and detected between February and July. Figure 6.4 shows the Landsat colour composite and the NDVI for the months when cloud free data was available; January, February, April, June, July, and August. As we can see in the Figure 6.4 during January and February all the lakes are full of water and all the river channels have got high NDVI. Indeed the NDVI is higher and more extensive in February suggest re-growth along the channels after being supplied with water by the flood that filled the lakes (Figure 6.3). During April some of the lakes start drying and the NDVI starts to decline as the weather starts warming. By June all but one of the lakes contain no surface water and the NDVI of the river channels has continued to decline. During July and August all the lakes stay dry and the NDVI stays low.

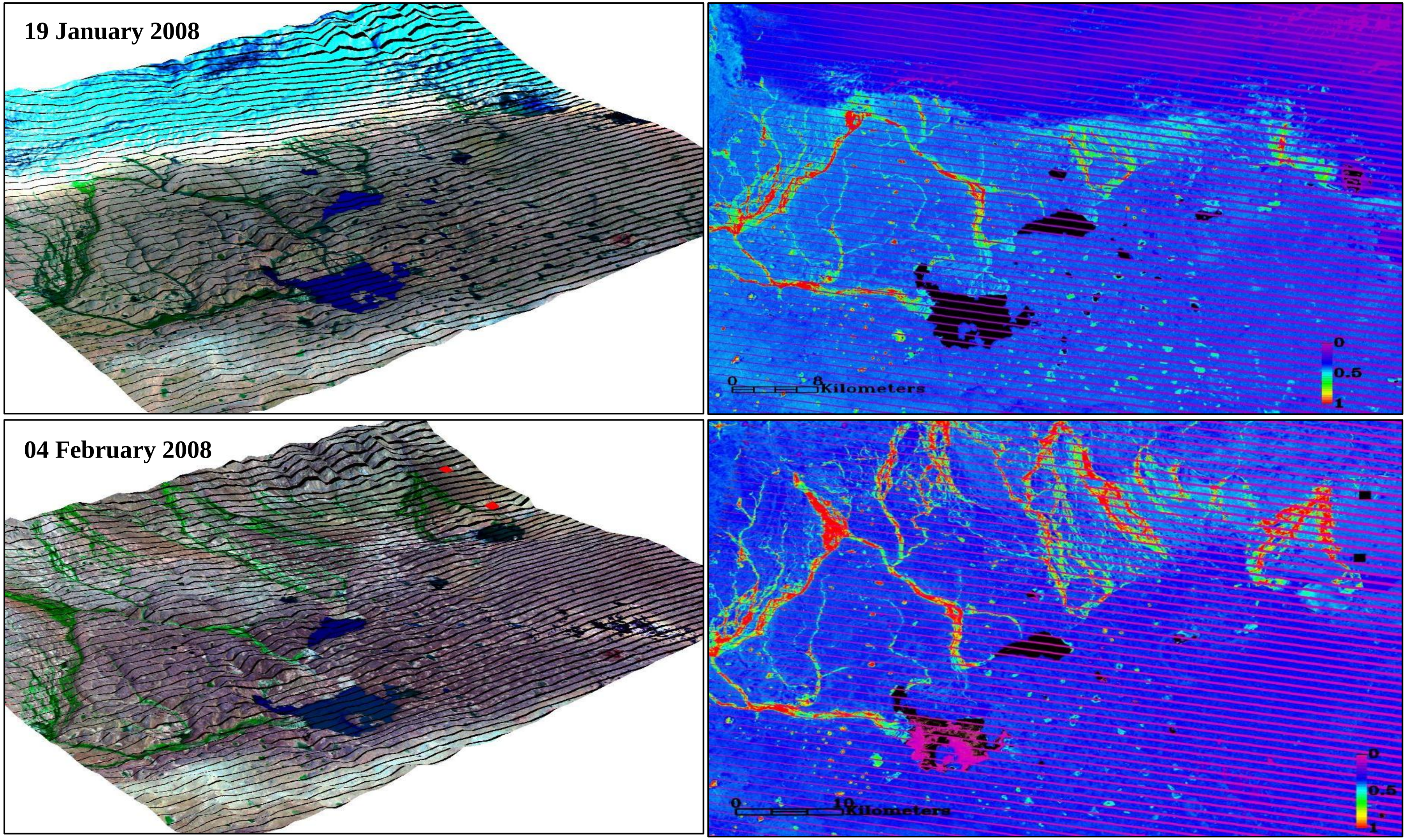
19 January 2008
0
8
Kilometers
0
0.5
1
04 February 2008
0
10
Kilometers
0
0.5
1

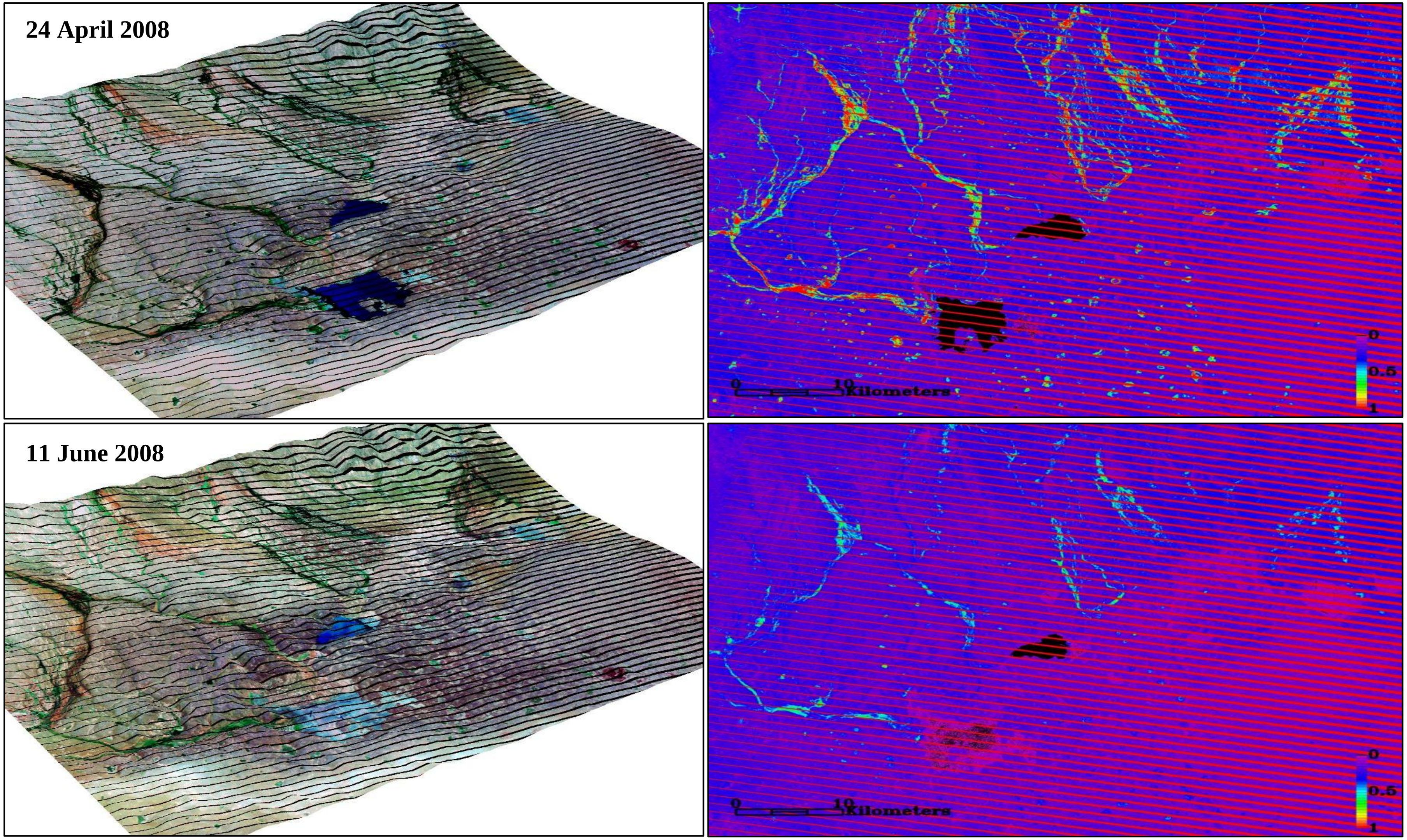
24 April 2008
0
10
Kilometers
0
0.5
1
11 June 2008
0
10
Kilometers
0
0.5
1

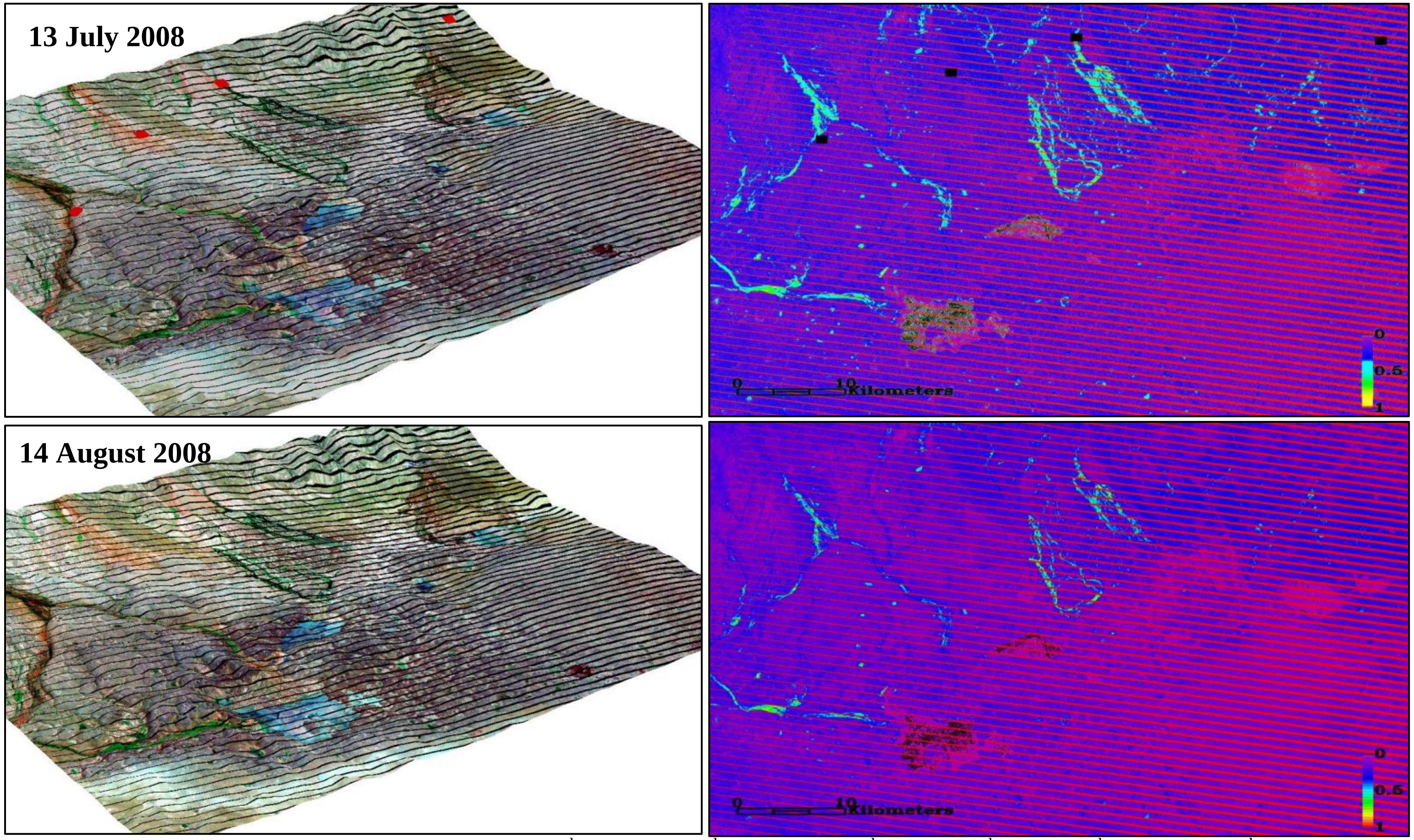


Figure 6.4 3D Landsat images and the NDVI for 19th January, 04th February, 24th April, 11th June, 13th July, and 14th August. The dust sources detected from southern Jabal Akhdar sub-region A during the listed months are displayed on both 3D Landsat and the NDVI images for each month. All the dust sources detected are plotted on the image of the same month or the nearest month if it is not available. The red rectangle in the Landsat images are represents the dust sources detected from alluvial fan. All the dust sources in the NDVI images are represented in black rectangle in order to avoid confusion with the NDVI colour scheme.

### 6.4.1.1 Dust Sources Detected From Alluvial Fans on 25th March 2008 in the Southern Jabal Akhdar Sub-Region A

Two of the six detected dust sources from southern Jabal Akhdar sub-region A detected during March are discussed here. These two dust sources are detected from Almekhili alluvial fan located in the east of the image (Figure 6.5). They are found in an area of low vegetation cover on the margins of the alluvial fan as is clearly shown in the NDVI image. The dust source detected on 25th of March will be described below and the other dust source is shown in the appendix.

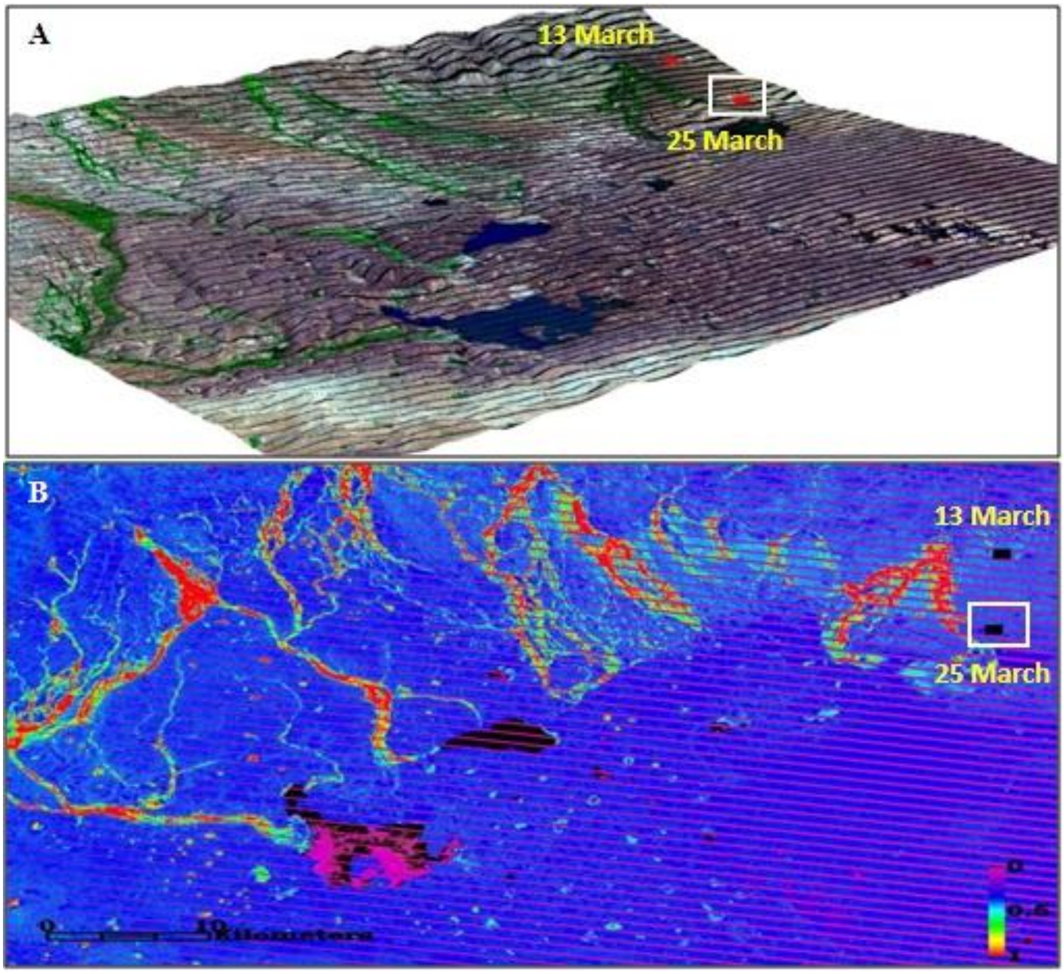


Figure 6.5 (A) 3D Landsat image dated 4th February shows the dust sources detected during March 2008 at south of Jabal Akhdar region. The red rectangle represents the dust sources detected from alluvial fan. (B) 3D NDVI map. The black rectangular box shows the location of all the dust sources detected on 25th March 2008 from Almekhili alluvial fan. The dust source detected on 25th March is highlighted by white rectangle.

The river channels are seasonal and generally flow episodically during winter. There is some agricultural activity along some of the rivers after the flows subside and the channels have been irrigated by the floodwaters. Figure 6.6 shows the Google Earth images and in them it is clear that the dust source is just off the vegetated part of the alluvial fan in a river channel, as is indicated by the NDVI (Figure 6.5 B). Thus the dust source is at the end of a river channel on the alluvial fan that did not experienced flooding and vegetation growth during 2008 and thus had unprotected sediments that could be deflated when the region experienced high wind speeds.

**A**

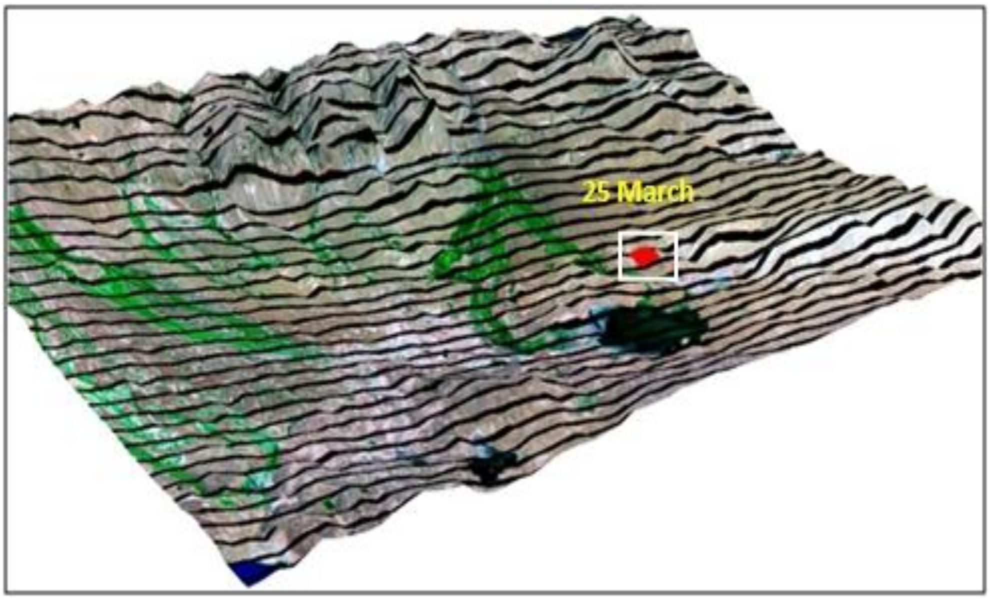

**B**

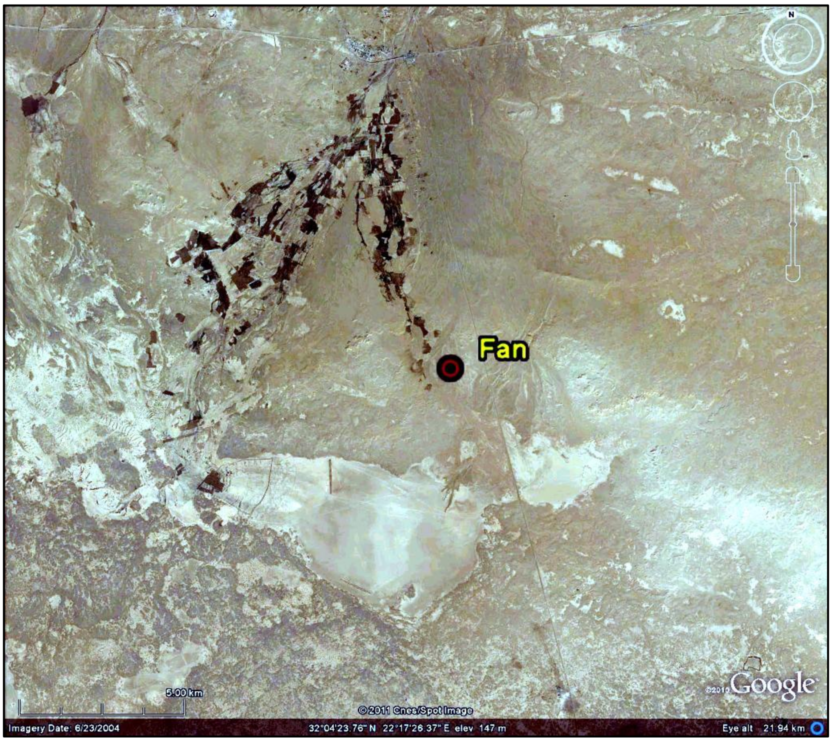


**C**

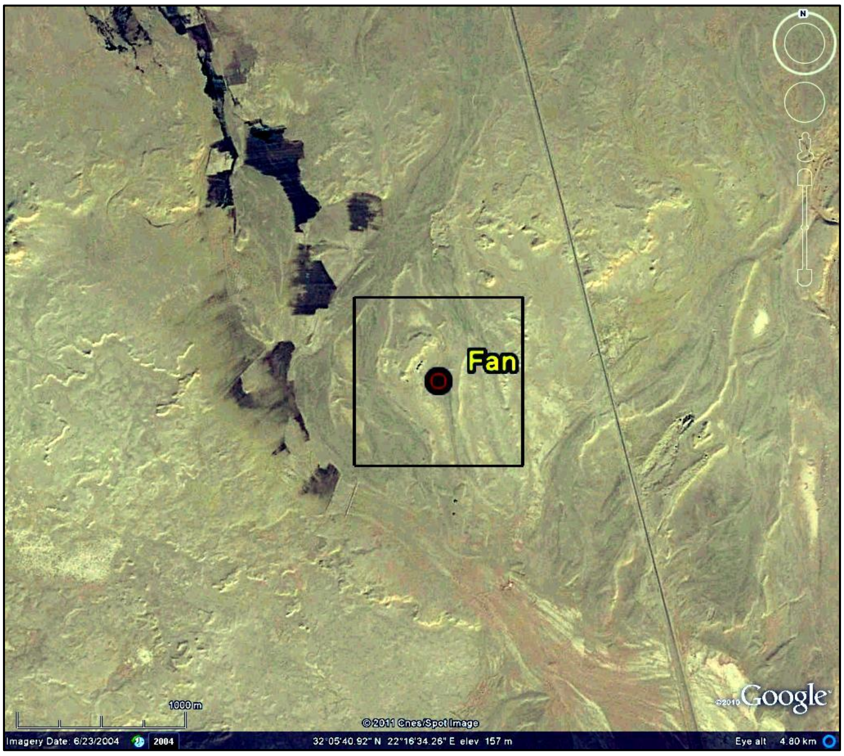


Figure 6.6 (A) 3D Landsat image dated 04th February 2008 shows the dust source detected on 25th March 2008. The red rectangle represent the dust source comes from alluvial fan, the dust source is highlighted by white rectangle. (B&C) Google Map images showing the spatial detail of the dust source at two different scales (B) 5km, and (C) 1km. The black square represents the size of one pixel from MODIS data which is used for the dust detection.

### 6.4.2 Dust Sources Detected From Southern Jabal Akhdar Sub-Region C

There are eleven dust sources detected at sub-region C that come from five different landforms; five from lakes, two from rivers, two from alluvial fans, one from an alluvial plain, and one from a multiple landform. It is clear that most sources are either from lakes or rivers. As we can see in Figure 6.7 the lakes in this region are dry throughout the year and this may explain why they are sources whilst the lakes that are inundated in sub-region A are not. Regarding the rivers, during January and February the rivers channels in the west have got high NDVI were as the rivers channels in the east have got lower NDVI. The presence of NDVI or 0.5 throughout most of the region in January suggests that the region experienced widespread rainfall, however, in the east a lack of water flows down the rivers is suggested by the lower NDVI. Indeed the rainfall throughout the region must have been much lower than in sub-region A as all the lakes remain empty throughout the year. By April the NDVI has declined, presumably due to the onset of the hot summer when most of the river channels are drying out. By June, July, and August the NDVI is very low along all the rivers suggesting that they are dry throughout this time.

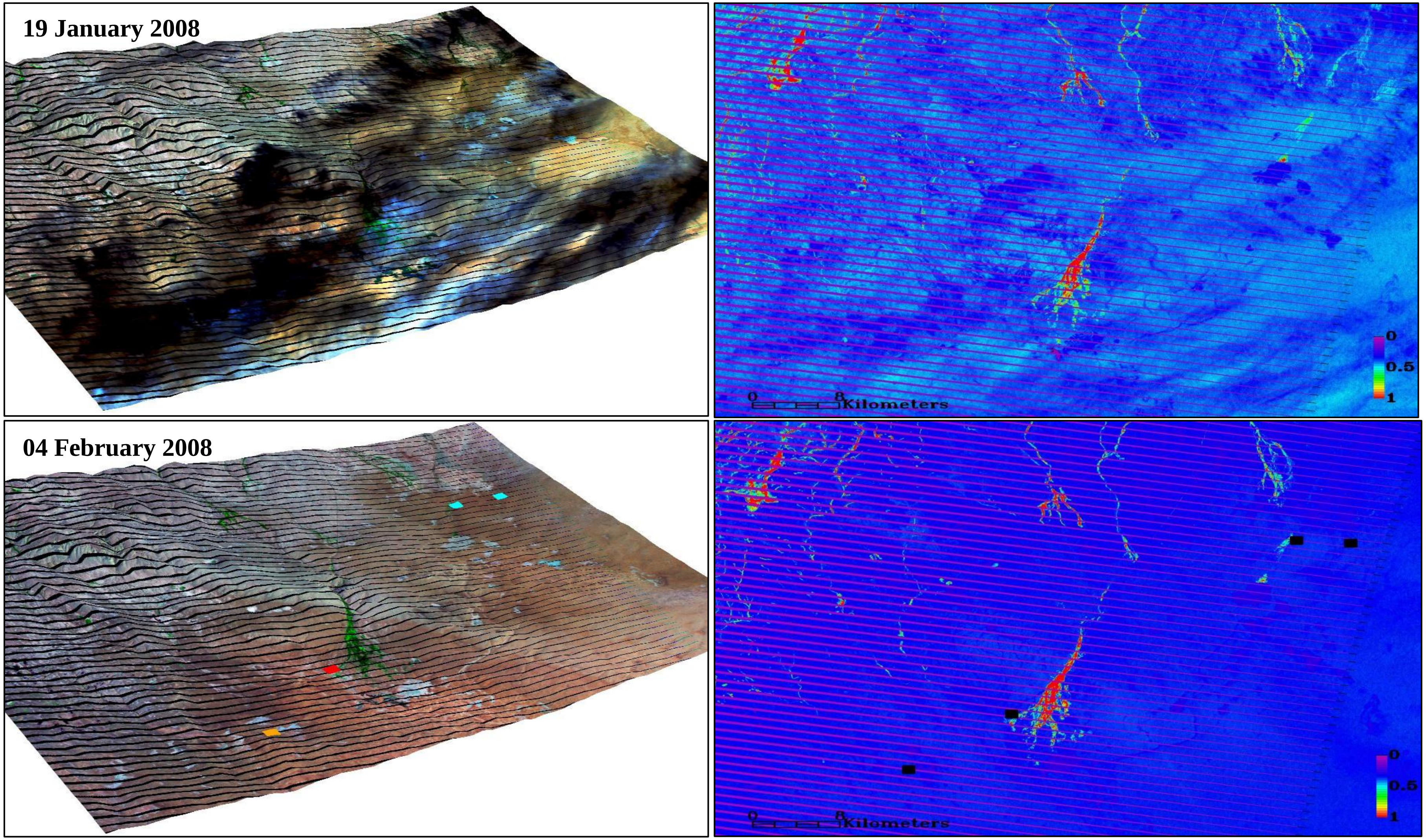
19 January 2008
0
0.5
1
0 8 Kilometers
04 February 2008
0
0.5
1
0 8 Kilometers

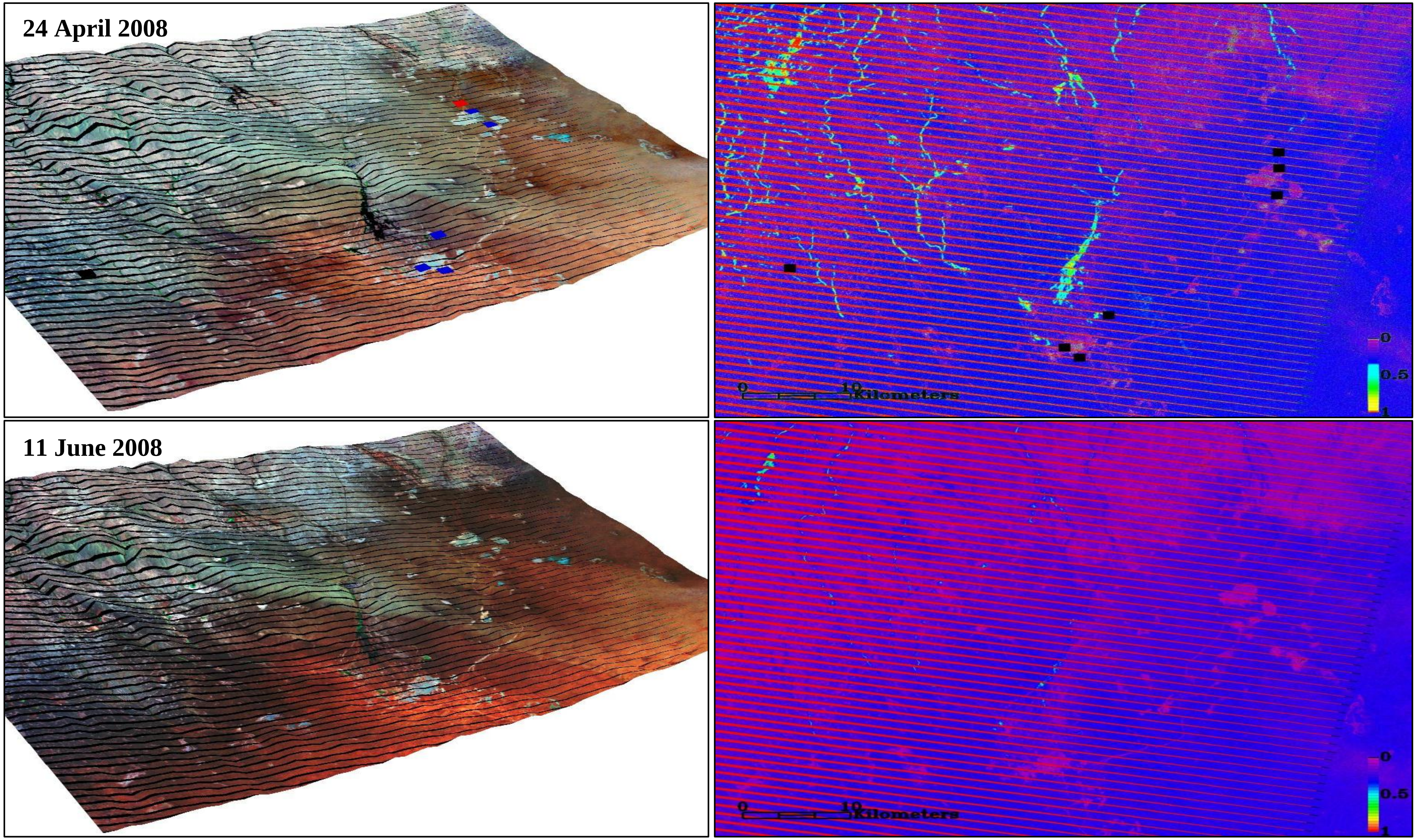
24 April 2008
0
10
Kilometers
0
0.5
1
11 June 2008
0
10
Kilometers
0
0.5
1

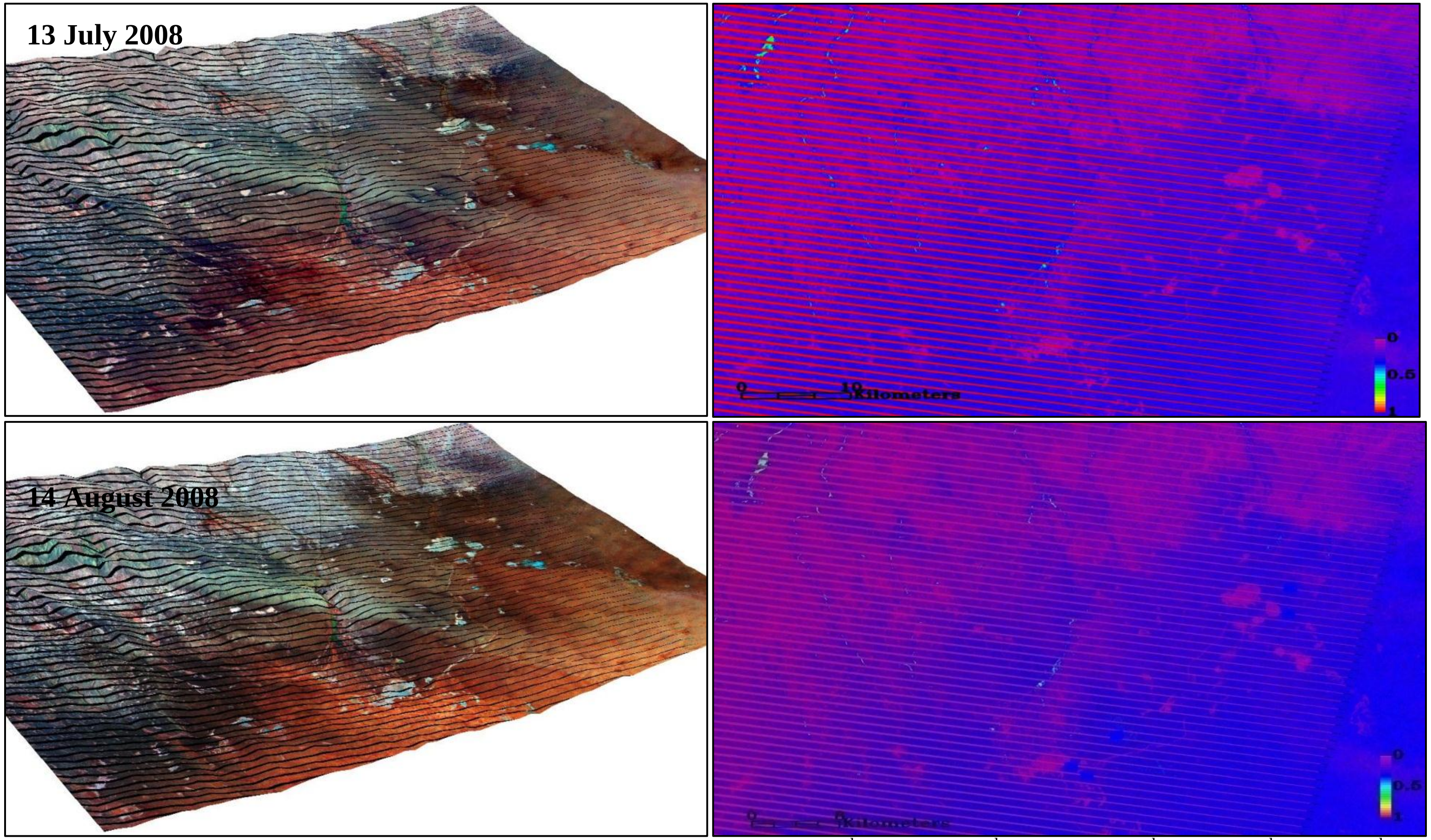


Figure 6.7 3D Landsat images and the NDVI file for the following months: 19th January, 04th February, 24th April, 11th June, 13th July, and 14th August. The dust sources detected from South of Jabal Akhdar sub-region C during the listed months are displayed on both 3D Landsat and the NDVI images for each month. All the dust sources detected are plotted on the image of the same month or the nearest month if it is not available. The orange rectangle in the Landsat images are represent the dust sources detected from alluvial plain, the red rectangle is alluvial fan, the blue rectangle is lake, and the cyan rectangle is river. All the dust sources in the NDVI images are represented in black rectangle in order to avoid confusion with the NDVI colour scheme.

#### 6.4.2.1 Dust Sources Detected From Rivers on 13th March 2008 in the Southern Jabal Akhdar Sub-Region C

There are only three dust sources detected from rivers during 2008, all of these sources are detected from the rivers draining Jabal Akhdar, one from sub-region B and two sub-region C. Rivers represent 6% from the total detected sources and all these are located near the mouths of the rivers where fine grained sediments can be expected to be deposited. The dust sources detected on the 13th March will be described below and the rest are shown in the appendix.

The river dust source detected on the 13th March is found in the north east of the image (Figure 6.8). The area is free of vegetation as is clearly shown in the NDVI image (Figure 6.8 B). Figure 6.9 A and B shows that three rivers flow off the Jabal Akhdar in this area, the two rivers located in the centre of the image merge together in one channel just before they flow into an ephemeral lake. It is just below this merger point where the dust source is detected. Figure 6.9 C shows that the central location of the dust source is just off the west side of the river, however, the 1km² pixel size of the MODIS covers the river and given that this is where a large amount of fines are located it is most likely that the dust comes from the river.

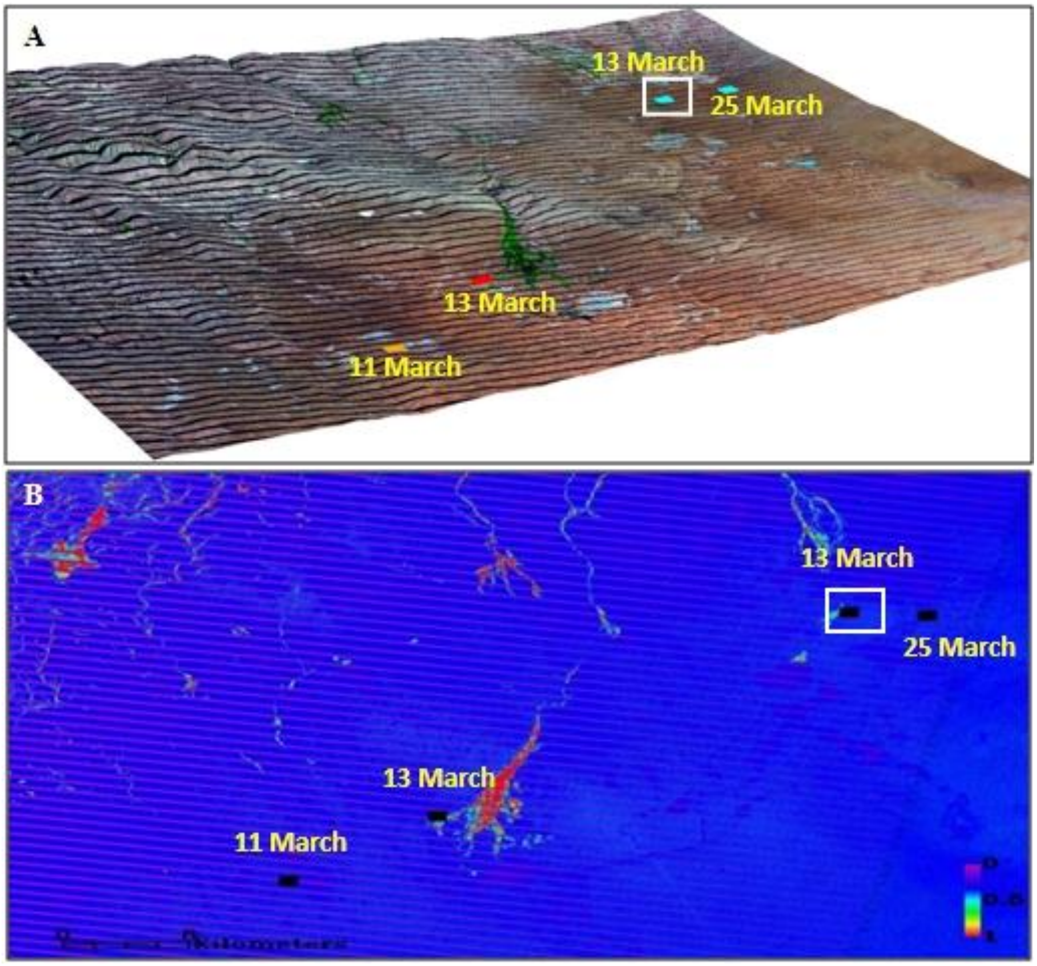


Figure 6.8 (A) 3D Landsat image dated 04th February 2008 showing the dust sources detected during March 2008 in the southern Jabal Akhdar region. The cyan rectangle in Figure 6.8-A represent the dust sources detected from river, red from alluvial fan, and orange from alluvial plain. (B) NDVI of Landsat image. The dust source detected on 13th March is highlighted by white rectangle. All the dust sources in Figure 6.8 B are represented in black rectangle in order to avoid confusion with the NDVI colour scheme.

**A**

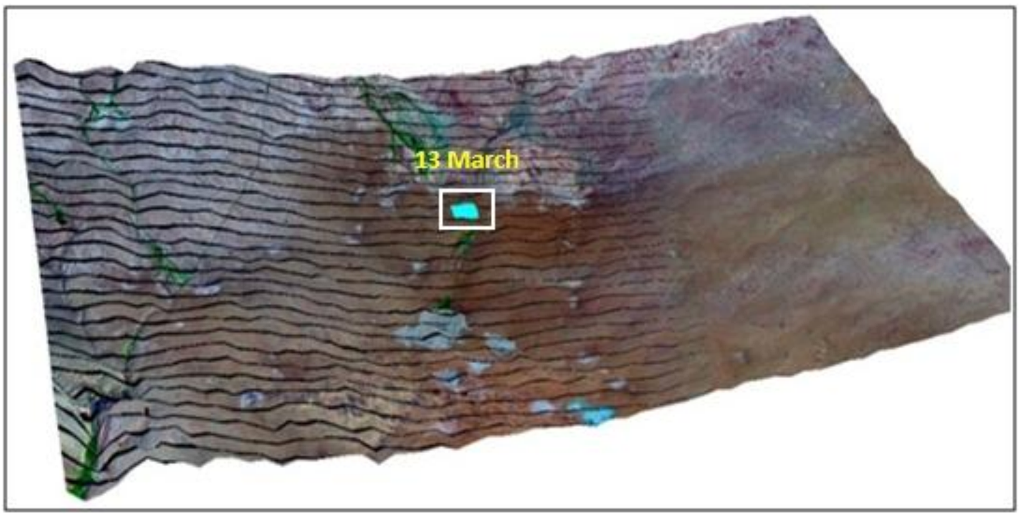

B

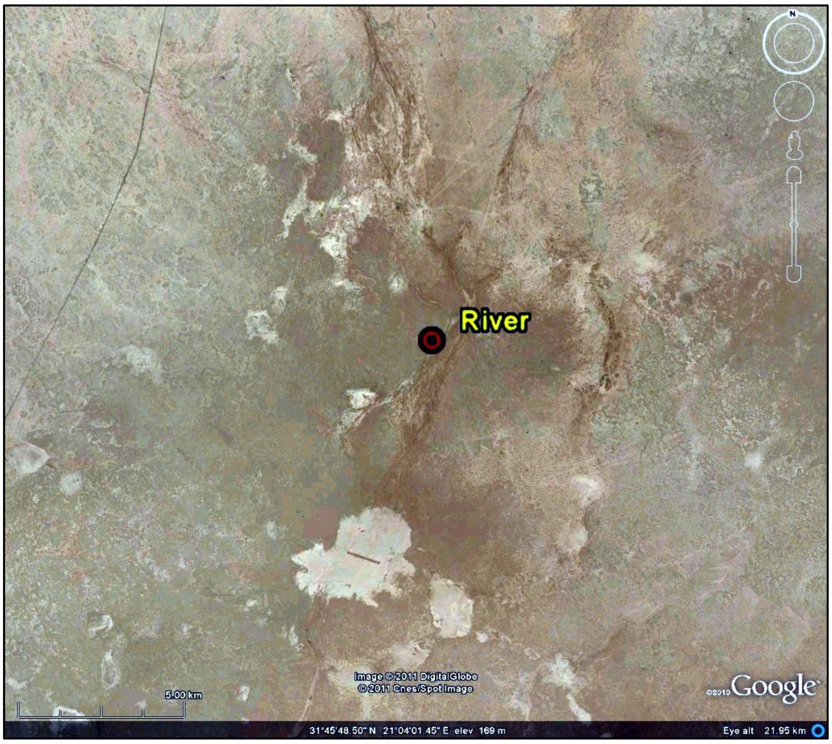


C

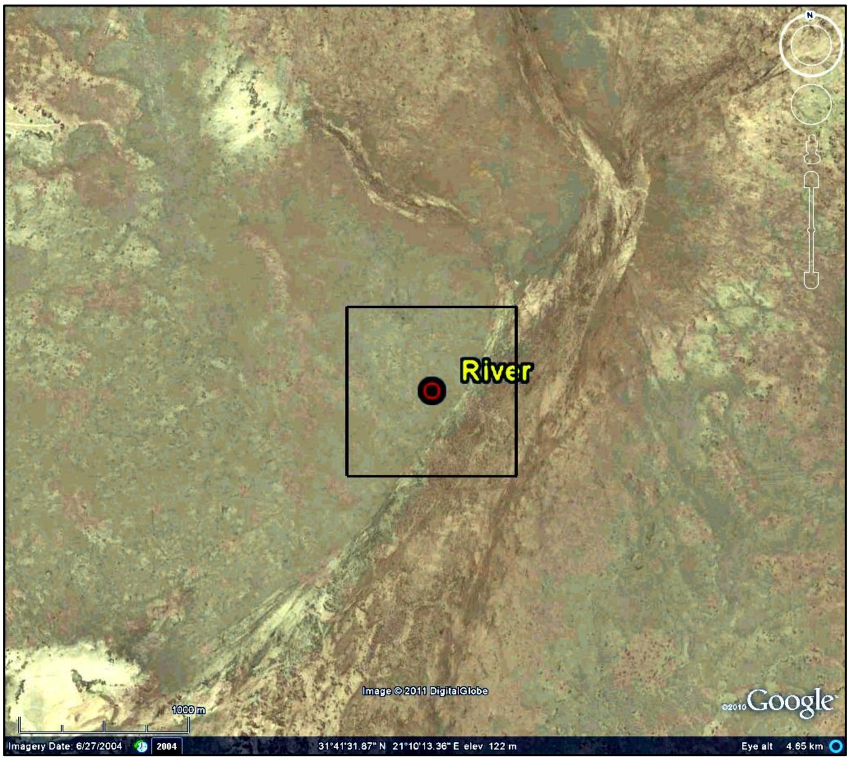


Figure 6.9 (A) 3D Landsat image dated 04th February 2008 shows the dust source detected on 13th March 2008. The cyan rectangle represent the dust source comes from river, the dust source is highlighted by white rectangle. (B&C) Google Map images showing the spatial detail of the dust source at two different scales (B) 5km, and (C) 1km. The black square represents the size of one pixel from MODIS data which is used for the dust detection.

### 6.4.2.2 Dust Sources Detected From Lakes on 18th May 2008 in the Southern Jabal Akhdar Sub-Region C

Figure 6.10 shows a 3D landsat image captured on the 24th of April 2008, this image is used to display the dust sources detected on May because no cloud free Landsat image was available during May 2008 and this is the closest date that an image was captured. During May six dust sources are detected in this region, five from lakes, one from alluvial fan, and one from multiple landforms as can be seen in Figure 6.10. Thus most of the dust sources detected during this month were from lakes, this is probably because all of the lakes were dry due to the fact that in this part of the Jabal Akhdar there was not enough rain to fill them. Indeed the highest percentage of dust sources detected from lakes in any one month is during May and theses sources are from the second largest dust storms detected at Cyrenaica during 2008.

On 18th May one of the dust sources is detected from the lake located in the north east of the image fed by a river from to the east of Jabal Akhdar (Figure 6.11A). There are two channels feeding the lake, one from the north and the second from the east probably through link between this lake and another small lake located north east of the lake in question (Figure 6.11A). Figure 6.10B clearly shows the network between the lakes and the channel comes from alluvial fans to the north and north-east of the lake. Moreover, there is link between this lake and another located further down south east of the lake (Figure 6.11 A,B).

The dust source detected is located in flat surface near the southern edge of the lake (Figure 6.11-C). None of the lakes in this sub-region contain water and because of this the dry clays and silts on the lake bed appear to be deflating. Presumably the sandblasting process on the bed lake is producing this dust.

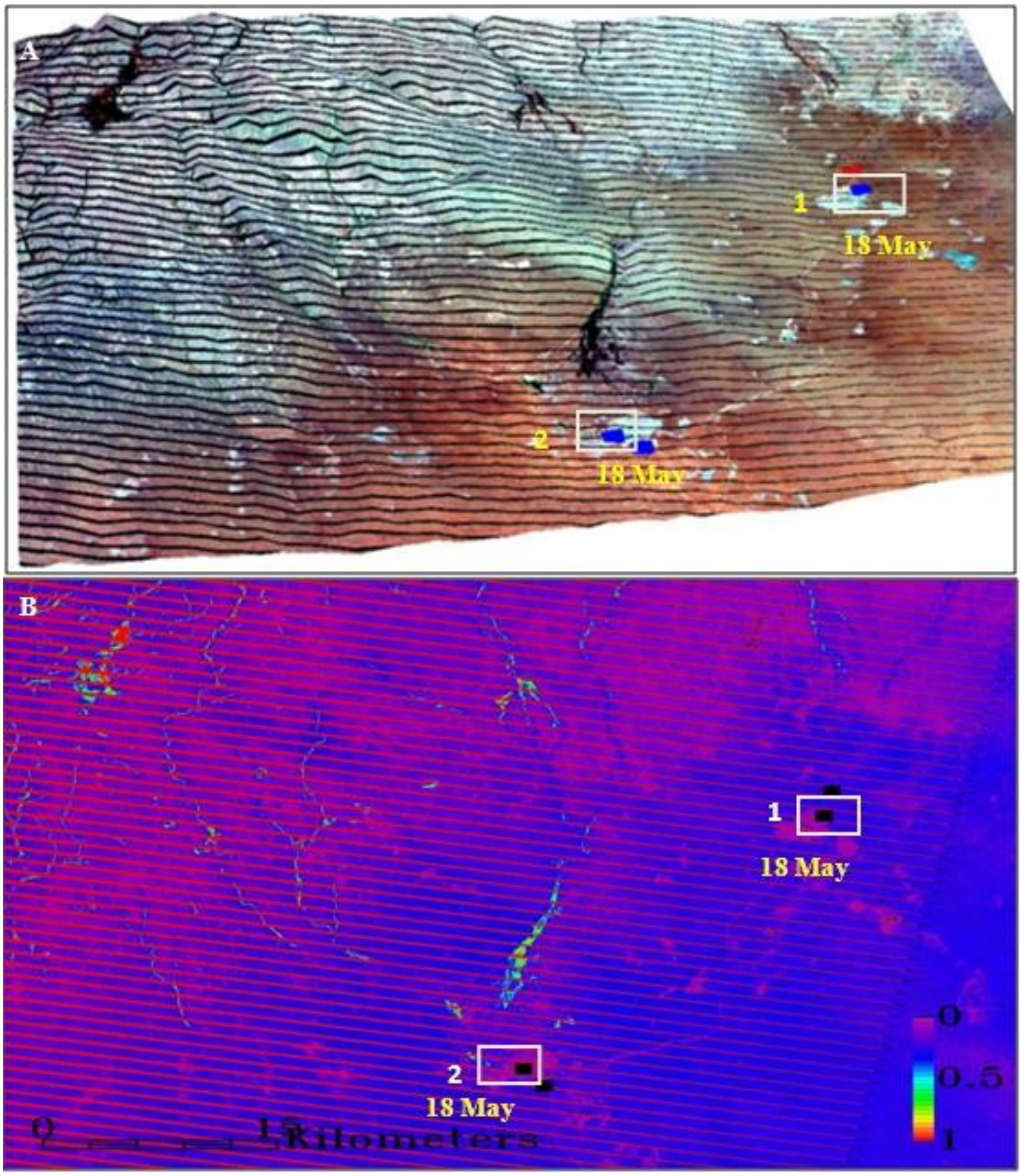


Figure 6.10 (A) 3D Landsat image dated 24th April 2008shows the dust sources detected during May 2008 at south of Jabal Akhdar region. The dust sources detected on 18th May from lake. (B) NDVI Index map for the Landsat image. The two white rectangles on figure 6.10-A display the two dust sources detected on 18th May 2008 from lake. The blue rectangle in Figure 6.10-A represent the dust sources detected from lake and the red from alluvial fan. All the dust sources in Figure 6.10-B are represented in black rectangle in order to avoid confusion with the NDVI colour scheme.

**A**

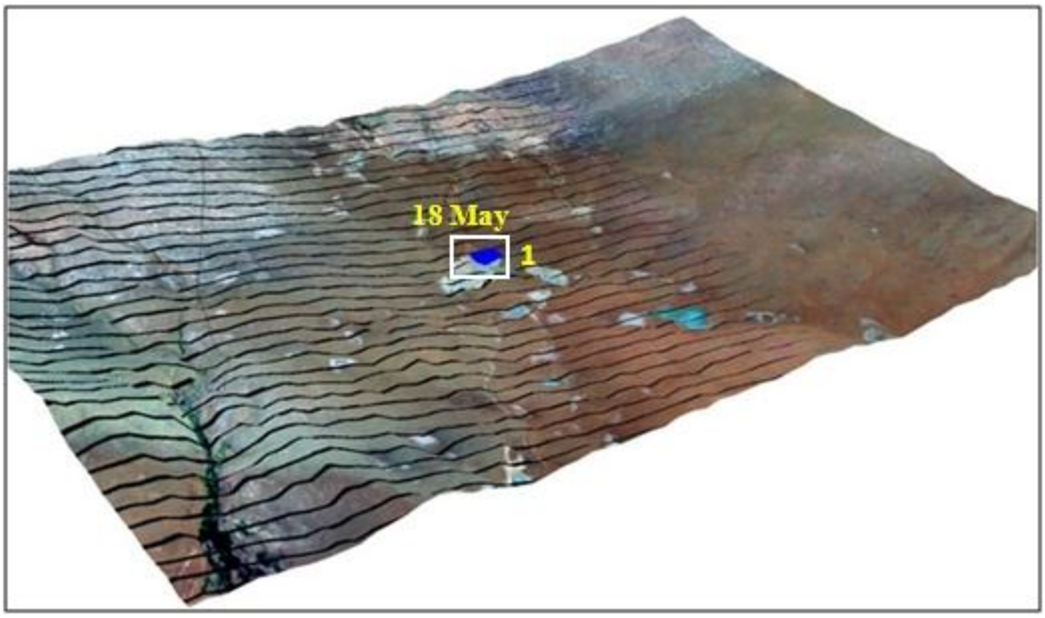
18 May
1

**B**

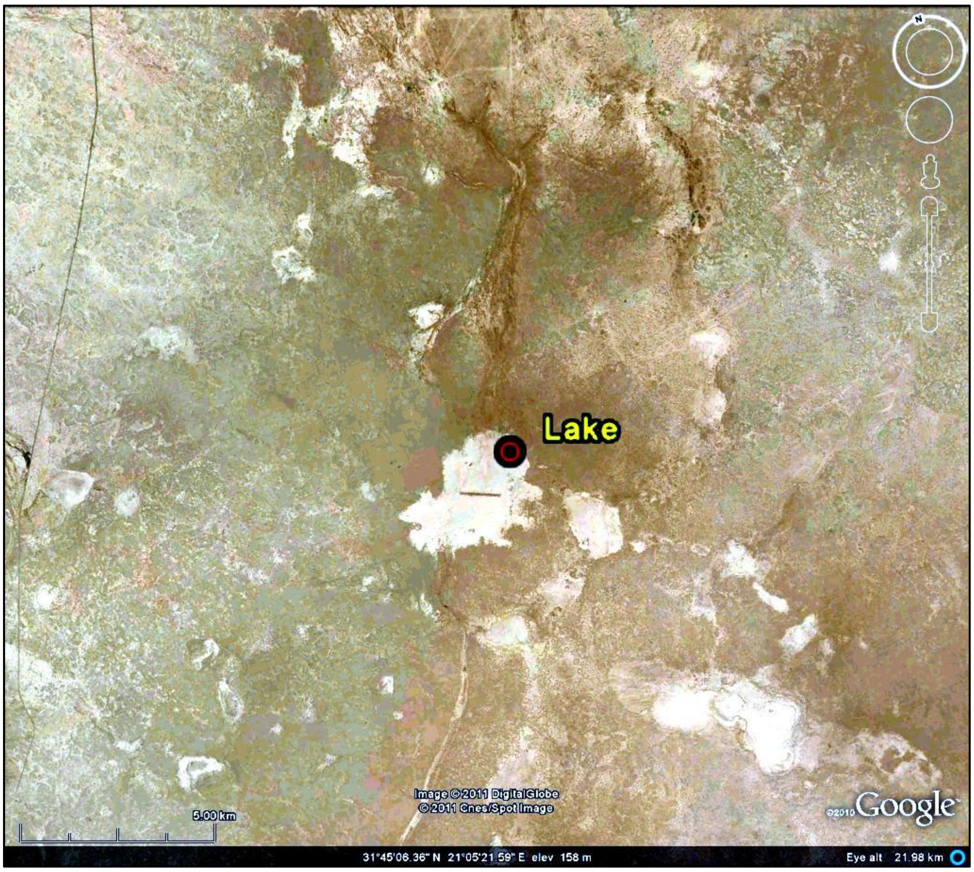
Lake
Image ©2011 DigitalGlobe
©2011 Cnes/Spot Image
5.00 km
31°45'06.36" N 21°05'21.59" E elev 158 m
Eye alt 21.98 km
©2010 Google

**C**

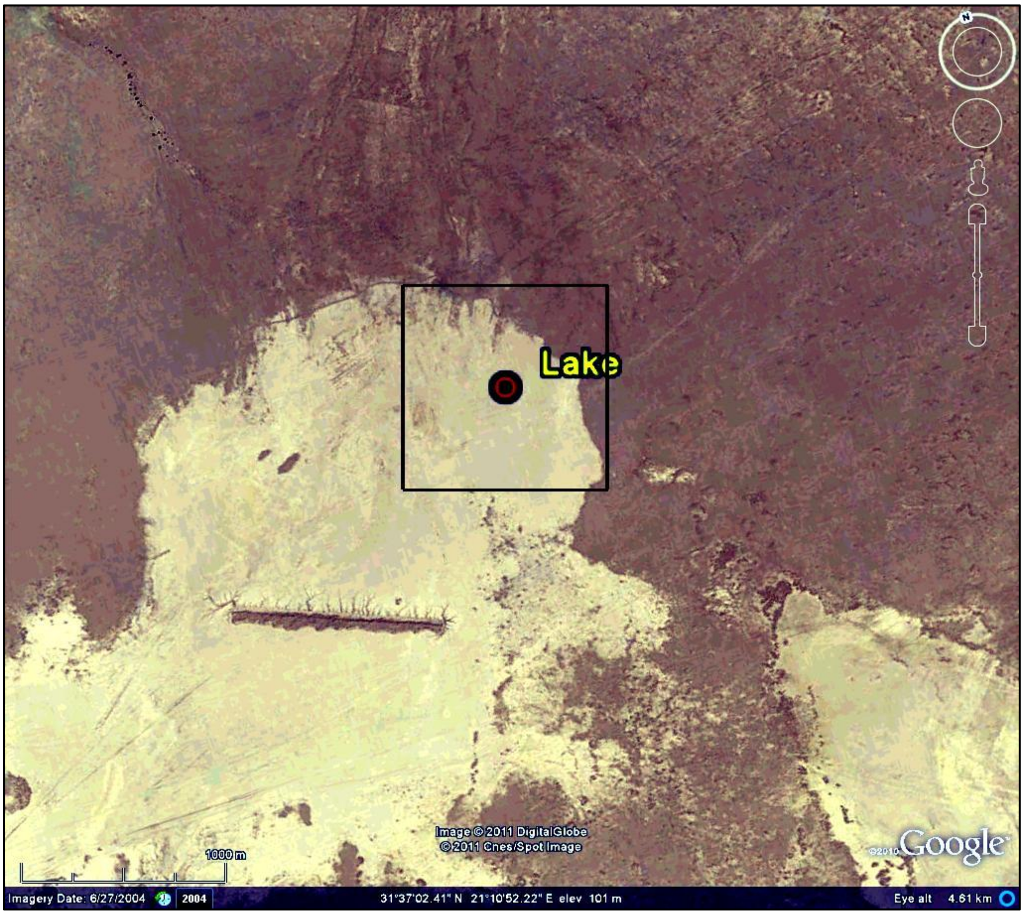


Figure 6.11 (A) 3D Landsat image dated 24th April 2008 shows the dust source detected on 18th May 2008. The blue rectangle represent the dust source comes from lake, the dust source is highlighted by white rectangle. (B&C) Google Map images showing the spatial detail of the dust source at two different scales (B) 5km, and (C) 1km. The black square represents the size of one pixel from MODIS data which is used for the dust detection.

On 18th May another dust sources are also detected on a lake in the south of the image (Figure 6, region 2) that is also fed by a river from eastern Jabal Akhdar (Figure 6.12A). Figure 6.12-B shows there are group of lakes here. The dust source is located on the eastern part of the largest lake, clearly within in the range of the 1km² presenting the MODIS pixel size (Figure 6.12-C). Like the previously described lake this one is completely dry during the and presumably the surface and deflation conditions are similar.

**A**

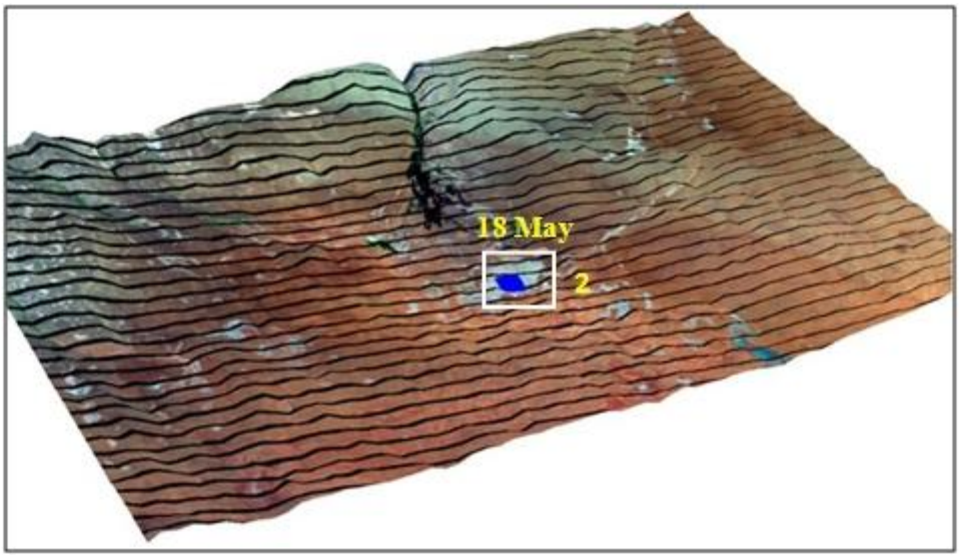
18 May
2

**B**

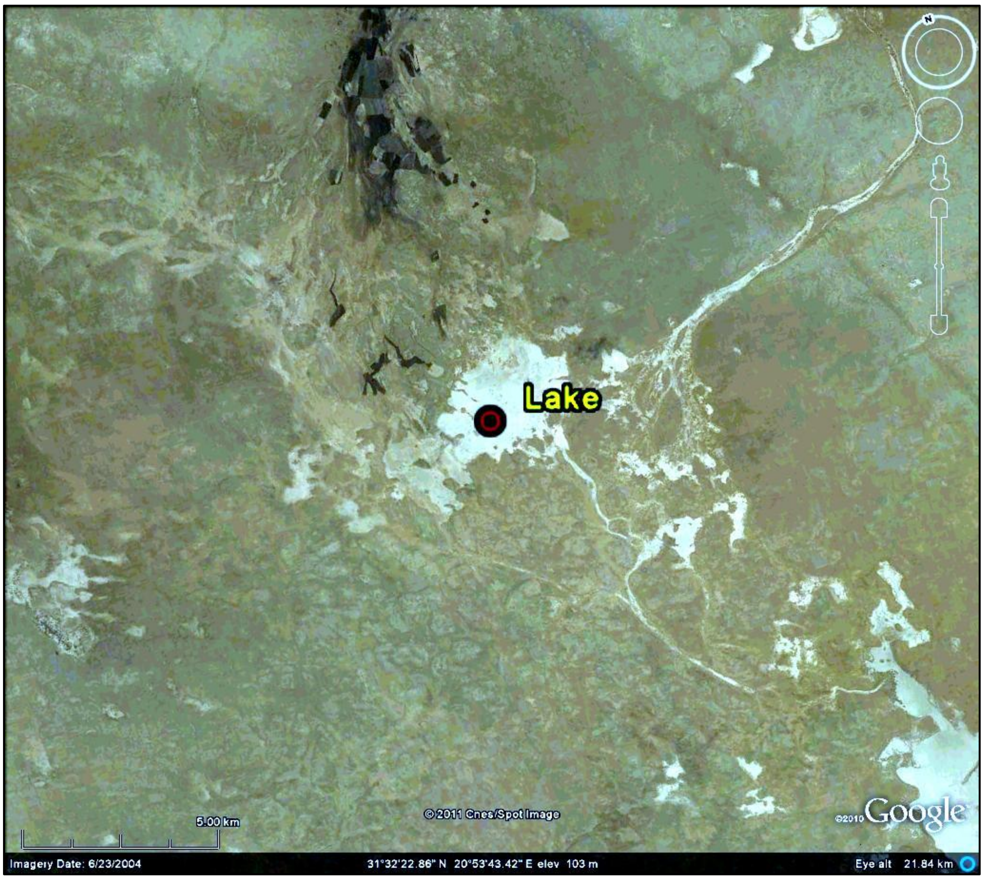
Lake
5.00 km
©2011 Cnes/Spot Image
©2010 Google
Imagery Date: 6/23/2004
31°32'22.86" N 20°53'43.42" E elev 103 m
Eye alt 21.84 km

**C**

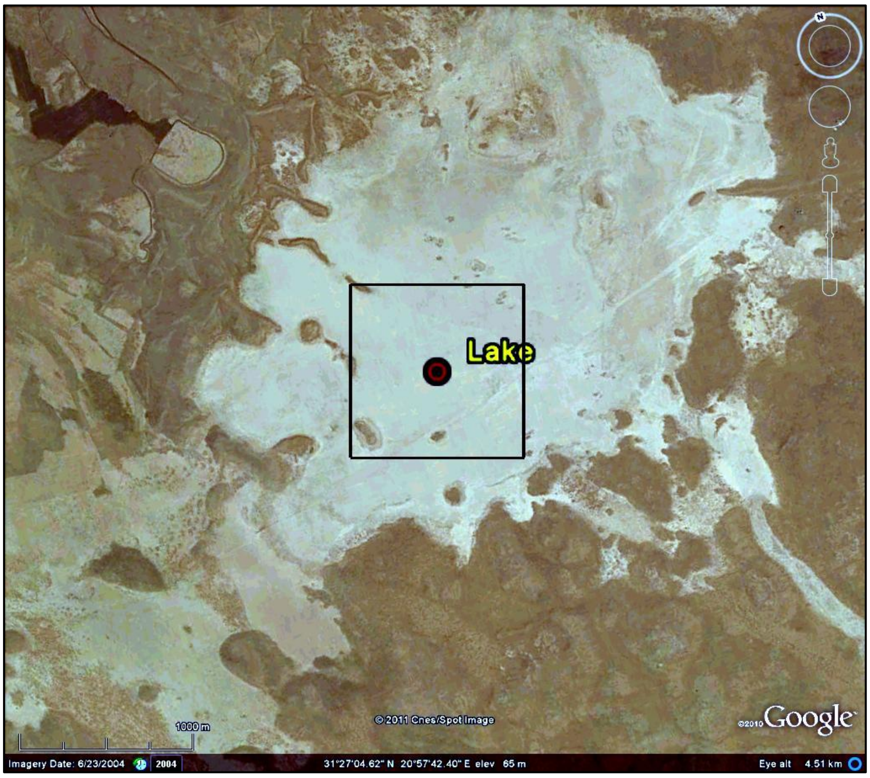


Figure 6.12 (A) 3D Landsat image dated 24th April 2008 shows the dust source detected on 18th May 2008. The blue rectangle represent the dust source comes from lake, the dust source is highlighted by white rectangle. (B&C) Google Map images showing the spatial detail of the dust source at two different scales (B) 5km, and (C) 1km. The black square represents the size of one pixel from MODIS data which is used for the dust detection.

### 6.4.3 Dust Sources Detected From Southern Jabal Akhdar Sub-Region B

Five dust sources are detected from sub-region B, all during March, May, and July, three of them from lakes and the other two from a fan and a river. As we can see in the Figure 6.13, the size of the lakes are small in this region compared to sub-region A. Regarding the rivers, in January and February many of the rivers channels in the eastern part of the image have got high NDVI, whereas the rivers channels at the west part of the image have got low NDVI due to lack of water flows down from Jabal Akhdar. Furthermore, the lakes in the east of the image (Figure 6.13) are full of water during January and February whilst those in the west are dry throughout the year. By April, the NDVI is low in general in the river channels and all the lakes are dry. During summer (June, July, and August) the rivers and lakes stay dry and the NDVI is very low.

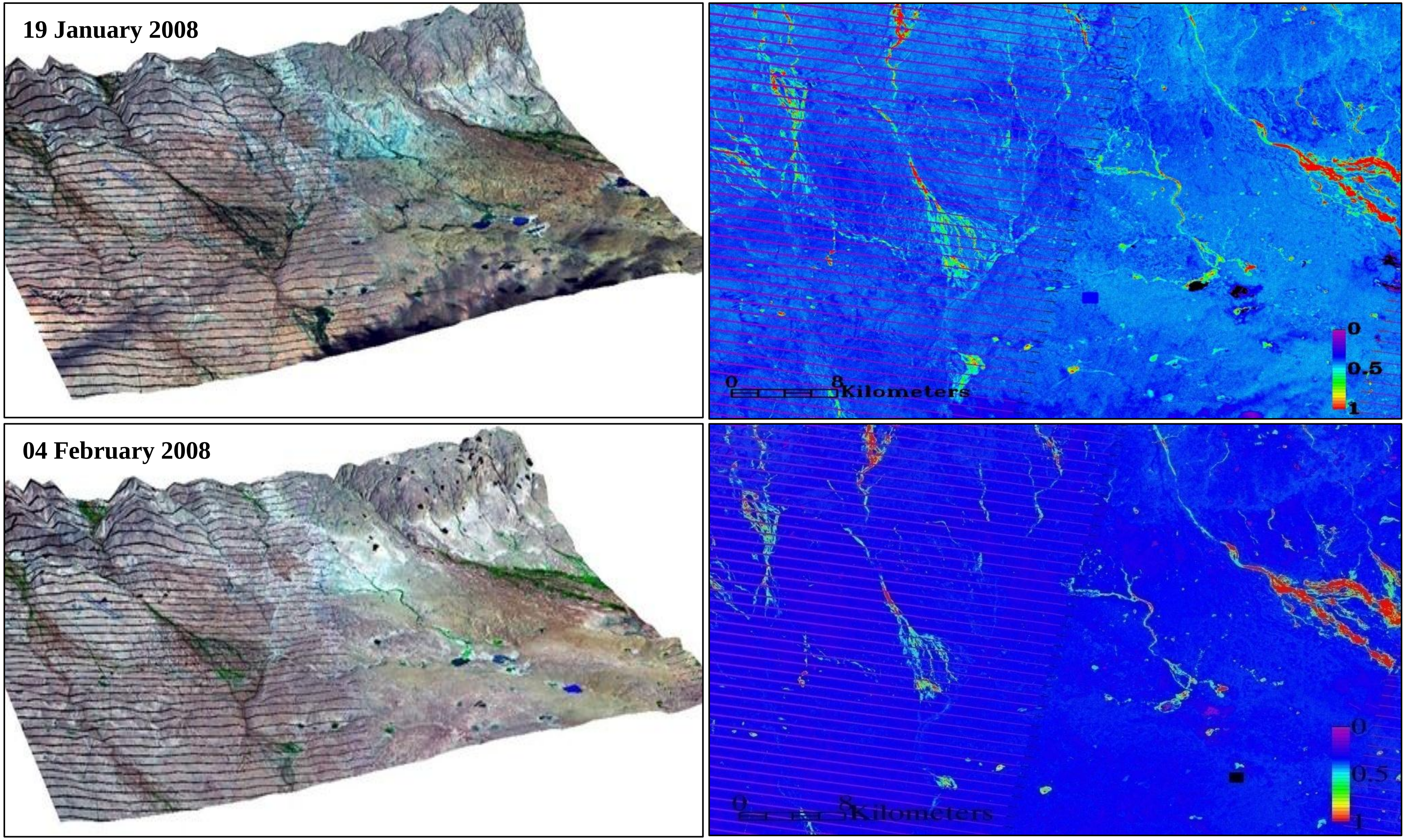
19 January 2008
04 February 2008
0
8
Kilometers
0
0.5
1
0
8
Kilometers
0
0.5
1

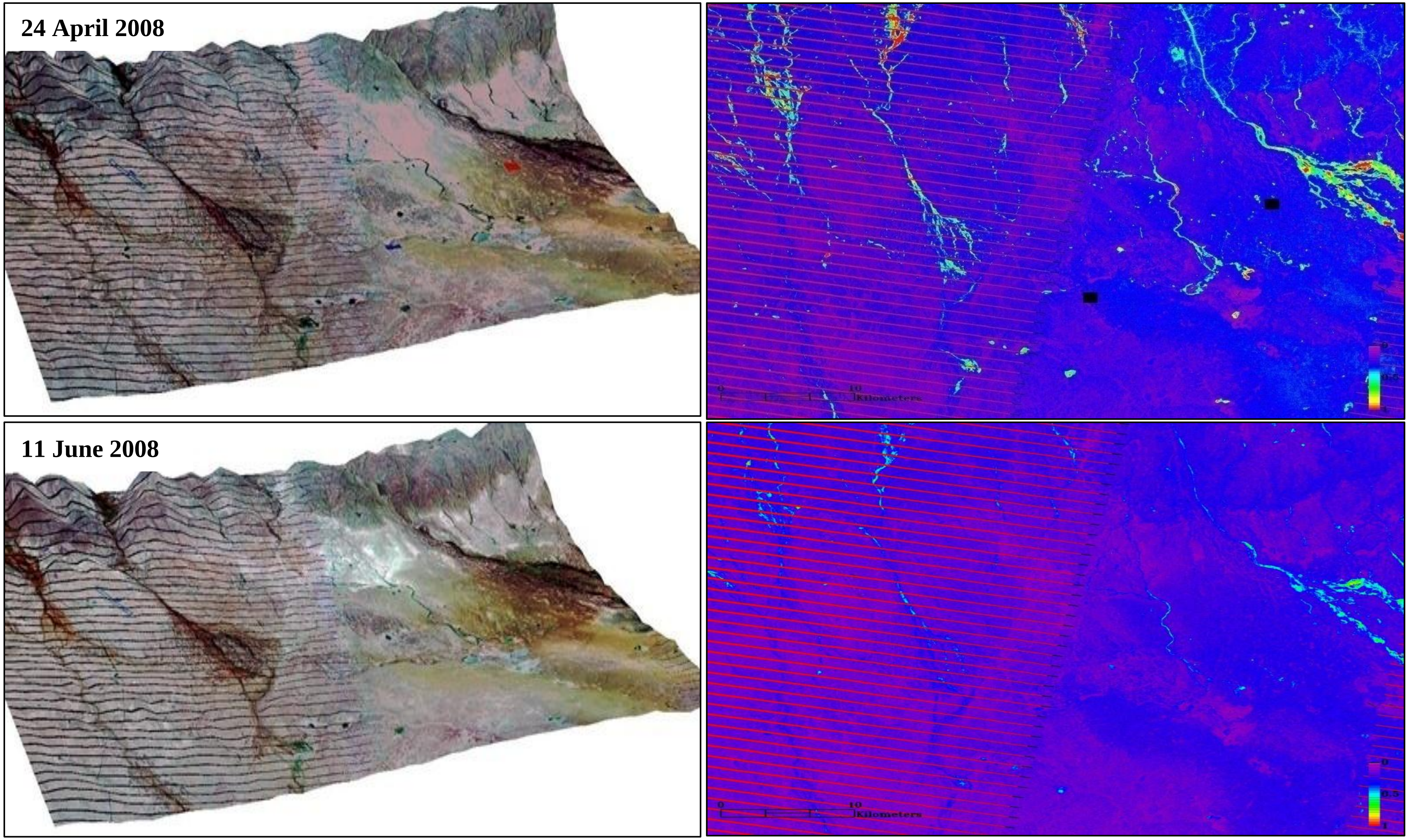
24 April 2008
11 June 2008
0
10
Kilometers
0
10
Kilometers

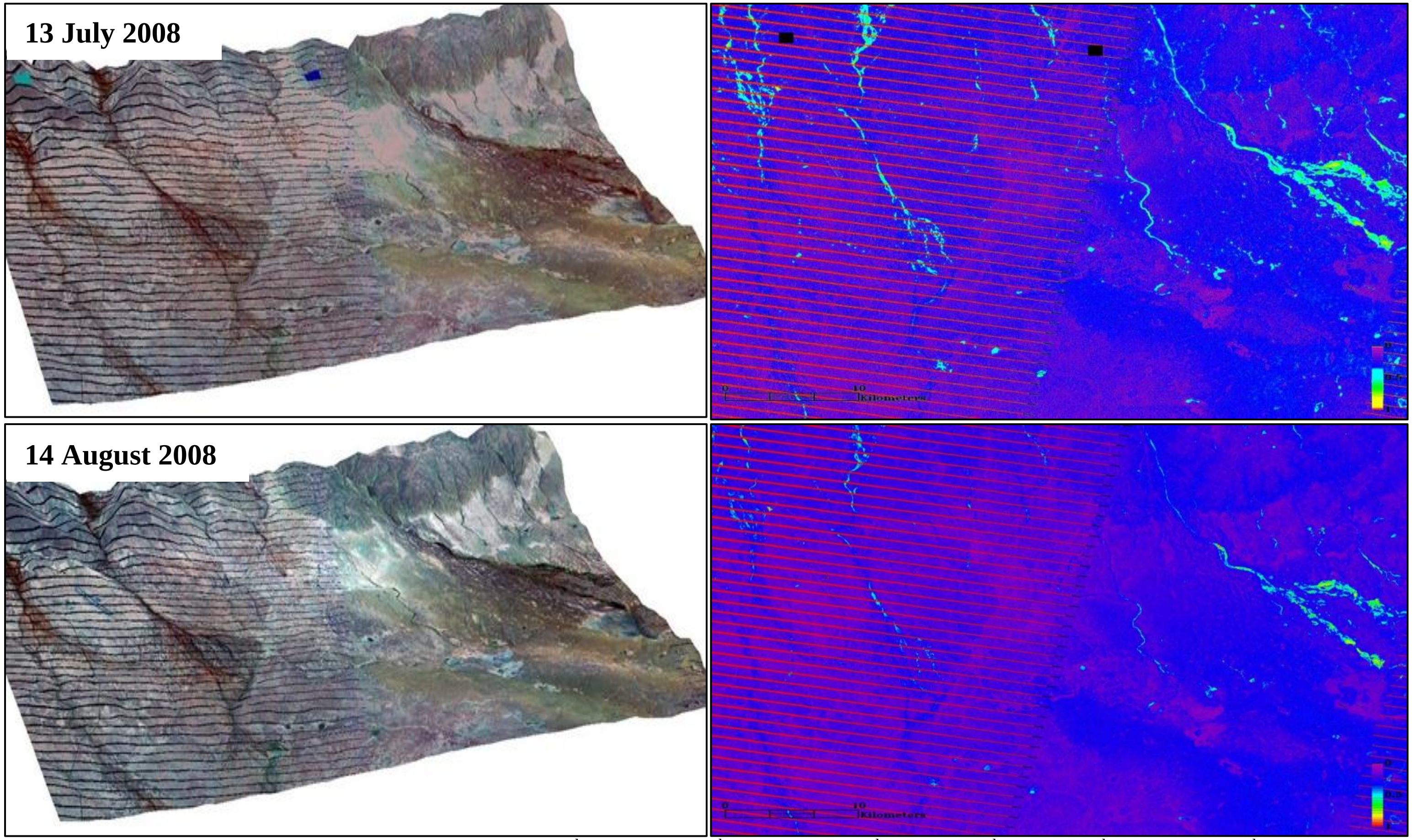


Figure 6.13 3D Landsat images and the NDVI for 19th January, 04th February, 24th April, 11th June, 13th July, and 14th August. The MODIS dust sources detected during this time are displayed on both 3D Landsat and the NDVI images for each month. All the dust sources detected are plotted on the image of the same month or the nearest month if it is not available. The red square in the Landsat colour composites shows the dust sources detected from alluvial fans, the blue square from lakes, and the cyan from rivers. All the dust sources in the NDVI images are represented in black rectangle in order to avoid confusion with the NDVI colour scheme.

### 6.4.3.1 Dust Sources Detected From River on 16 July 2008 in the Southern Jabal Akhdar Sub-Region C

During 2008 there are two large dust storms in Cyrenaica, the dust storm detected on the 16 July was one of these, six different sources were detected across the south of Jabal Akhdar, and two of these sources are detected from sub-region B (Figure 6.14) directed from north to south and caused probably by harmattan winds.

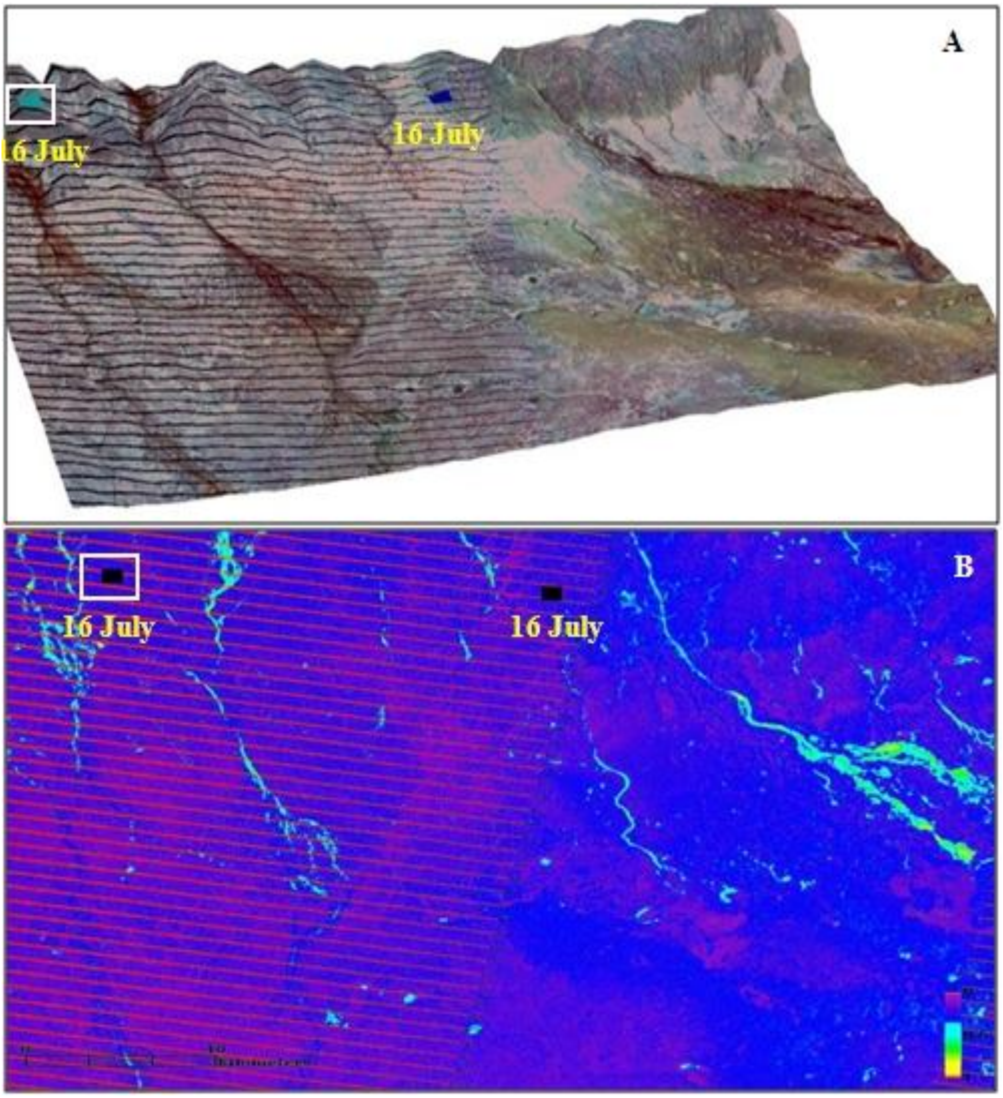


Figure 6.14 (A) 3D Landsat image dated 13th July 2008 showing the dust sources detected during July 2008. The two rectangles display the dust source detected on 16 July 2008 from river. The blue square represent the dust sources detected from lake, the cyan rectangle from river. (B) NDVI map for the Landsat image. All the dust sources are represented in black square in order to avoid confusion with the NDVI colour scheme. The dust source detected from river is highlighted by white rectangle.

A dust source is detected from river on 16 July 2008 and is highlighted in black rectangle (Figure 6.14B). The NDVI value at the dust source is almost zero indicating no vegetation at that branch from the main river. Furthermore, the NDVI value of the main river has got higher value compared to dust source, but still low < 0.5 suggesting low flow and a lack of rain in the catchment headwaters This dust was probably be generated from the dry unvegetated river bed. Probably sediments remained at the river from the previous water floods are used to complete the sandblasting process.

**A**

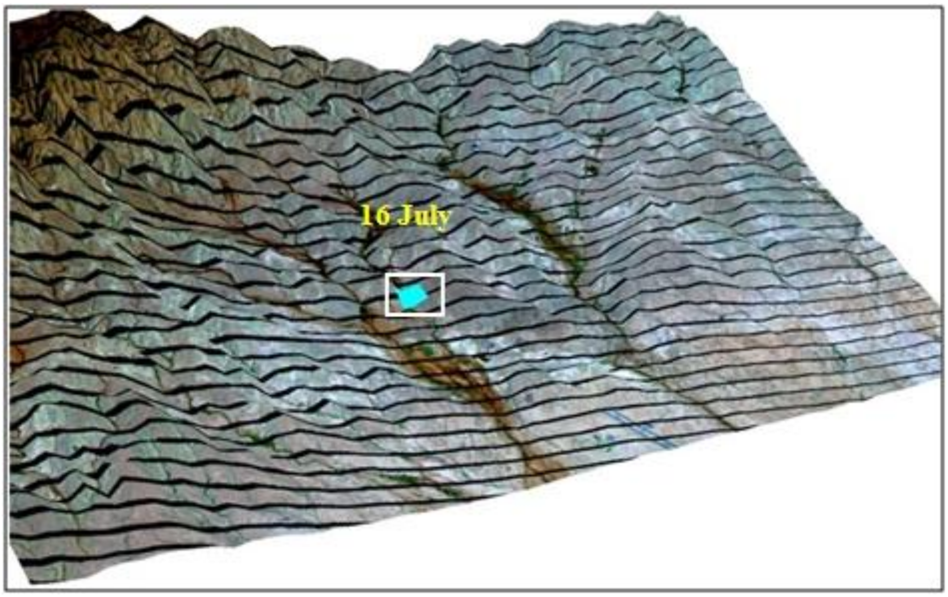


**B**

**C**

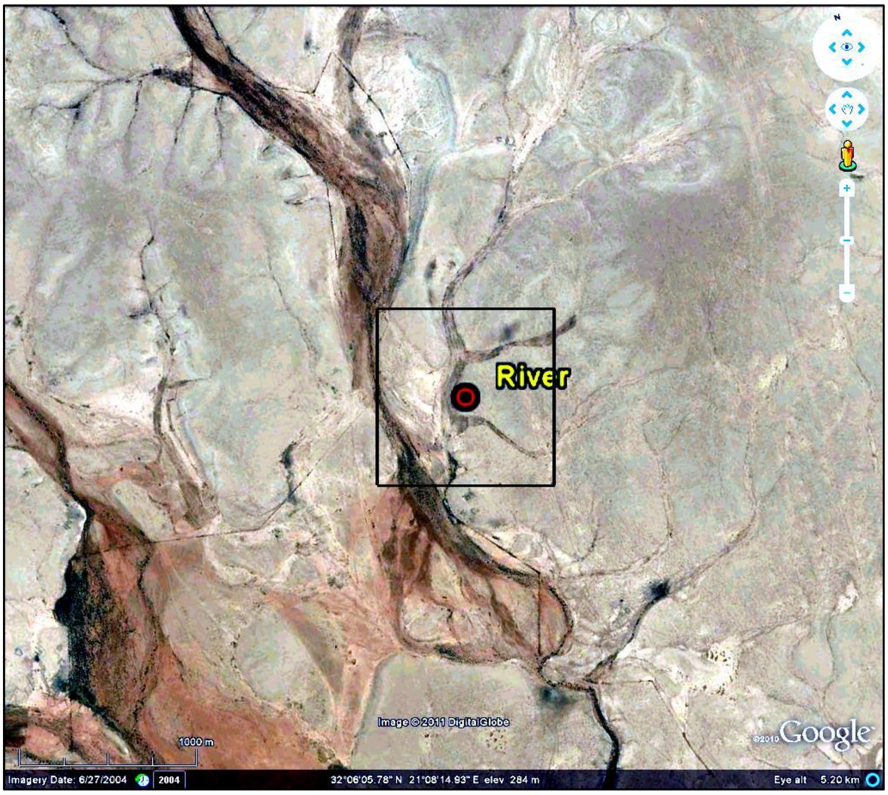


Figure 6.15 (A) 3D Landsat image dated 13th July 2008 shows the dust source detected on 16th July 2008. The cyan rectangle represent the dust source comes from river, the dust source is highlighted by white rectangle. (B&C) Google Map images showing the spatial detail of the dust source at two different scales (B) 5km, and (C) 1km. The black square represents the size of one pixel from MODIS data which is used for the dust detection.

## 6.5 Dust Sources detected From Benghazi Region

Twenty four dust sources were detected in Benghazi region during 2008 as shown in Figure 6.16. This represents 45% of dust sources detected during 2008. The Benghazi region has got different landforms and landuse from the southern Jabal Akhdar region discussed above and these results in different source characteristics. Benghazi region has the highest percentage of dust from alluvial fans (62%), and 100% of the dust sources detected from agriculture. This region is divided in to two sub-regions; (1) the southern Benghazi sub-region where twenty two dust sources are detected, the majority from alluvial fans and the rest from alluvial plains and agricultural regions; (2) the northern Benghazi sub-region where two dust sources are detected from agricultural regions (Figure 6.16).

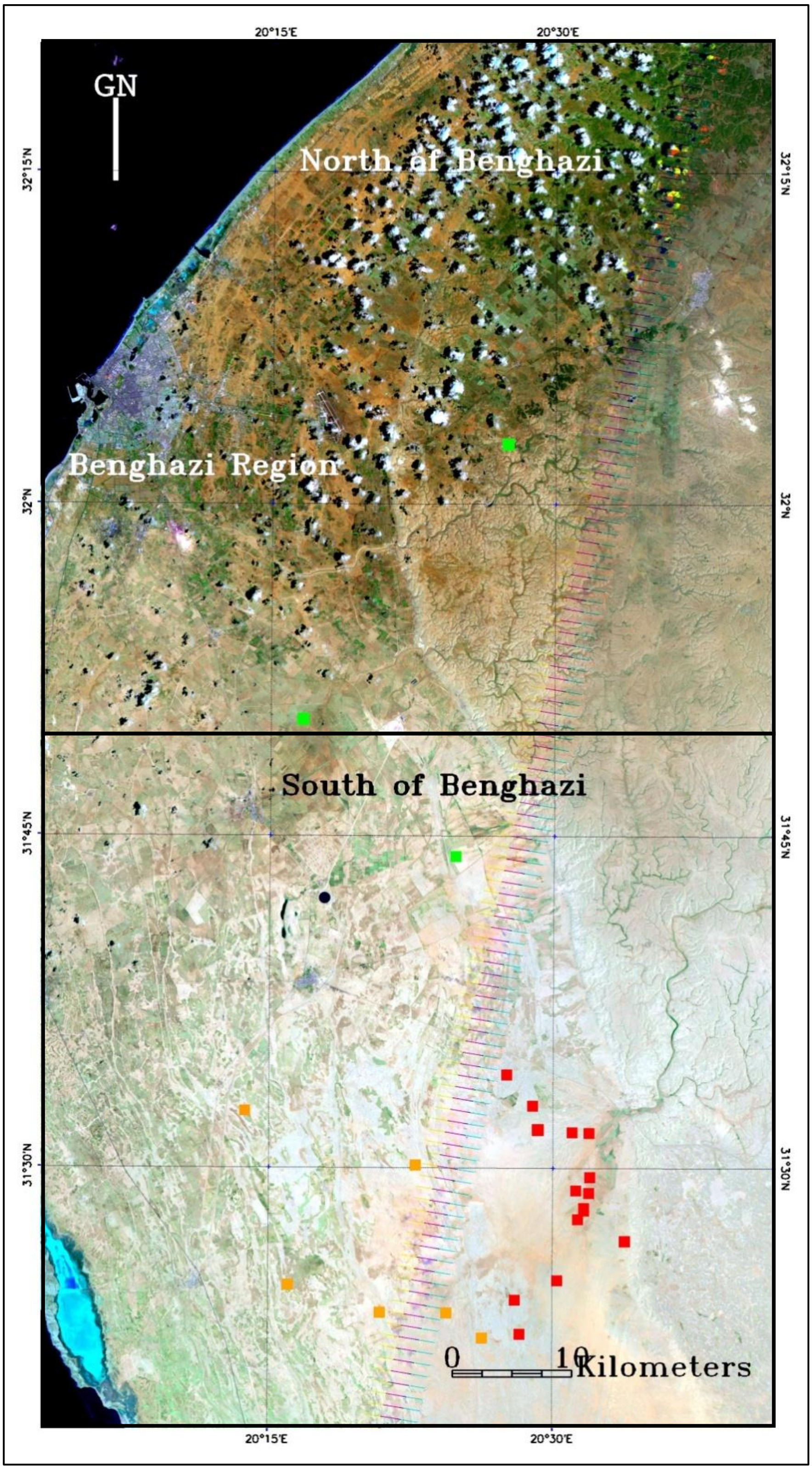


**Dust Sources: Alluvial Fan Alluvial Plain Agriculture**

Figure 6.16 Landsat image showing the two test regions and the 24 dust sources detected in Benghazi region 2008. Each source type been mapped in different colour as shown in the map key. Benghazi region is divided to two sub-regions; (North Benghazi and South Benghazi).

## 6.5.1 Dust Sources Detected From the Southern Benghazi Sub-Region

There are twenty two dust sources detected in the southern Benghazi sub-region from five different sources; fifteen from alluvial fans, six from alluvial plain, and one from agriculture. The dust sources for each month are plotted on the Landsat image of the same month or on the nearest month. Figure 6.17 shows Landsat colour composites in order to see the vegetation and the geomorphology and the landform of the sources. Only six months of Landsat imagery are used (March, June, July, August, October, and November) as the rest of months had high cloud cover. Figure 6.17 shows these Landsat colour composite images and the NDVI images with the dust sources plotted. The image from the 14 of March shows the dust sources detected during March and April, that from the 18 of June shows the dust sources detected during May and June, the rest of months are displayed using the dust sources for the same month that they were acquired.

The majority of dust deflation is detected from a large fan in southern Benghazi located in the south of the image (Figure 6.17). The presence of high NDVI (>0.5) throughout much of the west of the region because of rain fed agriculture and in the river channels in the east of the image during that drain the eastern flanks of Jabal Akhdar suggests that the region experienced widespread rainfall earlier in the year, however, in later months a lack of water is suggested by the reduction in the NDVI. From June to November the NDVI declines to near zero apart from in the main river channels were the NDVI remains ~0.5. This reduction is rapid in the west where it appears that agricultural fields have been cropped, however it is more gradual in the semi-natural vegetation in the river channels to the east.

The following sections will display and analyze some of these dust sources in more detail with those that are not displayed here shown in the appendix.

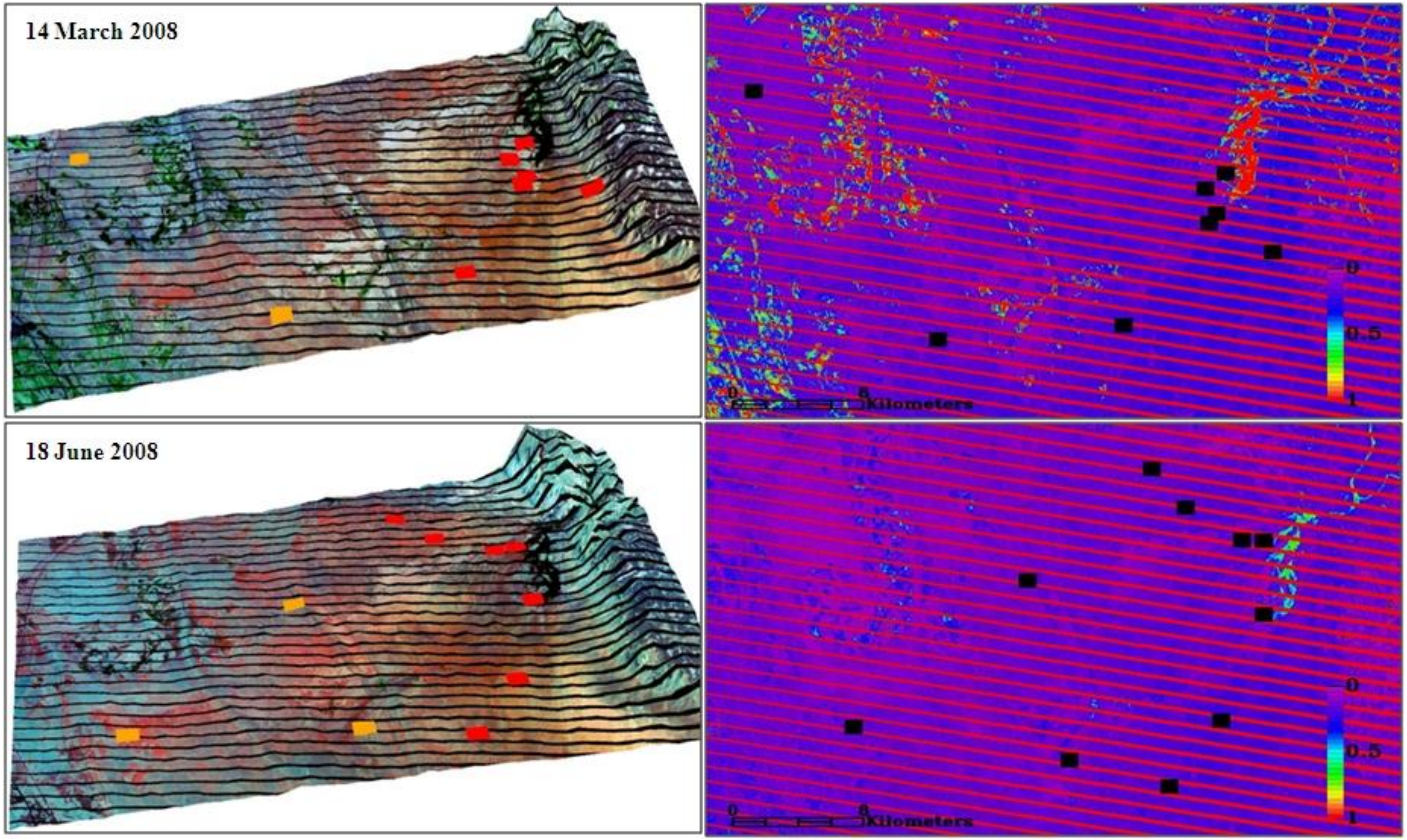
14 March 2008
18 June 2008
0
0.5
1
0
6
Kilometers

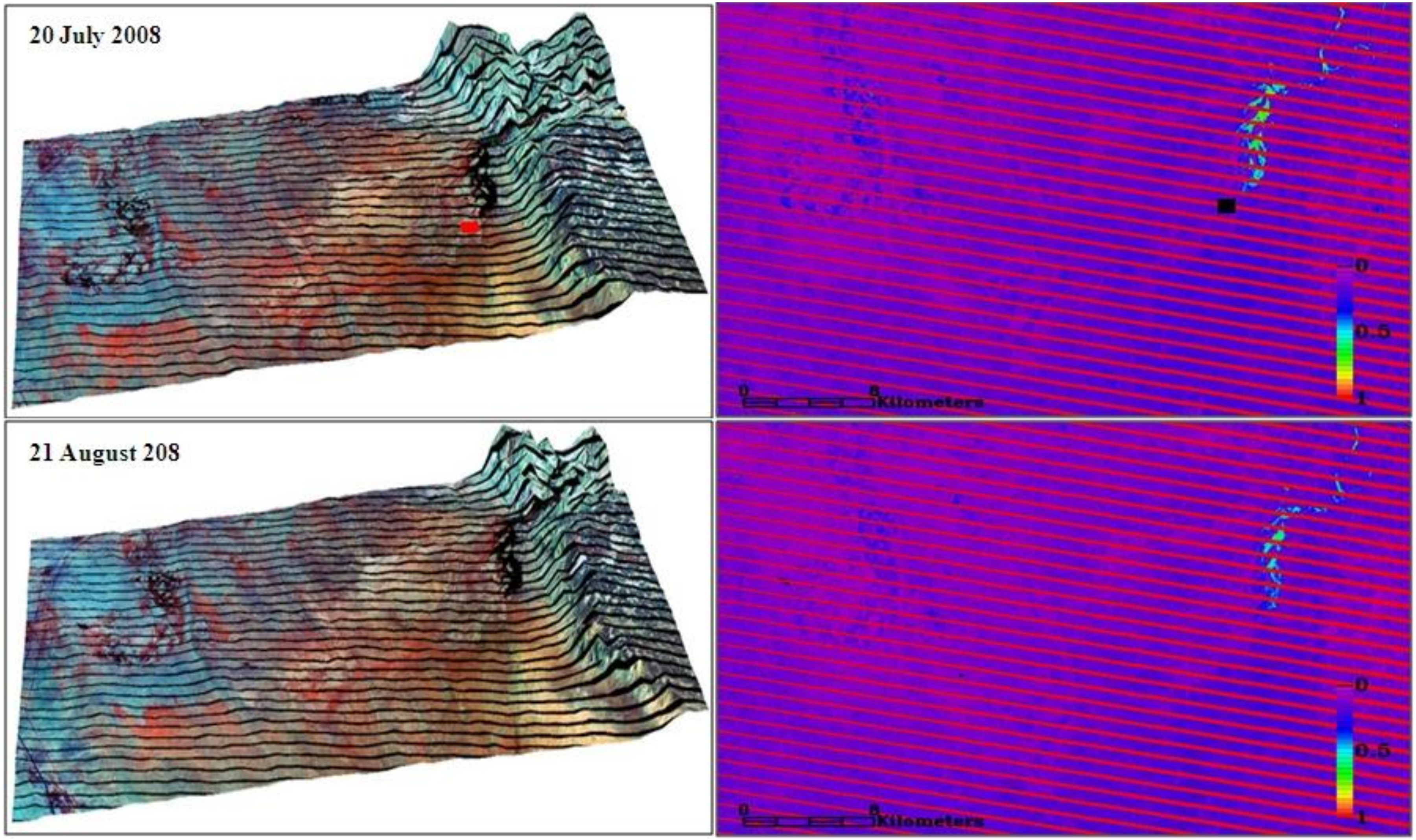
20 July 2008
21 August 208
0
8
Kilometers
0
0.5
1

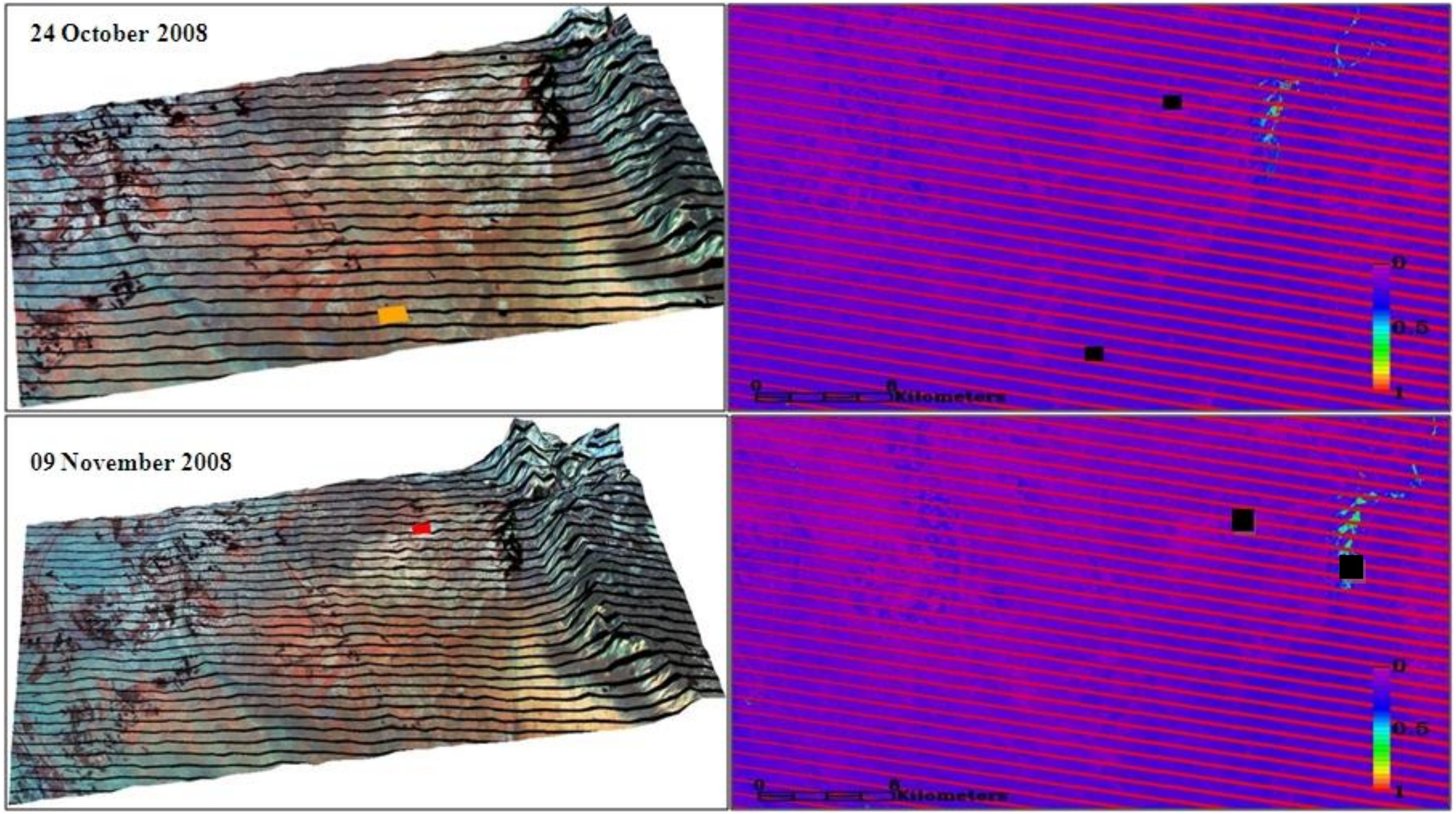


Figure 6.17 3D Landsat images colour composite 7,4,2 and the NDVI file for the following months:14thMarch, 18thJune, 20thJuly, 21stAugust, 24thOctober, and 09thNovember 2008 for dust sources detected south of Benghazi. All the dust sources detected are plotted on the image of the same month or the nearest month if it is not available. The orange rectangle in the Landsat images are represent the dust sources detected from alluvial plain, and the red rectangle is Alluvial fan. All the dust sources in the NDVI images are represented in black rectangle in order to avoid confusion with the NDVI colour scheme.

### 6.5.1.1 Dust Sources From Alluvial Fans South of Benghazi Sub-Region

Five low escarpments can be seen in the DEM (Figure 6.18-B) that decrease in elevation from east to west. The first escarpment is by far the largest and the region below it is dominated by a very large alluvial fan where a river that flows from Jabal Akhdar debouches across the plain. The fan consists of active channels cut into an older fan surface depositing clay silt and sand during the recession of floods. There is high NDVI in the channel and this presumably represents the most recently active channel on the alluvial fan surface where any recent flooding has been concentrated and has subsequently promoted vegetation growth.

The others escarpments are lower, much more subtle and are covered by alluvial plains with considerable agricultural activity on them during the spring. Fifteen dust sources in this sub-region are from the alluvial fan, representing the most active dust sources detected in the entire region. There appears to be some human activity on this alluvial fan, and it appears to be mainly used for agriculture, probably due to the fact that alluvial fan is fed by a seasonal river bringing periodic water flows from Jabal Akhdar during the rainy season. The fields are found close to the river to get the water flows from the Jabal Akhdar during the rain seasons (Figure 6.19).

Three dust sources from south of Benghazi region are detected in March, all of them are located on the large Alluvial fan (Figure 6.20), the dust sources detected on the $11^{th}$ and $13^{th}$ of March are highlighted by white rectangular in (figure 6.20) and will be discussed here. The rest are presented in the appendix.

A

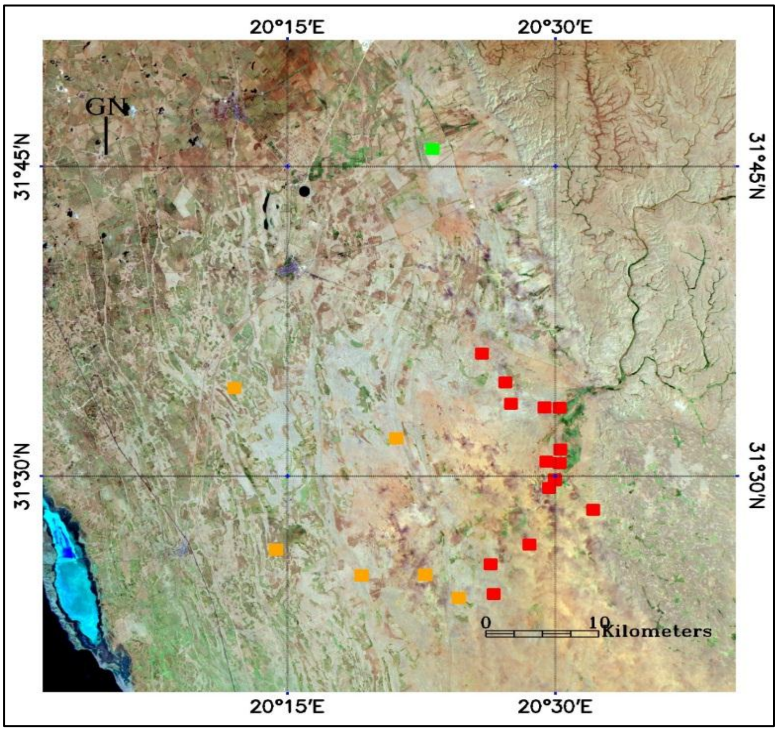


**(B) DEM Image**

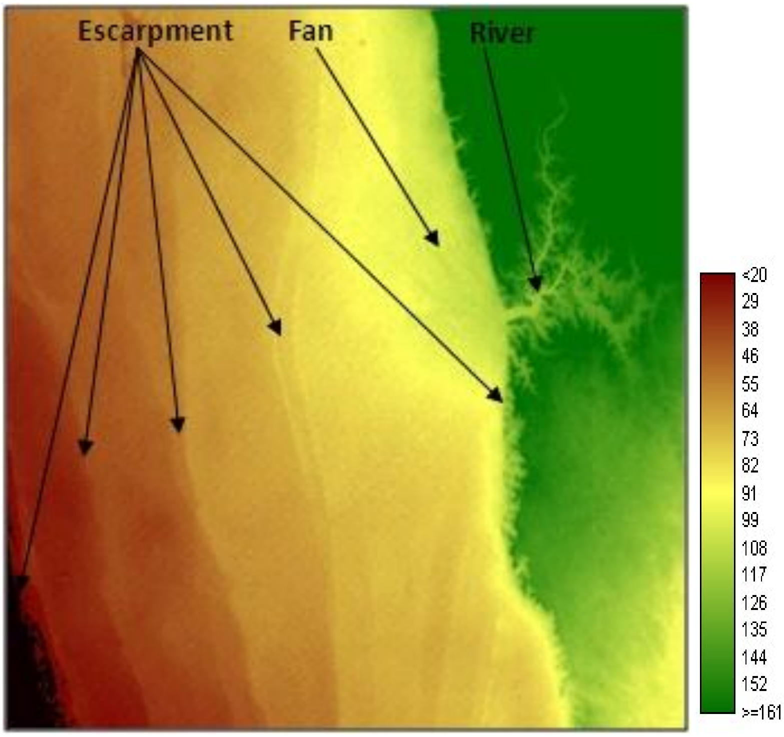


**Dust Sources: Alluvial Fan Agriculture Alluvial Plain**

Figure 6.18 (A) Landsat image showing the southern Benghazi region. Dust sources detected are mapped. Each source type been mapped in different colour as shown in the map key. (B) DEM covering the same area. There are five clear escarpments shown in the DEM.

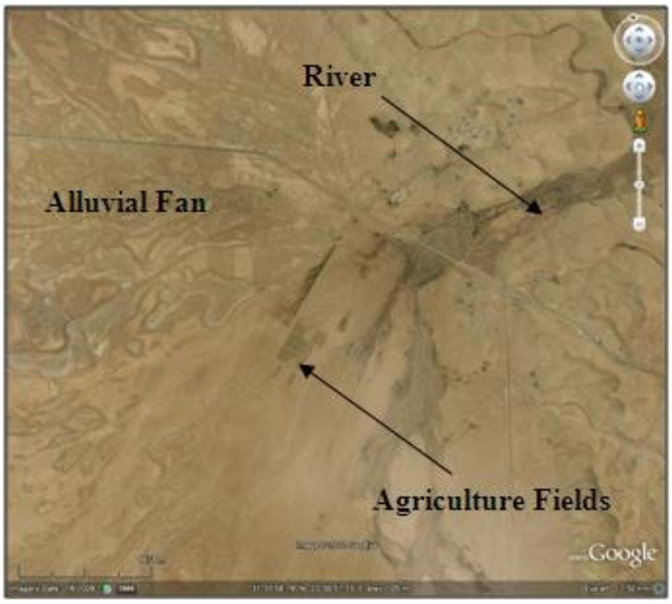


Figure 6.19 Google Earth image showing human activity on the alluvial fan.

#### 6.5.1.1.1 Dust Sources Detected From Alluvial fans on 11th March 2008

Figure 6.20 displays the 3D of the Landsat image dated 14 March 2008 and the NDVI for this image in order to see the location of the dust source detected on 11th of March. It is clear from the 3D image that the dust source is located on the fan just west of the escarpment. The dust source detected on the 11th of March has also been mapped on Google Earth imagery at two different scales in order to investigate the sources in more detail. Figure 6.21 B and C show the Google Earth view of the area surrounding the dust source. It is clear that the source is located on the lower part of the alluvial fan close to the end of the river channel in a region where many older channels are present. Thus the most likely explanation is that dust is being deflated from a previously active channel. The material carried by past water flows providing all the sedimentary factors required for the sandblasting process. All of the other dust sources detected at this alluvial fan appear to come from sources that are close to each other and have similar conditions (Figure 6.20).

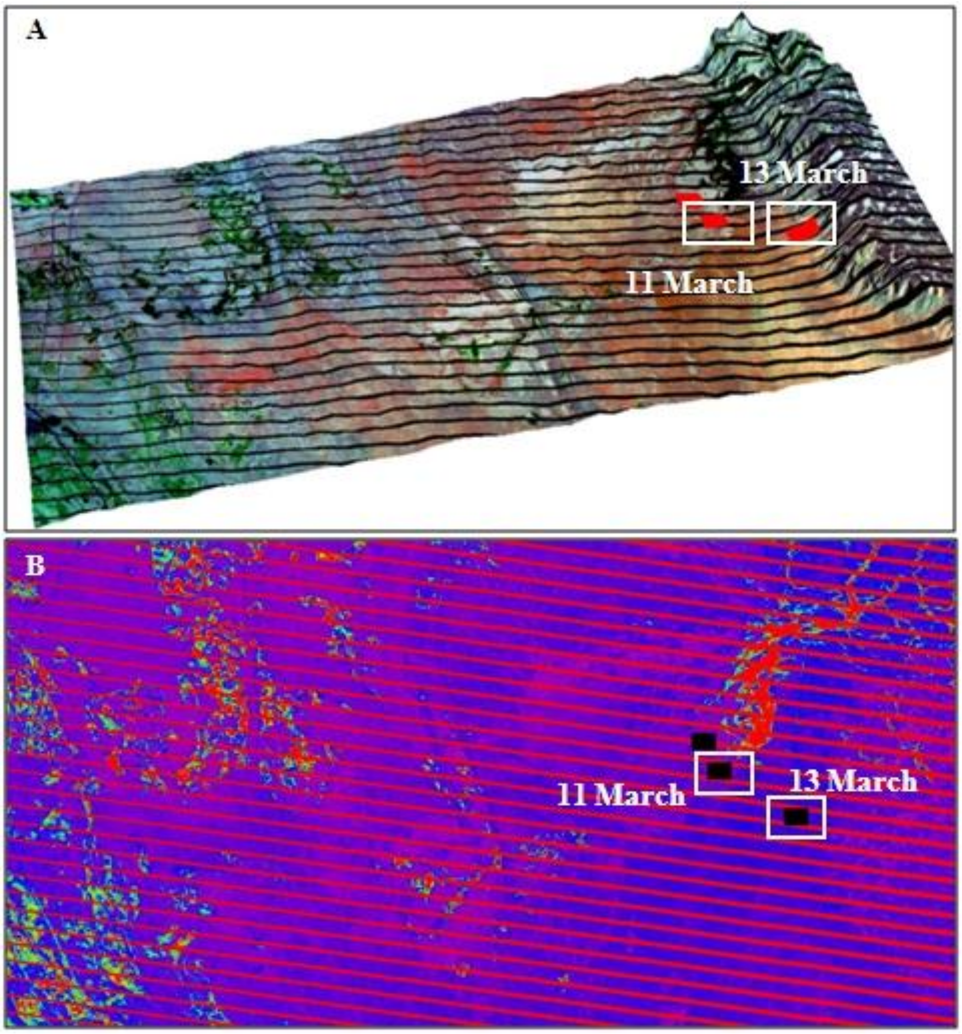


Figure 6.20 (A) 3D Landsat image dated 14th March 2008 shows the dust sources detected during March 2008 at south of Benghazi regions. (B) NDVI Index map for the Landsat image. The white rectangle on figure 6.20 highlight the dust source detected on 11th and 13th March 2008 from alluvial fan. The red rectangle is alluvial fan. All the dust sources in Figure 6.20 (B) are represented in black rectangle in order to avoid confusion with the NDVI colour scheme.

**A**

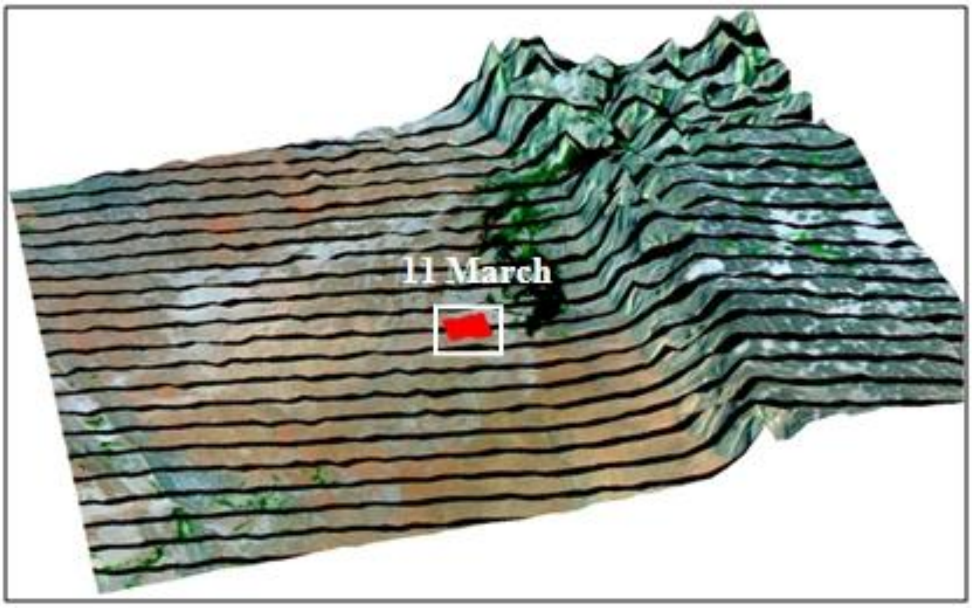
11 March

**B**

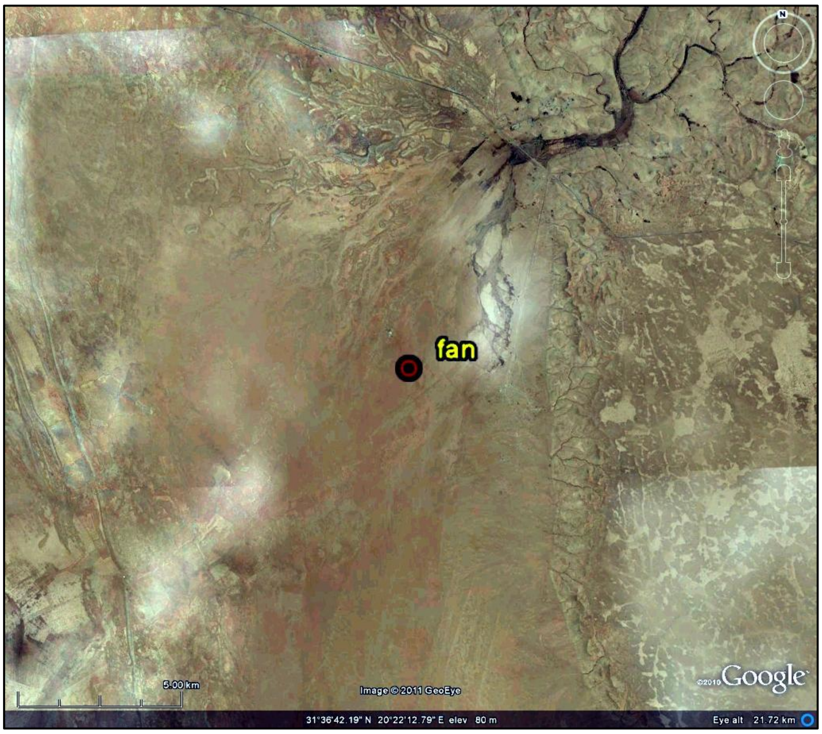
fan
5.00 km
Image © 2011 GeoEye
31°36'42.19" N 20°22'12.79" E elev 80 m
Eye alt 21.72 km
©2010 Google

**C**

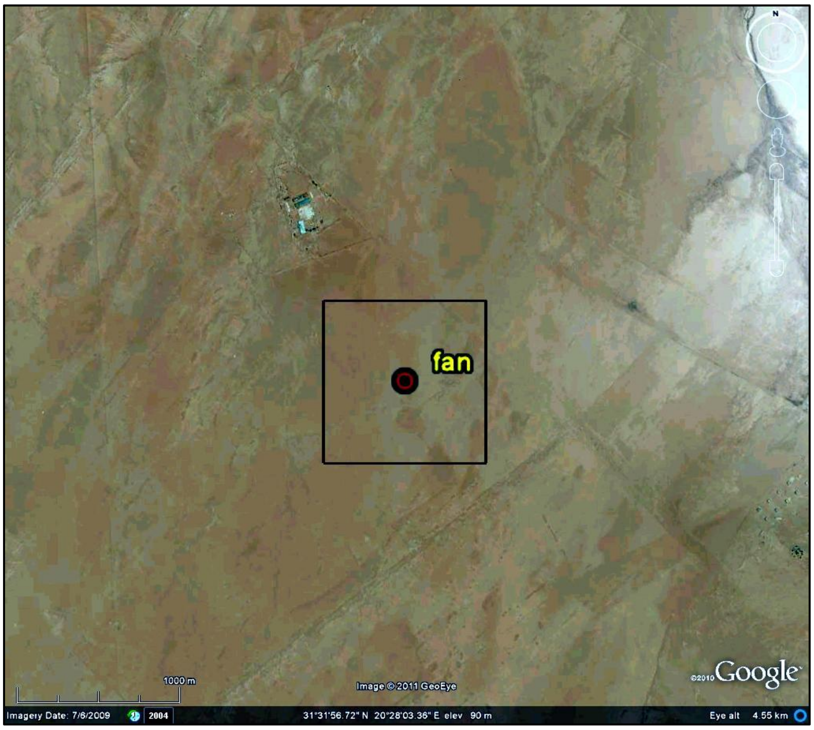


Figure 6.21 (A) 3D Landsat Image dated 14th March 2008 shows the dust source detected on 11th March 2008. The red rectangle represent the dust source comes from alluvial fan, the dust source is highlighted by white rectangle. (B&C) Google Map images showing the spatial detail of the dust source at two different scales (B) 5km, and (C) 1km. The black square represents the size of one pixel from MODIS data which is used for the dust detection.

### 6.5.1.1.2 Dust Sources From Alluvial fans on 13th March

The alluvial fan dust source mapped on 13thMarch is located on a small fan just to the south of the large fan described above that forms the prominent dust source (Figure 6.20A). The fan dust source is clearly shown in the 3D image. The alluvial fan appears far from the cultivated areas and no human activity can be seen, however, it has a small river channel which has probably remained dry as the NDVI is low and little recent vegetation growth can be detect in the source area.

**A**

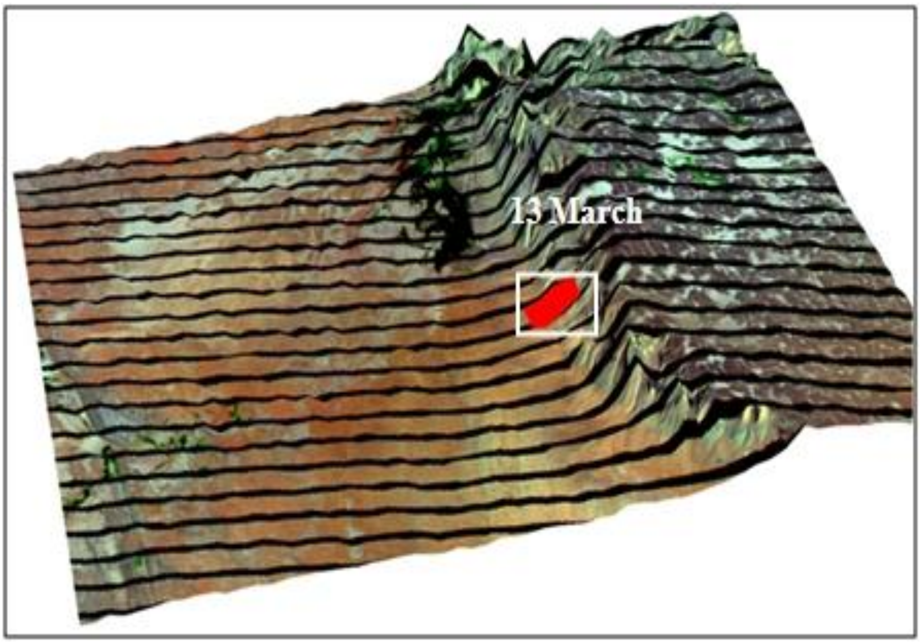
13 March

**B**

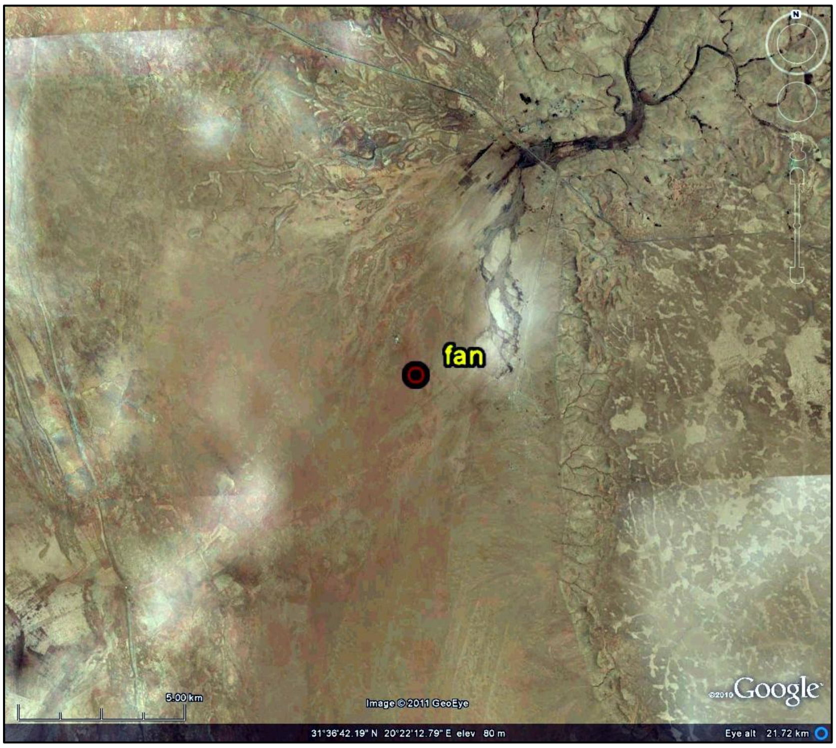
fan
5.00 km
Image © 2011 GeoEye
31°36'42.19" N 20°22'12.79" E elev 80 m
Eye alt 21.72 km
Google

**C**

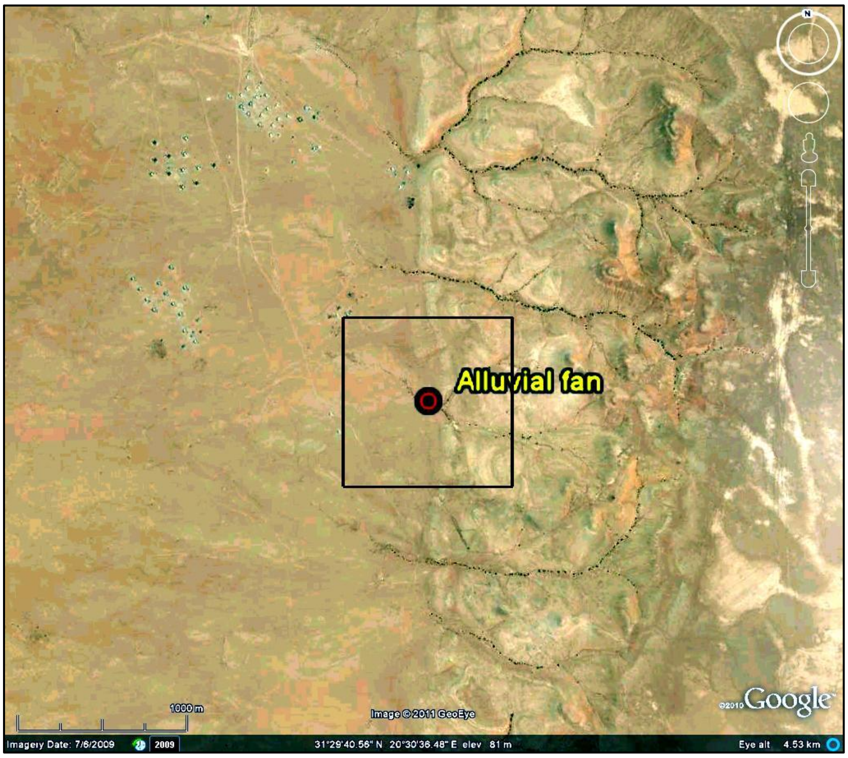


Figure 6.22 (A) 3D Landsat Image dated 14th March 2008 shows the dust source detected on 13th March 2008. The red rectangle represent the dust source comes from alluvial fan, the dust source is highlighted by white rectangle. (B&C) Google Map images showing the spatial detail of the dust source at two different scales (B) 5km, and (C) 1km. The black square represents the size of one pixel from MODIS data which is used for the dust detection.

### 6.5.1.2 Dust Sources Detected From Alluvial Plains South of Benghazi Sub-Region

Seven detected dust sources are generated from alluvial plains and this represents 13% of the total detected dust sources, all of them are located in Benghazi region, apart from one detected south of Jabal Akhdar. The dust source detected on 20th April (Figure 6.23) is described below and the rest are described in the appendix. The alluvial plains are similar to alluvial fans. Both are formed of alluvial deposition by unconfined river channels, however, alluvial plain do not exhibit a fan shape, rather a gently sloping surface of alluvium. The plains are found at the termination of the river channels that flow down from Jabal Akhdar and are found inter-mixed with and below the alluvial fans (Figure 6.23).

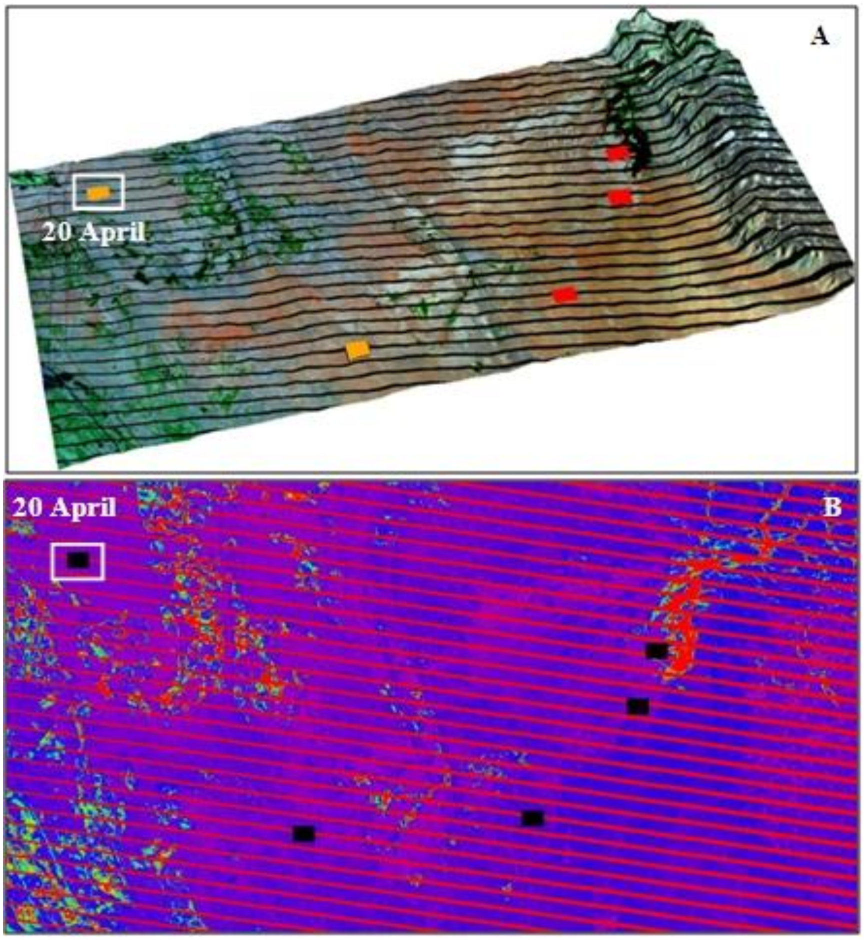


Figure 6.23 (A) 3D Landsat image dated 14th March 2008 shows the dust sources detected during April 2008 at south of Benghazi regions. (B) NDVI Index map for the Landsat image. The white rectangle on figure 6.23 highlight the dust source detected on 20th April 2008 from alluvial plain. The orange rectangle is alluvial plain. All the dust sources in Figure 6.23 (B) are represented in black rectangle in order to avoid confusion with the NDVI colour scheme.

## 6.5.1.2.1 Dust Sources From the Alluvial Plains on 20th April 2008

Figure 6.23 shows 3D Landsat image dated 14th March 2008. The dust source was detected on the 20thApril. The dust source is interpreted as an alluvial plain as it is located on a flat area with evidence for relict channels nearby. The NDVI shows that in the east of the image vegetation is mainly found along the channels of the rivers that flow down off the Jabal Akhdar and in the west of the image it is found in areas where there are agricultural fields. The source is found in a region surrounded by fields. However, the detected source is located in a vegetation free area. The dust probably comes from an area cultivated during the past but is not in use this year, and thus is largely bare and susceptible to deflation.

**A**

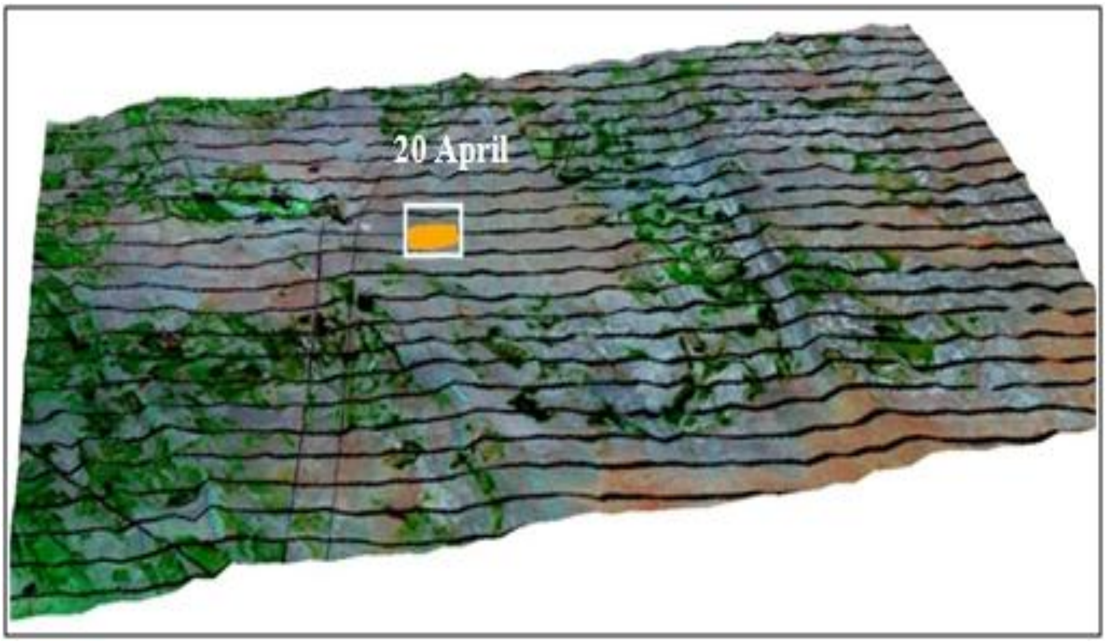
20 April

**B**


Alluvial Plain
5.00 km
Image © 2011 GeoEye
©2010 Google
Imagery Date: 8/24/2009
31°40'08.88" N 20°04'09.81" E elev 34 m
Eye alt 21.56 km

**C**

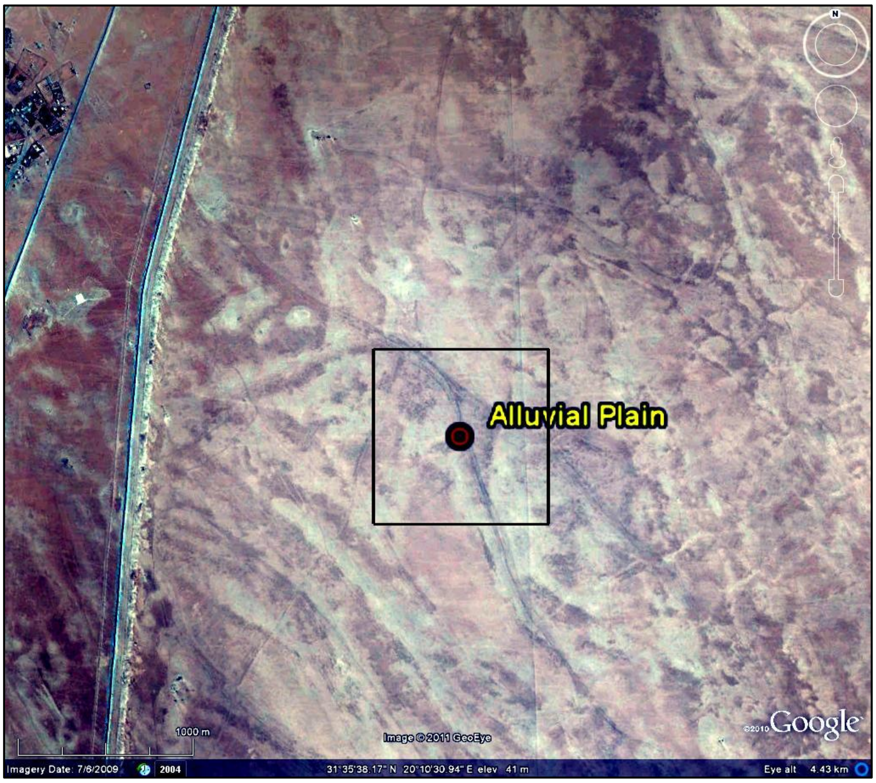


Figure 6.24 (A) 3D Landsat Image dated 14th March 2008 shows the dust source detected on 20th April 2008. The orange rectangle represent the dust source comes from alluvial plain, the dust source is highlighted by white rectangle. (B&C) Google Map images showing the spatial detail of the dust source at two different scales (B) 5km, and (C) 1km. The black square represents the size of one pixel from MODIS data which is used for the dust detection.

### 6.5.2 Dust Sources Detected From the Northern Benghazi Sub-Region

The Northern Benghazi region has a different landuse to those previously considered, consisting predominantly of agriculture fields that mainly depend on seasonal rainfall with a few fields fed by artificial irrigation systems, either feed by wells or from large tanks that form part from the Great Manmade River Project. There are just two dust sources detected from this sub-region, both from agricultural fields (Figure 6.25). Six months of Landsat imagery are available for this region; March, June, July, August, October, and November. The other months are not used because of the high cloud cover. These images are used to display the dust sources and to see the changes in the vegetation were the dust sources are detected. Some of these months has lack dust and are used only to see the changes in the vegetation.

## 6.6 Dust Sources Detected From Agriculture Northern Benghazi Sub-Region

Three dust sources are detected from agriculture during 2008 and represent 6% from the total detected dust sources, one of these sources is detected in the southern Benghazi region and the rest are detected here. Two of these sources are reported as a single location (13th June and 1st October), the other on the 16th July.

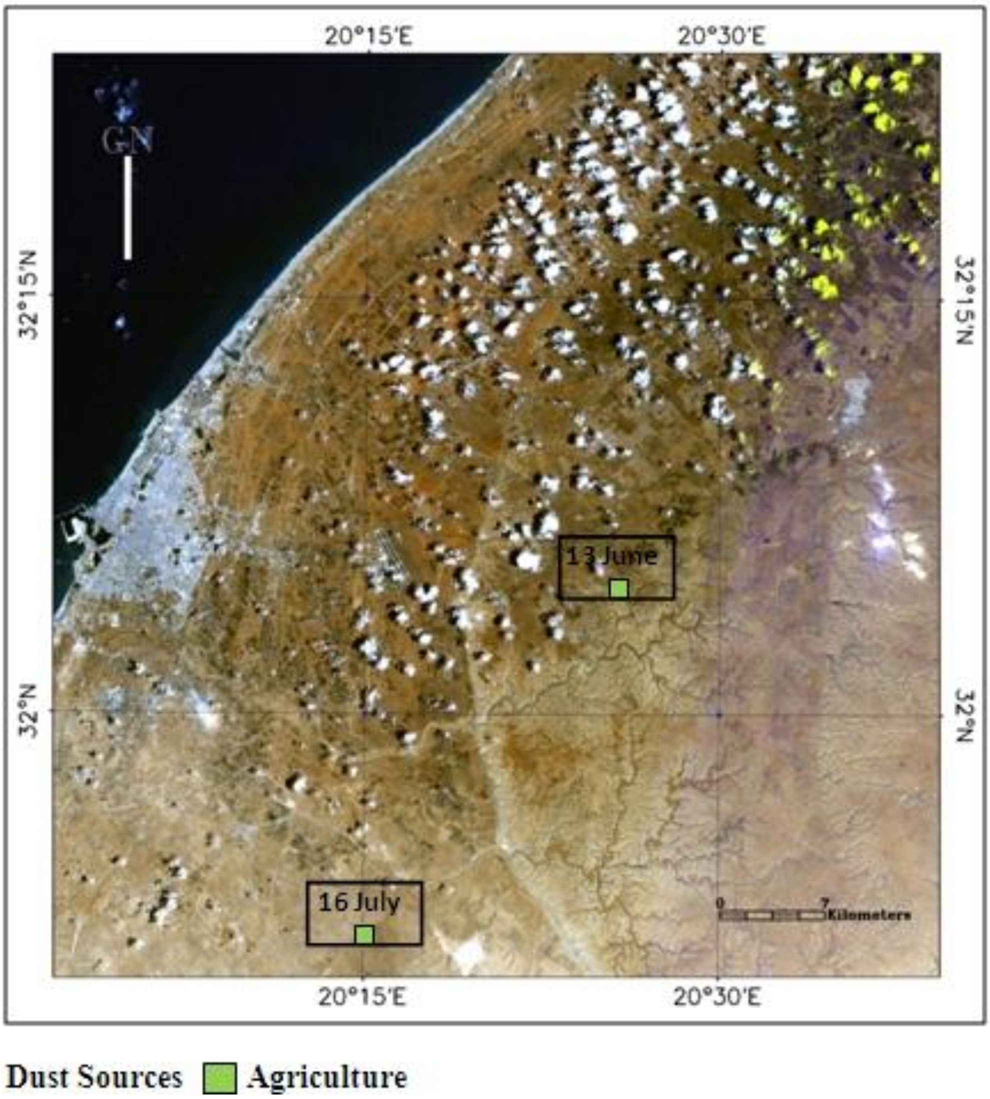


Figure 6.25 Landsat colour composite image showing all of the dust sources detected over North Benghazi region for 2008. The two green squares represent dust sources detected from agriculture.

Figure 6.27 shows the Landsat colour composites and the NDVI for March, June, July, August, October, and November with the dust sources plotted on the Landsat image of the nearest month. The Northern part of the images shows high NDVI ≥0.5 from March to July that starts to dry off during August. During October the NDVI increases again as it does in November. That suggests this area experiences sporadic rainfall throughout much of the year.

In the Southern part of the image, agricultural fields are located between two large water tanks (Figure 6.26) probably used for irrigation purposes.

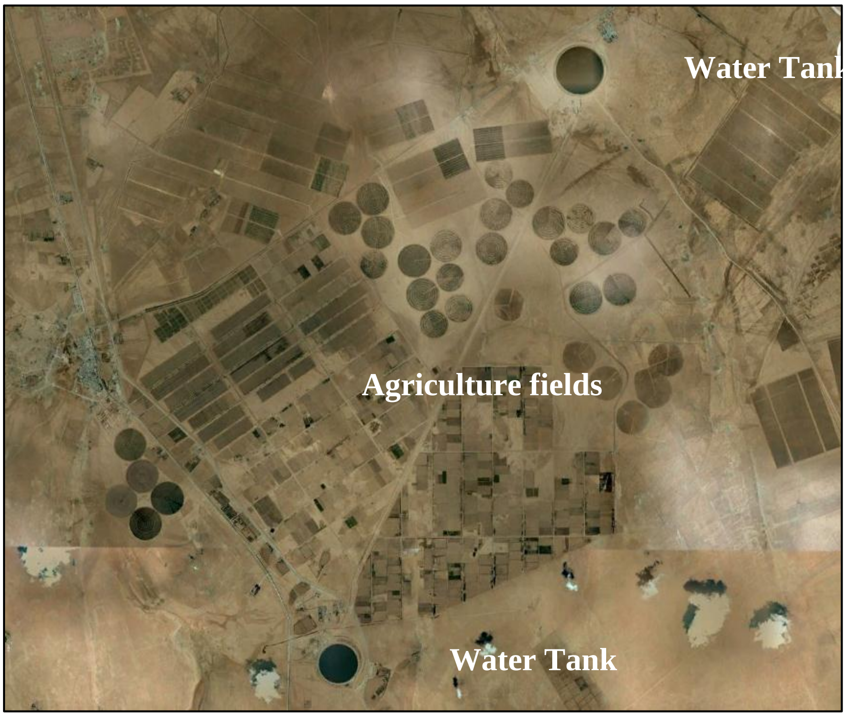


Figure 6.26 Google Earth image shows the agriculture fields and the two water tanks.

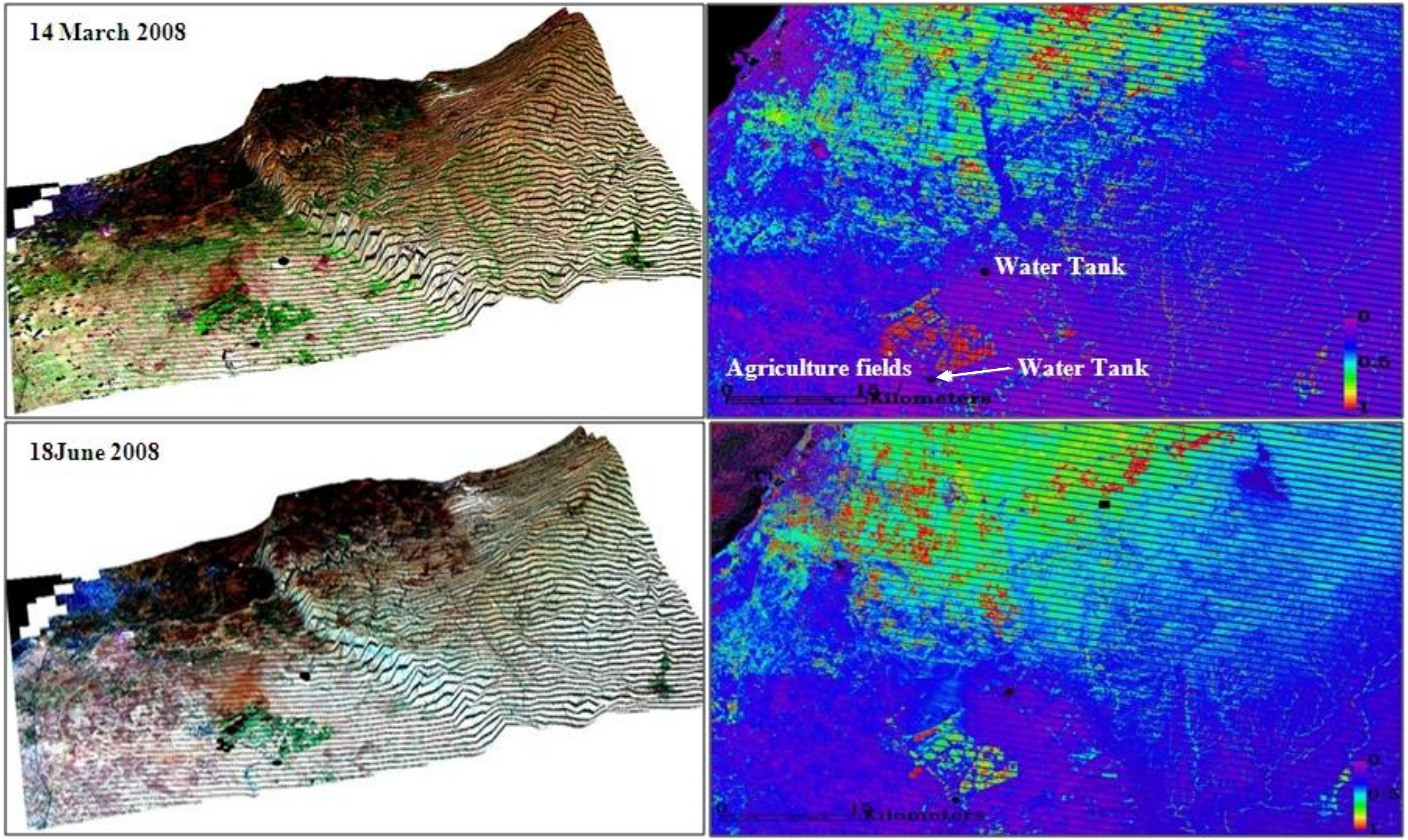
14 March 2008
Water Tank
Agriculture fields
Water Tank
0
15
Kilometers
0
0.5
1
18June 2008
0
15
Kilometers

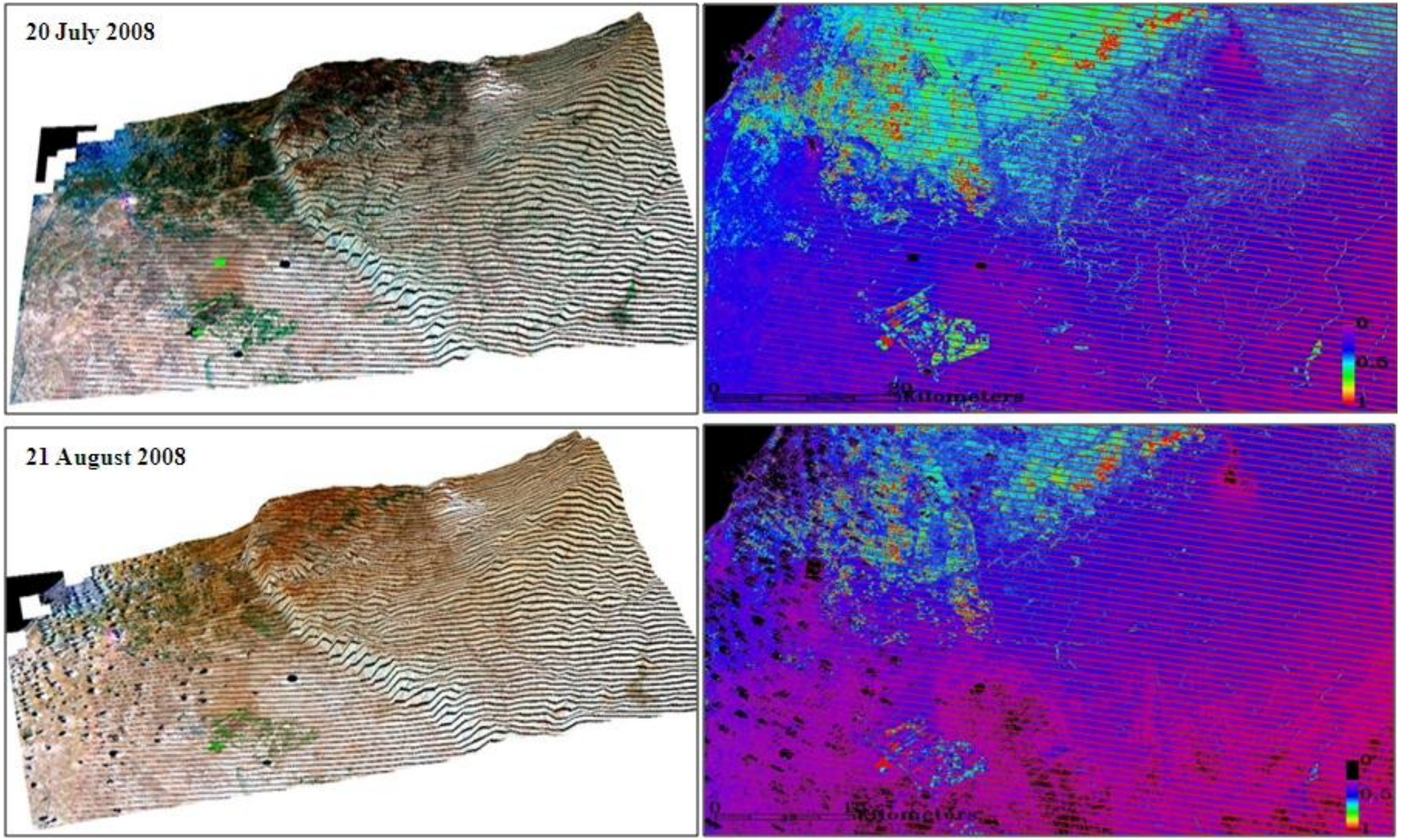
20 July 2008
21 August 2008
Kilometers
Kilometers

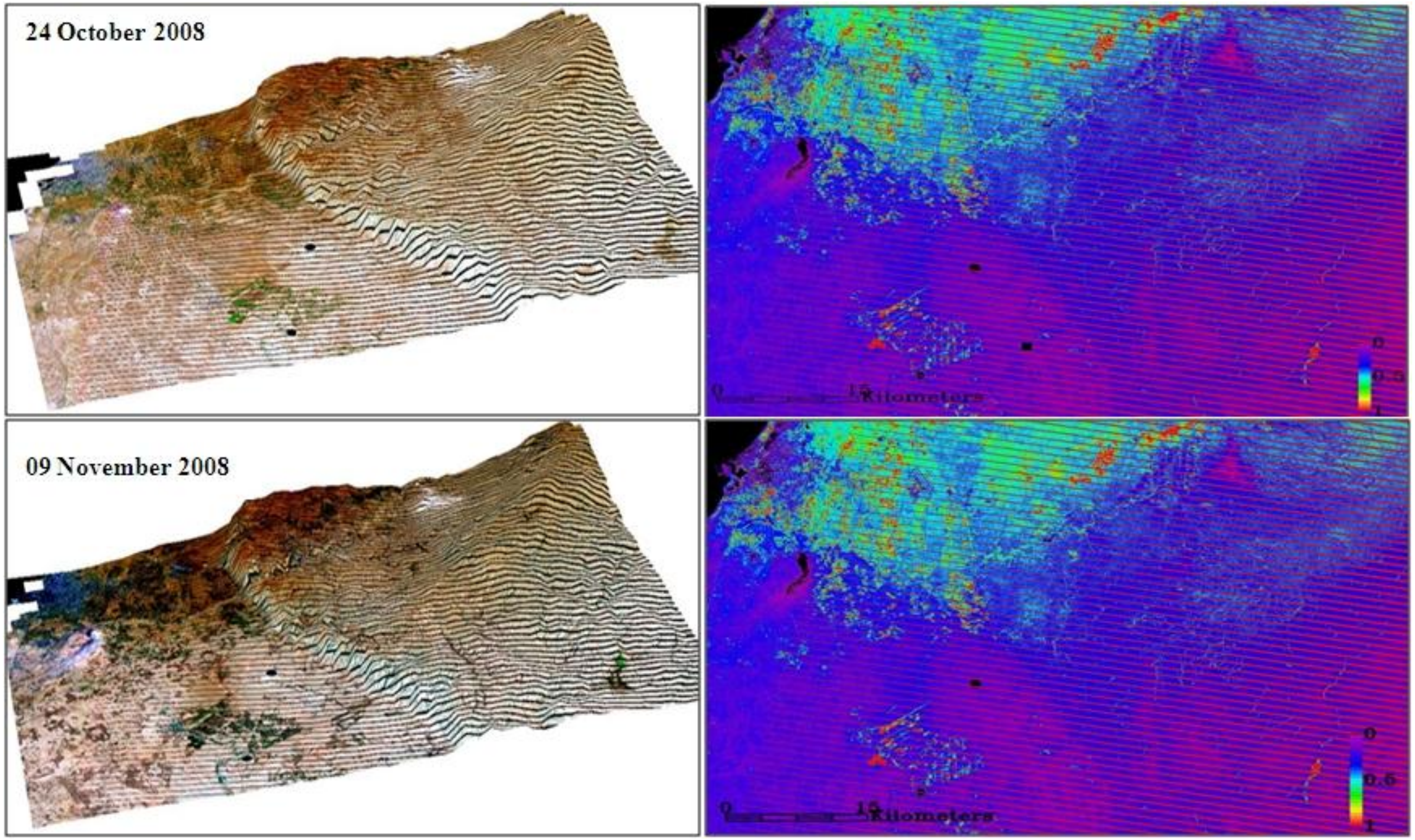


Figure 6.27 3D Landsat images colour composite 7,4,2 and the NDVI file for the following months:14thMarch, 18thJune, 20thJuly, 21stAugust, 24thOctober, and 09thNovember 2008 for dust sources detected north of Benghazi. All the dust sources detected are plotted on the image of the same month or the nearest month if it is not available. The green rectangles in the Landsat images are represent the dust sources detected from agriculture. All the dust sources in the NDVI images are represented in black rectangle in order to avoid confusion with the NDVI colour scheme.

## 6.6.1 Dust Sources Detected From Agriculture on 13 June 2008

On 13 June a single dust source is detected from a field east of Benghazi Airport (Figure 6.25). There are several fields in the region and thus past human activity at these fields probably causes dust deflation in the region. The dust source is close to fields with high vegetation (Figure 6.28 B) but at the dust source has a low vegetation index. This suggests that the field has recently been cropped/cleared exposing bare ground to deflation.

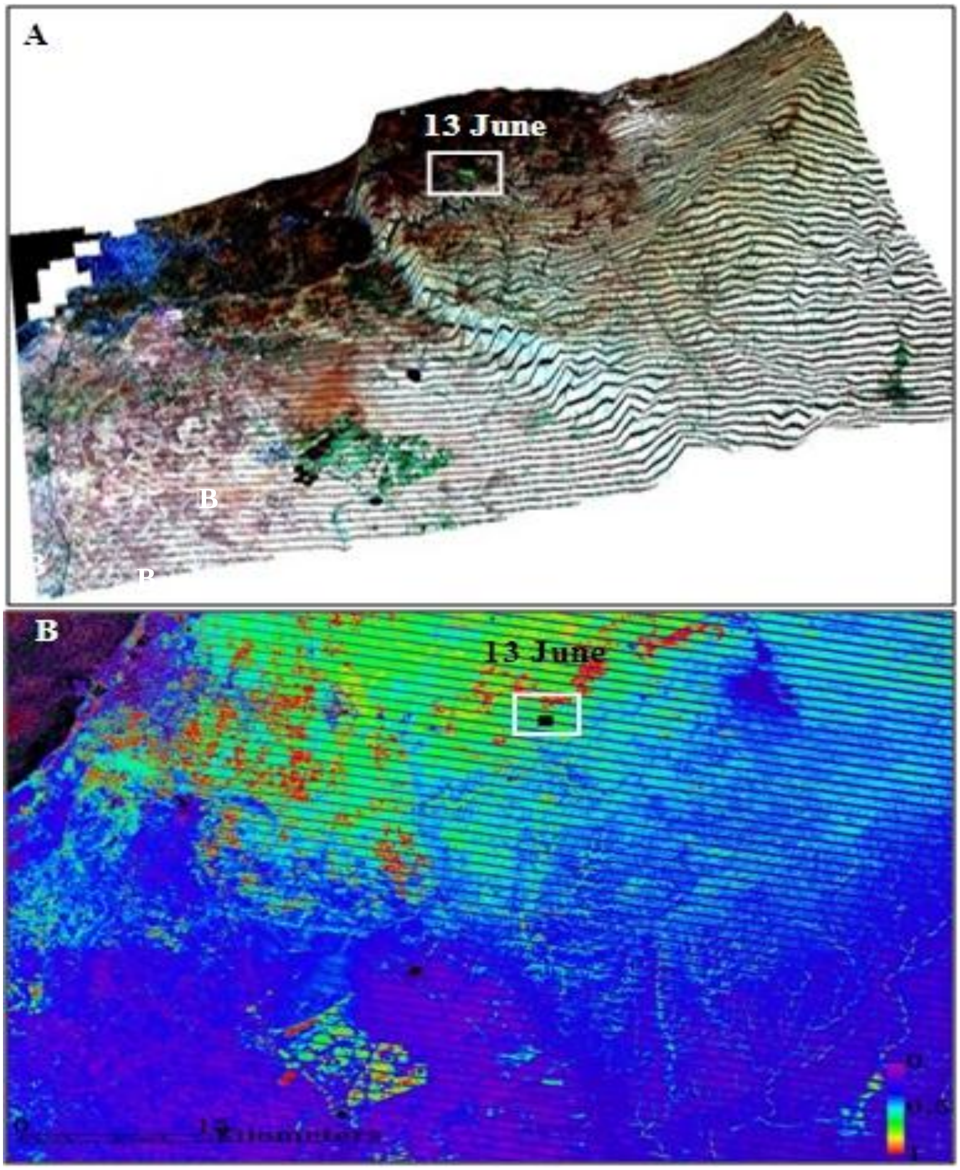


Figure 6.28 (A) 3D Landsat image dated 18th June 2008 shows the dust sources detected during June 2008 at north of Benghazi regions. (B) NDVI Index map for the Landsat image. The white rectangle on figure 6.28 highlight the dust source detected on 13th June 2008 from agriculture. The green rectangle is agriculture. All the dust sources in Figure 6.28 (B) are represented in black rectangle in order to avoid confusion with the NDVI colour scheme.

**A**

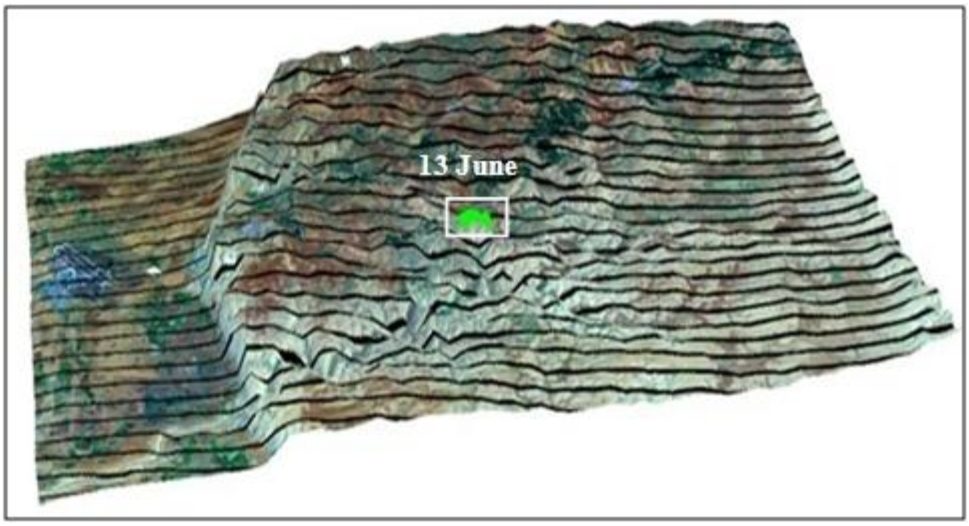
13 June

**B**


Agriculture
5.00 km
Image © 2011 GeoEye
©2010 Google
Imagery Date: 6/17/2009
32°11'43.93" N 20°19'47.41" E elev 117 m
Eye alt 21.88 km

**C**

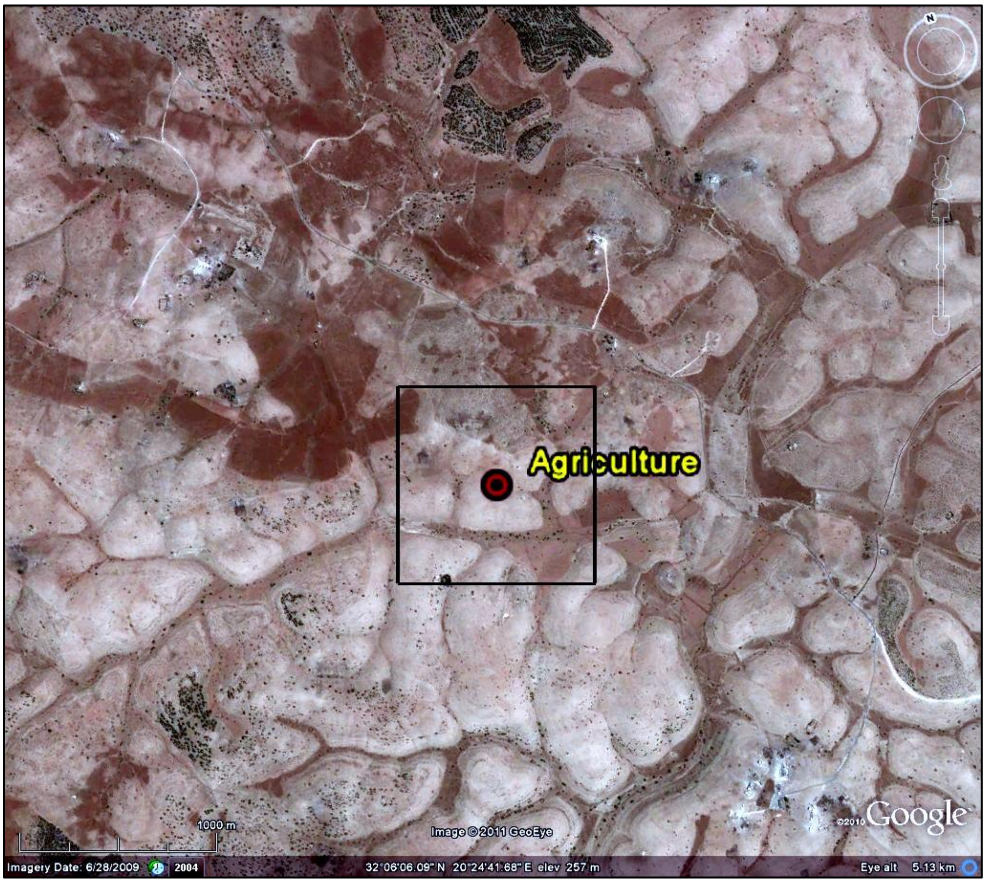


Figure 6.29 (A) 3D Landsat Image dated 18th June 2008 shows the dust source detected on 13th June 2008. The green rectangle represent the dust source comes from agriculture, the dust source is highlighted by white rectangle. (B&C) Google Map images showing the spatial detail of the dust source at two different scales (B) 5km, and (C) 1km. The black square represents the size of one pixel from MODIS data which is used for the dust detection.

## 6.6.2 Dust Sources Detected From Agriculture on 16 July 2008

The second dust source detected from agriculture /fields area is detected on 16 July 2008. Figure 6.30 shows the 3D image of the area, indicating that the dust source is located in flat area. The NDVI is low and the google earth images reveal numerous fields. Inddeed the dust source is located in an area of bare fields that may well have recently been harvested and this could explain why they produce dust.

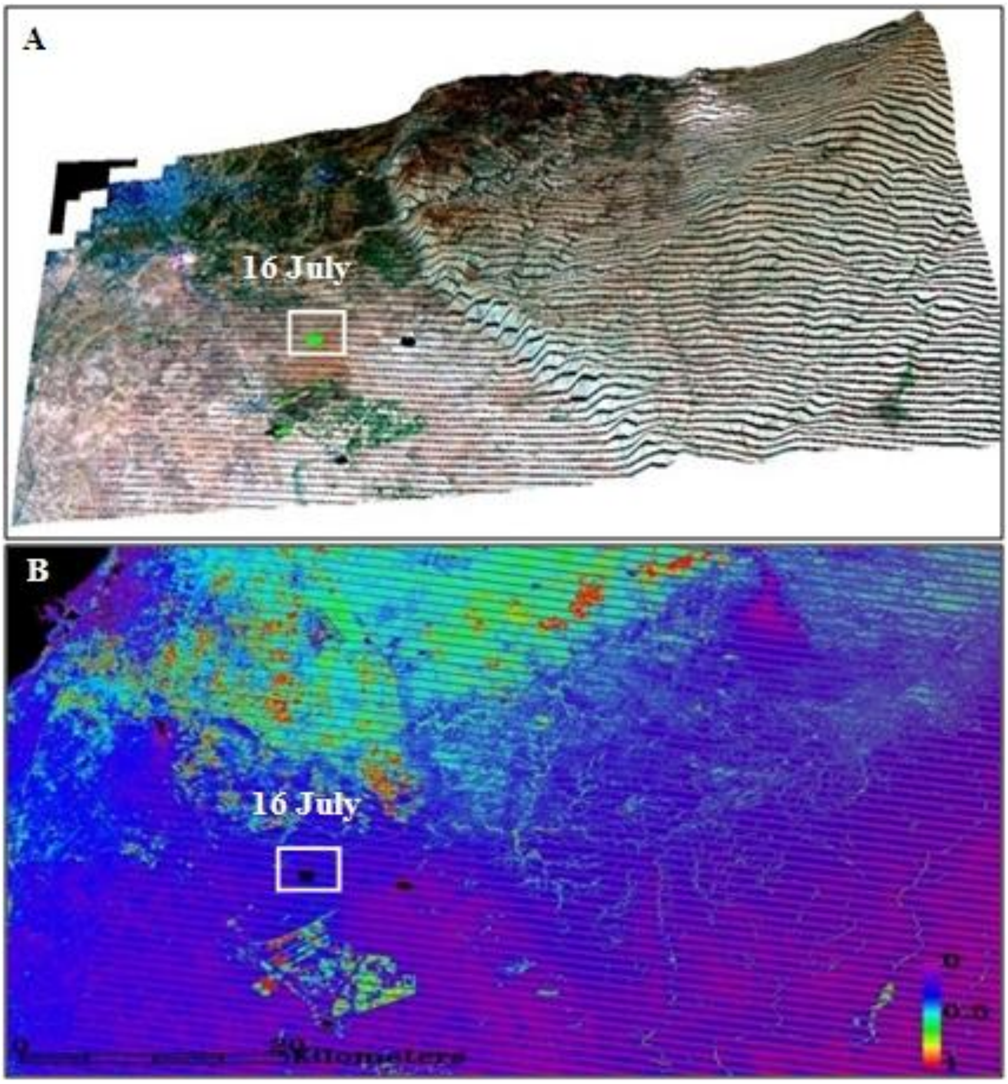


Figure 6.30 (A) 3D Landsat image dated 20th July 2008 shows the dust sources detected during July 2008 at north of Benghazi regions. (B) NDVI index map for the Landsat image. The white rectangle on figure 6.30 highlight the dust source detected on 16th July 2008 from agriculture. The green rectangle is agriculture. All the dust sources in Figure 6.30 (B) are represented in black rectangle in order to avoid confusion with the NDVI colour scheme.

Figure 6.31. (A) shows vegetation located both north and the south of the dust source and these probably depended on the irrigation from the large water tank located on the centre of the image as. Figure 6.31 (B and C) shows the fields were the dust source is detected, it looks these fields are mainly dry and clear from any vegetation.

**A**

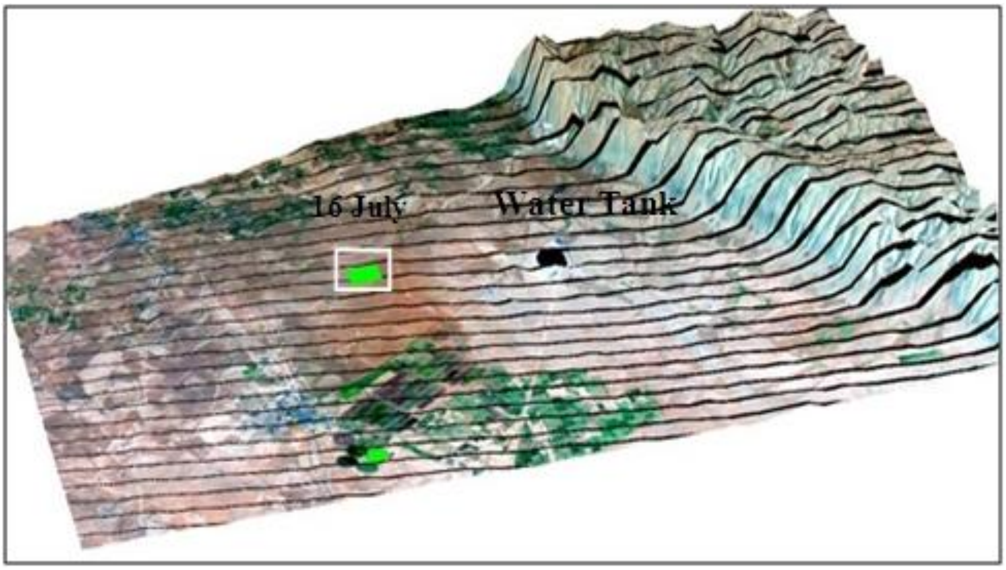
16 July
Water Tank

**B**

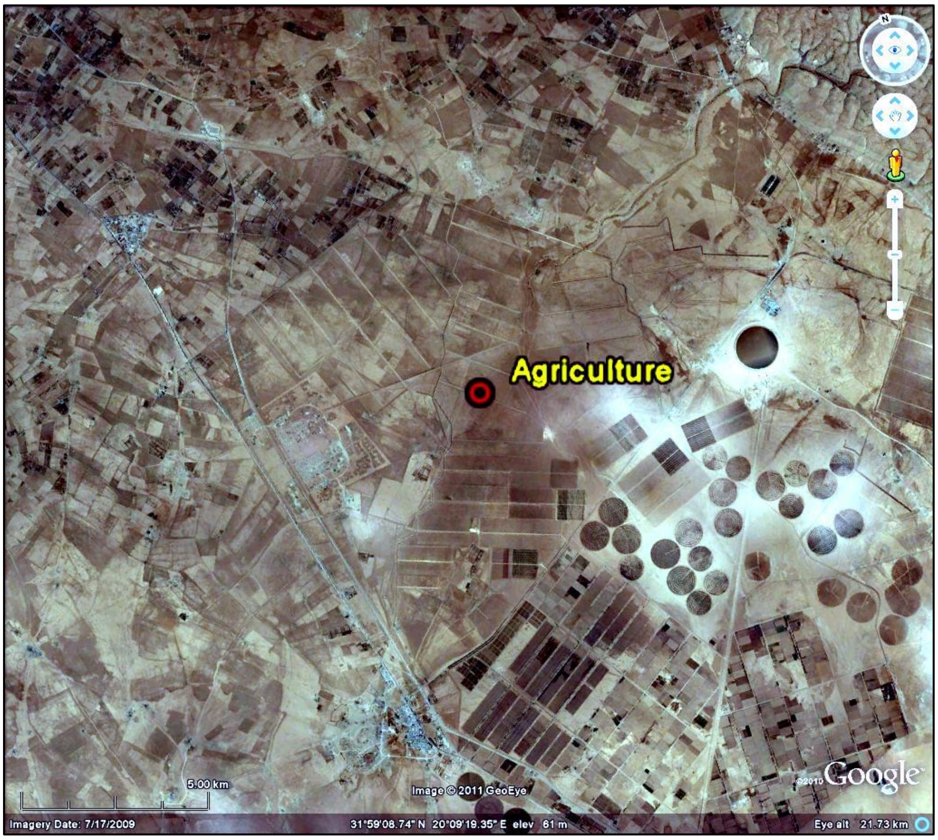
Agriculture
5.00 km
Image © 2011 GeoEye
©2010 Google
Imagery Date: 7/17/2009
31°59'08.74" N 20°09'19.35" E elev 61 m
Eye alt 21.73 km

C

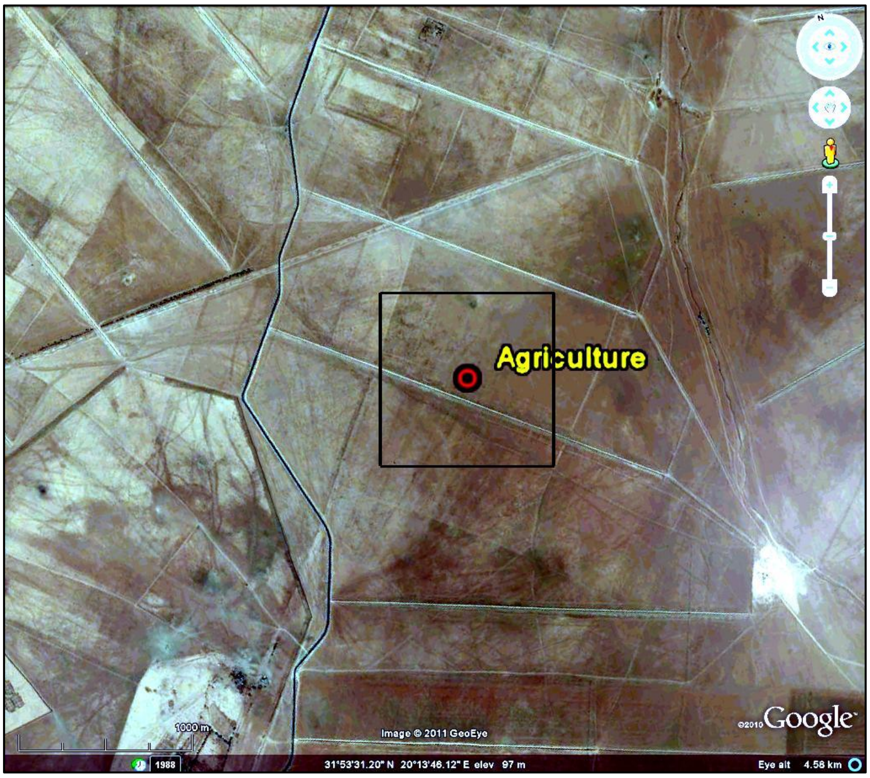


Figure 6.31(A) 3D Landsat Image dated 20th July 2008 shows the dust source detected on 16th July 2008. The green rectangle represent the dust source comes from agriculture, the dust source is highlighted by white rectangle. (B&C) Google Map images showing the spatial detail of the dust source at two different scales (B) 5km, and (C) 1km. The black square represents the size of one pixel from MODIS data which is used for the dust detection.

## 6.7 Defuse and Multiple Dust Sources

There are seven dust sources which it was not possible to trace the dusts to their sources, this represents 11% from the total. Only one dust sources were detected from multiple landforms, it is located south of Jabal Akhdar and is displayed in the appendix.

## 6.8 Discussion

The results presented here suggest that alluvial sources are more prevalent in the Cyrenaica region than lakes. One reason for this may be that some of the lakes are wet for much of the time and thus are not able to produce dust. To investigate this possibility further Landsat images from 2007 and 2009 were investigated (Figure 6.32). The rainfall in eastern Jabal Akhdar appears to be much stronger than in the west because the lakes in the east of fill with water in December 2007 and stay full until April 2008, whilst those in the west stay dry. The eastern lakes produce no dust during the 2008 study period, even when they have no surface water covering them, presumably because the surface is still moist. However, the lakes in the west stay dry and produce 15% of dust detected in this study (Figure 6.32).

**(a) 18December 2007 Landsat Band 7,4,2** **(b) NDVI**

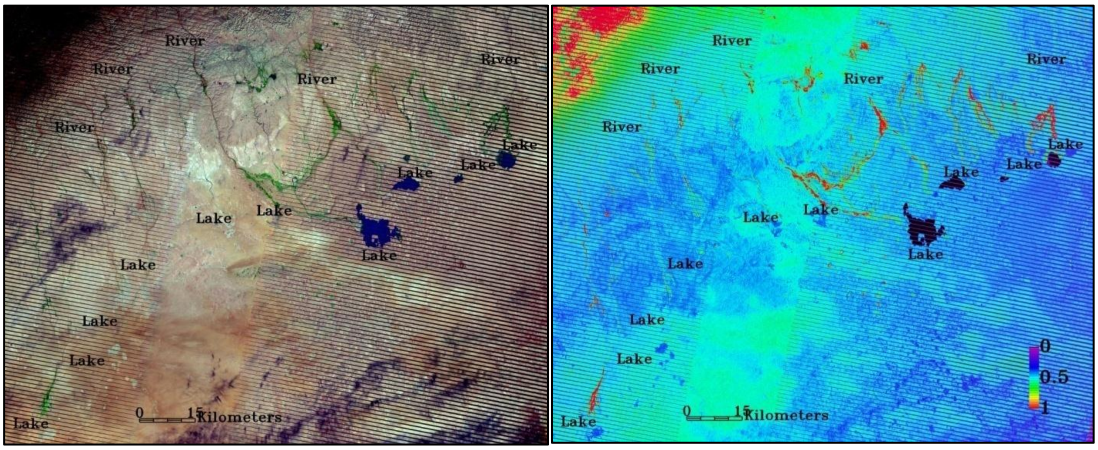


**(a) 19January 2008 Landsat Band 7,4,2** **(b) NDVI**

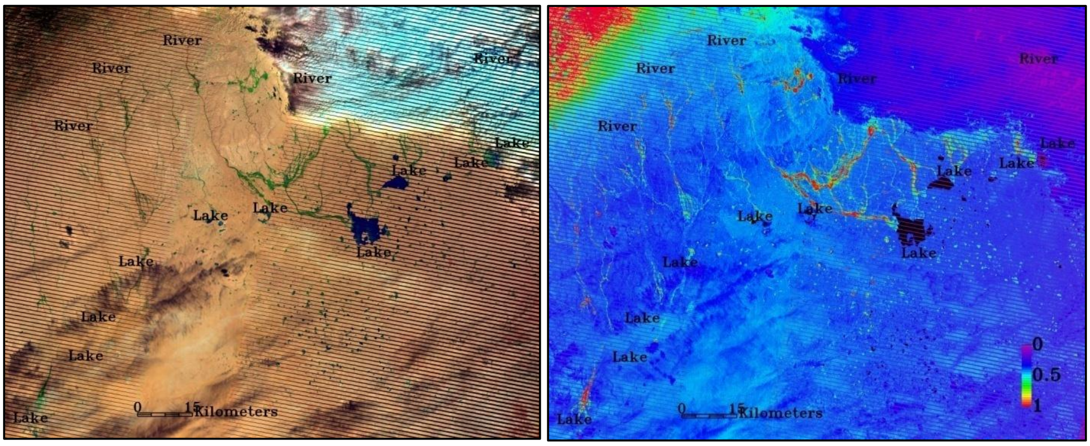

**(a) 04 February 2008 Landsat Band 7,4,2** **(b) NDVI**

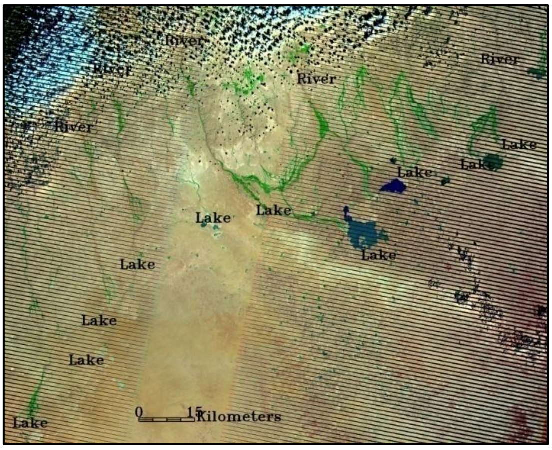


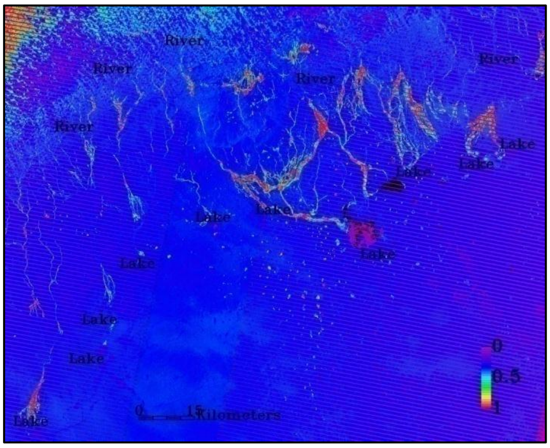


**(a) 24 April 2008 Landsat Band 7,4,2** **(b) NDVI**

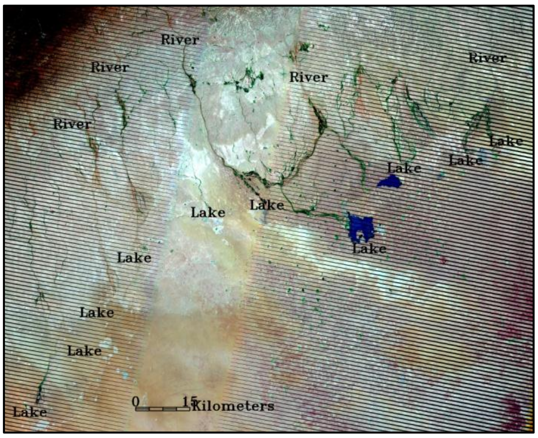


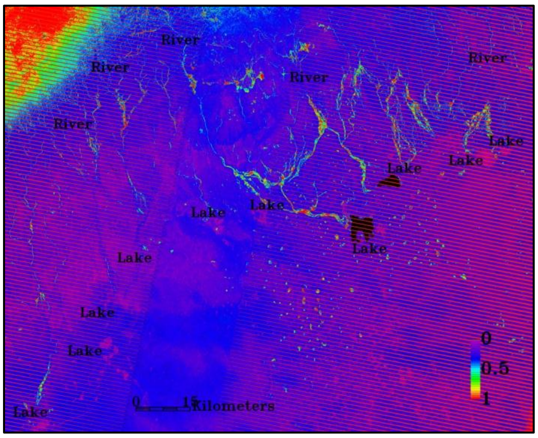


**(a) 11 June 2008 Landsat Band 7,4,2** **(b) NDVI**

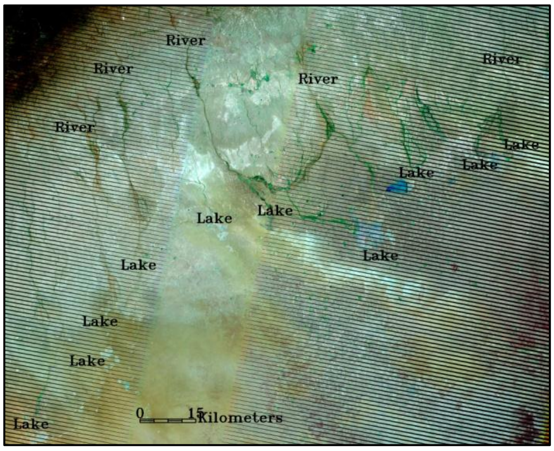


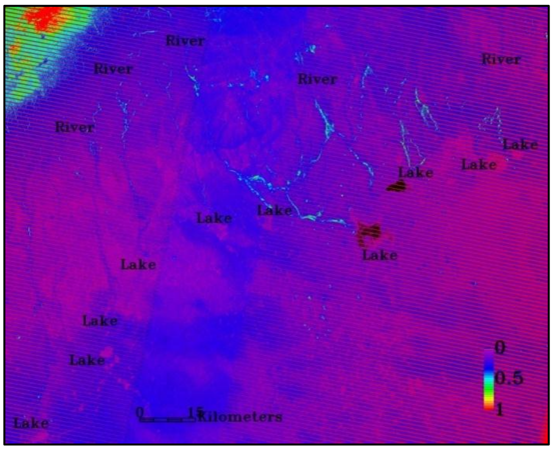

**(a) 13 July 2008 Landsat Band 7,4,2** **(b) NDVI**

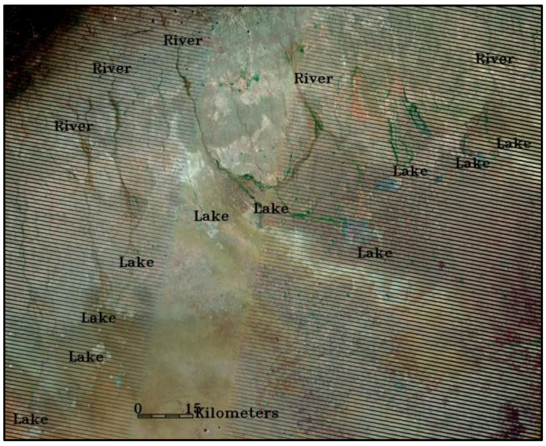


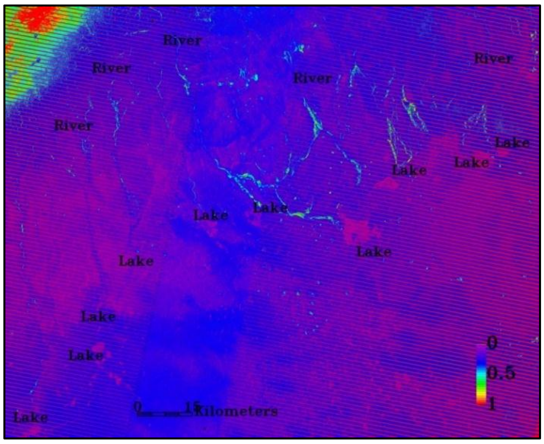


**(a) 14 August 2008 Landsat Band 7,4,2** **(b) NDVI**

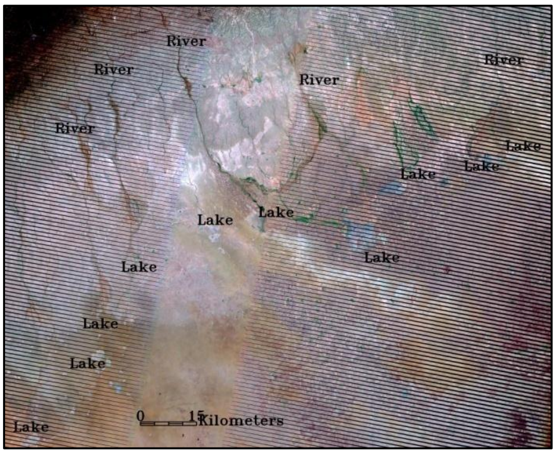


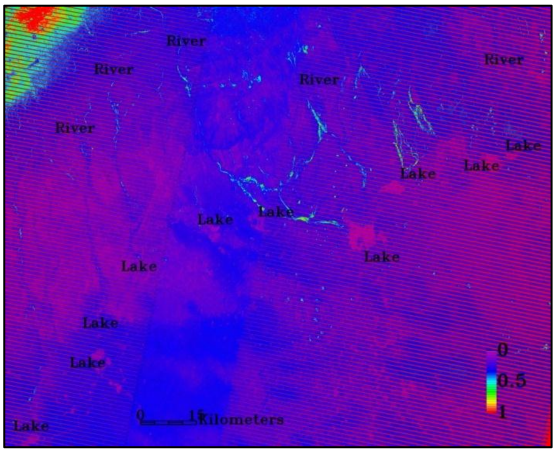


**(a) 06February 2009 Landsat Band 7,4,2** **(b) NDVI**

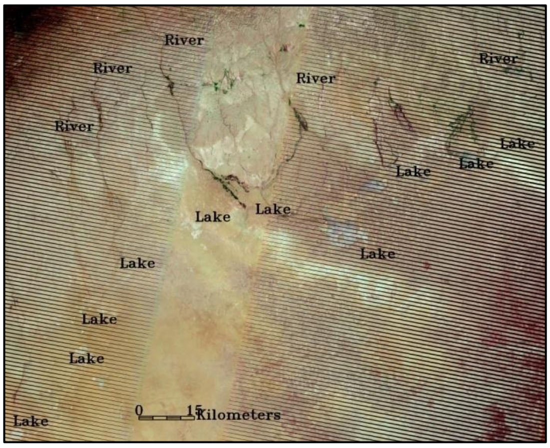


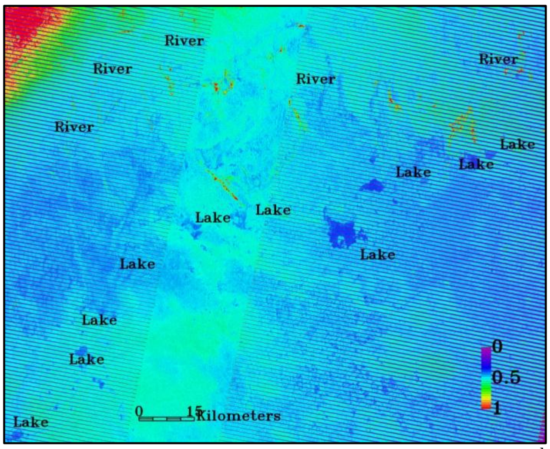


Figure 6.32 Landsat images shows the change of lakes during the year 2008 starting from 18th December 2007, 19th January 2008, 04th February, 24th April, 11th June, 13th July, 14th August,2008 and 06th February 2009 in south of Jabal Akhdar region, (a) Landsat Band 7,4,2 (b) NDVI.

One reason for the lack of lacustrine dust production in comparison to alluvial sources might be because 2008 is an untypically wet year. To investigate this, the Landsat TM quick looks were displayed and interpreted for the presence of surface water in the eastern and western Jabal Akhdar over the last 10 years. Table 6.4 lists the Cyrenaican lakes surface water cover from 2001-2010. The results support the view that 2008 is a rather wet year. Moreover, the results show the western Jabal Akhdar lakes remaining dry for the entire ten year period thus confirming that this region can produce dust from lakes over long periods of time. In contrast the eastern Jabal Akhdar was wet during 2002, 2005, and 2008 (Table 6.4), indeed they are wet for 18% of the time whereas those in the west are dry for the entire time. From Table 6.4 we can see that during July, August, and September all lakes in Cyrenaica appear to be dry throughout the ten monitoring period, the longest and heaviest dust storms monitored at this study has been detected during July were all the lakes are dry, however, we detect no dust coming from lakes that were previously wet in that year suggesting aspects of their surface condition precludes dust production. Thus the eastern lakes probably do not produce any dust during wet years, as was the case in 2008. Confirming this prediction is an important area of further study and may be illuminated by study of the nature of the lake surface during and after flooding.

The largest lake in the study region is Sebkah al Qenien with a surface area of well over 1000 $km^2$. No dust is seen deflating from this region in 2008. This is a surprise because lakes are generally thought to be prominent dust sources (Bullard et al., in press) and indeed the world’s largest dust source comes from the dried up bed of Lake Megachad (Warren et al., 2008). The probable reason for this that like the lakes in the east in 2008 Sebkah al Qenien is has a moist surface being feed by substantial quantities of groundwater.

Table 6.4 The condition of Lakes in Cyrenaica for ten years period as determined by interpretation of Landsat ETM quick looks.

| | 2001 | | 2002 | | 2003 | | 2004 | | 2005 | | 2006 | | 2007 | | 2008 | | 2009 | | 2010 | |
|---|---|---|---|---|---|---|---|---|---|---|---|---|---|---|---|---|---|---|---|---|
| | W | E | W | E | W | E | W | E | W | E | W | E | W | E | W | E | W | E | W | E |
| January | D | D | D | W | | | | | D | W | | | D | D | D | W | D | D | | |
| February | | | D | W | | | D | D | D | D | | | D | D | D | W | D | D | D | D |
| March | | | D | D | D | D | D | D | D | D | D | D | D | D | | | D | D | D | D |
| April | D | D | D | D | | | D | D | D | D | D | D | | | D | W | D | D | D | D |
| May | | | | | | | | | D | D | D | D | | | | | D | D | D | D |
| June | | | | | | | D | D | D | D | D | D | | | D | W | | | | |
| July | D | D | D | D | D | D | D | D | | | | | D | D | D | D | | | | |
| August | | | D | D | D | D | D | D | | | D | D | D | D | D | D | | | | |
| September | | | | | D | D | D | D | | | D | D | D | D | | | | | D | D |
| October | D | W | D | D | D | D | D | D | D | D | D | W | | | | | | | D | D |
| November | | | D | D | | | D | D | D | D | | | | | D | W | | | | |
| December | D | W | D | D | | | D | W | | | | | D | W | | | D | D | D | D |

W: West, E: East, D: Dry, W: Wet, White square: data is not available.

## 6.9 Explanation of Dust Sources: The Al Mekhili Paleo-lake and Fan Samples

In order to investigate the characteristics of the sediments of the eastern Jabal Akhdar fan and lake sources, and the factors that might control dust production on the ground, the Al Mekhili paleo-lake and fan region was visited in the field in April 2009 and 2010, soon after the 2008 flood had dried out and had stayed dry ever since. The region consisted of a paleo-lake located at the terminus of large fan that is fed by an ephemeral river system that flows from Jabal Akhdar. The fans in this region produce dust during all years, whereas the paleo-lakes do not produce dust during wet years. It was hoped that fieldwork might shed light on why those is and if the lakes produce dust during dry years. Investigation of the lake surface immediately shed light on this. In many areas the lake surface were covered in mud cracks formed soon after the drying of the lake (Figure 6.35B). In places sand sized particles of eroded mudcracks were found trapped in depressions on the lake surface showing that the lakes do erode during dry periods (Figure 6.35A).

Samples of these materials and those of the fan were investigated for their grain size to help understand the process of the dust production from fans and palaeo-lakes. Table 6.5 lists the four samples that were collected and shows their location (Lat/Long), the landforms they were derived from and the nature of the sample. Figure 6.33 shows the location of the samples in a Landsat colour composite.

Table 6.5 Particle size analogue sample locations and reasons for sampling

| Samples | Location | Lat/Lon | Material |
|---|---|---|---|
| Soil 6 | Al Mekhili paleo-lake | 32.0144<br>22.2733 | Mudcracks from lake |
| Lake | Al Mekhili paleo-lake | 32.0448<br>22.2652 | Windblown eroded mudcracks from lake |
| Soil 7 | Al Mekhili Fan | 32.0454<br>22.3002 | Sediment from alluvial fan |
| Soil 8 | Al Mekhili Fan | 32.03812<br>22.31943 | Eroded sediment trapped under vegetation on alluvial fan |

A

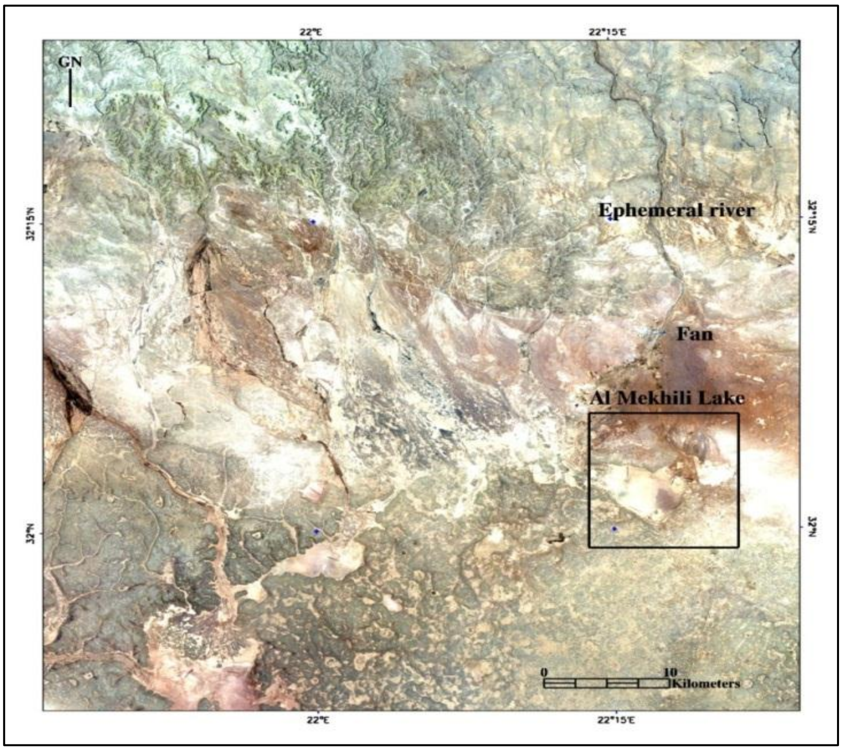


B

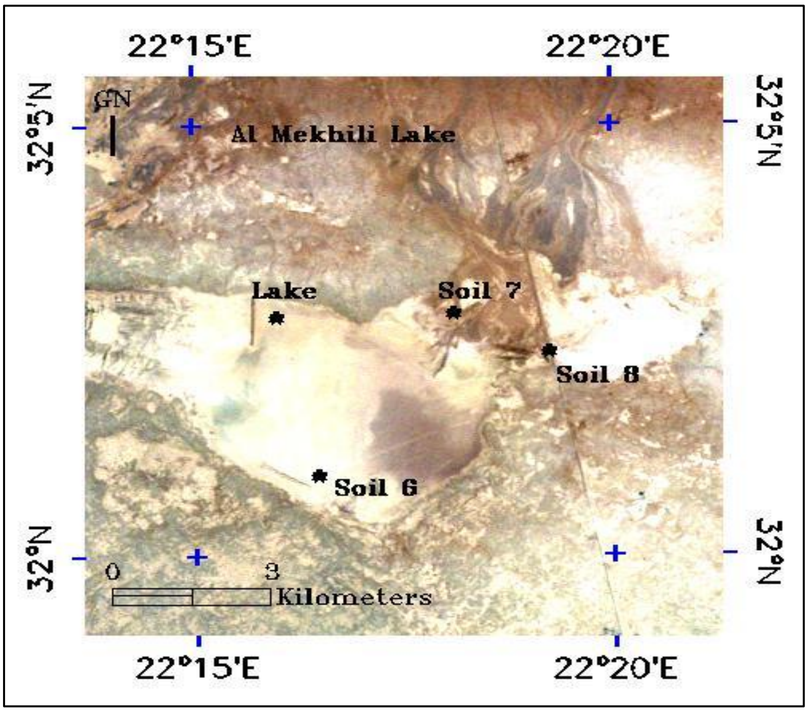


Figure 6.33 Landsat image shows Al Mekhili Lake and the location of the four samples used for the particle size analysis. (A) General view for the Al Mekhili Lake and the river connected to the lake. (B) Al Mekhili Lake with the fan attached to the lake and the four samples (Lake, Soil6, Soil7, and Soil8) displayed on the image.

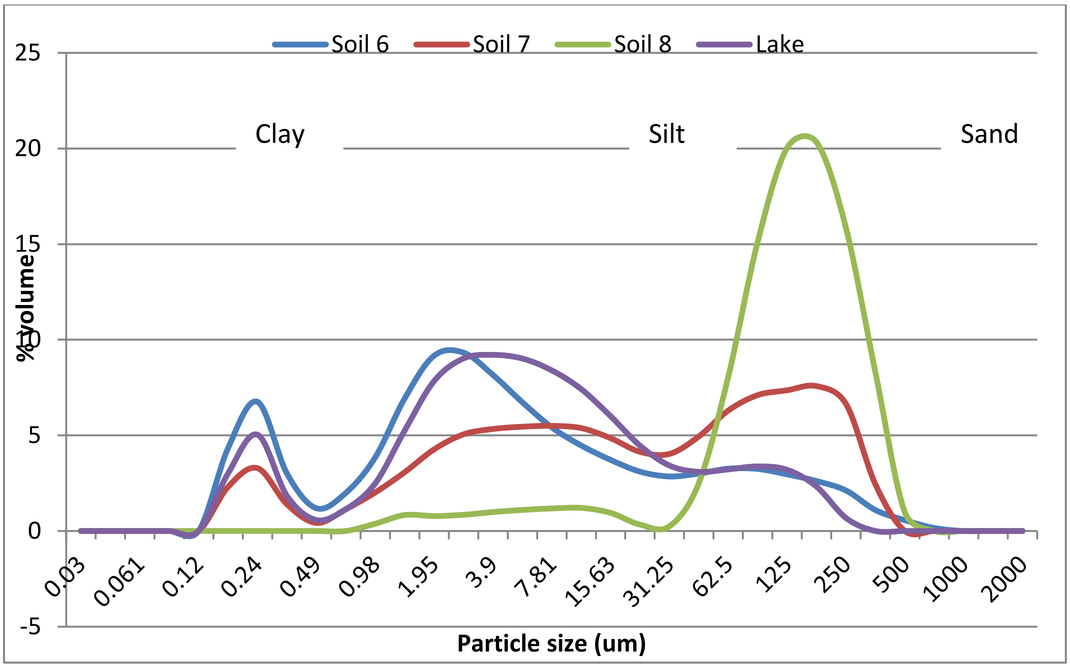


Figure 6.34 Graph display the particle size analysis for four samples from Al Mekhili paleo-lake (Source: Robyn Inglis).

Figure 6.34 shows the results of the grain size analysis and Figure 6.35 shows photographs of the sample sites. The sediments are bi-modal (e.g. Soil 8) and tri-modal (e.g. Soil 7) in character (Figure 6.34). The grain size distribution of the two lake surface samples, the mud cracks (Soil 6) and the deflated mud cracks (Lake) are similar and are dominated by clay and silt as shown in Figure 6.34. Sand concentrations are low and thus there is little sand on the lake surface to start the sandblasting process to enable deflation of dust from the lake. The sample characteristics suggest auto-abrasion whereby when the lake is dried up after a flooding event the mudcracks form on the lake surface and curl upwards as they dry (Figure 6.35B). During deflation events fragments of the curled up mud cracks (Figure 6.35B; sample soil 6) are saltated over the surface detaching other particles for saltation and also producing dust through abrasion. This scenario explains the presence of rounded crust fragments trapped in hollows on the lake surface (Figure 6.35A).

Grain size of the two samples from the alluvial fan that feeds into the lake (Soil 7 and 8) are both coarser than the paleo-lake sediments. Soil 7 comes from a ploughed field on the fan surface (Figure 6.35C) and is tri-modal, containing significant amounts of sand, silt and clay. Soil 8 is a sample of wind eroded fan sediment trapped by vegetation on the alluvial fan forming a Nebka (Figure 6.35D). This material thus represents deflated fan sediment that is re-deposited locally. The sample is predominantly sand and is very different from the un-eroded sample, the clay and silt having been deflated away leaving the saltated sand trapped behind vegetation. Thus it appears that the fans have enough sand for the sandblasting deflation process to be active and that these sands are concentrated and trapped on the fan surface by the small amounts of vegetation present. Little or no sand appears to make it onto the lake.

These results indicate that the sandblasting process dominates on the fans whereas auto abrasion dominates on the lake due to a lack of sand. This finding may also provide another reason why the fans are more prodigious dust sources than the lakes.

A

B

C

D

Figure 6.35 Photographs of the sample sites around Al Mekhili paleo-lake, (A)  Deflated mudcracks from lake, (B) Mud cracks on the lake surface, (C) Sediment from the alluvial fan, (D) Alluvial fan sediment trapped under vegetation (Source: Nick Drake).

## 6.10 Comparison of Results

There are now several studies in the literature that evaluate in the geomorphology of the dust sources using a similar methodology to that applied here. Dust storms are commonly detected from lakes, rivers and agricultural areas are as shown in Table 6.6. Bullard et al. (2008) shows that dust detected from lakes have got the highest percentage. This study and Drake et al. (2008) used the Sahara for their study, these results indicate the dust sources detected from alluvial sediments have the highest percentage at 64%, almost four times as much as the dust detected from lakes. In contrast Drake et al., (2008) found dust detected from alluvial sources was low, just 19% compared to 54% of dust sources detected from lakes. The low percentage of dust sources detected from lakes can be influenced by local climate at the time of this study. None of the lakes in the eastern part of Cyrenaica produce dust during 2008 because it stayed wet during most of the study period (see Section 6.8). This difference can also be interpreted as the result of the different geological background and the geomorphological context of Cyrenaica when compared to the western Sahara. This study implemented over North West of Sahara, on the margins of the desert, whereas Drake et al., (2008) implemented their studies in the much more arid Western Sahara. Bullard et al. (2008) used Lake Eyre for their study area and also found that the dust sources detected from lakes was a little higher than the dust detected from alluvial sources. Clearly fluvial and alluvial sources dominate in most regions, however, in different areas different factors can control the importance of different dust sources types, such as the geology and geomorphology and the time period of the study.

Table 6.6 Comparison of dust sources detected using remote sensing techniques. Adapted from (Bullard et al., 2011)

| | **Lake** | **Alluvial** | **Agriculture** |
|---|---|---|---|
| **This study** | 15% | 64% | 6% |
| **SW North America**<br>Lee et al., 2009 | 21% | 0% | 42% |
| **Lake Eyre Basin**<br>Bullard et al., 2008 | 29% | 26% | 0% |
| **Sahara**<br>Drake et al., 2008 | 54% | 19% | 2% |

## 6.11 Conclusion

Dust from alluvial fans forms the most important dust source in Cyrenaica in 2008 representing 45% of the total and occurring throughout much of the year. 62.5% of these sources are located on a single large fan located at south of Benghazi, 37.5% from alluvial fans spread along the southern margin of the Jabal Akhdar between Al Mekhili and the fan south of Benghazi.

Dust from lakes south of Jabal Akhdar on the margins of the Sahara forms the second most important source representing 15% of the total. This dust deflation occurs from March to July, a period of time when most of the lakes are dry. Most dust sources are detected from the western lakes and not from eastern lakes because the eastern lakes were flooded and presumably staid wet and/or moist for most of the year. Dust from the alluvial plain on the western coast of Cyrenaica is the third most important source representing providing 13% of the total detected dust sources. The deflation occurs mostly during April and May from the region to south of Benghazi. Dust generated from agriculture and rivers both provide 6% of the dust storms. Dust generated from agriculture usually happens during summer seasons were the fields have been cleared. The SEVIRI data, eye witnesses and unofficial sources report dust storms cover Benghazi many times each year. Much of this dust comes from the large alluvial fan that this thesis finds that most of reported dust comes from. In order to reduce or control the dust over Benghazi, we suggest re-vegetation of this region to prevent wind erosion. This would be a simple and cost effective way of improving the air quality of Benghazi.

When 2008 is compared to the previous two years it appears anomalously wet in the eastern part of Cyrenaica. The number and type of dust sources may be affected by this, with the amount of dust from lakes being lower than usual because of the excess moisture. However, investigation of lake and fans sediments and their deflation products provides another explanation suggesting that fans may produce more dust because their sediments promote the sand blasting process whilst those on the lakes do not.

When these results are compared to those from other parts of the Sahara that show Cyrenaica is a prominent alluvial source with 64% whereas in the Western Sahara lacustrine sources are predominant (54%). Indeed, when compared to other parts of the world the lacustrine sources are predominant with 29%, however, this is quite close to that of alluvial sources (26%).

## 7.1 Conclusion

There are two main aims of this research; (1) the first is to investigate and compare different techniques used to detect dust using remote sensing, (2) the second is to use the optimum technique of dust source detection in order to evaluate the dust sources in Cyrenaica.

The traditional techniques used to determine the dust sources, such as analysis of surface dust observations, back trajectory analysis of isobar data, and mineral tracers tell a different story regarding the Saharan dust sources. However, there is consensus about a few areas such as the Bodélé Depression, the western flank of the Hoggar Mountains, and area covering Southern Mauritania and Western Mali.

The comparison between the three remote sensing techniques that have been applied to dust source detection and that provide coverage of the entire Sahara for a year or more (TOMS AI, IDDI, and Schepanski et al., (2007)) shows some agreements between them,. especially in the two main dust sources areas identified by traditional methods (the Bodélé Depression and the western Hoggar Mountains). It was concluded that though TOMS and IDDI map the distributions of dust they detect both dust being deflated from sources and dust being transported from one region to another, whereas SEVIRI has the ability to trace the dust to their sources and build up a map of sources only. Thus it is the preferred method for dust source detection. However, the spatial resolution of SEVIRI is low and higher resolution satellites need to be employed if the nature of these sources is to be determined.

Several higher resolution satellites and associated remote sensing techniques have been investigated and these are reviewed in the literature review of chapter 2 in order to select techniques to use for dust source detection in this thesis. It is concluded that using MODIS Terra and Aqua sensors for the dust sources detection works well due to the reasonable ground pixel resolution of 1km and the twice a day temporal resolution (at 9:30 am and 12:30 pm local time).

Visible bands can be used to detect dust but have a problem detecting dust sources over the bright areas like the Sahara and can be used during day time only. The Deep Blue aerosol product has been developed to overcome this problem. However, it has got a poor spatial resolution of 10 km, making it difficult to identify the sources of dust. Moreover, based on the comparison of different types of cloud masks, it is shown that the Deep Blue product has not got poor cloud mask which misclassifies much dust as cloud.

Brightness temperature split windows (e.g. BTD (3.7 µm - 11 µm), BTD (8.6 µm - 11 µm), and BTD (11 µm - 12 µm)) are widely used for dust monitoring and have several advantages over the visible wavelengths; they and be used both day and night and work over bright backgrounds. Furthermore, techniques that use a combination of visible and thermal bands and have the advantage of both wavelengths and can be useful as they can try and combine the advantages of each wavelength whilst minimising the disadvantages. A number of these methods have recently been proposed and have provided promising results, though they are of course restricted to daytime use.

Baddock et al., (2009) utilised BTD (11 µm - 12 µm) split window methodology to provide a method of mapping and identifying dust sources using MODIS, to locate them in higher resolution Landsat imagery and to identify their nature. Bullard et al., (2008) used MODIS BTD (11 µm - 12 µm) from 2003 to 2006 to determine the dust emissions in the Lake Eyre Basin (LEB) and Zhang et al., (2008) used the same method to monitor dust storms events in China and Mongolia. Miller (2003) used BTD (12 µm - 11 µm) in combination with visible bands for detecting daytime airborne dust over both water and land. In contrast Ackerman (1989) investigated the BTD (3.7 µm – 11 µm) to track dust outbreaks but later (Ackerman 1997) suggested the BTD (8.6µm -11µm) split window for dust detection. Hansell et al., (2007) used a combination of BTD (8.6 µm - 11 µm) and BTD (11 µm - 12 µm) split windows to separate dust from cirrus clouds that were found to be affecting the dust detection when these split windows were used independently. Handley (2004) combined two other split windows (3.7 µm – 11 µm) and BTD (12 µm - 11 µm) to detect the dust whilst Roskovensky et al., (2005) combined BTD (11µm - 12µm) with visible bands to separate airborne dust from clouds.

A comparison of these different methods for dust source detection is needed to determine the optimum method. Baddock et al., (2009) provided a qualitative analysis, however, the ready availability of AERONET data makes a quantitative comparison relatively simple. This provides the first aim of this study. To achieve this five techniques were selected for the investigation and comparison, Ackerman (1989), Miller (2003), Hansell et al., (2007), Handley (2004), and Deep Blue (2003) Moreover, 4 different brightness temperature split windows are tested to find out if any of these provide accurate methods for detecting the dust.

Three methods were used for the evaluation of the dust indices: visual analysis, the M test that was used to study background effects and other statistical tests that were applied to evaluate the relationship between the AOT and each dust index. Visual analysis of the different dust indices suggests that they exhibit different performances in different regions. These discrepancies appear to be largely related to the different geological and geomorphologic background materials. Deep Blue (2003) is the worst visually, BTD (8.6 µm – 11 µm), and BTD (8.6 µm – 12 µm) also provide poor result visually over most of the backgrounds.

The mean of the M test over five different types of background provides contrasting results and indicates that Deep Blue (2003) exhibits the most contrast followed by Miller (2003). Ackerman (1989), BTD (3.7 µm – 12 µm), Handley (2004), Hansell et al., (2007), and BTD (12 µm – 11 µm) that have all got similar mean values and perform reasonably well. BTD (8.6 µm – 11 µm) and BTD (8.6 µm – 12 µm) have got a low mean M statistic and thus seem to perform poorly over most backgrounds. Almost all the M test results of the tested techniques are agree with the visual result and the statistical result apart from Deep Blue which has got the highest M value over the five tested background but visually is very hard to interpret. This is probably largely because Deep Blue has a poor spatial resolution 10km compared with the other techniques (used MODIS images 1 km) and that the cloud mask deletes much of the dust.

Other methods show much variation over specific backgrounds. Over the Limestone background Ackerman (1989) performs well whereas over the basalt background, BTD (12 µm – 11 µm) is the best method. Miller (2003) has got the best result over the quartz background. BTD (12 µm – 11 µm) is the best method over the granite whilst Ackerman (1989) is the best method to detect the dust over the diatomite background. This suggests that if the aim of a research project is to both detect sources and monitor concentrations then specific methods need to be applied to specific backgrounds, such as Ackerman or Miller over Limestone backgrounds. However, if the research needs to look over large areas that contain different backgrounds then a compromise method is needed and a good option here would be BTD (8.6 µm – 11 µm).

The statistical analysis of the relationship between the test indices and AOT suggested that Deep Blue has got the highest correlation $R^2 = 0.91$ and support by the result from Hsu et al., (2003) were the AOT of Deep Blue and the AOT from the AERONET shows good agreement. BTD (8.6 µm – 11 µm) and BTD (8.6 µm -12 µm) are the second and the fourth best according to the statistical comparison with AOT, $R^2 = 0.73$ and $R^2 = 0.69$ respectively. Ackerman (1989) is in third position according to the statistical results. BTD (11 µm – 12 µm), Handley and Hansell have the lowest correlations and highest RMS error. Ironically they have some of the highest M values suggesting that though they may be good for detecting dust by discriminating it from the background, increasing values of the index are not well related to higher dust concentrations.

The optimum method over Limestone, that of Ackerman (1989), was used to detect dust sources in Cyrenaica. A methodology involving numerous different satellites was developed to try and detect dust sources and identify their nature. The method starts by combining MODIS and SEVIRI. Both sensors are useful for detecting dust sources and understanding their meteorology. MODIS has high spatial resolution for tracing dust to its source whilst SEVIRI has got high temporal resolution (every 15 minutes), and ensures that we have not missed any dust storms not captured by MODIS. Moreover, SEVIRI was useful to determine the duration, direction, and synoptic climatology of the dust storms and then using this information infer the cause of each dust storm.

Once detected Landsat colour composite images (bands 7,4,2) was useful for evaluating the landforms and landuse of the identified dust sources. The scan line problems of the Landsat 7 sensor were problematic but did not preclude the interpretation of the geomorphology of the dust sources. Google Earth images were also found to be useful to help interpret the geomorphology of dust sources in areas of complex geomorphology and landuse because of its very high spatial resolution.

The results show that dust from alluvium forms the most important dust source in Cyrenaica with 45% from alluvial fan and 13% from alluvial plain and ?? from rivers. 62.5% of the fan sources are derived from a single large fan located at south of Benghazi. Much of this dust is transported northwards over Benghazi. Thus it may be possible to increase the air quality of Benghazi simply by managing the soil erosion on the fan by re-vegetating it. Alluvial sources are four times more common than lakes, th next most common dust source. In contrast Drake et al., (2008) found that in the western Sahara dust detected from alluvium provided only 19% of sources, nearly 3 times lower than dust sources detected from lakes. This is approximately the opposite result achieved in this study, yet both these studies were implemented in Sahara. Furthermore, the study of Lee et al., (2009) in SW North America does not show any alluvial dust sources. However, these regions have different geological, geomorphological, and climatological conditions perhaps explaining why these studies differ in their results.

Dust from lakes is derived from Jabal Akhdar region on the margins of the Sahara and form the second most important source representing 15 % of the total. Sebkah al Qenien is the largest lake in the study area, however, none of the dust sources detected from Cyrenaica comes from this lake because it has a moist surface, being below sea level and feed by substantial quantities of groundwater. The lakes located in eastern of Jabal Akhdar are full of water during most of 2008 and no dust is detected from them, whereas the lakes in the western Jabal Akhdar region are dry throughout the year and all of the dust is detected from these lakes. The study of Drake et al., (2008) indicates that dust from lakes forms 54% of sources in the western Sahara while the study of Lee et al., (2009) shows that dust detected from lakes was 21% in SW North America and the study of Bullard et al., (2008) in Lake Eyre Basin shows dust from lakes formed 29% of the total. Thus lakes in Cyrenaica are less prevalent dust souces than in other areas studies. This is probably because many of the lakes were wet throughout the year of study. The rainfall in eastern Jabal Akhdar in December 2007 and January 2008 appears to be much stronger than in the west because the lakes in the east filled with water in December 2007 and stay full until April 2008, whilst those in the west stayed dry. The eastern lakes produce no dust during the 2008 study period, even when they have no surface water covering them, presumably because the surface is still moist. However, the lakes in the west stay dry and produce 15% of dust detected in this study.

Finally by identifying the precise location of the dust sources at the small scale and providing geomorphological information about the dust sources as is done in this study, we provide information that can be used to improve the preferential dust source maps used to model global dust production. Moreover, meteorological information such as timing, direction, and cause of dust storms is useful information for managing soil erosion and its knock on effects in air quality and health warning prediction.

## 7.2 Further Work

This study was not conducted in a typical year, being wetter in the eastern Jabal Akhdar region than usual. In order to consolidate these results this study needs to cover longer period of time, continuous monitoring for ten years would provide interesting results.

Five different dust sources have been reported in this study throughout Cyrenaica, mapping each source in the field, recording its characteristics and collecting samples from each source type for subsequent grain size analysis would shed more light on the causes of deflation.

The size of Sahara is 8.6 million $km^2$, no previous study has looked at the geomorphology and climatology of dust sources in the entire of Sahara. This needs to be done to explain why the Sahara is the World's biggest dust source. The methods developed here could be used to do this.

In order to generalize the result of this study, it is useful to implement the selected techniques on the other parts of the Sahara to test the reliability of the technique and to find out how this technique is flexible to use in the entire of the Sahara and tested if it is possible to use globally.

## 8. References

Ackerman, S.A. (1989) Using the radiative temperature difference at 3.7 and 11 µm to track dust outbreaks, Remote Sensing of Environment, Vol. 27, pp 129-133.

Ackerman, S.A. (1997) Remote sensing aerosols using satellite infrared observations, Journal of Geophysical Research, Vol. 102, No. D14, pp. 17069-17079.

Ackerman, S. A., Moeller, C. C., Strabala, K. I., Gerber, H. E., Gumley, L. E., Menzel, W. P., Tsay, S. C. (1998) Retrieval of effective microphysical properties of clouds: A wave cloud case study, Geophysical Research Letter, Vol. 25(8), pp. 1121–1124.

Afeti, G.M. Resch, F.J. (2000) Physical characteristics of Saharan dust near the Gulf of Guinea, Atmospheric Environment, Vol. 34, pp. 1273-1279.

Alfaro, S.C., Gaudichet, A., Gomes, L., Maillé, M. (1997) Modelling the size distribution of a soil aerosol produced by sandblasting, Journal Geophysical Research, Vol. 102, No. D10, pp. 11,239-11,249.

Alfaro, S.C., Gaudichet, A., Gomes, L., Maillé, M. (1998) Mineral aerosol production by wind erosion: aerosol particle sizes and binding energies, Geophysical Research Letter, Vol. 25, No. 7, pp. 991-994.

Alfaro, S.C., Rajot, J.L., Nickling, W. (2004) Estimation of PM20 emissions by wind erosion: main sources of uncertainties, Geomorphology, Vol. 59, pp. 63–74.

Alpert, P., Ganor, E. (1993) A jet stream associated heavy dust storm in the eastern Mediterranean, Journal Geophysical Research, Vol. 98, pp. 7339-7349.

Anderson, R. Hallet, B., (1986) **S**ediment transport by wind: Toward a general model, Geological Society of America. Vol. 97, No. 5, pp. 523-535.

Avila, A., Queralt-Mitjans, I., Alarco´n, M. (1997) Mineralogical composition of African dust delivered by red rains over north-eastern Spain, Journal of Geophysical Research, Vol. 102, pp. 21977-21996.

Azizov, A., Ismailov, I. M., Kadyrov, K. G., Mirzazhanov, K. M., Toshov, B. R. (1979) Relation between the amount of loamy sand soil removed by wind and soil moisture [in Russian], Pochvovedeniye, Vol. 4, pp. 105-107.

Baddock, M. C., Bullard, J. E., Bryant, R. G. (2009) Dust source identification using MODIS: A comparison of techniques applied to the Lake Eyre Basin, Australia, Remote Sensing of Environment, Vol. 113, pp. 1511-1528.

Bagnold, R. A., (1941) The Physical of blown sand and desert dunes. Methuen, London. Brooks, N. (1999) Dust-climate interactions in the Sahel-Sahara zone of northern Africa, with particular reference to late twentieth century Sahelian drought, PhD Thesis. University of East Anglia.

Bergametti, G., Gomes, L., Remoudaki, E., Desbois M, Martin D, Buat-Me´nard, P. (1989) Present transport and deposition patterns of African dusts to the north-western Mediterranean. In: Leinen, M., and Sarnthein, M., (eds) Palaeoclimatology and palaeometerology: modern and past patterns of global atmospheric transport. NATO ASI Ser C 282: pp. 227-252.

Brooks, N. Legrand, M. (2000) Dust variability over northern Africa and rainfall in the Sahel, In: McLaren S.J., Kniverton D eds Linking land surface change to climate change, Kluwer, Dordrecht, pp. 1-25.

Bullard, J., Baddock, M., McTainsh, G., Leys J. (2008) Sub-basin scale dust source geomorphology detected using MODIS, Geophysical Research Letters, Vol. 35, L15404.

Bullard, J.E., Harrison, S.P., Baddock, M.C., Drake, N., Gill, T.E., McTainsh, G., Sun, Y. (2011) Preferential dust sources: A geomorphological classification designed for use in global dust-cycle models, Journal of Geophysical Research, Vol. 116, F04034, pp. 20 PP.

Carlson, T.N., (1978) Atmospheric Turbidity in Saharan Dust Outbreaks as Determined by Analyses of Satellite Brightness Data, Monthly Weather Review, Vol. 107. pp. 322-334.

Chiapello, I., Prospero, J.M., Herman, J.R. Hsu, N.C. (1999) Detection of mineral dust over the North Atlantic Ocean and Africa with the Nimbus 7 TOMS, Journal of Geophysical Research, Vol. 104, No. D8, pp. 9277-9291.

Chu, D.A., Kaufman, Y.J., Ichoku, C., Remer, L.A., Tanre, D., Holben, B.N. (2002) Validation of MODIS aerosol optical depth retrieval over land, Geophysical Research Letters, Vol. 29, No.12, pp. 8007.

Clark, R.N., Swayze. G.A., Gallagher, A.J., King, T.V.V., Calvin, W.M. (1993) The U. S. Geological Survey, Digital Spectral Library: Version 1: 0.2 to 3.0 microns, U.S. Geological Survey Open File Report 93-592, 1340 pages, http://speclab.cr.usgs.gov.

Cooke, R.U., Warren, A., Goudie, A. (1993) Desert geomorphology, UCL Press, London.

D'Almeida G.A. (1986) A model for Saharan dust transport, Journal of Climate and Applied Meteorology, Vol.25, pp. 903-916.

Darmenov, A., Sokolik, I.N. (2005) Identifying the regional thermal-IR radiative signature of mineral dust with MODIS, Geophysical Research Letters, Vol. 32, L16803

Darwen, C. (1893) Journal of Researches. T. Nelson and Sons, London.

Dave, J.V. (1972) Development of programs for computing characteristics of ultraviolet radiation, International Business Machines Corporation, Federal Systems Division, Gaithersburg, Technical Report.

De Paepe, B., Steven D. (2009) Dust Aerosol Optical Depth Retrieval over a Desert Surface Using the SEVIRI Window Channels. Journal Atmospheric Oceanic Technolgy, Vol. 26, Issue 4, pp. 704–718.

Drake, N.A., El-Hawat, A.S., Turner, P., Armitage, S.J., Salem M.J., White K.H., McLaren, S. (2008) Palaeohydrology of the Fazzan Basin and surrounding regions: The last 7 million years, Palaeogeography Palaeoclimatology Palaeoecology, Vol. 263 (3-4). pp. 131-145. ISSN 0031-0182.

Drury, S.K. (1990) A Guide to Remote Sensing. Oxford University Press, Oxford.

Dubief, J. (1953) Les vents de sable dans le Sahara Francais Colloques Internationaux de Centre National de Recherches Scientifiques, Paris, Vol. 35, pp. 45-70.

Dubovik, O., Holben, B., Eck, T.F., Smirnov, A., Kaufman, Y.J., King, M.D., Tanre, D., Slutsker, I. (2002) Variability of absorption and optical 336 properties of key aerosol types observed in worldwide locations, Journal of Atmospheric Sciences, Vol. 59, pp. 590– 608.

Duce, R.A. (1995) Sources, distributions, and fluxes of mineral aerosols and their relationship to climate. In: Charlson, R., J., Heintzenberg, J., (eds) Aerosol forcing of climate. Wiley, Chichester, pp. 43-72.

Ebdon, D., (1985) Statistics in Geography: A Practical Approach, second edition, United Kingdom.

El Hawat, A.S. Pawellek, T. (2005) A Field guidebook to the geology of Cyrenaica, Libya. RWE Dea North Africa/Middle East GmbH.

Falkowski, P.G., Barber, R.T., Smetacek, V. (1998) Biogeochemical controls and feedbacks on ocean primary production, Science Vol. 281, pp.200–206.

Fiol, L.A., Forno´s, J.J., Gelabert, B., Guijarro, J.A. (2005) Dust rains in Mallorca (Western Mediterranean): their occurrence and role in some recent geological processes, Catena 63: pp. 64-84.

Foody, G.M. (2002) Status of land cover classification accuracy assessment, Remote Sensing of Environment, Vol. 80, pp. 185– 201.

Ganor, E. Mamane, Y. (1982) Transport of Saharan dust across the eastern Mediterranean. Atmospheric Environmental, Vol. 16, Issue 3, pp. 581-587.

Ganor, E., Foner, H.A., Brenner, S., Neeman, E., Lavi, N. (1991) The chemical composition of aerosols settling in Israel following dust storms, Atmospheric Environmental Vol. 25, pp. 2665-2670.

Garrison, V.H., Shinn, E.A., Foreman, W.T., Griffin, D.W., Holmes, C.W., Kellogg, C.A., Majewski, M.S., Richardson, L.L., Ritchie, K.B., Smith, G.W. (2003) African and Asian dust: from desert soils to coral reefs, BioScience, Vol. 53, pp. 469-480.

Giglio, L., Descloitres, J., Justice, C.O., Kaufman, Y.J. (2003) An enhanced contextual fire detection algorithm for MODIS, Remote Sensing of Environment, Vol. 87, pp. 273 - 282.

Gillette, D.A., Adams J., Endo A., Smith D., Kihl, R. (1980) Threshold velocities for input of soil particles into the air by desert soils, Journal of Geophysical Research, Vol. 85, No. C10, pp. 5621-5630.

Gillette, D.A. Passi, R. (1988) Modelling dust emission caused by wind erosion, Journal of Geophysical Research, Vol. 93, No. D11, pp. 14233-14242.

Gillies, J.A., Nickling, W.G., McTainsh, G.H. (1996) Dust concentration and particle-size characteristics of an intense dust haze event: inland delta region, Mali, West Africa, Atmospheric Environmental, Vol. 30, pp. 1081-1090.

Ginoux, P., Chin, M., Tegen, I., Prospero, J.M., Holben, B., Dubovik, O., Lin, S.J. (2001) Sources and distributions of dust aerosols simulated with the GOCART model, Journal of Geophysical Research, Vol. 106, pp. 20255-20273.

Godon, N.A. Todhunter, P.E. (1998) A climatology of airborne dust from the Red River Valley of North Dakota, Atmospheric Environmental, Vol. 32, pp. 1587-1594.

Goldsmith, V., Rosen, P., Gertner, Y. (1988) Eolian sediment transport on the Israeli coast, final report to US-Israel Binational Science Foundation, Jerusalem.

Goudie, A.S., Washington, R., Todd, M., Swann, M. (2003) North African dust production: Source areas and variability, Exchanges, No.27, pp 1-4.

Goudie, A.S., Middleton, N.J. (2001) Saharan dust storms: nature and consequences, Earth Science Reviews, Vol. 56, pp. 179-204.

Goudie, A.S. Middleton, N.J. (2006) Desert Dust in the Global System, Publisher: Springer, Oxford, UK.

Greeley, R., Lancaster, N., Gaddis, L., Rasmussen K.R., White B.R., Saunders, R.S., Wall, S., Dobrovolskis, A.R., Iversen, J.D. (1990) Relationships between topographic roughness and aeolian processes, Acta Mechanica, Vol. 2, pp. 77-88.

Griffin, D.W., Kellogg, C.A., Garrison, V.H., Lisle, J.T., Borden, T.C., Shinn, E.A. (2003) Atmospheric microbiology in the northern Caribbean during African dust events, Journal of Aerobiologia, Vol. 19, pp. 143-157.

Griggs, M (1975) Measurements of atmospheric aerosol optical thickness over water using ERTS-1 data, Journal of the Air Pollution Control Association, Vol. 25, pp. 622-626.

Griggs, M. (1978) Satellite observations of atmospheric aerosols during the E0MET cruise, Journal of the Atmospheric Sciences, Vol. 36, pp. 695-697.

Gruber, N. Sartmiento, J.L. (1997) Global patterns of marine fixation and denitrification, Global Biogeochemical Cycles, Vol. 11, pp. 235-266.

Handley, P. (2004) Detecting sources of dust within the Sahara, MSc thesis, King's College, London.

Hansell, R.A., Ou, S.C., Liou, K.N., Roskovensky, J.K., Tsay, S.C., Hsu, C. (2007) Simultaneous detection/separation of mineral dust and cirrus clouds using MODIS thermal infrared window data, Geophysical Research Letters, Vol. 34, pp. L11808.

Hao, X. Qu, J.J. (2007) Saharan dust storm detection using moderate resolution imaging spectroradiometer thermal infrared bands, Journal of Applied Remote Sensing, Vol. 1, pp. 013510.

Haywood, J.M., Francis, P.N., Glew, M.D., Taylor, J.P. (2001) Optical properties and direct radiative effect of dust, A case study of two Saharan outbreaks using data from the U,K, Met office C-130, Journal of Geophysical Research, Vol. 106, No. 18, pp. 417-430.

Herman, J.R., Bhartia, P.K., Torres, O., Hsu, C., Seftor, C., Celarier, E. (1997) Global distribution of UV-absorbing aerosols from Nimbus 7/TOMS data, Journal of Geophysical Research, Vol. 102, pp. 16911-16922.

Herrmann, L., Stahr, K., Jahn, R. (1999) The importance of source region identification and their properties for soil-derived dust: the case of Harmattan dust sources for eastern West Africa, Contribution of Atmospheric Physics, Vol. 72, pp. 141-150.

Holben, B.N., Eck, T.F., Slutsker, I., Tanre, D., Buis, J.P., Setzer, A., Vermote, E., Reagan J.A., Kaufman, Y.J., Nakajima, T., Lavenu, F., Jankowiak, I., Smirnov A. (1998) AERONET-A federated instrument network and data archive for aerosol characterization, Remote Sensing of Environment, Vol. 66, No 1, pp. 1-16.

Hotta, S., Kubota, S., Katori, S., Horikawa, K. (1984) Sand transport by wind on a wet sand surface, Proceedings of the 19th Coastal Engineering Conference, ASCE, New York, pp. 1263–1281.

Hsu, N.C., Tsay, S., King, M.D., Herman, J.R. (2004) Aerosol properties over bright-reflecting source regions, IEEE Transactions on Geosciences and Remote Sensing, Vol. 42, No. 3, pp. 557-569.

Hu, X.Q., Lu, N.M., Tiu, T., Zhang, P. (2008) Operational retrieval of Asian sand and dust storm from FY-2C geostationary meteorological satellite and its application to real time forecast in Asia, Atmospheric Chemistry and Physics, Vol. 8, pp. 1649–1659.

Hunt, G.R., Salisbury, J.W., Lenhoff , C.J. (1974) Visible and near-infrared spectra of minerals and rocks, IX. basic and ultrabasic igneous rocks, Modern Geology, Vol. 5, pp. 15- 22.

Idso, S.B. (1976) Dust storms. Scientific American, Vol. 235, pp. 108-111, 113-14.

Inglis, R., (2008) Human occupation and changing environments at the Middle-Upper Palaeolithic transition: Soil micromorphology at the Haua Fteah, Libya, PhD thesis, University of Cambridge.

IPCC - Intergovernmental Panel on Climate Change (2001) Third Assessment Report.

Israelevich, P., Ganor, E., Levin, Z., Joseph, P. J. (2003) Annual variations of physical properties of dust over Israel, Journal of Geophysical Research, 108/D13:4381.

Kalu, A.E., (1975) On the meteorology of dusty atmosphere. Q. Meteorology Magazine, Meteorology Department, Lagos, Nigeria. Under review for publication.

Kalu, A.E., (1979) The African dust plume: its characteristics and propagation across West African winter in Morales C ed Saharan dust: mobilization, transportation, and deposition. Chichester, Wiley pp. 95-118.

Kaufman, Y.J., Wald, A.E., Remer, L.A., Gao, B., Li, R., Flynn, L. (1997) The MODIS 2.1-μm Channel – Correlation with visible reflectance for use in remote sensing of aerosol, IEEE, Geoscience and Remote Sensing, Vol. 35, No. 5, pp. 1286-1298.

Kaufman, Y.J., Tanr´e D. Remer, L.A., Vermote, E.F., Chu, A. (1997) Operational remote sensing of tropospheric aerosol over land from EOS moderate resolution imaging spectroradiometer, Journal of Geophysical Research, Vol. 102, D14, pp. 17,051-17,067.

Kaufman, Y.J., Karnieli, A. Tanre, D. (2000) Detection of dust over deserts using satellite data in the solar wavelengths, IEEE, Geoscience and Remote Sensing, Vol. 38, No. 1, pp. 525-531.

Kaufman, Y.J., Koren, I., Remer, L. A., Tanre, D., Ginoux P., Fan S. (2005) Dust transport and deposition observed from the Terra-Moderate Resolution Imaging Spectroradiometer (MODIS) spacecraft over the Atlantic Ocean, Journal of Geophysical Research, Vol. 110, D10s12.

King, M.D., Kaufman, Y.J., Tanre, D., Nakajima, T. (1999) Remote Sensing of tropospheric aerosols from space: Past, present and future, Bulletin of the American Meteorological Society, Vol. 80, No.11, pp 2229-2259.

King, M.D., Menzel, W.P., Kaufman, Y.D., Tanre, D., Gao,B., Platnick, S., Ackerman, S., Remer, L., Pincus, R., Hubanks, P.A. (2003) Cloud and aerosol properties, precipitable water, and profiles of temperature and water vapour from MODIS, IEEE, Geoscience and Remote Sensing, Vol. 42, No. 2, pp. 442-458.

Klüser, L. Schepanski, K. (2009) Remote sensing of mineral dust over land with MSG infrared channels: A new Bitemporal Mineral Dust Index, Remote Sensing of Environment, Vol. 113, pp. 1853–1867.

Koren, I, Joseph, J.H. Israelevich, P. (2003) Detection of dust plumes and their sources in northeastern Libya, Candian Journal of Remote Sensing, Vol.29, N0.6, pp. 792-796.

Koren, I, Kaufman, Y.J. (2004) Direct wind measurements of Saharan dust events from Terra and Aqua satellites, Geophysical Research Letters, VOL. 31, L06122.

Kriebel, K.T., Saunders, R.W. (1988) An improved method for detecting clear sky and
cloudy radiances from AVHRR data, International Journal of Remote Sensing, Vol. 9, pp 123-150.

Kubilay, N., Cokacar, T., Oguz, T. (2003) Optical properties of mineral dust outbreaks over the Northeastern Mediterranean, Journal of Geophysics Research, Vol. 108: D21.

Kubilay, N., Oguz T., Mocak M., Torres O. (2005) Ground-based assessment of Total Ozone Mapping Spectrometer (TOMS) data for dust transport over the Northeastern Mediterranean, Global Biogeochemical Cycles, Vol. 19, GB1022.

Legrand, M., Desbois, M., Vovor, K. (1994) Satellite Detection of Saharan Dust: Optimized Imaging during Nighttime, Journal of Climate, Vol. 1, pp 256-264.

Legrande, M., Plana-Fattori, A. N'doume, C. (2001) Satellite detection of dust using the IR imagery of Meteosat1. Infrared difference dust index, Journal of Geophysical Research, Vol. 106, No. 16, pp 251-274.

Lee, J.A., Gill, T.E., Mulligan, K.R., Acosta, M.D., Perez, A.E. (2009) Land use/land cover and point sources of the 15 December 2003 dust storm in south western North America, Geomorphology, Vol. 105, pp. 18-27.

Lepple, F.K., Brine, C.J. (1976) Organic constituents in eolian dust and surface sediments from north west Africa, Journal Geophysical Research, Vol. 81, pp. 1141-1147.

Liou, K.N., Hansen, J.E. (1971) Intensity and polarization for single scattering by polydisperse spheres: A comparison of ray optics and Mie theory, Journal of the Atmospheric Sciences, Vol. 28, pp. 995-1004.

Liu, D., Wang, Z., Liu, Z., Winker, D., Trepte, C. (2008) A height resolved global view of dust aerosols from the first year, Journal of Geophysical Research, Vol. 113, D16214.

Lyon (1964) Mid-Infrared Spectroscopy: Laboratory Data, Remote Geochemical Analysis.

Marticorena B., Bergametti G. (1995) Modeling the atmospheric dust cycle: 1-design of a soil derived dust production scheme, Journal of Geophysical Research, Vol. 100, pp. 16,415–16,430.

McBurney, C.B.M. Hay, R.W. (1955) Prehistory and Pleistocene Geology in Cyrenaica Libya. Cambridge University Book

McCauley, A., Jones, C. (2005) Managing for soil erosion, Montana state university.

McTainsh, G.H., Walker, P.H. (1982) Nature and distribution of Harmattan dust, Zeitschrift Für Geomorphologie, Vol. 26, pp. 417–435.

Middleton N.J. (1986) The geography of dust storms, PhD thesis. University of Oxford, UK.

Middleton N.J. (1986a) Dust storms in the Middle East, Journal of Arid Environmental, Vol. 10, pp. 83-96.

Middleton N.J. (1991) Dust storms in the Mongolian People's Republic, Journal of Arid Environmental, Vol. 20, pp. 287-297.

Middleton N.J., Betzer P.R., Bull P.A. (2001) Long-range transport of 'giant' Aeolian quartz grains: linkage with discrete sedimentary sources and implications for protective particle transfer. Marin Geology, Vol. 177, Issues 3-4, pp. 411-417.

Middleton N.J., Goudie, A.S. (2001) Saharan dust: sources and trajectories. The Institute of British Geographers, Vol. 26, pp. 165-181.

Miller, S.D. (2002) An improved land/ocean dust enhancement applicable to MODIS. In: 12th Conference on satellite meteorology and oceanography. [Available Online] http://ams.confex.com/ams/pdfpapers/53832.pdf [Accessed 03 April 2004].

Miller, S.D. (2003) A consolidated technique for enhancing desert dust storms with MODIS. Geophysical Research Letter, Vol. 30, No. 20, pp 2071-2074.

Mishchenko, M., Geogdzhayev, I.V., Cairns, B., Rossow, W.B., Lacis, A.A. (1999) Aerosol retrievals over the ocean by use of channels 1 and 2 AVHRR data: sensitivity analysis and preliminary results, Applied Optics Journal, Vol. 38, No. 36, PP. 7325-7341.

Moulin, C., Lambert, C.E., Dayan, U., Masson, V., Ramonet, M., Bousquet, P., Legrand, M., Balkanski, Y.J., Guelle, W., Marticorena, B., Bergametti, G., Dulac, F., (1998) Satellite climatology of African dust transport in the Mediterranean atmosphere. Journal of Geophysical Research, Vol. 103, No. D11, pp. 13,137–13,144.

Nickling W.G., (1978) Eolian sediment transport during dust storms: Slims River Valley, Yukan Territory. Canadian Journal of Earth Sciences, Vol. 15, No. 7, pp. 1069-1084.

Norman, J.M., Becker, F., (1995) Terminology in thermal infrared remote sensing of natural surfaces, Agricultural and Forest Meteorology, Vol. 77, pp. 153-166.

Norton C.C., Mosher, F.R., Hinton, B., Martin, D.W., Santek, D., Kuhlow, W., (1980) A Model for Calculating Desert Aerosol Turbidity over the Oceans from Geostationary Satellite Data, Journal of Applied Meteorology, Vol. 19, No. 6, pp. 633-644.

N'Tchayi, G.M., Bertrand, J.J., Nicholson, S.E., (1997) The diurnal and seasonal cycles of wind-borne dust over Africa north of the Equator. Journal of Applied Meteorology, Vol. 36, pp. 868-882.

O'Loingsigh, T., McTainsh, G.H., Tapper, N.J., Shinkfield, P. (2010) Lost in code: A critical analysis of using meteorological data for wind erosion monitoring. Aeolian Research, Article in Press, Vol. 2, Issue 1, pp. 49-57.

Offer, Z.Y., Azmon, E., (1994) Chemistry and mineralogy of four dust storms in the northern Negev Desert, Israel. (1988-1992). Science of the Total Environment, Vol. 143, Issues 2-3, pp. 235-243.

Orgill, M.M., Sehmel, G.A., (1976) Frequency and diurnal variation of dust storms in the contiguous U.S.A., Atmospheric Environmental, Vol. 10, pp. 813-825.

Patterson, E.M., Gillette, D.A. (1977a) Measurements of visibility vs mass-concentration for airborne soil particles, Atmospheric Environment Vol. 11, pp. 193-196.

Payannis, A., Amiridis, V., Bösenberg, J., Chaikovski, A., De Tomasi, F., Freudenthaler, V., Grigorov, I., Mattis, I., Mitev, V., Munoz, C., Pappalardo, G., Nickovic, S., Pisani, G., Puchalski, S., Rizi, V., Trickl, T., Vaughan, G., (2005) First systematic observations of Saharan dust over Europe (2000-2003): statistical analysis and results, Geophysical Research Abstracts, Vol. 7, No. 04016.

Pereira, J.M.C. (1999) A comparative evaluation of NOAA/AVHRR vegetation indices for fire scar detection and mapping in the Mediterranean type regions. IEEEE, Geoscience and Remote Sensing, Vol. 37, No. 1, pp 217-226.

Pieters, C.M., Englert, P.A.J., (1993) Remote Geochemical Analysis: Elemental and Mineralogical Composition, Cambridge University Press, Cambridge.

Pisano G., Spinelli N., D'Avano L., Boselli A., Wang X., Papayannis A. (2005) Atmospheric African mineral dust monitoring with Raman Lidar over Napoli. Geophysics Research Abstract, Vol. 7, No. 09752.

Prata, A.J. (1989) Observations of volcanic ash clouds in the 10-12 μm window using AVHRR/2 data, International Journal of Remote Sensing. Vol. 10, pp. 751-761.

Prata, A.J. (1993). Land surface temperatures derived from the advanced very high resolution radiometer and the along-track scanning radiometer. Journal of Geophysical Research, Vol. 98, pp. 16689– 16702.

Prospero, J.M. (1991) The Atmosphere Ocean Chemistry Experiment, an overview. Abstract of paper of American Chemistry. 201: 21-NUCL Part 2.

Prospero, J.M., Bonatti, E., Schuber, C., Carlson, T.N., (1970) Dust in the Caribbean traced to an African dust storm, Earth and Planetary Science Letters, Vol. 9, pp. 287-293.

Prospero J.M., Glaccum, R.A., Nees R.T. (1981) Atmospheric transport of soil dust from Africa to South America, Nature Letter, Vol. 289, pp. 570-572.

Prospero, J.M. (1999) Assessing the Impact of Advected African Dust on Air Quality and Health in the Eastern United States, Human and Ecological Risk Assessment: An International Journal, Vol. 5, Issue 3, pp. 471 – 479.

Prospero, J.M., Ginoux, P., Torres, O., Nicholsom, S.E. Gill, T.E. (2002) Environmental characterization of global sources of atmospheric soil dust identified with Nimbus 7 Total Ozone Mapping Spectrometer (TOMS) absorbing aerosol product. Reviews of Geophysics. Vol. 40, No. 1, pp 1-45.

Prospero, J.M., Lamb, P.J., (2003) African droughts and dust transport to the Caribbean: Climate Change Implications, Science, Vol. 302, Issue 5647, pp. 1024-1027.

Pye, K., (1987) Aerolian dust and dust deposits, Academic, San Diego, California.

Qu, J.J., Hao, X., Kafatos, M., Wang, L., (2006) Asian Dust Storm Monitoring Combining Terra and Aqua MODIS SRB Measurements**,** Geoscience and Remote Sensing Letters, IEEE Volume 3, pp. 484 – 486.

Rasmussen, K., Sorensen, M., Willetts B.B., (1985) Measurement of saltation and wind strength on beaches, Proceedings of the International Workshop on the Physics of Blown Sand, 301–325. Memoirs No. 8, 1985, Department of Theoretical Statistics, University of Aarhus.

Röhlich, P. (1978) Geological development of Jabal al Akhdar, Libya, Geologische Rundschau, Volume 67, Issue 2, pp.401-412.

Roskovensky, j.k., Liou, K.N. (2005) Differentiating airborne dust from cirrus clouds using MODIS data. Geophysical Research Letters, Vol. 32, L12809.

Safar, M.I., (1985) Dust and dust storms in Kuwait, Directorate of General Civil Aviation, Meteorological Department, State of Kuwait.

Salisbury J.W., Wald, A., (1992) The role of volume scattering in reducing spectral contrast of reststrahlen bands in spectra of powdered minerals, Icarus, Vol. 96, pp. 121-128.

Sassen K., DeMott P.J., Prospero J.M., Poellot, M.R., (2003) Saharan dust storms and indirect aerosol effects on clouds: CRYSTAL-FACE results, Geophysical Research Letters, Vol. 30, Issue 12, pp.1-4.

Satheesh, S.K. Moorthy, K.K. (2005) Radiative effects of natural aerosols: A review, Atmospheric Environment, Vol. 39, Issue 11, pp. 2089-2110.

Savoie, D.L. Prospero, J.M. (1982) Particle size distribution of nitrate and sulphate in the marine atmosphere, Geophysical Research Letters, Vol. 9, NO. 10, pp. 1207-1210.

Schepanski, K., Tegen, I., Laurent, B., Heinold, B., Macke, A., (2007) A new Saharan dust source activation frequency map derived from MSG-SEVIRI IR-channels. Geophysical Research Letters, Vol. 34, Issue 18, pp. 1-5.

Schepanski, K., Tegen, I., Todd, M. C., Heinold, B., Bo¨nisch, G., Laurent, B., Macke, A., (2009) Meteorological processes forcing Saharan dust emission inferred from MSG-SEVIRI observations of subdaily dust source activation and numerical models. Journal of Geophysical Research, Vol. 114, D10201.

Schütz, L., Jaenicke, R., Pietrek, H., (1981) Saharan dust transport over the North Atlantic Ocean. In: Pe´we´ T., L., (ed) Desert dust. Geological Society of America Spec Pap 186, pp. 87-100.

Schwartz, S.E., Wagener, R. Nemesure, S. (1995) Microphysical and compositional influences on shortwave radiative forcing of climate by sulphate aerosols. Abstracts of papers of the American chemical society. Vol. 208 No. 2.

Shi, Z., Krom, M.D., Bonneville, S., Baker, A.R., Bristow, C., Drake, N., Mann, G., Carslaw, K., McQuaid, J.B., Jickells, T., Benning, L.G. (2011) Influence of chemical weathering and aging of iron oxides on the potential iron solubility of Saharan dust during simulated atmospheric processing. Global Biogeochemical Cycles, Vol. 25, GB2010.

Shinn, E.A., Smith, G.W., Prospero, J.M., Betzer, P., Hayes, M.L., Garrison, V., Barber, R.T. (2000). African Dust and the Demise of Caribbean Coral Reefs. Geophysical Research Letters. 27(19), pp. 3029-3032.

Simpson, J.J, Huffird, G.L., Servranckx, R., Berg, J. Pieri, D. (2003) Airborne Asian Dust: Case study of long-range transport and implications for the detection of volcanic dust. Weather and Forecasting. Vol. 18, pp. 121-141.

Smith, T.E.L. (2008) Towards a field method for retrieving the spectral emissivity of urban surfaces. Dissertation for the MSc in Environment, King's College London.

Sokolik, I.N., Toon, O.B. (1996) Direct radiative forcing by anthropogenic airborne mineral aerosols. Nature. Vol. 381 (6584), pp. 681-683.

Swap, R, Ulanski, S, Cobbett, M. Garstand, M. (1996) Temporal and spatial characteristics of Saharan dust outbreaks. Journal of geophysical research. Vol. 101, No. D2, pp. 4205-4220.

Swap, R.M., Garstang, M. Greco, S. (1992) Saharan dust in the Amazon Basin. Tellus. Vol. 44, No.2 pp 133-149.

Tanre, D., Kaufman, Y. J., Herman, M., Mattoo, S. (1997) Remote sensing of aerosol properties over oceans using the MODIS/EOS spectral radiances. Journal of geophicical research, Vol. 102, No. D14, pp. 16971-16988.

Tegen, I. (2003) Modeling the mineral dust aerosol cycle in the climate system. Quarternary Science Reviews. Vol. 23, pp. 1821-1834.

Tegen, I., Fung, I. (1994) Modeling of mineral dust in the atmosphere: Sources, transport, and optical thickness. Journal of Geophysical Research, Vol. 99, pp. 22,897-22,914.

Tegen, I., Fung, I., (1995) Contribution to the atmospheric mineral aerosol load from land surface modifi cation. Journal of Geophysical Research, Vol. 100, pp. 18707–18726.

Tegen, I., Harrison, S. P., Kohfeld, K., Prentice, C., Coe, M., Heimann M. (2002). The impact of vegetation and preferential source areas on global dust aerosol: Results from a model study, Journal Geophysical Research, Vol. 107(D21), pp. 4576.

Toon, O.B., (2003) African dust in Florida clouds, Nature Vol. 424, pp. 623-624.

Torres, O., Bhartia, P.K., Herman, J.R., Ahmad, Z. Gleason, J. (1998) Derivation of aerosol properties from a satellite measurements of backscattered ultraviolet radiation: Theoretical basis. Journal of Geophysicals Research. Vol. 103, No. 17, pp. 99-110.

Udden, J.A. (1898) The mechanical composition of wind deposits, Augustana College.

Vermote E.F., Justice, C.O., Descloitres, J., Saleous, N.E., Ray, J., Roy, D., Margerin, B., Gonzalez, L. (2001) A global monthly coarse resolution reflectance data set from SeaWiFS for use in Land, Ocean and Atmosphere applications, International Journal of Remote Sensing, Vol. 22, pp. 1151-1158.

Wang, S., Wang, J., Zhou, Z., Shang, K. (2005a) Regional characteristics of three kinds of dust storm events in China. Atmospheric Environment Vol. 39, Issue 3, pp. 509-520.

Wang, X., Zhou Z., Dong Z. (2006) Control of dust emissions by geomorphic conditions, wind environments and land use in northern China: an examination based on dust storm frequency from 1960 to 2003, Geomorphology, Vol. 81, pp. 292-308.

Warren, A., Chappell, A., Todd, M., Bristow, C., Drake, N., Engelstaedter, S., Martins, V., M'bainayel, S., Washington, R. (2007) Dust-raising in the dustiest place on earth, Geomorphology, Vol. 92, pp. 25-37.

Washington, R., Todd, M., Middleton, N.J. Goudie, A.S. (2003) Dust-storm source areas determined by the Total Ozone Monitoring Spectrometer and surface observations, Annals of the Association of American Geographers, Vol. 93, No. 2, pp 297-313.

Washington, R., Todd, M.C., Engelstaedter, S.M., Mitchell, F. (2006) Dust and the low-level circulation over the Bodélé Depression, Chad: Observations from BoDEx 2005, Journal of Geophysical Research, Vol. 111, D03201.

Wald, A.E., Kaufman, Y.J., Tanre, D., Gao, B. (1998) Daytime and night-time detection of mineral dust over desert using infrared spectral contrast. Journal of Geophysical Research, Vol. 103, No. 32, pp. 307-313.

Wendling, P., (1977) Albedo and reflected radiance of horizontally inhomogeneous clouds, Journal of the Atmospheric Sciences, Vol. 34, pp. 642-650.

Wiggs, G.F.S., O'Hara, S.L., Wegerdt, J., Van Der Meers, J., Small, I., Hubbarb, R. (2003) The dynamics and characteristics of Aeolian dust in dryland Central Asia: possible impacts on human exposure and respiratory health in the Aral Sea basin. The Geographical Journal, Vol. 169, No. 2, pp. 142-157.

Wooster, M.J. Rothery, D.A. (1997). Thermal monitoring of Lascar Volcano, Chile using infrared data from the Along Track Scanning Radiometer: a 1992-1995 time-series. Bulletin of Volcanology, Vol. 58, pp. 566-579.

Wu, L., Braun, S.A., Qu, J.J., Hao, X. (2006) Simulating the formation of Hurricane Isabel (2003) with AIRS data, Geophysical Research Letters, VOL. 33, L04804.

Wurzler, S., Reisin, T.G., Levin, Z. (2000) Modification of mineral dust particles by cloud processing and subsequent effects on drop size distributions, Journal of Geophysical Research, Vol. 105, pp 4501-4512.

Xianjun Hao, John J. Qu (2000) Saharan dust storm detection using moderate resolution imaging spectroradiometer thermal infrared bands, Journal of Applied Remote Sensing, Vol. 1, No. 013510.

Xiong, X., Wu, A., Sun, J., Wenny, B. (2006) An Overview of Inter-comparison Methodologies for Terra and Aqua MODIS Calibration. Process of SPIE Vol. 6296 62960C-1.

Yaalon, D.H., Ganor, E. (1979) Rate of aeolian dust accretion in the Mediterranean and desert fringe environments of Israel, 19th International Congress of Sedimentology, 169-74.

Yoshioka, M., Mahowald, N., Dufresne, J.L., Luo, C. (2005) Simulation of absorbing aerosol indices for African dust. Journal Geophysical Research, 110, D18S17.

Zatchar, D. (1982) Soil Erosion, developments in soil science 10, Czechoslovakia.

Zhang, B., Tsunekawa, A., Tsubo, M., (2008) Contributions of sandy lands and stony deserts to long-distance dust emission in China and Mongolia during 2000-2006. Global and Planetary Change, Vol. 60, Issue 3-4, pp. 487-504.